NASA CR 114758
Contractor Report No.
LG74ER0070

AVAILABLE TO THE PUBLIC

SMALL SCALE WIND TUNNEL MODEL INVESTIGATION OF HYBRID HIGH LIFT SYSTEMS COMBINING UPPER SURFACE BLOWING WITH THE INTERNALLY BLOWN FLAP

By W. L. Waites and Y. T. Chin

June , 1974

Prepared under Contract NAS2-7812 (Task II) by
LOCKHEED GEORGIA COMPANY

86 South Cobb Drive
Marietta, Georgia

for

Ames Research Center

NATIONAL AERONAUTICS AND SPACE ADMINISTRATION

ABSTRACT

A small-scale wind tunnel test of a two engine hybrid model with upper surface blowing on a simulated expandable duct internally blown flap was accomplished in a two phase program. The low wing Phase I model utilized 0.126c radius Jacobs/Hurkamp flaps and 0.337c radius Coanda flaps. The high wing Phase II model was utilized for continued studies on the Jacobs/Hurkamp flap. Principal study areas included: basic data both engines operative and with an engine out, control flap utilization, horizontal tail effectiveness, spoiler effectiveness, USB nacelle deflector study and USB/IBF pressure ratio effects.

TABLE OF CONTENTS

LIST OF TABLES

LIST OF FIGURES

SYMBOLS

General Notation

AR	Aspect ratio, b^2/S
b	Wing span, centimeters (inches)
BLC	Boundary layer control
c	Chord, centimeters (inches)
$\bar{c}$, MAC	Mean aerodynamic chord, centimeters (inches)
C_D	Drag coefficient, $\frac{\text{drag}}{qS}$
C_L	Lift coefficient, $\frac{\text{lift}}{qS}$
$Cm_{\bar{c}/4}$	Pitching moment coefficient about $0.25\bar{c}$, $\frac{\text{pitching moment}}{qS\bar{c}}$
C_n	Yawing moment coefficient, $\frac{\text{yawing moment}}{qSb}$
C_R	Rolling moment coefficient, $\frac{\text{rolling moment}}{qSb}$
C_T	Thrust coefficient, $\frac{\text{static gross thrust}}{qS}$
Cy	Side force coefficient, $\frac{\text{side force}}{qS}$
IBF	Internally blown flap
F_A	Axial force, N (lb)
F_g	Gross thrust from calibration, N (lb)
F_N	Normal force, N (lb)
F_R	Resultant force $\sqrt{F_A^2 + F_N^2}$, N (lb)
J/H	Jacobs/Hurkamp
L	Left side operative
PR	Pressure ratio, total pressure/tunnel static pressure
q	Freestream dynamic pressure, N/square meter (lb/square foot)
R	Right side operative
S	Wing area, square meters (square feet)

General Notation (Continued)

x	Chordwise station, centimeters (inches)
y	Spanwise station, centimeters (inches)
z	Vertical distance from wing chord plane, centimeters (inches)
α	Fuselage reference line angle of attack, degrees
β	Angle of sideslip, $-\Psi$, degrees
δ_j	Jet deflection angle, $\tan^{-1} F_N/F_A$ degrees
Ψ	Angle of yaw of plane of symmetry, degrees
η	Spanwise position, $\frac{2y}{b}$
η_f	Flap static turning efficiency, F_R/F_g

Model Notation

B^{1A}	Fuselage. C-141 modified.
b^1	Bullet.
D^2	Dorsal. Free faired dorsal to approximate lines of EBF QUESTOL.
E^3	Aspect ratio 4.0 nozzle with center and edge bodies.
f_x^{23c}	Leading edge flap. 17 percent local wing chord, cambered and cut out for USB nacelles. Deflection from stowed position normal to hinge line denoted by subscript x.
f_x^{33}	Main Jacobs/Hurkamp flap. Nominal streamwise deflection angles denoted by x.
f_x^{34}	Auxiliary Jacobs/Hurkamp control flap. Nominal streamwise deflection angles denoted by x.
f_x^{35}	Main Coanda flap nominal trailing edge upper surface deflection angles denoted by x.
H_x^2	Horizontal stabilizer. Deflections denoted as subscript x.
N_x^{12}	Nacelles. Aspect ratio 4.0 slot nozzles. Nominal nacelle exit placement in percent local chord denoted by subscript x.
S^1	S^2 plus $D^2V^2b^1$.
S^2	$B^{1A}W^2f_x^{23c}\ Z^{w1}$ (high wing) or $B^{1A}W^1f_x^{23c}\ Z^{w2}$ (low wing).

Model Notation (Continued)

s_x^4	Spoiler. Full trailing edge flap span. Deflections from stowed position denoted by subscript x.
$s_x^{5A, B, C}$	Spoiler. Part span. A, inboard half flap span. B, outboard half flap span. C, inboard quarter flap span. Deflections from stowed position denoted by subscript x.
s_x^6	Spoiler, full trailing edge flap span with 50% porosity. Deflections from stowed position denoted by subscript x.
$s_x^{6A, B, C}$	Spoiler. Part span with 50% porosity, AR 1.0 tabs. A, B and C as with S^5. Deflections from stowed position denoted by subscript x.
U_x^4	Thrust deflector with open sides. Deflections denoted by subscript x.
U_x^5	U^4 thrust deflector with closed sides. Deflections denoted by subscript x.
V^2	Vertical stabilizer.
W^1	Wing. Sweep of c/4 = 30.000°.
W^2	Wing. Sweep of c/4 = 14.918°.
Z^{w1}	Wing-fuselage fillet, high wing.
Z^{w2}	Wing-fuselage fillet, low wing.

Pitch and Yaw Schedules

A	Pitch schedule; -8 degrees through stall in 4 degree increments.
B	Yaw schedule; -20 to +20 degrees in 5 degree increments.
C	Pitch schedule; minimum to define C_L at α of zero degrees and stall.

SUMMARY

An investigation has been conducted to determine the aerodynamic characteristics of a small scale model with a hybrid propulsive lift system. The hybrid concept represents a combination of the upper surface blowing (USB) system with the internally blown flap (IBF) to augment lift and provide control. The model was tested in low and high wing configurations in Phase I and Phase II programs, respectively. The wing sweep at the quarter chord was 30 degrees on the low wing model and 15 degrees on the high wing. Results were obtained for a variety of nacelle exit nozzle configurations in combination with two simulated expandable duct trailing edge flap systems, (1) the basic flap with knee radius 12.6 percent local chord and blowing at the knee and trailing edge, and (2) the Coanda flap with knee radius 33.7 percent local chord and blowing at the trailing edge only. Results were obtained for several flap deflections at nominal thrust coefficients from 0 to 3.0. Selected six-component longitudinal, lateral and directional data are presented with two engines operating and with an engine out.

Proper nacelle exit tailoring made the efficient utilization of the basic small radius flap possible. A maximum lift coefficient of 9.55 at a thrust coefficient of 3.0 was obtained with this small radius IBF surface and two USB nacelles equipped with 10 degree exit deflectors.

INTRODUCTION

The hybrid propulsive lift concept represents a combination of two high lift systems which utilize external blowing on the wing upper surface and internal blowing from the wing flap. Earlier independent investigation of these two systems is reported in reference 1 for the upper surface blowing (USB) concept and in reference 2 for the internally blown flap (IBF) concept. Both systems hold promise and are currently being considered independently in selected STOL transport designs. The upper surface blowing system depends upon the Coanda effect to turn engine jet exhaust and/or fan discharge air over the flap, and possesses possible noise advantages. The internally blown flap offers high aerodynamic efficiency with control of the boundary layer in conjunction with power transfer to reduce engine-out asymmetry. The use of large quantities of low pressure air requires large flow areas, and both of the hybrid systems investigated in the tests reported herein would utilize expanding internally blown flaps on the airplane. The Jacobs/Hurkamp (J/H) flap provides large flow areas for spanwise internal flow, but allows compact stowing of the flap in the clean configuration. The J/H flap attains increased internal flow area with flap deflection by proper location of the flap upper and lower surface hinge lines. The Coanda flap concept for this test also provides expanding area in a fashion similar to that of the J/H flap, but also requires a flexible upper surface in order to provide the large flap leading edge radii.

The obvious complimentary nature of the USB and the IBF systems pointed to the need to investigate the hybrid concept. This investigation was undertaken in the Lockheed V/STOL Wind Tunnel in a two phase program. The Phase I program was initiated in September, 1973, and 158 runs were secured. The Phase II program followed in November, 1973 with 242 runs. Results were obtained on small (J/H) and large (Coanda) radius flaps at several deflections with various nacelle exit configurations at thrust coefficients from zero to three. The Phase I data were obtained at Reynolds numbers from 0.137 to 0.308 million, based on a mean aerodynamic chord (MAC) of 0.31m and at dynamic pressures from 312.6 to 1393.2 N/m^2 (6.53 to 29.1 psf), respectively. Phase II results were obtained at slightly lower Reynolds numbers since the MAC was reduced to 0.29m.

MODEL

Figures 1 and 2 show the Phase I and II models installed in the 4.95 m (16.25 ft.) by 7.09 m (23.25 ft.) low speed test section of the Lockheed V/STOL Tunnel. The wing is located in the approximate center of the test section. Pertinent dimensional data for Phase I (low wing) and Phase II (high wing) models are given in table 1. The geometry of the basic models is shown in figures 3(a) and 3(b).

Wing

The Phase I wing had a quarter chord sweep of 30 degrees and aspect ratio of 6.5, while the Phase II wing sweep was reduced to 14.92 degrees and resulting aspect ratio of 7.73. Both models utilized the same physical wing set to the prescribed sweep angles. The basic airfoil was a Gelac TAC/STOL section with 0.125c thickness at the root and a linear taper to 0.095c at the tip. The ordinates of these sections are tabulated and plotted in table II.

Leading Edge Flaps

Full span 0.17c leading edge flaps were used to increase the stall angle of the models. The flap reference line was deflected down 60 degrees from the wing chord line. This was equivalent to a 110 degree deflection from the stowed position. The trailing edge of the lead ing edge device was placed forward of the basic airfoil nose 0.015c and up 0.005c perpendicular to the wing chord line. This gap and deflection of the leading edge flaps was maintained throughout the tests. Leading edge flap ordinates are tabulated and plotted in table III.

Trailing Edge Flaps

The two trailing edge flap systems investigated are presented in figure 4. Both are the expanding-duct type to provide sufficient duct area to supply the trailing edge blowing. The basic flap studied was the Lockheed Jacobs/Hurkamp (J/H) type with a typical small ki radius of 0.126c. This flap system, with a 0.095c control flap at the trailing edge, was set in the aft 0.40c of the wing. The Coanda flap was formed by adding a larger radius

piece to the basic J/H flap upper surface. This increased the flap radius to 0.337c and overall length to 0.43c. Both flap systems on high and low wing configurations spanned approximately 60 percent of the wing. Trailing edge flap deflections from 22 to 60 degrees were set with selected control flap articulation giving an additional $\pm$30 degrees.

Spoilers

The Phase II model was equipped with 0.10c spoilers. These spoilers were deflected up from the wing surface 10, 20 and 30 degrees. Solid and porous types were investigated. The porous type had a 50 percent porosity with sections removed to give aspect ratio 1.0 tabs. Spoilers covered the full flap span, inboard half flap span, inboard quarter flap span and outboard half flap span. The part-span porous spoilers are pictured in figure 5.

Fuselage

The fuselage had a constant 25.908 cm (10.2 in.) diameter center section. Forward and aft fairings were added to give a total length of 206.726 cm (81.388 in.) and fineness ratio of 7.98. Overall contouring represents a typical transport fuselage with aft loading capability.

Tail

The empennage is also a typical STOL transport configuration with geometry detailed in table 1. The horizontal tail incidence was set at 0 degrees for all base runs and deflected from -5 to +10 degrees in selected cases.

Nacelles

Both Phase I and Phase II models represented two engine aircraft configurations. The installation of the nacelle on the wing with the J/H flap is presented in figure 6. The nacelles were powered pneumatically and each had 40.325 square cm exit area. The basic exit had an aspect ratio of 4.0 (width of 12.7 cm and height of 3.175 cm), and was nominally placed at 0.20c, 0.35c and 0.50c positions on the wing. The majority of the tests were performed at the nominal 0.35c position. The variety of exit tailoring devices

that were deployed are shown in figure 7. The zero degree deflector was utilized in the majority of the Phase I tests, and the 10 degree deflector was installed for the main portion of Phase II tests. The model nacelles had no inlet and therefore the test results do not include engine ram drag. All model blowing systems operated at a nominal pressure ratio of 1.5, unless otherwise noted.

TESTS

Table IV is an index to both Phase I and II investigations. Forces and moments were measured through an angle-of-attack range from -8 to 26 degrees, or through stall in Schedule "A", and yaw range from -20 to 20 degrees, at zero angle of attack in Schedule "B". An abbreviated pitch schedule to define zero-alpha and maximum lift was also run as Schedule "C". The wind tunnel dynamic pressure was varied from 312.6 N/m^2 (6.53 psf) to 1393.2 N/m^2 (29.1 psf) giving a Reynolds number range from 0.137 to 0.308 million. Nominal thrust coefficients from zero to three were set by these variations in dynamic pressure.

The thrust coefficients shown herein are the sum of the individual system $C_{T's}$ for each run. Note that this procedure results in an "installed" C_T, i.e., as measured including any scrubbing drag, but that side force components are excluded in that only the lift and drag forces are vectorially summed.

The distribution of blowing inputs was held to specific nominal levels during the principal tests. The individual exit areas were adjusted to provide the desired thrust split at the slot total pressures. Specified thrust coefficients were then obtained by varying the tunnel dynamic pressure. Configurations with equal pressure ratios at nacelle and knee blowing points produce a nominal thrust split of 95%/5%; the nacelle and trailing edge thrust split was 85%/15%; and blowing from nacelle, knee, and trailing edge was distributed 80%/5%/15%.

Static Tests

Static thrust calibrations for each of the nacelles were made on the wind tunnel balance, a separate calibration being determined for each nacelle exit configuration. Each low wing test nacelle had three total pressure probes located just inside the nozzle exit. These probes required continual repair, and the subsequent high wing tests utilized a modified two probe design. The nacelle thrust was set during the runs utilizing the appropriate curve of thrust versus nozzle pressure ratio. The nacelle thrust utilized in this report is the vectorially summed thrust as calibrated from the balance normal and axial forces with the wing trailing edge flaps set at zero degrees.

The thrust of each of the BLC systems was also obtained on the balance with concurrent measurement of the pressure ratio in the appropriate system. Each wing semispan included three total pressure probes in the knee BLC system and three in the trailing edge BLC system. These probes were located as close to the exit slots as space permitted in order to obtain slot total pressure with minimum achievable error. The BLC lift and (negative) drag components were then vectorially summed for each model configuration, and this sum was used in the calculation of C_T.

Static tests were conducted in the wind tunnel with the wind off to determine the static jet angle and turning efficiency of each principal configuration. Phase I static tests include both one and two engine comparisons on the small and large radius flaps. Phase II static results are all based on the J/H flap and two engines operative, with the exception of a limited number of engine out checks.

The static turning angle was determined from the vecter resolution of lift and drag forces on the model. The efficiency was also based on this assessment along with the calibrated input forces, flaps up.

Wind-On Tests

The Phase I wind-on investigations included the following items:

Item		Runs		
		Small Radius Jacobs/Hurkamp Flap	Large Radius Coanda Flap	Total
Calibration		19	2	21
USB Nacelle Integration		38	20	58
Base Data				
All Engines	60° Flaps	18		18
	44° Flaps		16	16
	22° Flaps	18		18
Engine Out	60° Flaps	12		12
	22° Flaps	5		5
Control Flap Utilization		2		2
Horizontal Tail Effectiveness		8	—	4
		120	38	158

The Phase II test included the following items:

Item	Runs			
	60° Flaps	30° Flaps	22° Flaps	Total
Calibration	28	2	2	32
Base Data				
All Engines	16	12	16	44
Engine Out	17	8	12	37
Control Flap Utilization	30	15		45
Horizontal Tail Effectiveness	9	2	8	19
Spoiler Effectiveness	15	7	3	25
USB Nacelle Deflector Study	25			25
USB/IBF PR Effects	15			15
	155	46	41	242

The wind-tunnel test results, as six-component balance data, were reduced on-line during the test and off-line after the test using the Control Data Corporation 1700 computer. Normal wind tunnel corrections accounting for balance interactions, weight tares, trapeze tares, wind tunnel wall effects, and freestream flow angularities were applied to the data. Wing lift data required for wall-effects corrections were obtained from appropriate tail-off configurations run during the test. Corrections for support system tare and interference were not made.

RESULTS

Static Tests

The static turning efficiencies (η_f) and static turning angles (δ_j) for all principal configurations in Phase I and II test programs are presented in table V. Phase I results are given for 60 degree J/H flaps with a variety of nacelle exit configurations (slot, E^3, U_o^4, U_{10}^4). The 22 degree J/H flap was checked only with the U_o^4 exit deflector. The 58 and 44 degree Coanda flaps were investigated with the slot, U_o^4 and U_{10}^4 nacelle exits. The U_o^4 deflector on the nacelle at 35 percent chord was selected for the Phase I base runs. Phase II static results are given for 60, 30 and 22 degree J/H flaps. The 60 degree flap was checked with U_o^4, U_{10}^4 and U_{20}^4 nacelle exit deflectors and the U_{10}^4 was selected for use on the 30 and 22 degree flaps. The U_{10}^4 deflector set on the nacelle at 35 percent chord was selected for the main body of Phase II wind-on tests. The 60 degree J/H flap had an upper surface angle of 73.25 degrees and turned the jet 67.4 degrees under these conditions. The 30 degree J/H flap with an upper surface of 42.83 degrees turned the flow 38.4 degrees, and the 22 degree J/H flap with a 34.27 degree upper surface turned the flow 30.4 degrees.

Wind-On Tests

The basic stability axis results for the Phase I and II tests are presented in this section. C_L, C_D and $C_{m_{c/4}}$ coefficient data are plotted for pitch runs and C_R, C_n and C_y data are plotted for the yaw runs. These results from the Phase I and II test programs are presented in the following figures:

Phase I J/H Flap	Figure
USB Nacelle Integration	8, 9
Base Data	10-17
Base Data Engine Out	18-22
Control Flap Utilization	23
Horizontal Stabilizer Effectiveness	24, 25

Wind-On Tests (Continued)

Phase I Coanda Flap	
USB Nacelle Integration	26
Base Data	27-30
Phase II J/H Flap	
Base Data	31-42
Base Data Engine Out	43-62
Control Flap Utilization	63-78
Horizontal Stabilizer Effectiveness	79-83
Spoiler Effectiveness	84-91
USB Nacelle Deflector Study	92-97
USB/IBF PR Effects	98-102

These results were secured with detailed attention given to the setting of the model geometry and blowing levels for each symmetric and asymmetric configuration. However, in selected cases it was not possible to "zero" all lateral-directional forces and moments during symmetric configurational runs. Under these conditions the side force and yawing moment were zeroed with some attendant rolling moment. Efforts to isolate the cause of this asymmetry were unsuccessful.

DISCUSSION

This section presents selected effects data based on the Phase I and II general results already given.

Phase I USB Nacelle Integration (J/H and Coanda Flaps)

Figure 103 shows the static turning angle and efficiency for AR 4.0 slot, U_0^4, and U_{10}^4 deflector nacelle exits as a function of the nominal chordwise nacelle position on the wing with 60 degree J/H flaps. As the slot nozzle nacelle is moved forward on the wing the jet angle increases and the efficiency decreases. Installation of the U_{10}^4 deflector reduces this effect as the jet angle is constant at approximately 60 degrees with 96 percent efficiency. Figure 104 presents the same type results for 58 degree Coanda flaps. The installation of the deflectors improves the static turning and efficiency of the basic slot nozzle. The deflector unit spreads and thins the jet efflux to aid in turning by reducing the jet height at the flap knee. The increase in efficiency is considered to be the result of flow changes from the nacelle in the static flaps-up calibration configuration and the flaps down static efficiency evaluation. Flaps-up calibration of the nacelles with deflectors results in considerable spanwise flow out of the open ends of the deflectors. Calibration thrust is based on the vector sum of only the normal and axial thrust components. When the flaps are deflected down the spanwise flow components from the nacelle tend to be drawn to the negative pressure region directly behind the nacelle and are reclaimed in the normal-axial plane. Figures 105 and 106 present wind-on results for the J/H and Coanda flaps deflected 60 and 44 degrees, respectively. The exit tailoring devices utilized statically were also used in wind-on runs. The static tendency of these devices to increase jet angle results in higher lift coefficients in the low alpha range and at stall. The J/H flap maximum lift increases from about 5.0 to 6.2 in going from the slot nozzle to U_{10}^4 deflector.

Phase I Base Data (J/H and Coanda Flaps)

The J/H flap in Phase I tests was investigated with 60 and 22 degree deflections. The Coanda flap was checked at a 44 degree deflection. Figure 107 illustrates the development of lift at zero alpha for these flaps as a function of thrust coefficient. At a thrust

coefficient of 1.8 the 60 degree J/H flap C_L is 4.4 and the 22 degree C_L is 2.4. Articulation of the aft control flap on the basic 22 degree J/H flap causes a $\pm \Delta C_L$ variation of approximately 0.6. The Coanda flap performance is also included in this figure. The larger radius does not seem to offer any performance advantage as shown in figure 108. J/H and Coanda flap upper surface angles are plotted against C_L at a C_T of 1.8 and all fall on the same general trend line. Figures 109 and 110 present the drag and pitching moment results for the same flap configurations. In figure 111 the maximum lift of the Coanda flap is noted to have dropped to the J/H 22 degree flap level.

Phase I Base Data, Engine Out (J/H Flap)

Figure 112 illustrates the impact of selected type engine failures on lift development with the 60 degree J/H flap. The all-engines operating case is shown with circle symbols. The box symbols represent an engine failure with the remaining engine powering the IBF system symmetrically on both sides of the model. At a nominal C_T of 1.0 the zero-alpha lift is unchanged and the maximum lift is down approximately 0.5. Triangular symbols represent an engine failure in a cross ducted arrangement where the loss of an engine results also in the loss of the IBF system on the opposite side of the model. The lift loss with this system is higher as zero-alpha lift is down 0.4 and maximum lift is down 1.1 at a C_T of 1.0.

Phase I Control Flap Utilization (J/H Flap)

Figure 113 shows the influence of the aft control flap articulation on zero-alpha and maximum lift. This small device is powerful in altering lift (and drag) and controlling flight path.

Phase I Horizontal Stabilizer Effectiveness (J/H Flap)

Figures 114 and 115 present the tail on runs with 60 and 22 degree J/H flaps, respectively. For both flap deflections the C_m change is -0.08 per degree of tail incidence.

Phase II Base Data

The Phase II test program was given completely to the J/H flap system. Three flap deflections (60, 30 and 22 degrees) are presented in figure 116. Zero-alpha and

maximum lift is given as a function of nominal thrust coefficient. At a thrust coefficient of 2.0 the lift coefficient at zero-alpha is 6.2 and the maximum lift is 7.9 with 60 degree flaps. The zero-alpha lift of 6.2 compares with 5.0 from Phase I (figure 105). This increase is attributed to reduced wing sweep (30 to 15 degrees) and reduced jet shear interference between USB and IBF jet efflux, increased aspect ratio (6.5 to 7.73), and increased body lift carryover.

Phase II Base Data, Engine Out

Figure 117 shows the result of an engine-out condition with cross ducting from left nacelle to right IBF. At a nominal thrust coefficient of 1.5 the 60 degree flap zero-alpha lift is 4.1, 30 degree flap lift is 3.3 and 22 degree flap lift is 2.5. In figure 118, a variety of engine out conditions is presented with 60 degree flaps. Those failures where the knee BLC is retained on both left and right wings are noted to have less lift loss than the failure case with knee BLC out. Trailing edge blowing is noted to have a secondary effect. Circle symbols present the case with right nacelle and left IBF system operative. The zero-alpha lift of 3.9 at a C_T of 1.0 has a rolling moment coefficient of -0.04. Box symbols represent the case of an engine out and all IBF systems operative. The lift in this case is up to 4.5 but the rolling moment is -0.22.

Phase II Control Flap Utilization

The aft vane of the trailing edge flap system is capable of being articulated to a maximum of 30 degrees, up (-) or down (+). The ability of the flap system to statically turn the jet efflux was investigated on 60 degree flap with +15, -15, +30 and -30 degree control flap articulation. The 30 degree flap was checked with +15 and -15 degree control flap deflections. Figure 119 presents the variation of jet angle and turning efficiency plotted against the flap upper surface angle. The basic 60 degree flap with upper surface angle of 73.25 degrees turns the flow 67.4 degrees. A +30 degree control flap deflection brings the upper surface angle to 103.25 with resulting jet angle of 84.5 degrees. The variation of jet angle with flap upper surface angle is approximately linear. The 30 degree flap with $\pm$15 control flap articulation closely follows the trend line for main flap deflections of 22, 30 and 60 degrees. This indicates that the control flap is as effective as the main flap in flow vectoring in the low flap deflection range. The static

jet angle variation produces a wind-on lift variation presented in figure 120 for 60 degree flaps. At a nominal thrust coefficient of 2.0 the zero-alpha lift coefficient varies from 2.9 to 6.85. Figures 121 and 122 show the drag and pitching moment coefficient for the same flap variations. Maximum lift varies from 5.9 to 8.05 under the same conditions as shown in figure 123. Maximum lift development on the 60 degree flap with positive control flap deflection is noted to be limited to about 8.0. The high static jet angles (67.4 to 84.5 degrees) with the additional stall pitch angle pointed to a possible problem. The tunnel test section floor was tufted and the jet was found to be striking the floor under the model with some flow reversal, wind on.

The usefulness of the control flap as a flight path control device is pointed out in figures 124 and 125 as the lift and drag increments for control flap articulation on a basic 60 degree flap are shown. At a nominal thrust coefficient of 2.0 a symmetric +15 degree articulation produces a ΔC_L of 0.45 and ΔC_D of 0.62. The 30 degree flap results presented in figures 126 and 127 indicate a ΔC_L of 1.0 and ΔC_D of 0.45 under the same thrust and articulation conditions. In each of these cases thrust is supplied to the USB nacelles and IBF knee and trailing edge. The impact of variations in thrust input to these points is illustrated in figure 128 as the thrust to the trailing edge is reduced and then eliminated. Next, the knee blowing is eliminated and in this case the ability to vary lift by control flap articulation is still present. This would tend to indicate the flow is being turned effectively on the main flap before it reaches the trailing edge control flap.

Asymmetric deflection of the control flap as a lateral control device indicates a significant cross coupling in yaw and side force. Figure 129 shows the influence of a $\pm$15 and $\pm$30 degree control flap articulation on roll, yaw and side force coefficient. At a C_L of 5.7 the C_R is 0.1, C_n is -0.23 and C_y is 0.28 for a +30 left and -30 right control flap deflection on 60 degree flaps.

Phase II Horizontal Stabilizer Effectiveness

Tail-on runs were made with 60, 30 and 22 degree flaps. In each case the horizontal tail incidence was varied from -5 (leading edge down) to +10 degrees. The zero-alpha

variation of C_m with incidence is -0.08 per degree on 60 degree flaps as shown in figure 130.

Phase II Spoiler Effectiveness

Ten-percent chord spoilers which spanned the trailing edge flaps were investigated with 10, 20 and 30 degree deflections. The spoiler hinge line was 0.10c forward of the flap knee BLC slot and this BLC slot remained unchanged with spoiler deflection. Figure 131 shows the effect of symmetric spoiler deployment with 60 degree J/H flaps. At a nominal thrust coefficient of 2.0 the zero-alpha lift coefficient is 6.2. The 10 degree spoiler reduces the lift to 3.5, 20 degree spoiler lift is 2.5 and 30 degree spoiler lift is 1.9. This solid spoiler spanning the complete trailing edge flap is a very powerful device. Spoiler deployment at other flap deflection produces the results given in figure 132. The spoiler's deflection largely controls the lift level, and for all flap deflections tested the 30 degree spoiler lift is constant. Part span solid spoilers were also investigated to reduce this drastic effect. Inboard half and quarter flap span spoilers were checked along with outboard half span units. Twenty-degree spoiler results are shown in figure 133 at a nominal thrust coefficient of 2.0 with 60 degree J/H flaps. Starting without spoilers the zero-alpha lift is 6.2, outboard half span spoiler lift is 5.6, inboard quarter span spoiler lift is 4.2, inboard half span lift is 3.0 and full span spoiler lift is 2.5. Part span spoilers offer considerable variation in effectiveness. Figure 133 also shows the impact of cutting the spoilers to 50 percent porosity by spacing AR 1.0 tabs across the span. Porosity greatly reduces the spoiler effectiveness, and in conjunction with spanwise positioning the spoiler effectiveness can be set to a desired level.

These spoilers can also be deflected on one wing as a lateral control device. Figure 134 presents the resulting rolling moment change as the right spoiler is deflected 20 degrees. Outboard half span (#2), inboard half span (#4) and full right side (#5) spoilers are included. Asymmetric control flap results of $\pm$15 degree (#1) and $\pm$30 degree (#3) are also included for comparison.

Phase II USB Nacelle Deflector Study

A series of nacelle exit deflectors was attached to the basic aspect ratio 4.0 exit. The U^4 configuration was deflected down from the initial 20 degree closure angle by 0 (U^4_0),

10 (U^4_{10}) and 20 (U^4_{20}) degrees. The aspect ratio of these units was 4.9, 5.9 and 11.4 respectively. The nozzle exit height to flap knee radius ratio was 0.64 (U^4_0), 0.53 (U^4_{10}) and 0.44 (U^4_{20}). The U^5_{10} deflector was formed from the U^4_{10} by enclosing the deflector sides. The U^4_0 maximum lift was 7.2 as shown in figure 135. This increases to 7.9 and then 8.1 for U^4_{10} and U^4_{20} deflectors. The U^4_{10} value of 7.9 is reduced to 6.7 when the deflector sides are closed to form the U^5_{10} unit. The edge tailoring of exhaust deflectors is thus shown to be important in aerodynamic performance optimization. The U^4_{10} was selected to further investigate the influence of nacelle chordwise position on the wing. Nominal 20, 35 and 50 percent chord nacelle positions were investigated. Figures 136 and 137 show the influence of nacelle position, and at a thrust coefficient of 2.0 maximum lift varies from 7.7 to 8.3 as the nacelle is moved forward on the wing. This forward movement allows increased spreading of the jet efflux over a greater portion of the flap span.

Figures 138 and 139 compre the U^4_{10} and U^5_{10} deflectors. Figure 138 presents static results and 139 presents wind-on results. Figure 138 indicates the U^5_{10} deflector static jet angle was influenced by pressure ratio variations while the U^4_{10} was not. The loss in jet angle with increasing PR in figure 138 is also reflected in a slight zero-alpha lift loss from 3.6 to 3.4 as the PR increases from 1.23 to 1.50. Figure 140 shows a lift comparison of the U^4_{10} and U^5_{10} units as a function of thrust coefficient. At a thrust coefficient of 1.0 the zero-alpha and maximum lift of the U^4_{10} is 0.8 higher than the U^5_{10}.

Phase II USB/IBF Pressure Ratio Effects

A more detailed study of pressure ratio effects was made with the U^4_{10} deflector and selected blowing from the IBF knee and trailing edge. Figure 141 presents lift results with selected blowing from the nacelles; nacelles and knee; nacelles and trailing edge; and nacelles, knee and trailing edge. In the PR range from 1.2 to 1.6 little effect is recorded. The variation in lift was principally a function of blowing combinations and figure 142 shows the zero-alpha lift variation for selected blowing. The nacelle-alone lift was approximately 5.2, and the addition of trailing edge blowing increases lift to 5.6. The importance of knee blowing is emphasized as nacelle and knee blowing lift increases to 6.2 and the addition of trailing edge blowing to this configuration at a

1.5 PR shows little lift increase. Another important factor investigated in this section was the variation in relative USB and IBF pressure ratios. Selected nacelle-knee and nacelle-knee-trailing edge cases are shown in figure 143. A 20 percent reduction in knee PR below the USB nacelle PR level results in a zero-alpha lift reduction from 6.1 to 5.4.

CONCLUSIONS

The following conclusions are drawn from the Phase I and II small scale wind tunnel tests:

1. Phase I and II static tests indicate the hybrid powered lift concept offers high turning efficiency with minimum jet turning lag (difference between flap upper surface angle and static jet angle).

2. The small radius Jacobs/Hurkamp flap with knee BLC was found to work as well aerodynamically as the larger continuous radius Coanda flap without knee BLC.

3. The Phase I low wing performance level was not as high as the Phase II high wing. Phase II performance increases are attributed to increased aspect ratio, reduced sweep and resulting reduced shear between the USB and IBF jet efflux, and increased body lift carryover.

4. Nacelle exit tailoring is important in aerodynamic performance optimization. Nacelle exit deflectors with open sides (U^4) were found to be better than those with closed sides (U^5).

5. Nacelle movement forward on the wing tends to give small increases in aerodynamic efficiency which must be traded against structural efficiency.

6. Nacelle pressure ratio effects were found to be minimum in the 1.2 to 1.6 range when the nacelle was fitted with an exit deflector.

7. Nacelle and IBF pressure ratio differentials were found to be detrimental when the IBF knee PR dropped below the nacelle value.

8. Retention of the BLC at the flap knee was found to be the key in retaining high aerodynamic efficiency by attaching flow on the outboard flap span not influenced by the USB nacelles. Trailing edge blowing from the IBF system was found to have a secondary effect.

9. The hybrid powered high lift concept offers powerful flight path control effectiveness by the use of an aft control flap mounted at the main flap trailing edge.

10. The hybrid concept is very sensitive to spoiler deployment in the USB input regions on the wing. Spoiler position and porosity were found to be powerful in controlling effectiveness.

REFERENCES

1. Aoyagi, Kiyoshi; Falarski, Michael D.; Koenig, David G.: Wind Tunnel Investigation of a Large-Scale Upper Surface Blown-Flap Transport Model Having Two Engines. NASA TM X-62,296, August 1973

2. Aiken, Thomas N.; Aoyagi, Kiyoshi; Falarski, Michael D.: Aerodynamic Characteristics of a Large-Scale Model With a Swept Wing and a Jet Flap Having an Expandable Duct. NASA TM X-62,281, September, 1973

TABLE I. - MODEL DIMENSIONAL DATA

Wing	Low Wing Phase I Model		High Wing Phase II Model	
Area, square meters (square feet)	0.5988	(6.446)	0.6033	(6.494)
Span, centimeters (inches)	197.287	(77.672)	216.052	(85.026)
MAC length, centimeters (inches)	31.468	(12.389)	28.928	(11.387)
Sweep of c/4, degrees	30.000		14.918	
Taper ratio	0.501		0.509	
Aspect ratio	6.500		7.731	
Incidence, degrees	3.0		3.0	
Twist, degrees	0		0	
Anhedral, degrees	0		0	
Thickness ratio, % local wing chord				
Root	12.5		13.7	
Tip	9.5		10.5	
Leading Edge Flaps				
Chord length, % local wing chord	17		17	
Deflection angle, degrees	60		60	
Flap-wing gap, % local wing chord				
Horizontal	1.5		1.5	
Vertical	0.5		0.5	
Trailing Edge Flaps				
Jacobs/Hurkamp Flap:				
Knee radius at nacelle ℄, centimeters (inches)	4.064	(1.6)	4.064	(1.6)
Knee radius, % local wing chord	12.6		12.6	
Flap chord length, % local wing chord	40		40	
Control flap chord length, % local wing chord	9.5		9.5	
Flap span, % wing span	61		60.2	
Coanda Flap:				
Knee radius at nacelle ℄, centimeters (inches)	11.125	(4.38)		
Knee radius, % local wing chord	33.7			
Flap chord length, % local wing chord	43			

Trailing Edge Flaps (Continued)

Control Flap chord length, % local wing chord	9.3			
Flap span, % wing span	61			
Fuselage				
Length, centimeters (inches)	206.726	(81.388)	206.726	(81.388)
Maximum frontal area, square meters (square feet)	0.0527	(0.567)	0.0527	(0.567)
Maximum diameter, centimeter (inches)	25.908	(10.200)	25.908	(10.200)
Horizontal Tail				
Area, square meters (square feet)	0.210	(2.264	0.210	(2.264)
Span, centimeters (inches)	97.450	(38.366)	97.450	(38.366)
MAC length, centimeters (inches)	23.101	(9.095)	23.101	(9.095)
Sweep of c/4, degrees	24.4		24.4	
Taper ratio	0.37		0.37	
Aspect ratio	4.52		4.52	
Anhedral, degrees	0		0	
Thickness ratio, % local chord	10.4		10.4	
Tail length, in wing MAC	3.485		4.201	
Tail height, in wing MAC	2.278		1.526	
Vertical Tail				
Area, square meters (square feet)	0.124	(1.339)	0.124	(1.339)
Span, centimeters (inches)	42.448	(16.712)	42.448	(16.712)
MAC length, centimeters (inches)	30.112	(11.855)	30.112	(11.855)
Sweep of c/4, degrees	26.5		26.5	
Taper ratio	0.55		0.55	
Aspect ratio	1.449		1.449	
Thickness ratio, % local chord				
Root	12.0		12.0	
Tip	11.2		11.2	
Bullet length, centimeters (inches)	33.528	(13.2)	33.528	(13.2)
Tail length, in wing span	0.454		0.469	
Nacelles				
Length, centimeters (inches)	30.480	(12.00)	30.480	(12.00)
Max. width, centimeters (inches)	19.050	(7.50)	19.050	(7.50)

Nacelles (Continued)

Max. depth, centimeters (inches)	6.985	(2.75)	6.985	(2.75)
Toe angle, degrees	0		0	
Basic nozzle aspect ratio	4.0		4.0	
Exit area, square centimeters (square inches)	40.325	(6.25)	40.325	(6.25)
Exit width, centimeters (inches)	12.700	(5.00)	12.700	(5.00)
Exit height, centimeters (inches)	3.175	(1.25)	3.175	(1.25)
Spanwise nacelle ℄, centimeters (inches)	27.000	(10.63)	29.018	(11.448)
Spanwise location, % wing semi-span	27.4		26.9	
Longitudinal location of nozzle, % local chord	20.0		20.6	
	35.2		35.6	
	50.5		52.1	

Nacelle Exit Devices

Deflector length, % chord at nacelle ℄	7.7		8.4	
0° deflector exit height, centimeters (inches)	2.593	(1.021)	2.593	(1.021)
10° deflector exit height, centimeters (inches)	2.159	(0.85)	2.159	(0.85)
20° deflector exit height, centimeters (inches)			1.791	(0.705)
Insert center body radius, centimeters (inches)	1.588	(0.625)		
Insert edge body radius, centimeters (inches)	3.175	(1.25)		

TABLE II. - WING SECTION CONTOURS OF ROOT AND TIP SECTIONS

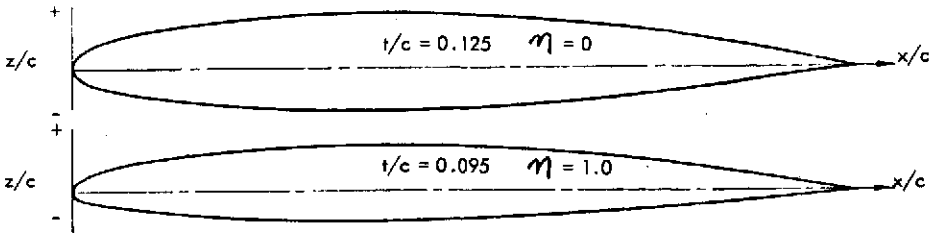

x/c	z/c			
	Upper		Lower	
	η = 0	η = 1.0	η = 0	η = 1.0
0.0	0.0	0.0	0.0	0.0
0.00125000	0.00572317	0.00443440	-0.00537467	-0.00391100
0.00250000	0.00812602	0.00636791	-0.00745688	-0.00536297
0.00375000	0.00997585	0.00787970	-0.00900261	-0.00641807
0.00500000	0.01153987	0.00917388	-0.01027016	-0.00726702
0.00625000	0.01291596	0.01032104	-0.01136523	-0.00799216
0.00750000	0.01415987	0.01136577	-0.01233640	-0.00862732
0.01000000	0.01636764	0.01323777	-0.01401720	-0.00970796
0.01250000	0.01830336	0.01489240	-0.01545995	-0.01062228
0.01875000	0.02238220	0.01841221	-0.01842389	-0.01246779
0.02500000	0.02575428	0.02134313	-0.02082859	-0.01394589
0.05000000	0.03555018	0.02982411	-0.02792389	-0.01837053
0.07499999	0.04222788	0.03544696	-0.03316647	-0.02183691
0.09999990	0.04733524	0.03966150	-0.03737882	-0.02470893
0.14999998	0.05509348	0.04610780	-0.04366652	-0.02894142
0.19999999	0.06074440	0.05085341	-0.04810718	-0.03186756
0.25000000	0.06488276	0.05436992	-0.05124890	-0.03388572
0.29999989	0.06777489	0.05686748	-0.05333706	-0.03517465
0.34999990	0.06954688	0.05844624	-0.05448649	-0.03581752
0.39999998	0.07025450	0.05915145	-0.05474475	-0.03584716
0.44999999	0.06991160	0.05899128	-0.05413271	-0.03528224
0.50000000	0.06853825	0.05798045	-0.05267122	-0.03413878
0.54999989	0.06615323	0.05612940	-0.05038956	-0.03244295
0.59999990	0.06277531	0.05344871	-0.04731639	-0.03022005
0.64999998	0.05841661	0.04993883	-0.04348744	-0.02750618
0.69999999	0.05309385	0.04560722	-0.03893371	-0.02433011
0.75000000	0.04681299	0.04044509	-0.03369706	-0.02073700
0.79999989	0.03957576	0.03443734	-0.02782363	-0.01677852
0.84999990	0.03137351	0.02755326	-0.02137010	-0.01252209
0.89999998	0.02217282	0.01972492	-0.01441823	-0.00807286
0.94999999	0.01188206	0.01079715	-0.00710873	-0.00362475
0.97499990	0.00624426	0.00578988	-0.00341987	-0.00154595
1.00000000	0.0	0.0	0.0	0.0

TABLE III. - LEADING EDGE FLAP CONTOURS

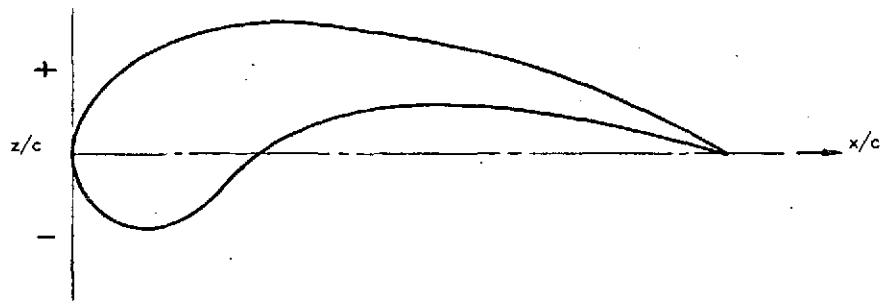

x/c	z/c	
	Upper	Lower
0.0	0.0	0.0
0.025	0.0714	-0.0715
0.050	0.104	-0.0925
0.075	0.1275	-0.1078
0.100	0.1450	-0.1141
0.150	0.1720	-0.1113
0.200	0.189	-0.0825
0.250	0.200	-0.0295
0.300	0.202	0.0105
0.400	0.198	0.0552
0.500	0.181	0.0724
0.600	0.161	0.0760
0.700	0.134	0.0646
0.800	0.100	0.0475
0.900	0.059	0.0248
1.000	0.0	0.0

TABLE IV. WIND TUNNEL TEST RUN INDEX
PHASE I LOW WING

CONFIGURATION	α Deg.	Ψ Deg.	NOMINAL THRUST COEFFICIENT 0	1.0	2.0	3.0	St.	REMARKS PRESS. RATIO VAR. NAC.	KN.	T.E
USB NACELLE INTEGRATION										
$S^2N_{35}^{f}{}^{12,33}_{60}{}^{f}{}^{34}_{0}$ (Left Wing Powered)	0	0					24,25 39	1.2-1.6	1.0	1.0
	↓	↓					34		As Nac.	↓ As
							35		↓	Nac.
							32, 33	↓	1.5	1.0
$S^2N_{35}^{f}{}^{12,33}_{60}{}^{f}{}^{34}_{0}U_0^4$	0	0					40	1.2-1.7	1.0	1.0
							37		As Nac.	As Nac.
U_{10}^4							41		1.0	1.0
							36	↓	As Nac.	As Nac.
$S^2N_{35}^{f}{}^{12,33}_{60}{}^{f}{}^{34}_{0}E^3$	0	0					38	1.2-1.6		
$S^2N_{20}^{f}{}^{12,33}_{60}{}^{f}{}^{34}_{0}$	0	0					44	1.3-1.6		
N_{50}^{12}							43			
U_{10}^4							42	↓	↓	↓
$S^2N_{35}^{f}{}^{12,33}_{60}{}^{f}{}^{34}_{0}U_0^4$	0	0		69	69	69	68	1.6	1.5	1.4
				71	71	71	72	1.4		
				78	78	78	77	1.6		
U_{10}^4				75	75	75	74	1.7		
f_{22}^{33} U_0^4				164	164	164	163	1.6		
f_{60}^{33}	A*				70			1.6		
					73			1.4		
					79			1.6		
U_{10}^4					76			1.7		

* Pitch and yaw schedules given on page xx

TABLE IV. WIND TUNNEL TEST RUN INDEX
PHASE I LOW WING

CONFIGURATION	∝ Deg.	Ψ Deg.	NOMINAL THRUST COEFFICIENT 0	1.0	2.0	3.0	St.	REMARKS
BASE DATA								
$S^2N_{35}^{12}f_{60}^{33}f_{0}^{34}U_0^4$	A	0	82	80	70	81	68	
	0	B	87	86	85	84	88	
f_{22}^{33}	A	0	167	166	165	112	163	
	0	B	116	115	114	113		
S^1 H_0^2	A	0	122	123	124	125		Run 126, C_T=4.0
	0	B	118	119	120	121		
f_{60}^{33}	A	0	95	94	93	92		
	0	B	91	90	89	88		
BASE DATA-ENGINE OUT								RIGHT NAC OUT; LEFT IBF OUT
			C_T=	.5	1.0	1.5		
$S^2N_{35}^{12}f_{60}^{33}f_{0}^{34}U_0^4$	A	0		107	106	105		
	0	B			108			
f_{22}^{33}	A	0			136			
	0	B			135			
S^1 H_0^2	A	0			133		131	
	0	B			134			
f_{60}^{33}	A	0			111		109	
	0	B			110			
	A	0			101		100	ALL IBF ON
	0	B			102			
S^2	A	0			104			
	0	B			103			

TABLE IV. WIND TUNNEL TEST RUN INDEX
PHASE I LOW WING

CONFIGURATION	α Deg.	ψ Deg.	NOMINAL THRUST COEFFICIENT 0	1.0	2.0	3.0	St.	REMARKS PRES. RATIO NAC	KN	VAR. TE
CONTROL FLAP UTILIZATION										
$S^2N^{12}_{35}f^{33}_{22}f^{34}_{+15}U^4_0$	A	0			137					
↓ ↓ ↓ f^{34}_{-15} ↓	↓	↓			138					
HORIZONTAL STABILIZER EFFECTIVENESS										
$S^1N^{12}_{35}f^{33}_{60}f^{34}_{0}H^2_{-5}U^4_0$	A	0	99	98	97	96				
↓ ↓ f^{33}_{22} ↓ ↓ ↓	↓	↓	127	128	129	130				
USB NACELLE INTEGRATION										
$S^2N^{12}_{35}f^{35}_{58}f^{34}_{0}$ (Right Wing Powered)	0	0					23	1.1-1.3	1.0	1.0 As
↓ ↓ ↓ ↓ ↓ ↓	↓	↓					46	1.2-1.3	1.0	Nac.
							58	1.2-1.4	1.3-1.5	1.2
U^4_0							56	↓	1.0	1.2-1.3
↓							50	1.2-1.6	↓	1.0
U^4_{10}							49	↓	↓	
↓							57	1.2-1.4	1.3-1.5	1.1-1.2
↓ ↓							47 48	↓	1.0	1.2-1.3
N^{12}_{20}							53	1.2-1.5	↓	1.0
↓							52	1.2-1.4	↓	1.2-1.3
N^{12}_{50}							54	↓	↓	1.2-1.3
↓ ↓ ↓ ↓ ↓	↓	↓					55	1.2-1.5	↓	1.0
$S^2N^{12}_{35}f^{35}_{44}f^{34}_{0}$	0	0	142	142	142	142	141			
U^4_0	↓	↓		146	146	146	145			
↓ ↓ ↓ ↓ U^4_{10}	↓	↓		144	144	144	143			

TABLE IV. WIND TUNNEL TEST RUN INDEX
PHASE I LOW WING

CONFIGURATION	α Deg.	Ψ Deg.	NOMINAL THRUST COEFFICIENT 0	1.0	2.0	3.0	St.	REMARKS
BASE DATA								
$S^2 N_{35}^{12} f_{44}^{35} f_{0}^{34} U_{0}^{4}$	A	0	150	147	148	149		
	0	B	151	152	153	154		
$S^1 \quad f_{0}^{34} \quad H_{o}^{2}$	A	0	159	162	161	160		
	0	B	158	157	156	155		

TABLE IV. WIND TUNNEL TEST SUMMARY
PHASE II HIGH WING

CONFIGURATION	∝ Deg.	Ψ Deg.	NOMINAL THRUST COEFFICIENT 0	1.0	2.0	3.0	St.	REMARKS
BASE DATA								
$S^2 N_{35}^{12,33} f_{60}^{33,34} f_0^4 U_{10}$	A	0	45	44	153 42	43		
	0	B	64	63	61	62		
f_{30}^{33}	A	0	162		158	161		
	0	B	163		159	160		
f_{22}^{33}	A	0	243	239	235	238		
	0	B	242	240	236	237		
S^1 H_0^2	A	0	222	219	215	218		
	0	B	221	220	216	217		
f_{30}^{33}	A	0	200		196	199		
	0	B	201		197	198		
f_{60}^{33}	A	0	72	69	65	68		
	0	B	71	70	66	67		
BASE DATA ENGINE OUT			$C_T=$	0.5	1.0	1.5	3.0	
$S^2 N_{35}^{12,33} f_{60}^{33,34} f_0^4 U_{10}$	A	0		92	89	90	94	LEFT NAC OUT; RT IBF OUT
	0	B		93	88	91		
f_{30}^{33}	A	0			188	191		
	0	B			189	190		
f_{22}^{33}	A	0		233	229	232		
	0	B		234	230	231		
f_{60}^{33}	A	0		98	96	97		ALL IBF ON RT. T.E. OUT
	A	0			95			

TABLE IV. WIND TUNNEL TEST SUMMARY
PHASE II HIGH WING

CONFIGURATION	α Deg.	Ψ Deg.	NOMINAL THRUST COEFFICIENT 0	1.0	2.0	3.0	St.	REMARKS
BASE DATA ENGINE OUT			$C_{T=}$	0.5	1.0	1.5		LEFT NAC OUT RT IBF OUT
$S^1N^{12}_{35}f^{33}_{60}f^{34}_{0}\ U^4_{10}\ H^2_0$	A	0		86	82	85		
	0	B		87	83	84		
	A	0			192	195		
	0	B			193	194		
f^{33}_{22}	A	0		227	223	226		
	0	B		228	224	225		↓ ↓
CONTROL FLAP UTILIZATION		$C_{T=}$	0	1.0	2.0	3.0		
$S^2N^{12}_{35}f^{33}_{60}f^{34}_{15}\ U^4_{10}$	A	0	114	113	111	112		
f^{34}_{30}					128			
f^{34}_{-15}			122	120	118	119		
f^{34}_{-30}					129			
$f^{33}_{30}f^{34}_{15}$			174	173	171	172		
f^{34}_{-15}	↓	↓	188	182	179	181		
$S^2N^{12}_{35}f^{33}_{60}f^{34}_{+15L-15R}\ U^4_{10}$	A	0	127	126	123	124		
$f^{34}_{+30L-30R}$					131			
$f^{33}_{30}f^{34}_{+15L-15R}$	↓	↓	178	177	175	176		
$f^{33}_{60}f^{34}_{+30L-30R}$	0	0	133	133	133	133		
			$C_{T=}$	0.5	1.0	1.5		
$S^2N^{12}_{35}f^{33}_{60}f^{34}_{+15L-15R}U^4_{10}$	A	0		137	135	136		LEFT NAC OUT RT IBF OUT
$f^{34}_{+30L-30R}$					134			
$f^{33}_{30}f^{34}_{+15-15R}$	↓	↓		187	185	186		↓ ↓
			$C_{T=}$	1.0	2.0	3.0		
$S^2N^{12}_{25}f^{33}_{60}f^{34}_{+15}\ U^4_{10}$	A	0			115			NAC & KN T.E. PR 1.5 PR 1.2
f^{34}_{-15}	↓	↓			116			↓ ↓

TABLE IV. WIND TUNNEL TEST SUMMARY
PHASE II HIGH WING

CONFIGURATION	α Deg.	Ψ Deg.	NOMINAL THRUST COEFFICIENT 0	1.0	2.0	3.0	St.	REMARKS
$S^2N^{12,33}_{25}f^{34}_{60}f^{4}_{0}\ U^{4}_{10}$	A	0			117			NAC. KN. T.E.
$S^2N^{12,33}_{35}f^{34}_{60}f_{+15}$	↓	↓			34			1.5 1.0 1.0
↓ f^{34}_{-15}	↓	↓			38			1.5 1.5 1.0
↓	↓	↓			35			1.5 1.0 1.0
↓	↓	↓			37			1.5 1.5 1.0
HORIZONT.STAB.EFFECT.								
$S^1N^{12,33,34}_{35}f^{2}_{60}f_{0}H^{2}_{-5}\ U^{4}_{10}$	A	0	76	75	73	74		
↓ H^2_{+10}	↓	↓	80	79	77	78		
$f^{33}_{30}\ H^2_{-5}$					202			
↓ H^2_{+10}					203			
$f^{33}_{22}\ H^2_{-5}$			214	213	211	212		
↓ ↓ H^2_{+10}			210	209	207	208		
↓ ↓ $f^{33}_{60}f^{34}_{0}H^2_{+5}$ ↓	↓	↓			81			
SPOILER EFFECTIVENESS								SPOILERS
$S^2N^{12,33,34}_{35}f^{4}_{60}f_{0}s^{4}_{10}\ U^{4}_{10}$	A	0	141	140	138	139		Full Span
↓ ↓ ↓ ↓ s^4_{20} ↓	↓	↓			142			↓
s^4_{30}					144			
s^{5A}_{20}					143			Inbd. Half Span
s^{5B}_{20}					145			Outbd. Half Span
s^{5C}_{20}					149			Inbd. Quar. Span
s^{6A}_{20}					151			Porous Inbd. Hf. Span
s^{6B}_{20}					150			Por. Outbd. Hf. Span
↓ ↓ ↓ ↓ s^{6C}_{20} ↓	↓	↓			152			Por. Inbd. Qtr. Span

TABLE IV. WIND TUNNEL TEST SUMMARY
PHASE II HIGH WING

CONFIGURATION	∝ Deg.	Ψ Deg.	NOMINAL THRUST COEFFICIENT 0	1.0	2.0	3.0	St.	REMARKS
$S^2N^{12}_{35}f^{33}_{30}f^{34}_{0}s^{4}_{10}U^{4}_{10}$	A	0	167	166	164	165		SPOILERS Full Span.
s^{5A}_{+20}	↓	↓			168			Inbd. Hlf. Span
s^{5B}_{20}	↓	↓			169			Outbd. Hlf. Span
s^{4}_{20}	↓	↓			170			Full Span
$S^2N^{12}_{35}f^{33}_{60}f^{34}_{0}s^{4R}_{20}$	↓	↓			148			Right Spoilers only
s^{5AR}_{20}	↓	↓			147			↓
s^{5BR}_{20}	↓	↓			146			
$S^2N^{12}_{35}f^{33}_{22}f^{34}_{0}s^{4}_{20}$	↓	↓			244			Full Span
s^{5A}_{20}	↓	↓			245			Inbd. Half Span
s^{4}_{30}	↓	↓			246			Full Span
USB NACELLE DEFLECTOR STUDY								
$S^2N^{12}_{35}f^{33}_{60}f^{34}_{0}U^{4}_{0}$	A	0			47			
U^{4}_{10}	↓	↓	45	44	42	43		
U^{4}_{20}	↓	↓			48			
N^{12}_{20} U^{4}_{10}	↓	↓	52	51	49	50		
N^{12}_{50}	↓	↓	57	56	54	55		
$S^2N^{12}_{35}f^{33}_{60}f^{34}_{0}U^{5}_{10}$	A	0	258	257	254	256		
f^{34}_{+15}	↓	↓			259			
f^{34}_{-15}	↓	↓			260			
f^{34}_{0} s^{4}_{20}	↓	↓			261			Nac. PR 1.6 Knee/TE PR 1.0
	↓	↓			262			↓
	↓	↓			263			1.38
	↓	↓			263			1.26
	↓	↓			264			Knee T.E. 1.5 1.0
	↓	↓			264			1.60

TABLE IV. WIND TUNNEL TEST SUMMARY
PHASE II HIGH WING

CONFIGURATION	α Deg.	Ψ Deg.	NOMINAL THRUST COEFFICIENT 0	1.0	2.0	3.0	St.	REMARKS
USB/IBF PRESSURE RATIO EFFECTS								PRESSURE RATIO VARIATIONS Nac. Ka. T.E.
$S^2N^{12}_{35}f^{33}_{60}f^{34}_{0}U^{4}_{10}$	C	0			26			1.2 1.0 1.0
↓	↓	↓			27			1.4 ↓ ↓
					28			1.5
					29			1.6
					40			1.2 1.2
↓	↓	↓			40			1.6 ↓ 1.6
$S^2N^{12}_{35}f^{33}_{60}f^{34}_{0}U^{4}_{10}$	C	0			31			1.2 1.2 1.0
↓	↓	↓			30			1.5 1.5 ↓
					31			1.6 1.6
					46			1.2 1.2 1.2
					46			1.4 1.5 1.5
					42			1.5 1.5 1.7
					33			1.4 1.2 1.0
					32			↓ 1.6 ↓
					41			1.5 1.0 1.5
					39			↓ ↓ 1.6
					41			↓ ↓ 1.7
					59			1.4 1.2 1.2
↓	↓	↓			58			↓ 1.55 1.7

TABLE V. - STATIC TURNING DATA SUMMARY
(FULL-SPAN TESTING UNLESS NOTED)

Test Phase	Run No.	Flap Config.	δ_f Upper Surface	Nacelle Exit Position	Nacelle Exit Config.	Blowing			δ_j	η_f	Remarks
						Nac	Kn.	TE			
I	44	$f_{60}^{33,34} f_0$	72.7°	N_{20}^{12}	Slot	*	*	*	51.1°	.930	Semi-Span Testing
	43			N_{50}^{12}					47.0°	.997	
	42				U_{10}^{4}				60.9°	.916	
	36			N_{35}^{12}					59.3°	.958	
	37				U_0^4				57.9°	.969	
	38				E^3				47.3°	.953	
	35				Slot				48.4°	.958	
	34							0	44.8°	.930	
	39						0		38.5°	.921	
	41				U_{10}^{4}				59.7°	.938	
	40				U_0^4				55.8°	.933	
	68						*	*	60.6°	.940	
	74				U_{10}^{4}				62.2°	.972	
	77				Slot				51.8°	.880	
	IBF					0			62.1°	.990	
	163	$f_{22}^{33,34} f_0$	32.0°	N_{35}^{12}	U_0^4	*			30.8°	.975	
	52	$f_{58}^{35,34} f_0$	54.7°	N_{20}^{12}	Slot		0		38.4°	.933	Semi-Span Testing
	54			N_{50}^{12}					37.2°	.915	
	55							0	33.7°	.882	
	53			N_{20}^{12}					37.0°	.937	
	23			N_{35}^{12}					34.2°	.978	
	49				U_{10}^{4}				47.2°	1.014	

TABLE V. - STATIC TURNING DATA SUMMARY
(FULL-SPAN TESTING UNLESS NOTED)

Test Phase	Run No.	Flap Config.	δ_f Upper Surface	Nacelle Exit Position	Nacelle Exit Config.	Blowing			δ_j	η_f	Remarks
						Nac	Kn	TE			
I	50	$f^{35}_{58} f^{34}_{0}$	54.7°	N^{12}_{35}	U^{4}_{0}	*	0	0	44.2°	1.007	Semi-Span Testing
	56				↓			*	43.0°	.988	
	46				Slot				37.6°	.926	
	48				U^{4}_{10}				45.2°	.995	
	57				↓		*		46.4°	.998	
	58				Slot				39.4°	.919	
	141	$f^{35}_{44} f^{34}_{0}$	44.3°		↓		o		34.1°	.908	
	143				U^{4}_{10}				41.6°	1.014	
	145				U^{4}_{0}				39.7°	.984	
II	49	$f^{33}_{60} f^{34}_{0}$	73.25°	N^{12}_{20}	U^{4}_{10}	*	*	*	65.5°	1.021	
	54			N^{12}_{50}					67.1°	1.098	
	42			N^{12}_{35}					67.4°	1.04	
	138								49.7°	.835	S^{4}_{10}
	142								42.4°	.682	S^{4}_{20}
	143								42.6°	.673	S^{5A}_{20}
	144								25.9°	.606	S^{4}_{30}
	145								67.5°	1.072	S^{5B}_{20}
	149								56.2°	.824	S^{5C}_{20}
	150								67.3°	1.070	S^{6B}_{20}
	151								65.8°	.907	S^{6C}_{20}

TABLE V. - STATIC TURNING DATA SUMMARY
(FULL-SPAN TESTING UNLESS NOTED)

Test Phase	Run No.	Flap Config.	δ_f Upper Surface	Nacelle Exit Position	Nacelle Exit Config.	Blowing			δ_j	η_f	Remarks
						Nac	Kn	TE			
II	152	$f_{60}^{33} f_{0}^{34}$	73.25°	N_{35}^{12}	U_{10}^{4}	*	*	*	65.3°	.958	S_{20}^{6C}
	48				U_{20}^{4}				66.1°	1.00	
	47				U_{0}^{4}				65.0°	1.05	
	254				U_{10}^{5}				58.6°	1.043	
	261								20.9°	.790	S_{20}^{4}
	264							0	56.8°	.980	
	262						0		51.5°	.948	
	28				U_{10}^{4}				67.8°	.995	
	39							*	66.7°	1.05	
	30						*	0	68.5°	1.05	
	38	$f_{60}^{33} f_{15}^{34}$	88.25°						77.7°	1.00	
	34						0		77.3°	.986	
	111						*	*	77.0°	1.00	
	259				U_{10}^{5}	*	*	*	63.0°	.964	
	260	$f_{60}^{33} f_{-15}^{34}$	58.25°						52.0°	.99	
	116				U_{10}^{4}				60.5°	1.02	
	118								59.4°	1.05	Semi-Span Testing
	36							0	61.3°	1.03	
	35						0		60.8°	1.01	
	128	$f_{60}^{33} f_{30}^{34}$	103.25°				*	*	84.5°	.94	
	129	$f_{60}^{33} f_{-30}^{34}$	43.25°						51.4°	1.06	

TABLE V. - STATIC TURNING DATA SUMMARY
(FULL-SPAN TESTING UNLESS NOTED)

Test Phase	Run No.	Flap Config.	δ_f Upper Surface	Nacelle Exit Position	Nacelle Exit Config.	Blowing			δ_j	η_f	Remarks
						Nac	Kn	TE			
II	157	$f_{30}^{33} f_{0}^{34}$	42.83°	N_{35}^{12}	U_{10}^{4}	*	*	*	38.4°	1.087	
	164								40.6°	.925	S_{10}^{4}
	168								37.4°	.82	S_{20}^{5A}
	169								37.9°	.888	S_{20}^{5B}
	170								37.9°	.81	S_{20}^{4}
	171	$f_{30}^{33} f_{15}^{34}$	57.83°						50.9°	1.067	
	179	$f_{30}^{33} f_{-15}^{34}$	27.83°						28.3°	1.03	
	235	$f_{22}^{33} f_{0}^{34}$	34.27°						30.4°	1.092	
	215								28.0°	1.080	H_{0}^{2}
	211								30.3°	1.096	H_{-5}^{2}
	207								30.0°	1.108	H_{+10}^{2}
	244								33.4°	.845	S_{20}^{4}
	246								24.0°	.743	S_{30}^{4}
	245								33.1°	.860	S_{20}^{5A}

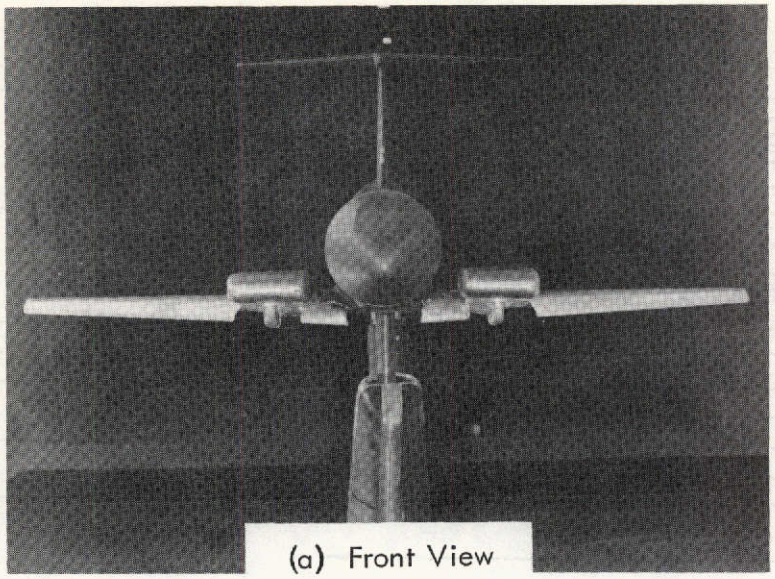

(a) Front View

(b) Side View

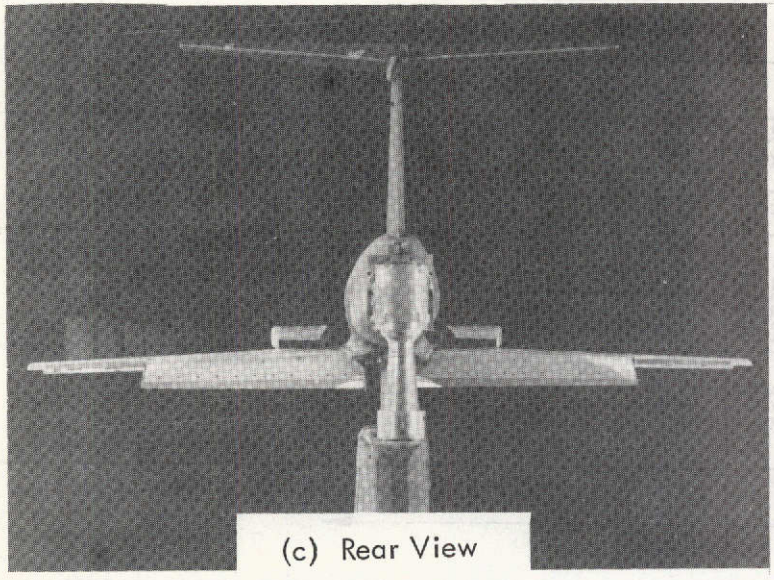

(c) Rear View

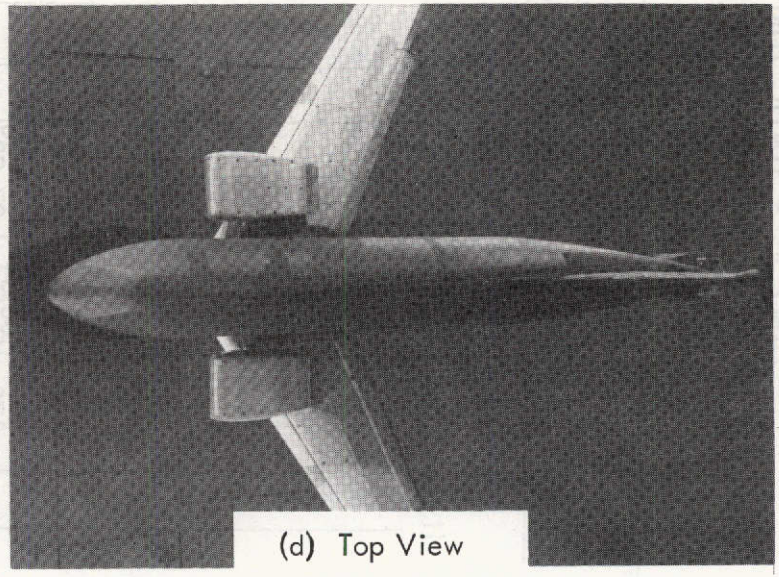

(d) Top View

Figure 1. - Low Wing Model in Lockheed V/STOL Tunnel

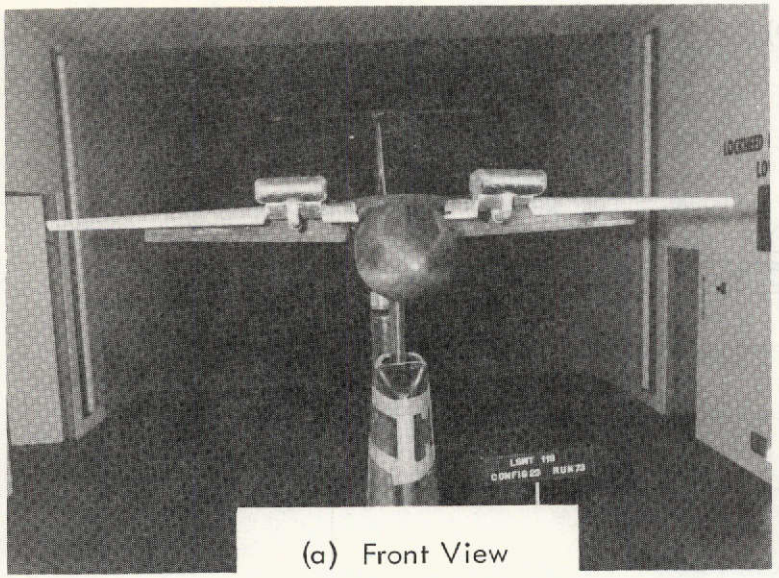

(a) Front View

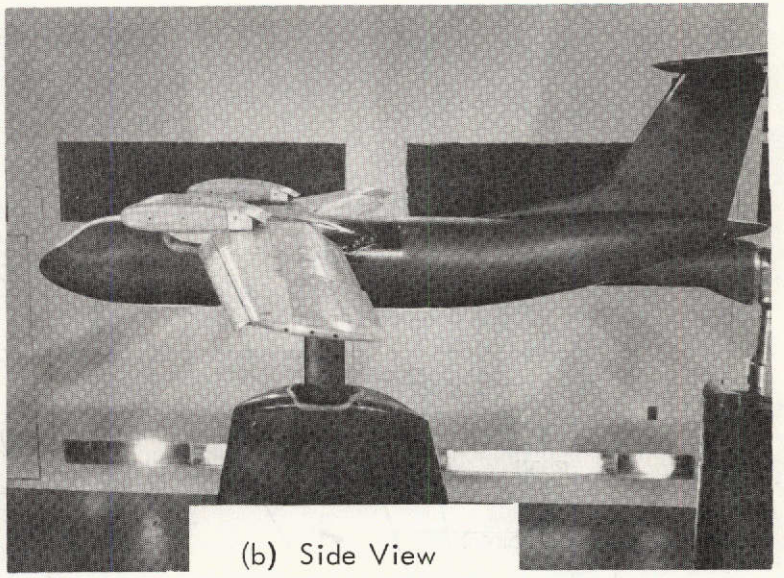

(b) Side View

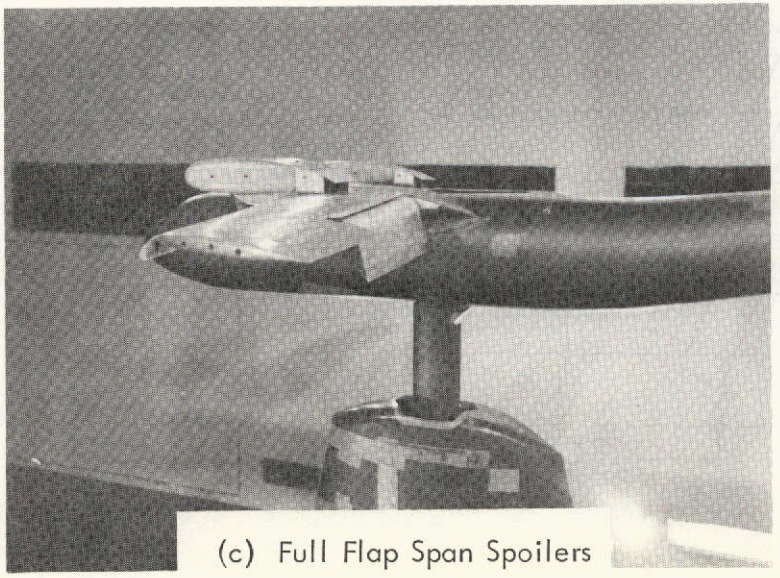

(c) Full Flap Span Spoilers

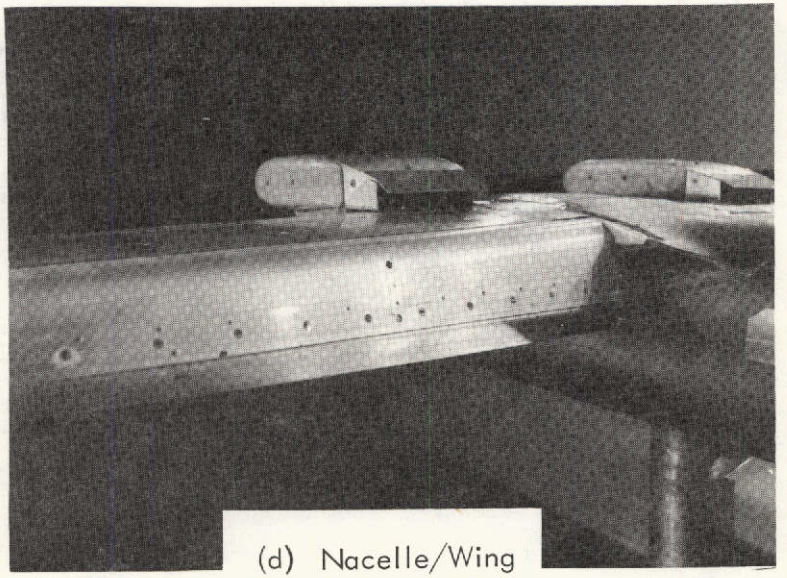

(d) Nacelle/Wing

Figure 2. - High Wing Model in Lockheed V/STOL Tunnel

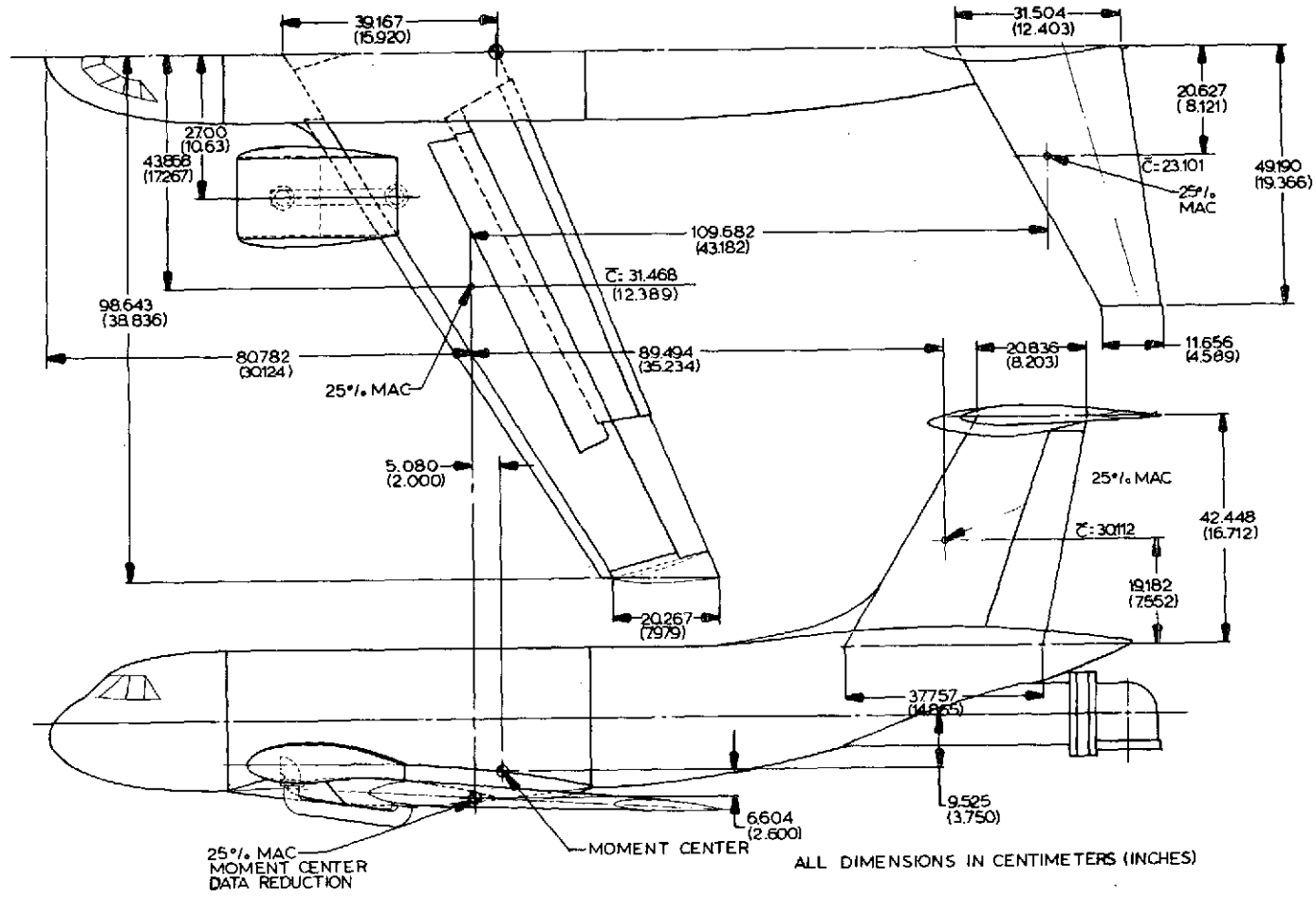

(a) Phase I Model

Figure 3. - Geometric Details of the Model

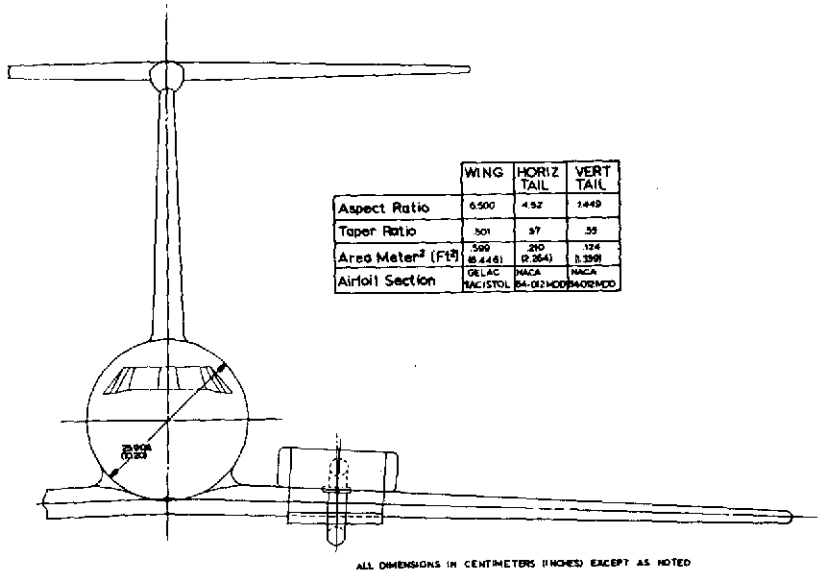

Figure 3(a). - Continued

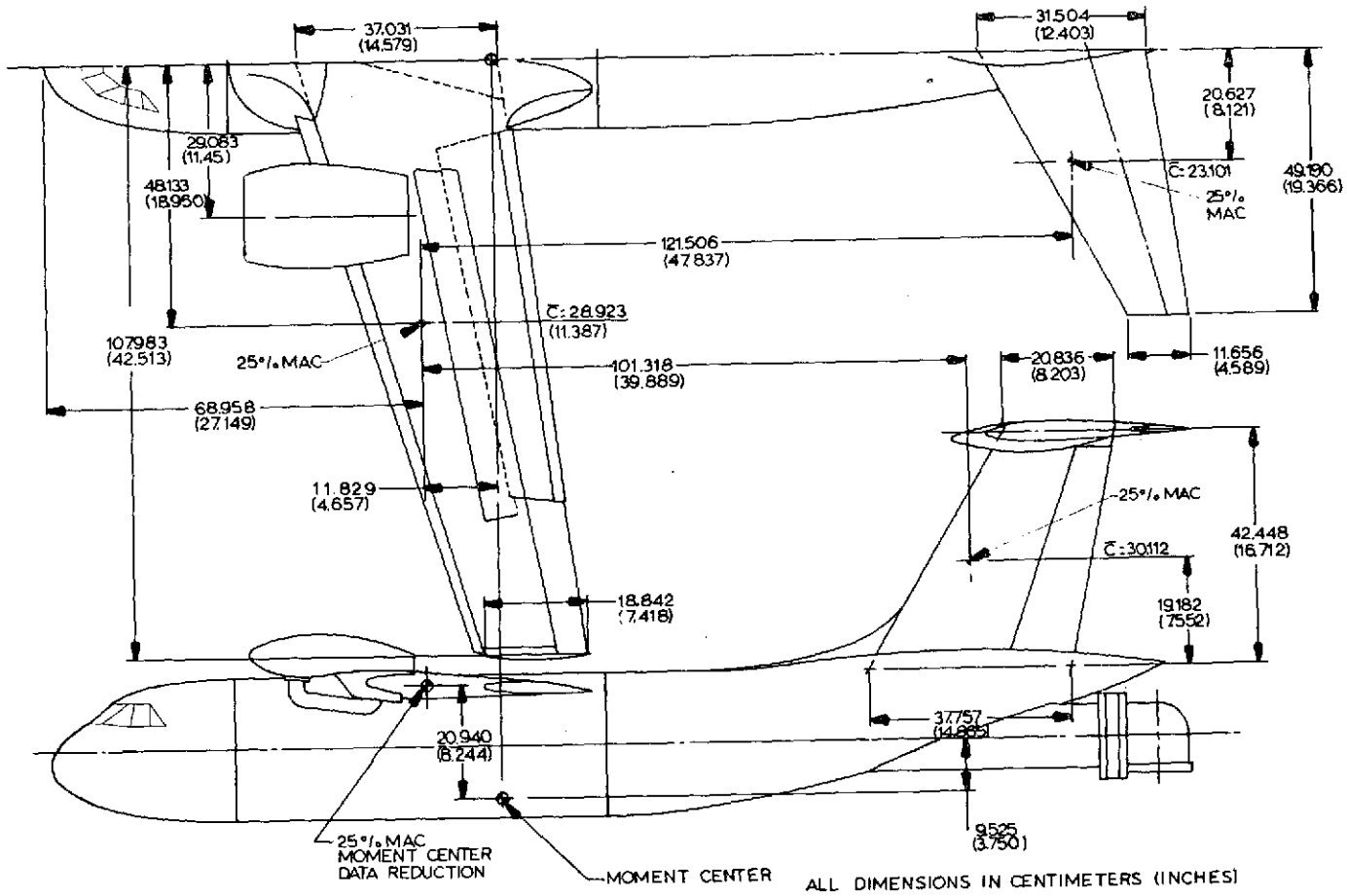

(b) Phase II Model

Figure 3. - Geometric Details of the Model

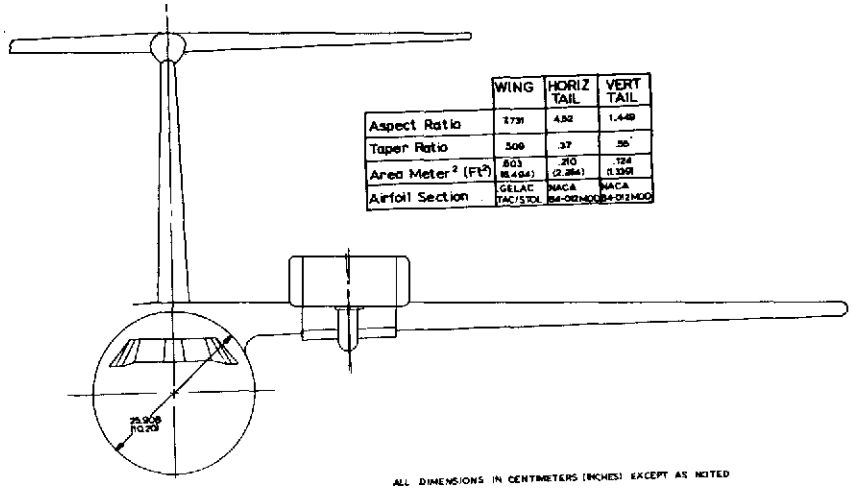

Figure 3(b). - Continued

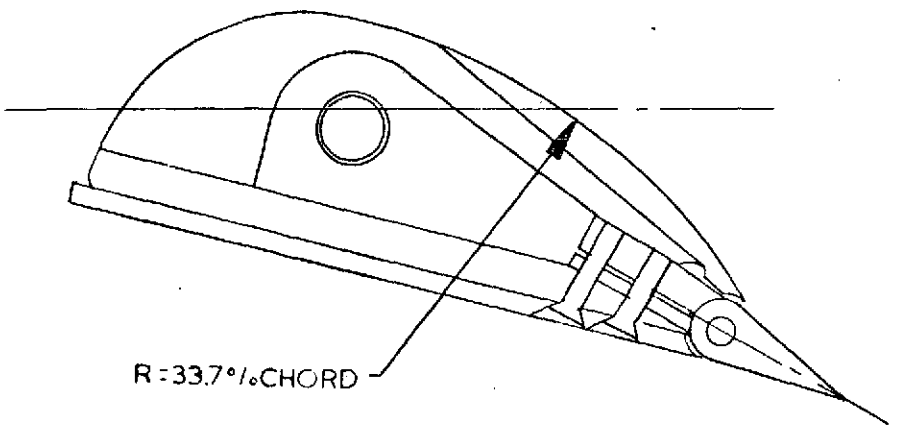

COANDA FLAP

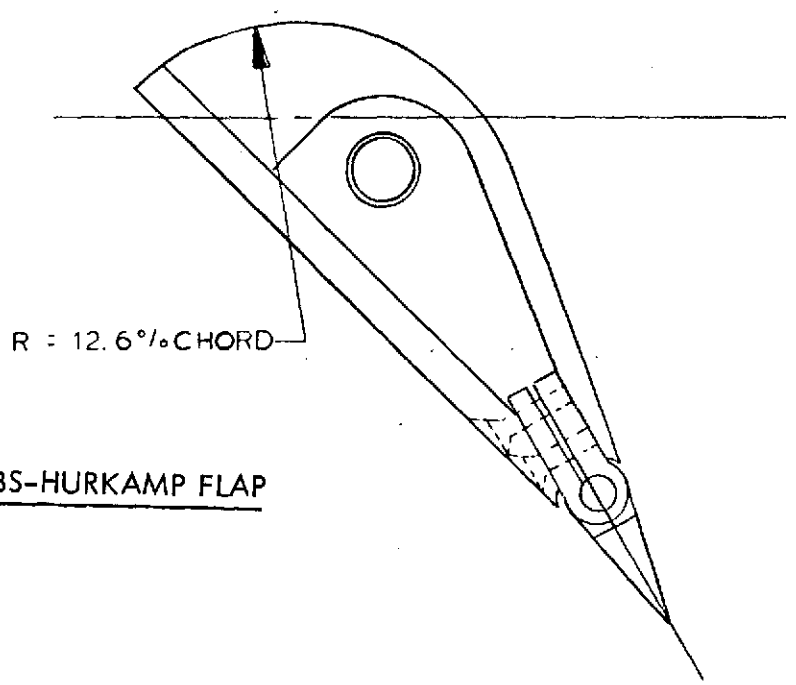

JACOBS-HURKAMP FLAP

Figure 4. - Trailing Edge Flap Sections

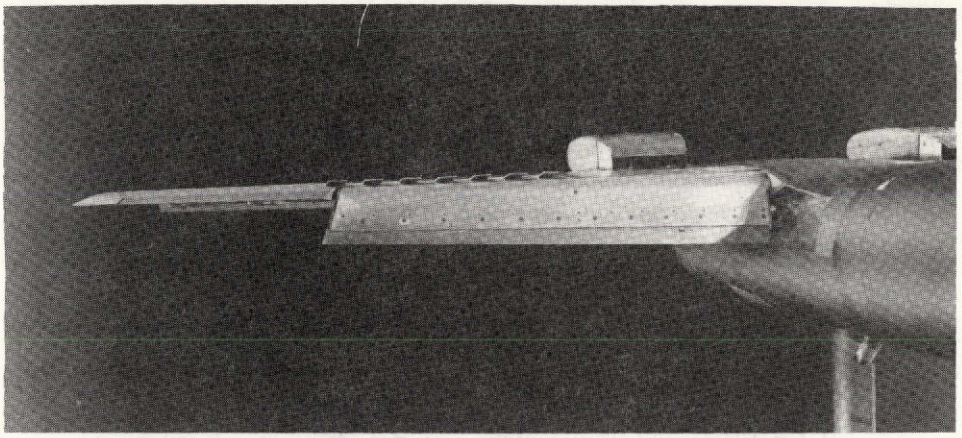

(a) 20° Spoiler on Outboard Half Flap Span

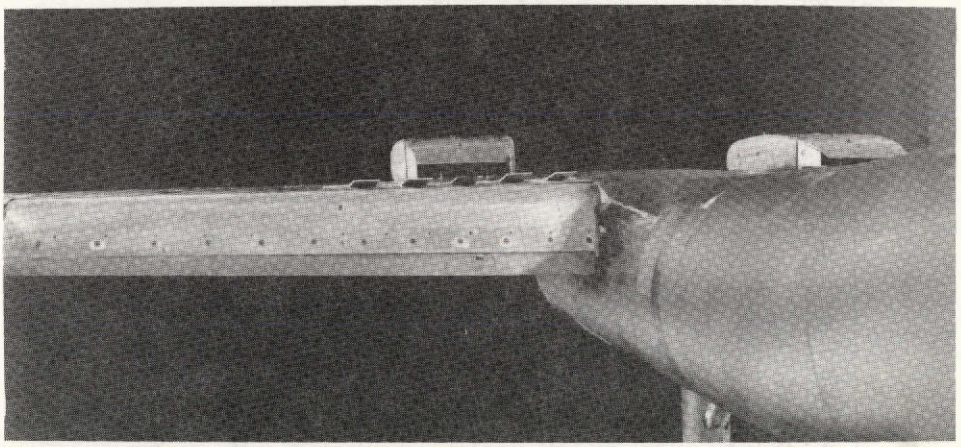

(b) 20° Spoiler on Inboard Half Flap Span

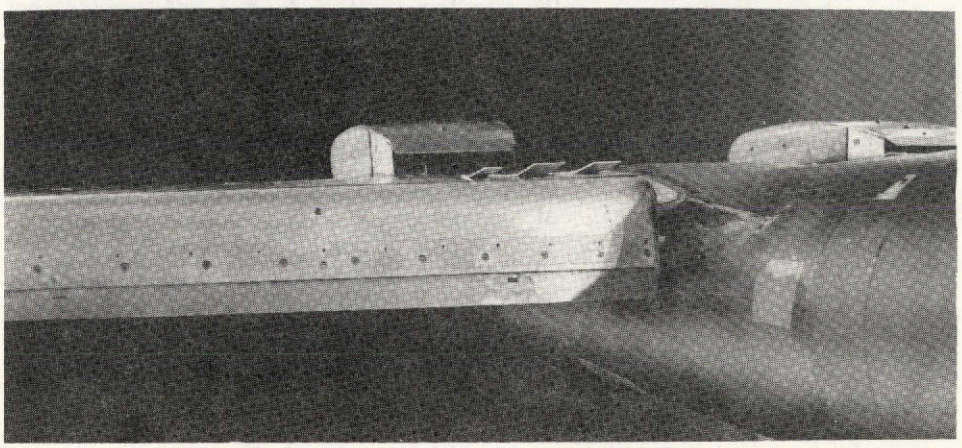

(c) 20° Spoiler on Inboard Quarter Flap Span

Figure 5. - Spoilers, 0.10c, 50% Porosity

Configuration	A	B	C	D°/o	E°/o	F°/o
30° SWEEP	6.99 (2.75)	12.32 (4.85)	17.65 (6.95)	.200	.352	.505
15° SWEEP	6.60 (2.60)	11.68 (4.60)	16.76 (6.60)	.206	.356	.521

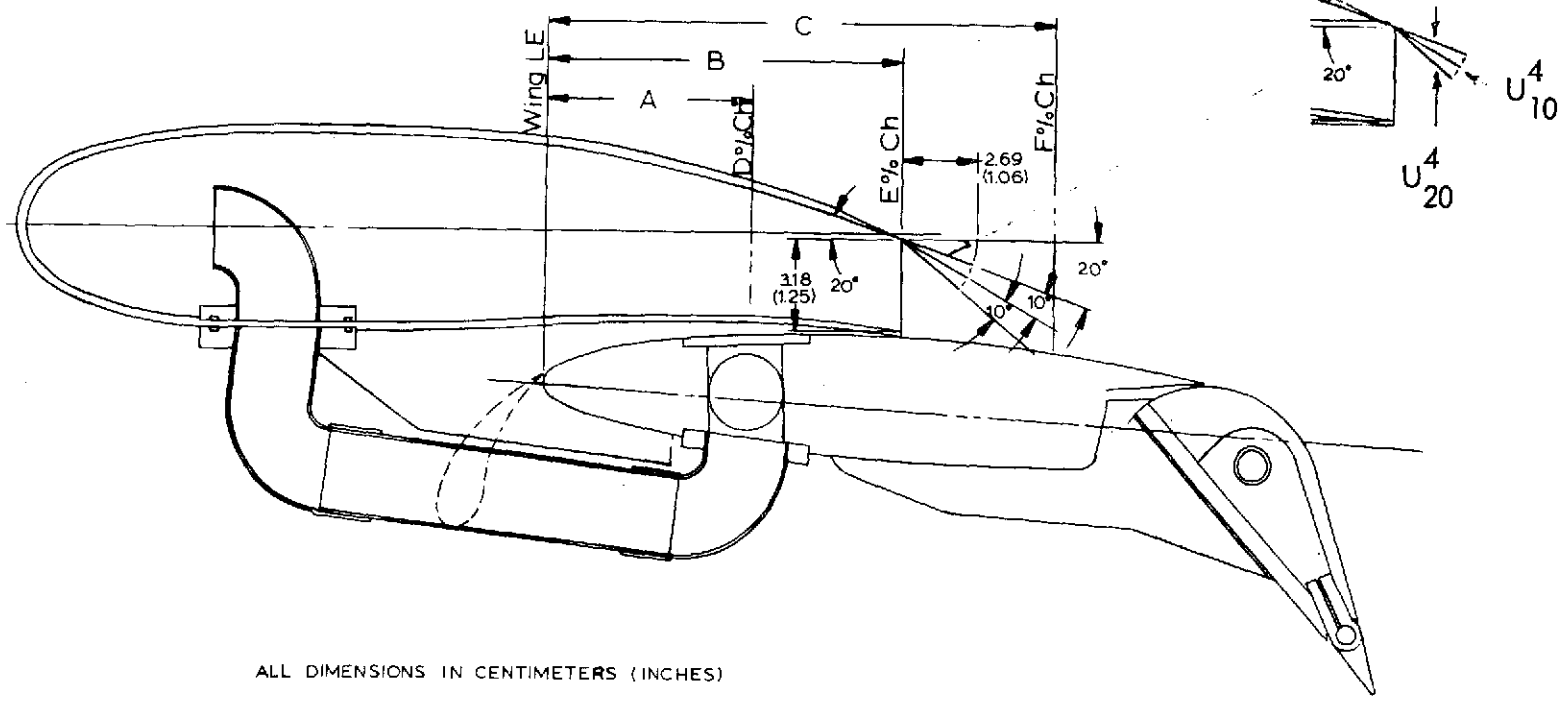

ALL DIMENSIONS IN CENTIMETERS (INCHES)

Figure 6. - Nacelle/Wing Geometry Details

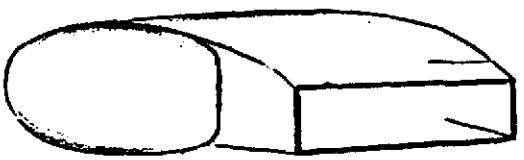

(a) Basic Nacelle Exit, AR = 4.0

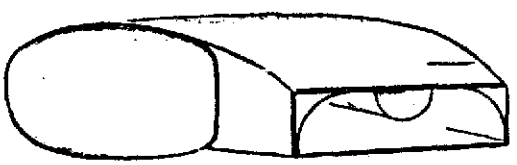

(b) E^3 Exit Insert

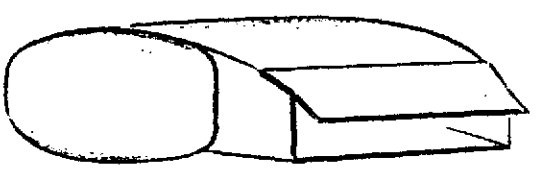

(c) U^4 Exit (Open Deflector)

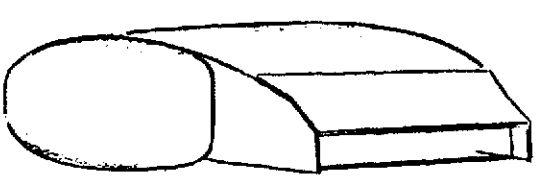

(d) U^5 Exit (Closed Deflector)

Figure 7. - Nacelle Exits

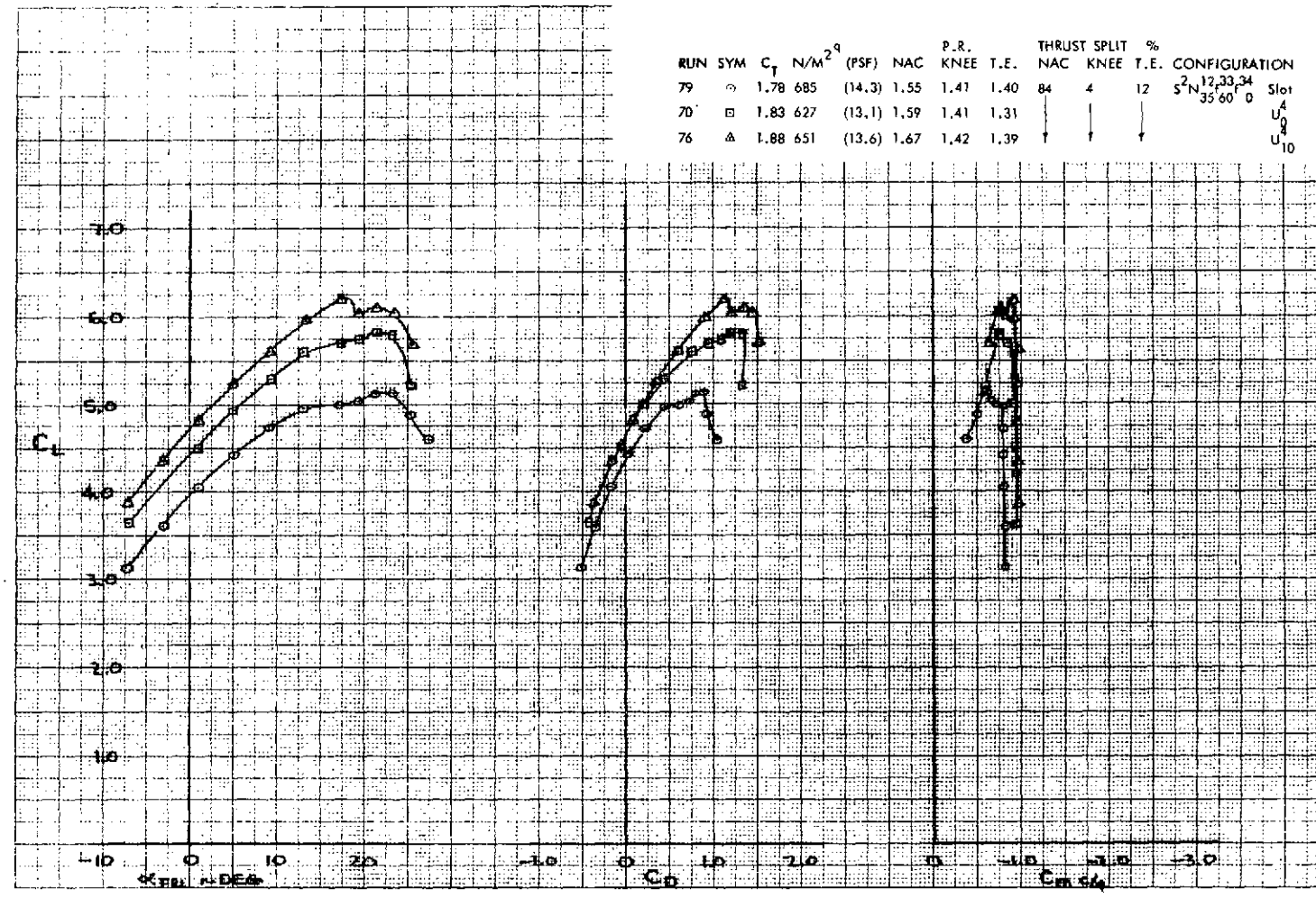

Figure 8. - Effects of Nozzle and Deflector Configurations on Longitudinal Characteristics of the Low Wing Model, 60°/0° J/H Flap, Tail Off

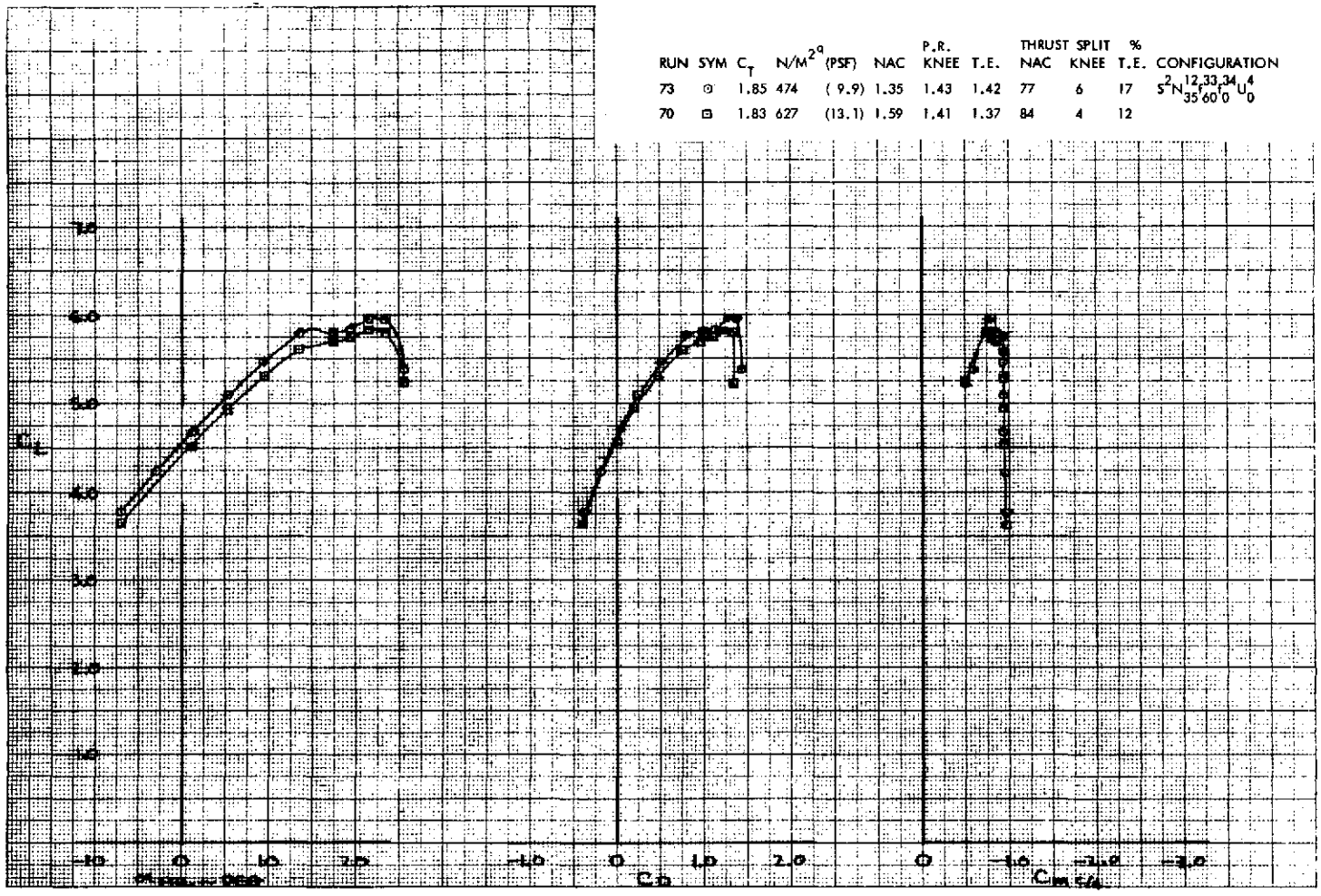

Figure 9. - Effects of Nacelle Pressure Ratio on Longitudinal Characteristics of the Low Wing Model, $60^\circ/0^\circ$ J/H Flap, 0° Open Deflector, Tail Off

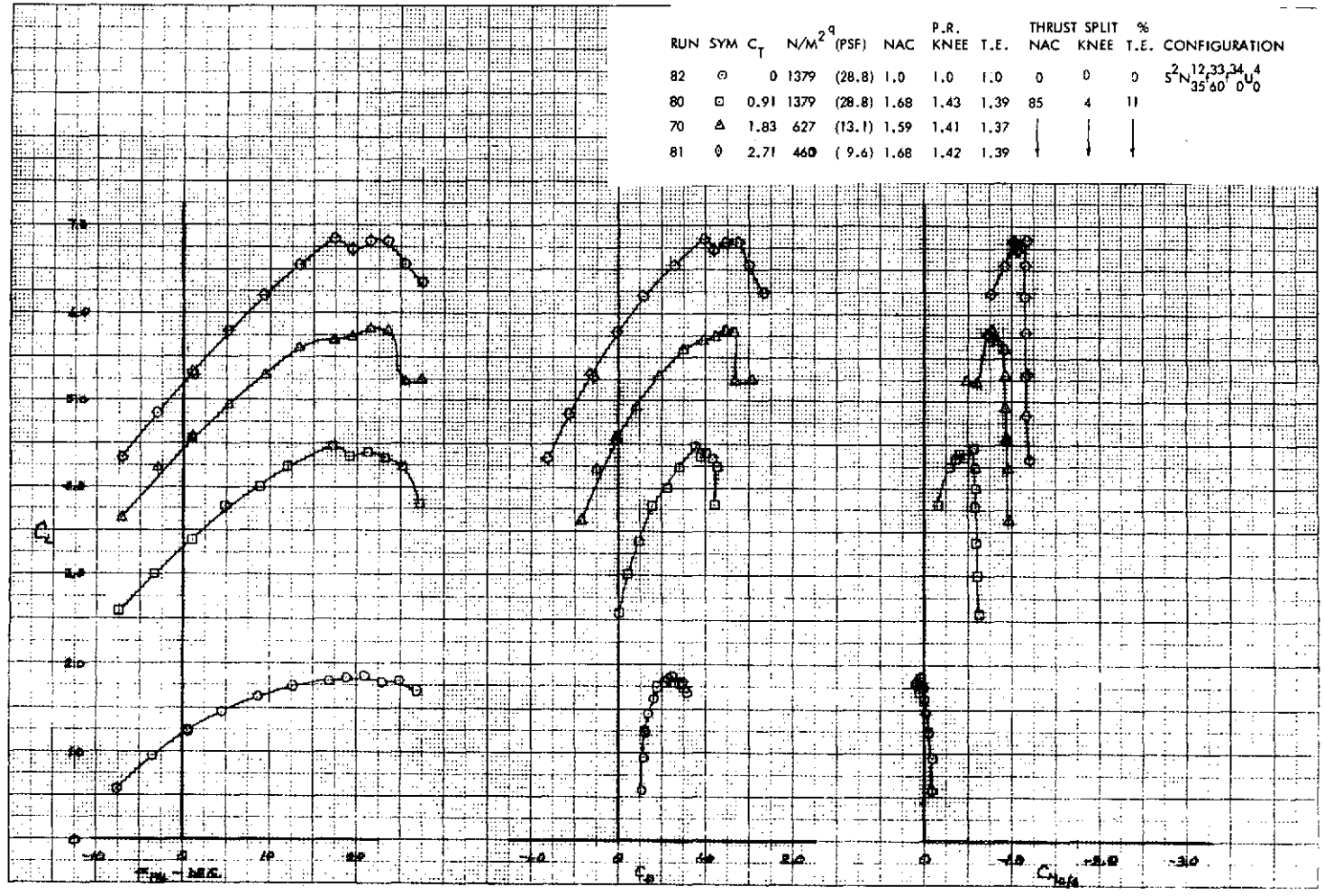

Figure 10. - Longitudinal Characteristics of the Low Wing Model, $60^\circ/0^\circ$ J/H Flap, 0° Open Deflector, Tail Off

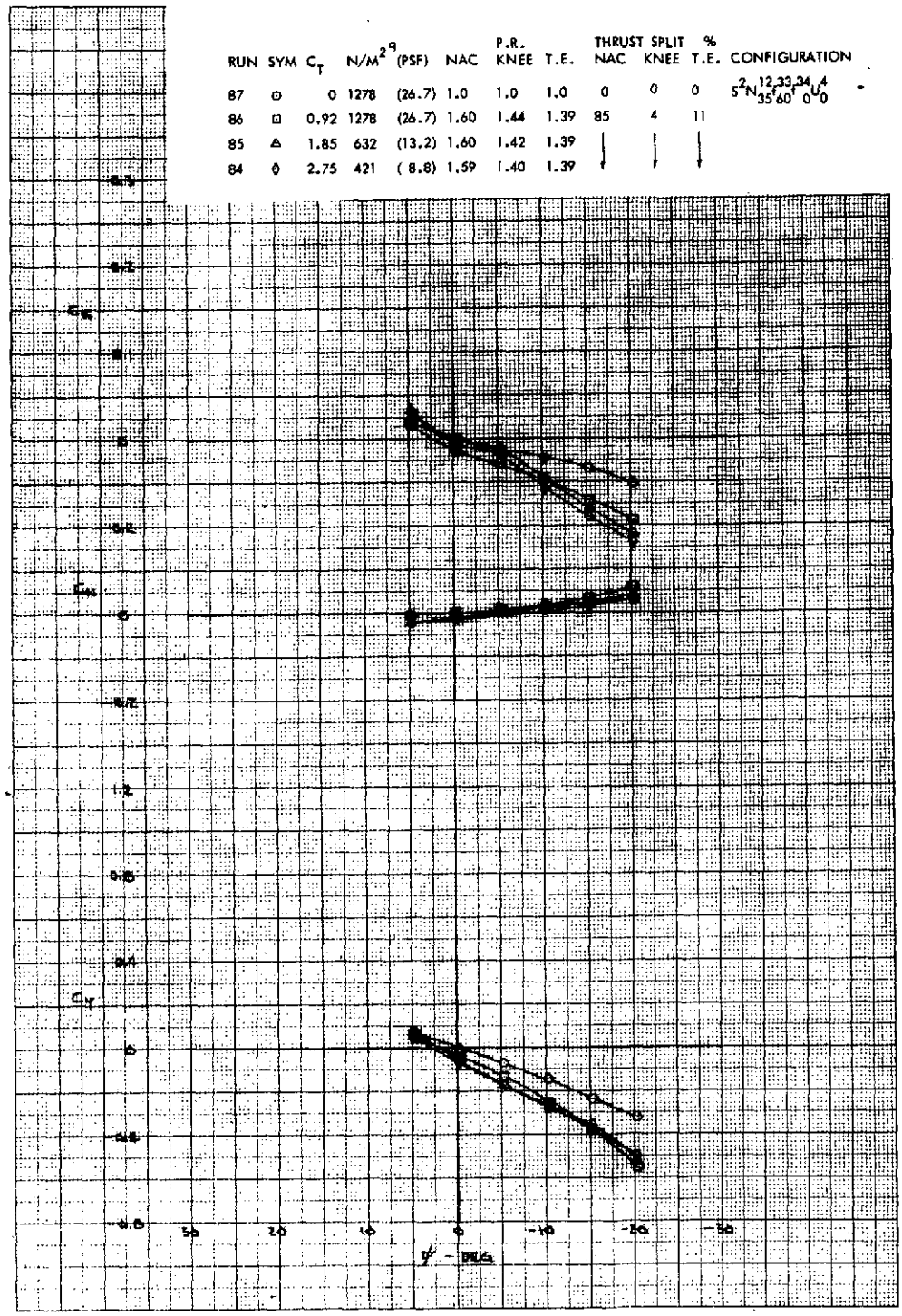

Figure 11. - Lateral-Directional Characteristics of the Low Wing Model, 60°/0° J/H Flap, 0° Open Deflector, Tail Off

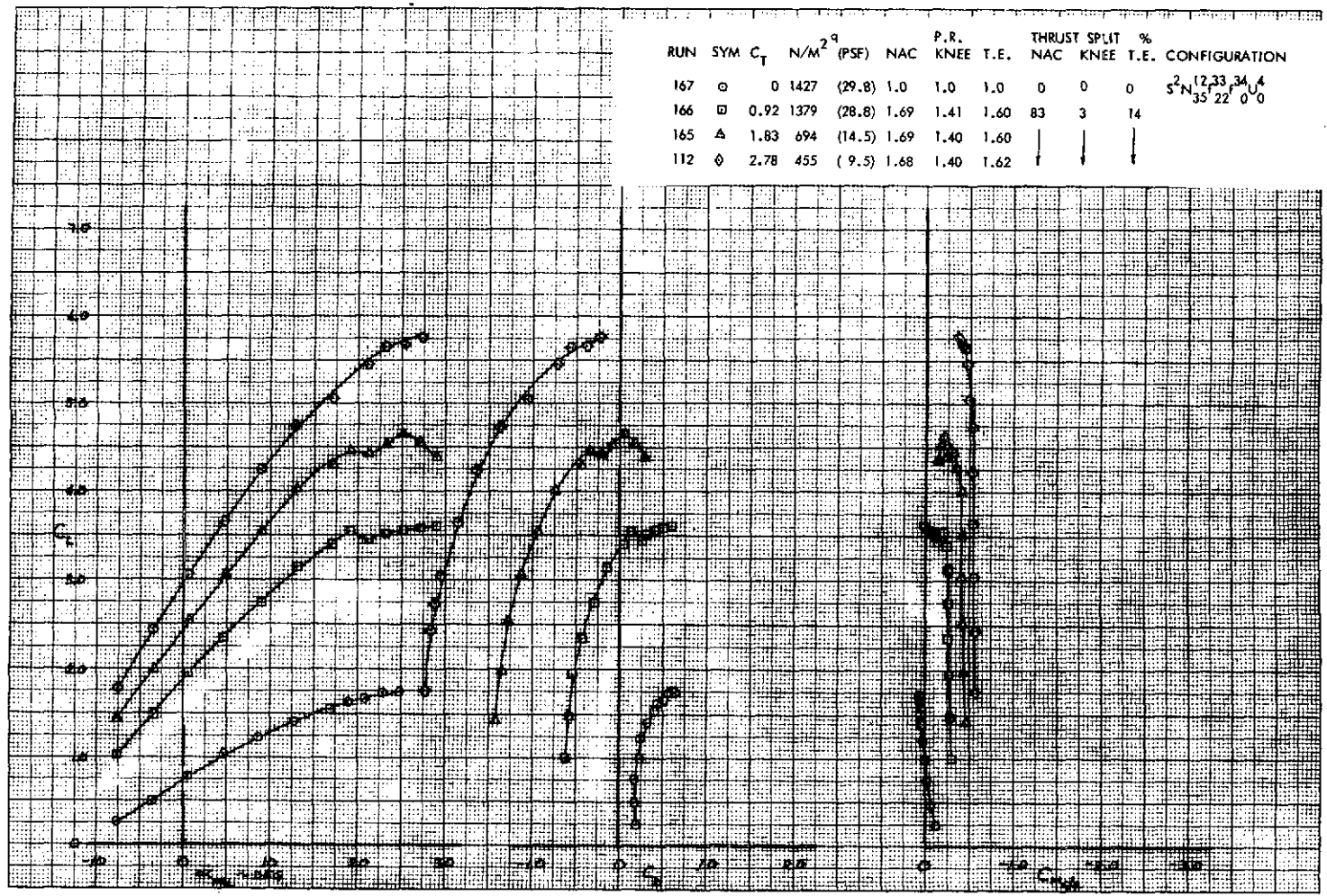

Figure 12. - Longitudinal Characteristics of the Low Wing Model, $22^{\circ}/0^{\circ}$ J/H Flap, 0° Open Deflector, Tail Off

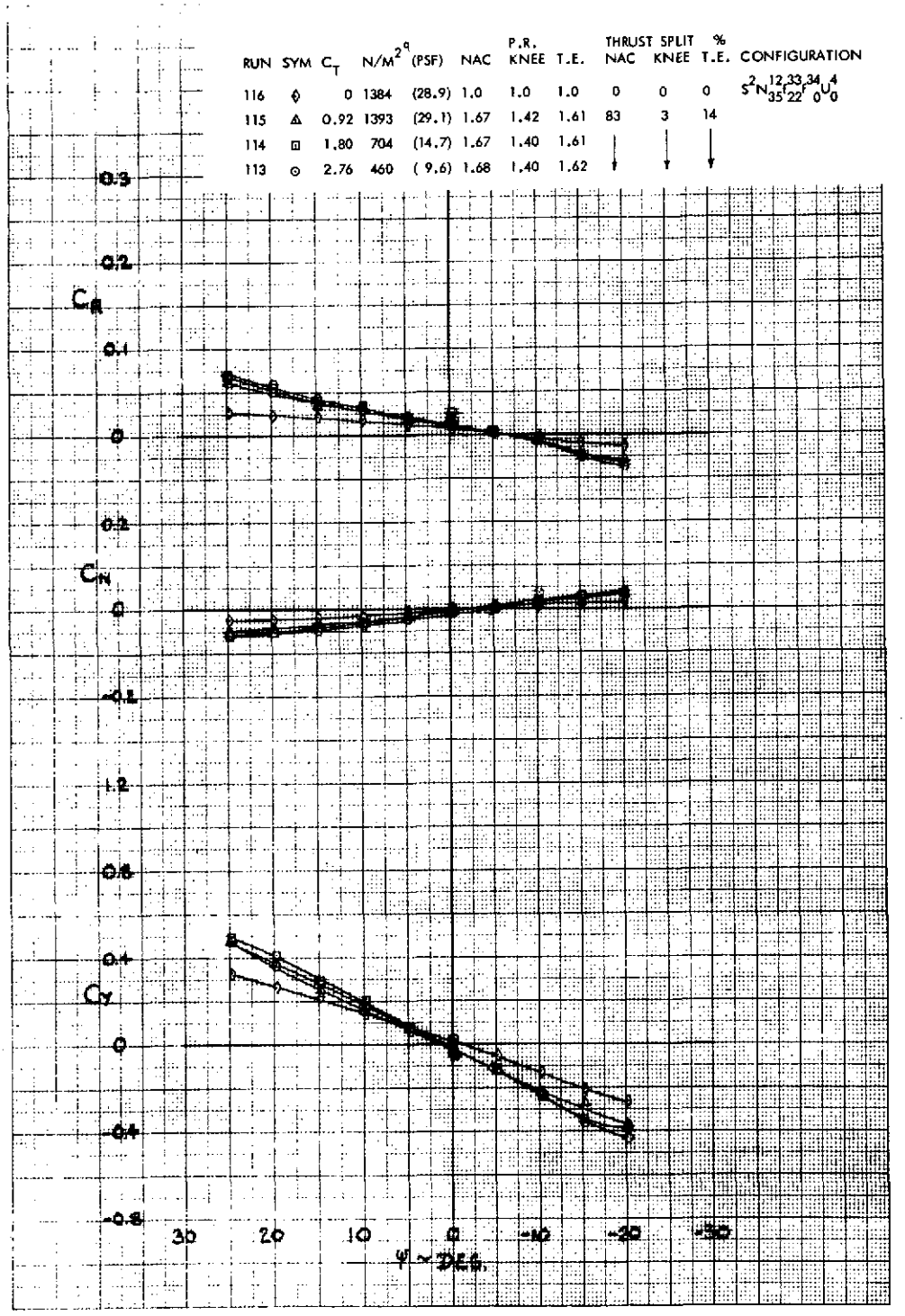

Figure 13. - Lateral-Directional Characteristics of the Low Wing Model, 22°/0° J/H Flap, 0° Open Deflector, Tail Off

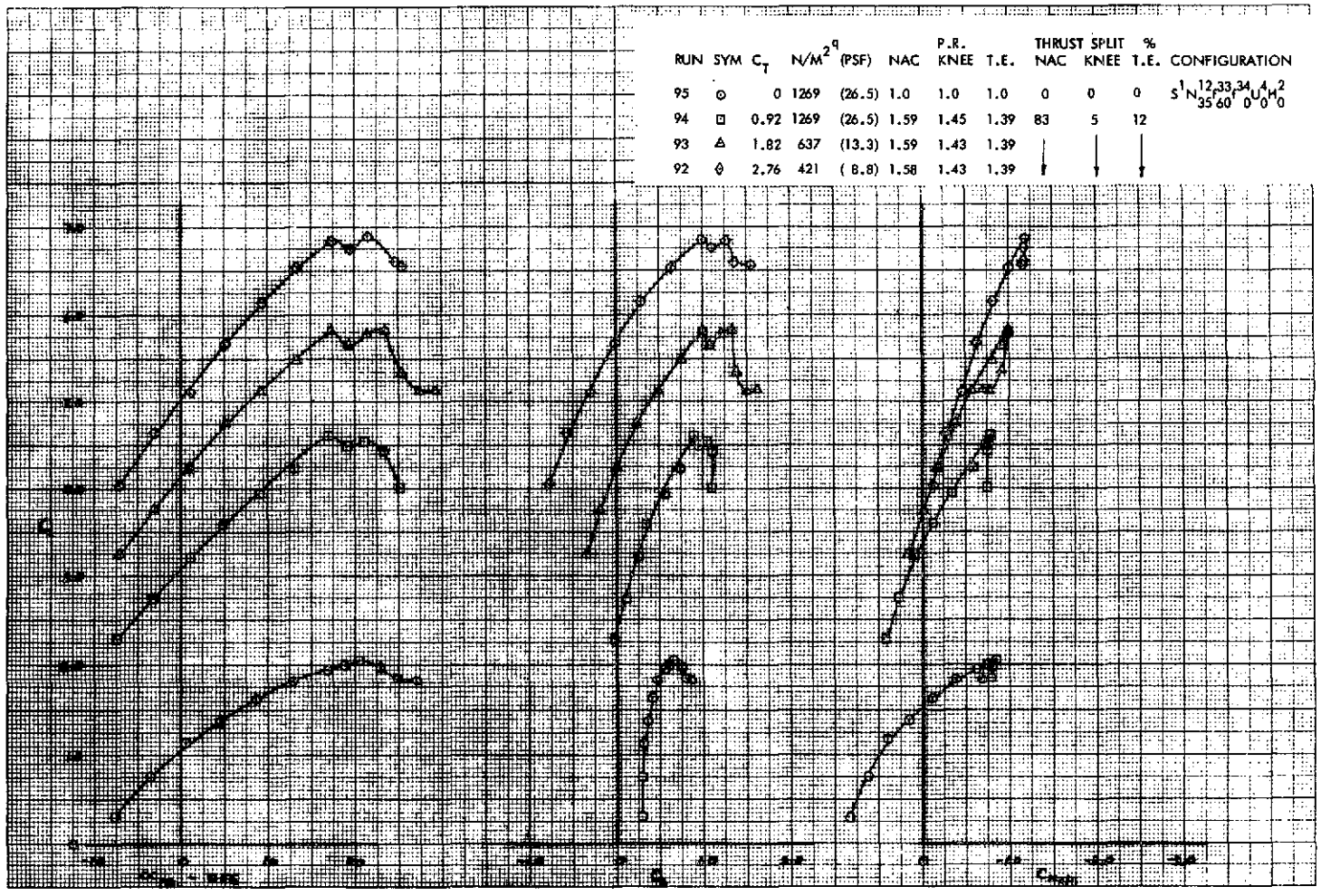

Figure 14. - Longitudinal Characteristics of the Low Wing Model, $60^\circ/0^\circ$ J/H Flap, 0° Open Deflector, Tail On

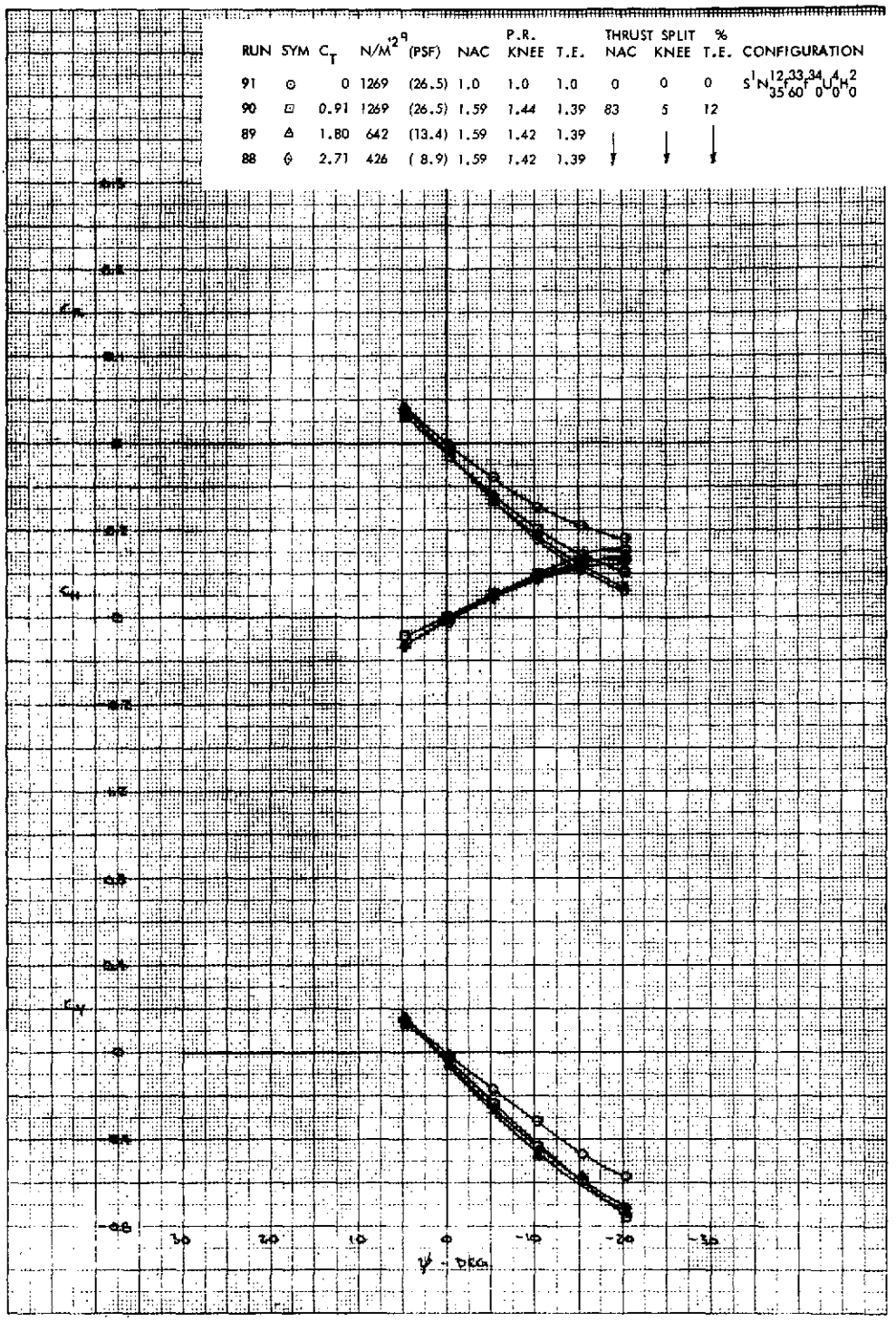

Figure 15. - Lateral-Directional Characteristics of the Low Wing Model, 60°/0° J/H Flap, 0° Open Deflector, Tail On

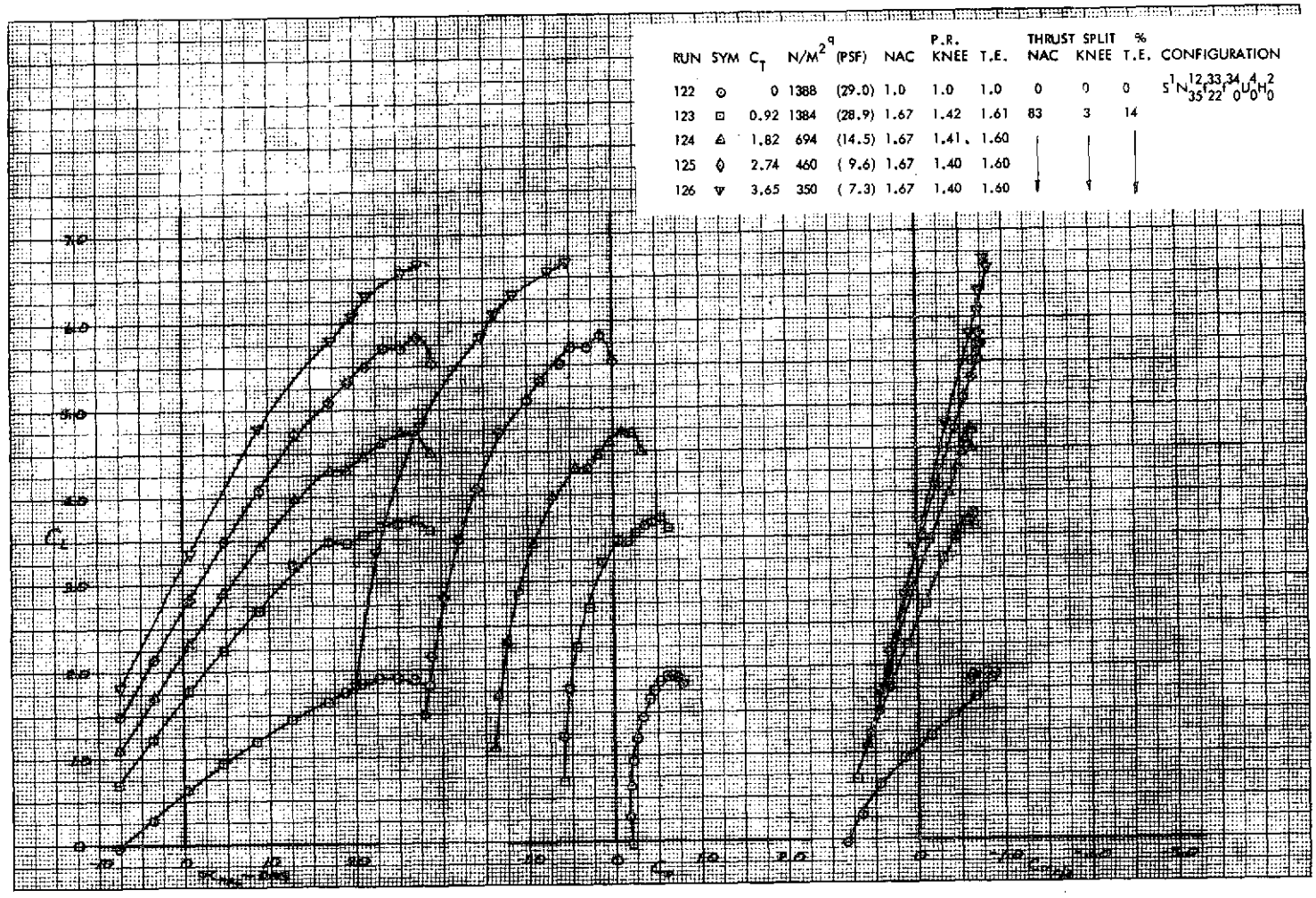

Figure 16. - Longitudinal Characteristics of the Low Wing Model, $22^{\circ}/0^{\circ}$ J/H Flap, 0° Open Deflector, Tail On

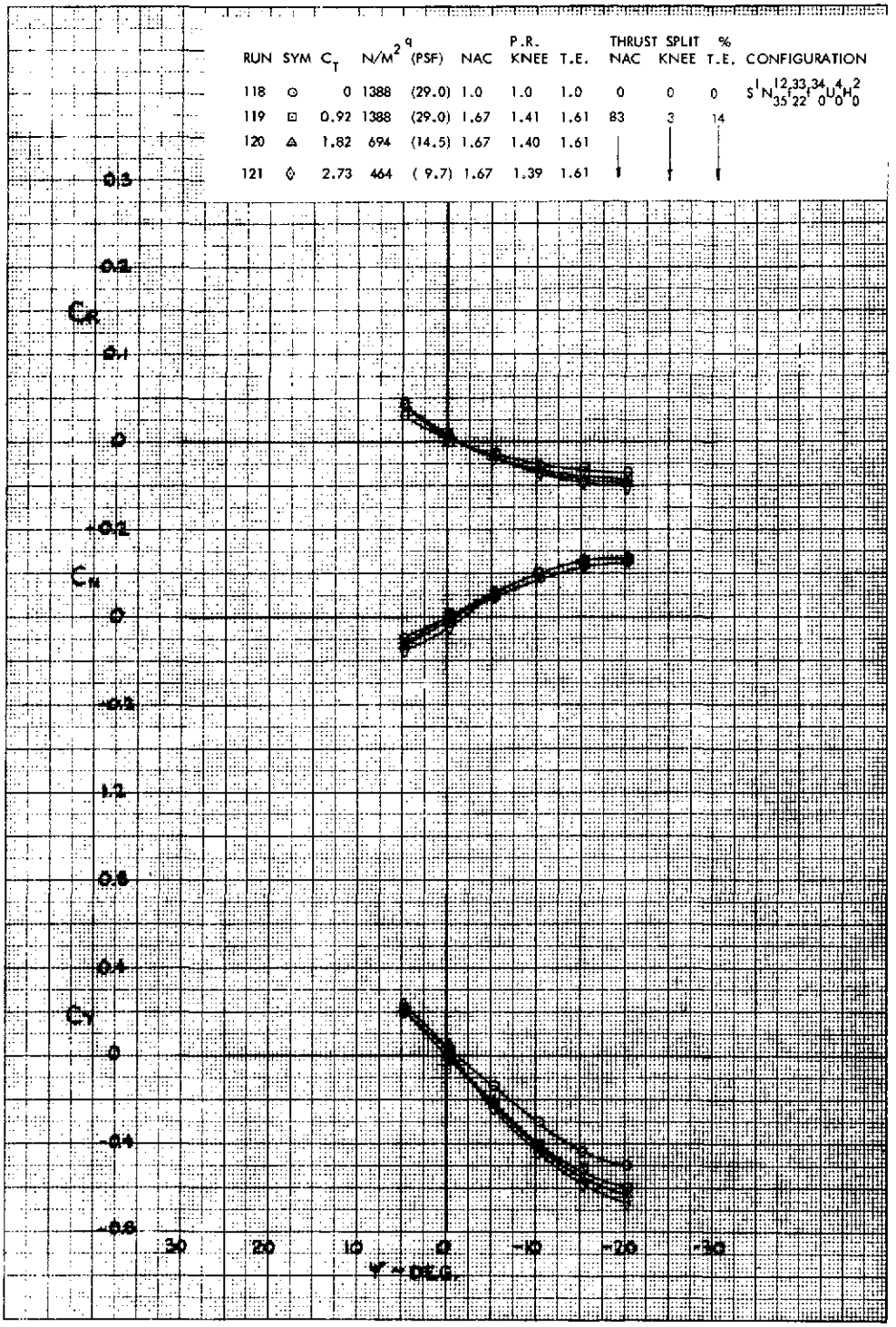

Figure 17. - Lateral-Directional Characteristics of the Low Wing Model, 22°/0° J/H Flaps, 0° Open Deflector, Tail On

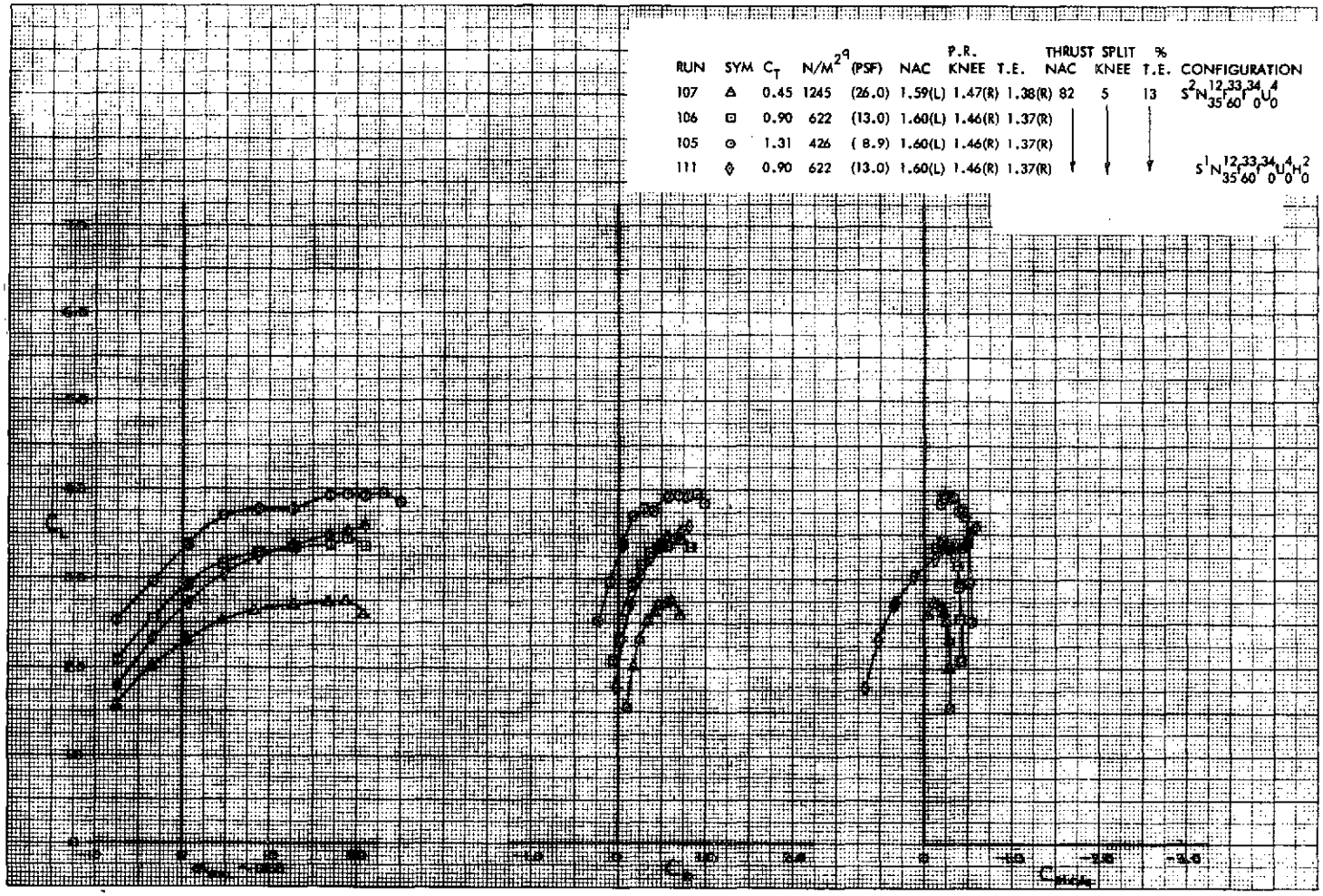

Figure 18. - Longitudinal Characteristics of the Low Wing Model with One Engine Inoperative, $60^\circ/0^\circ$ J/H Flap, 0° Open Deflector, Tail On

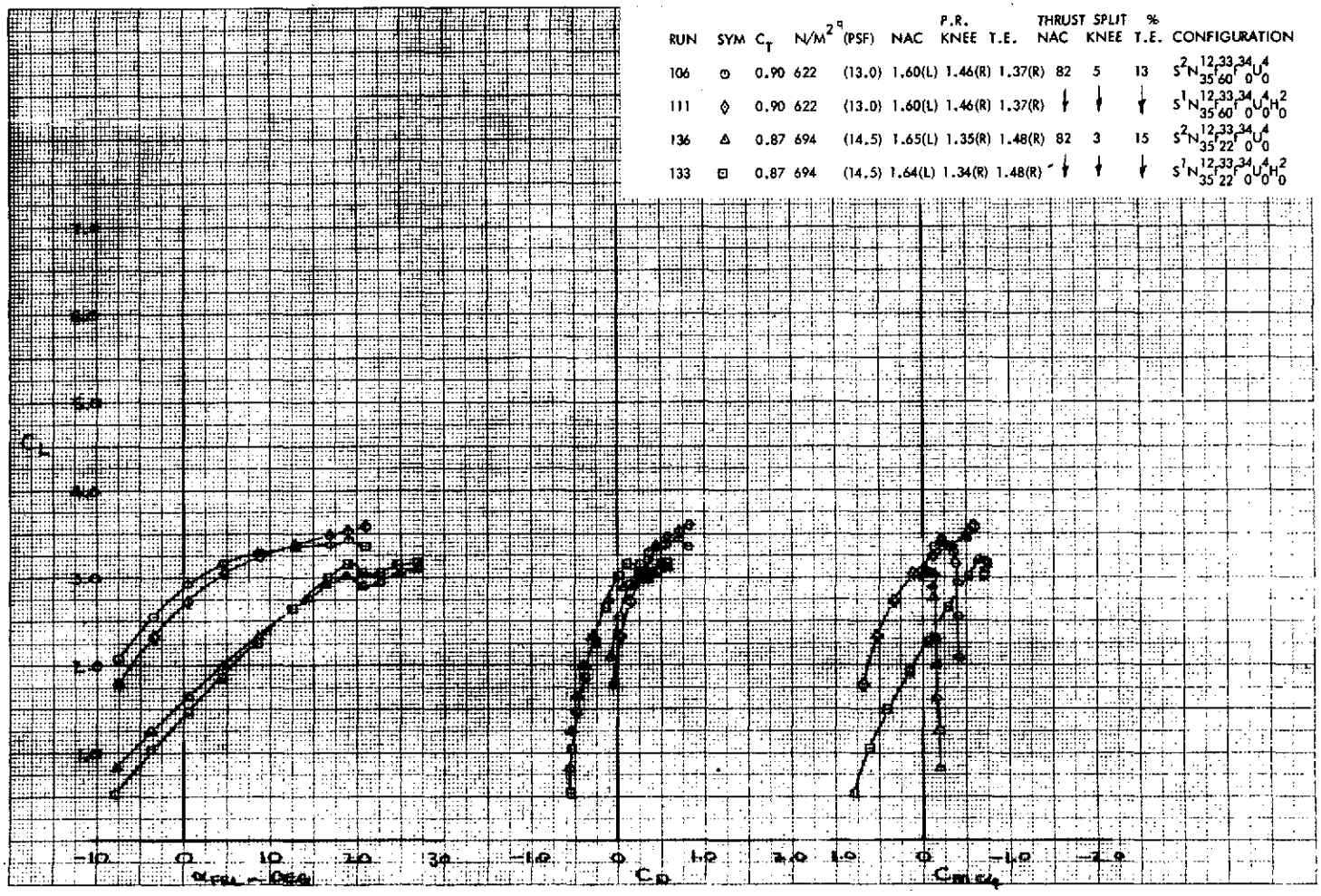

Figure 19. - Longitudinal Characteristics of the Low Wing Model with One Engine Inoperative, $60^\circ/0^\circ$ and $22^\circ/0^\circ$ J/H Flap, 0° Open Deflector, Tail On and Off

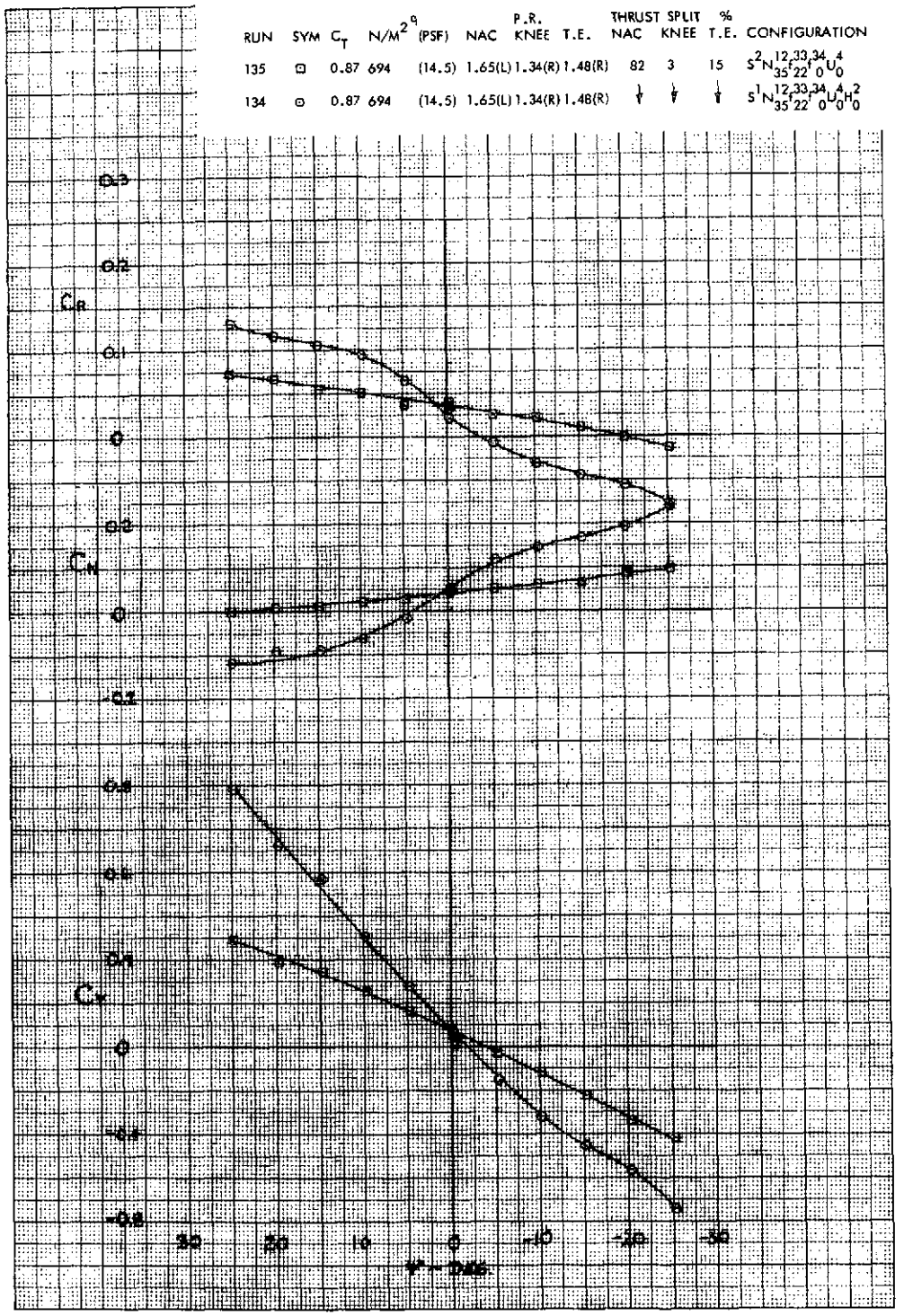

Figure 20. - Lateral-Directional Characteristics of the Low Wing Model with One Engine Inoperative, $60^{\circ}/0^{\circ}$ J/H Flap, 0° Open Deflector, Tail On and Off

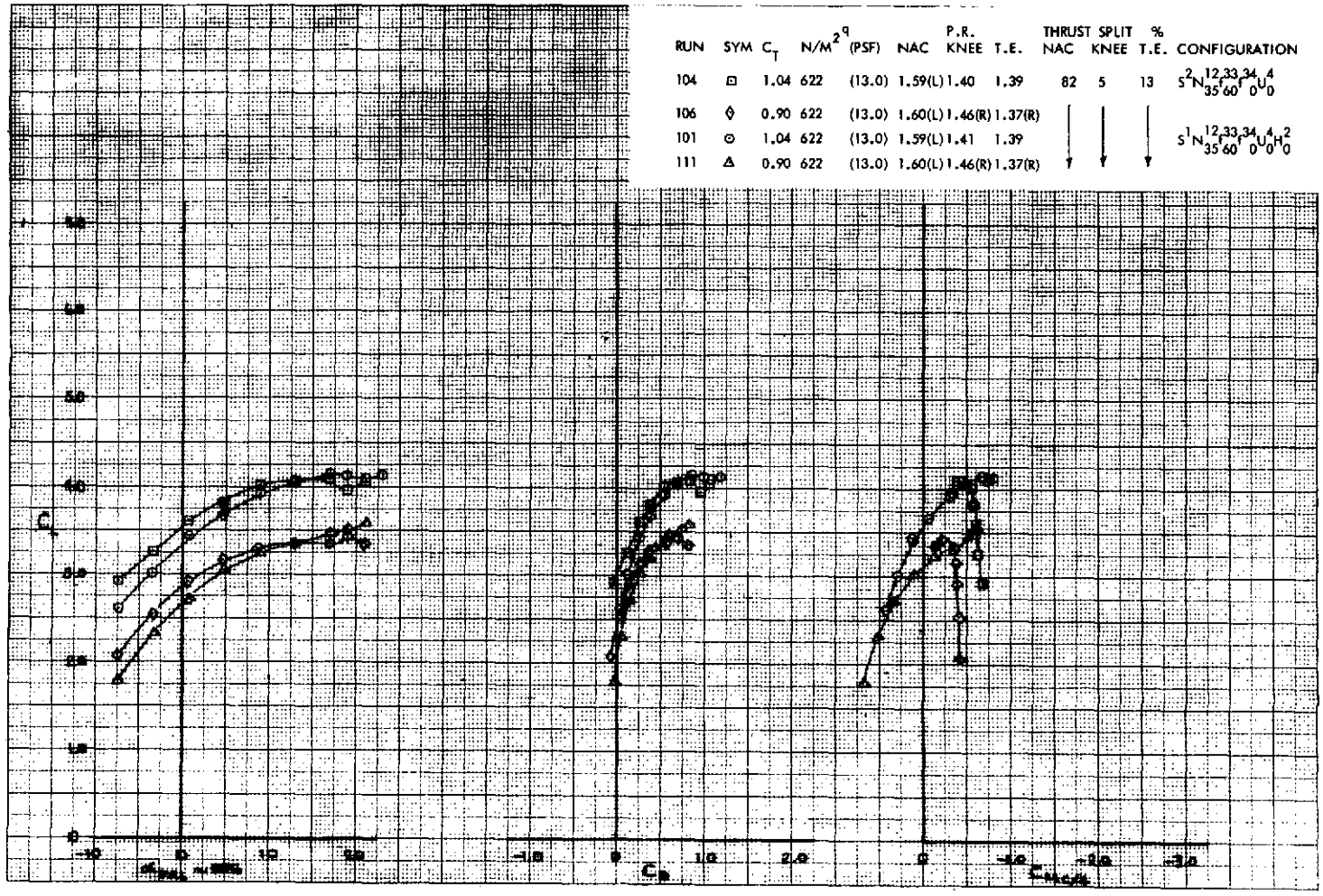

Figure 21. - Longitudinal Characteristics of the Low Wing Model with the Right Engine Inoperative and with BLC Variations, 60°/0° J/H Flap, 0° Open Deflector, Tail On and Off

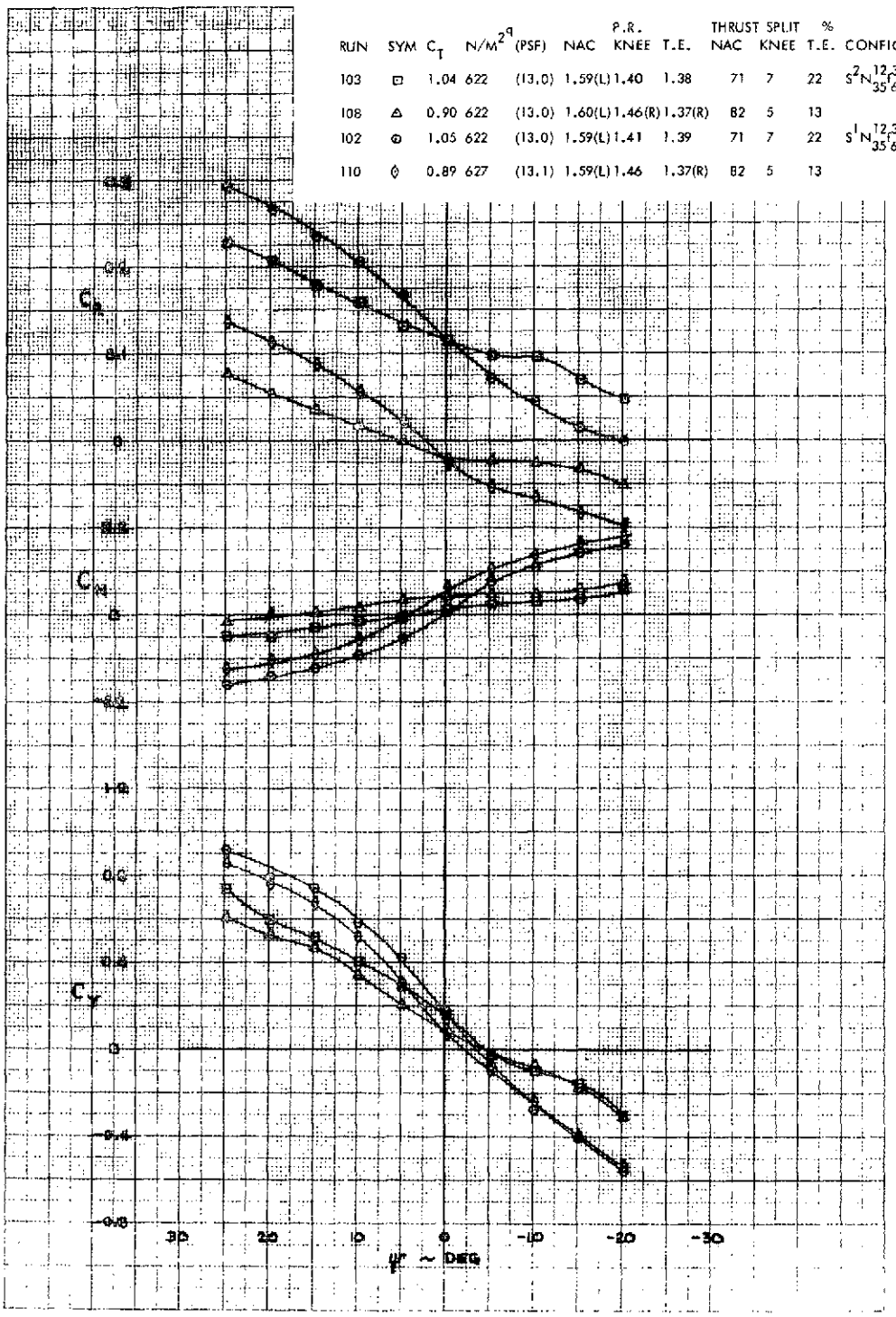

Figure 22. - Lateral-Directional Characteristics of the Low Wing Model with the Right Engine Inoperative and with BLC Variations, $60^\circ/0^\circ$ J/H Flap, 0° Open Deflector, Tail On and Off

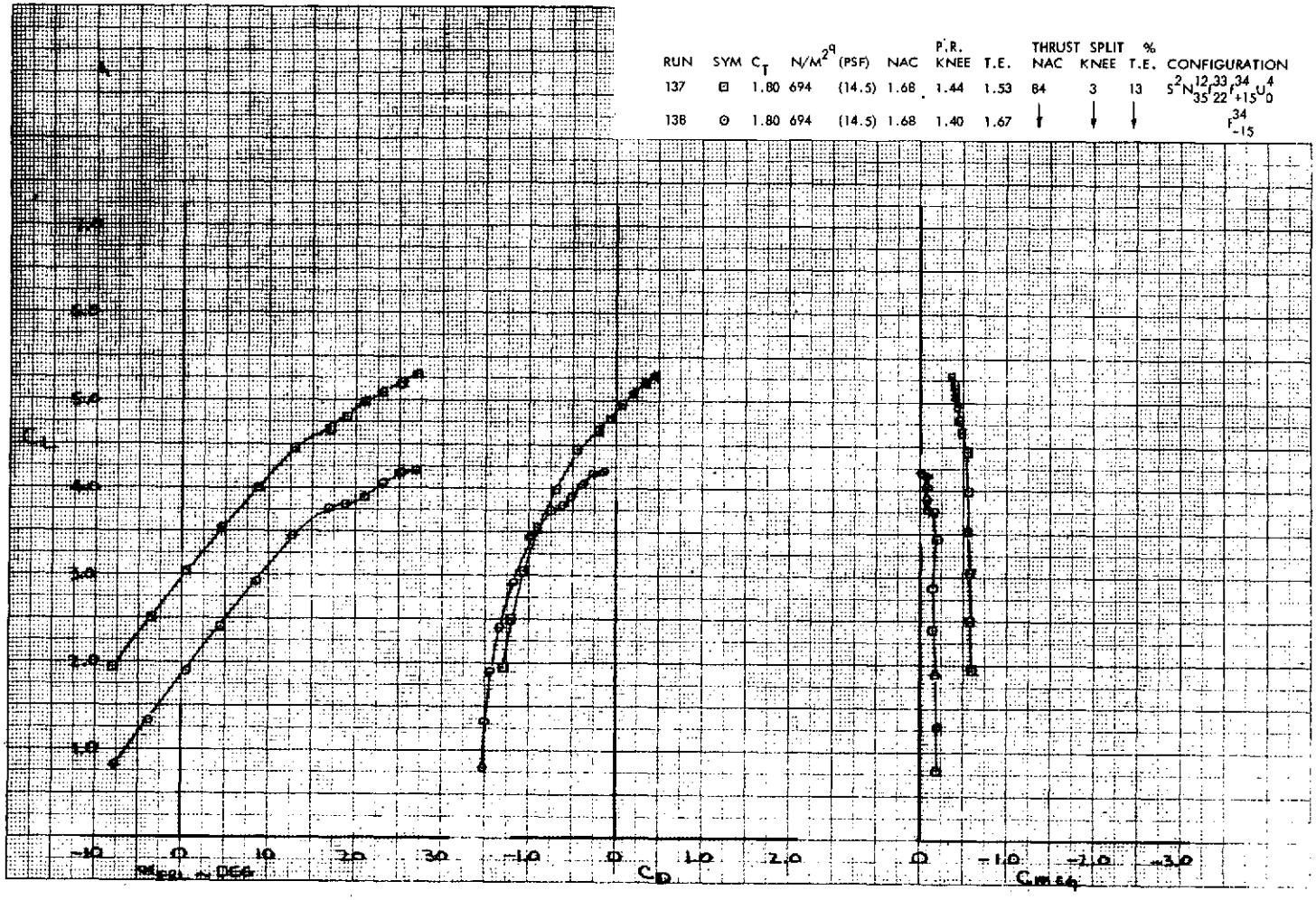

Figure 23. - Longitudinal Characteristics of the Low Wing Model, Symmetric $22^\circ/15^\circ$ and $22^\circ/-15^\circ$ J/H Flap, 0° Open Deflector, Tail Off

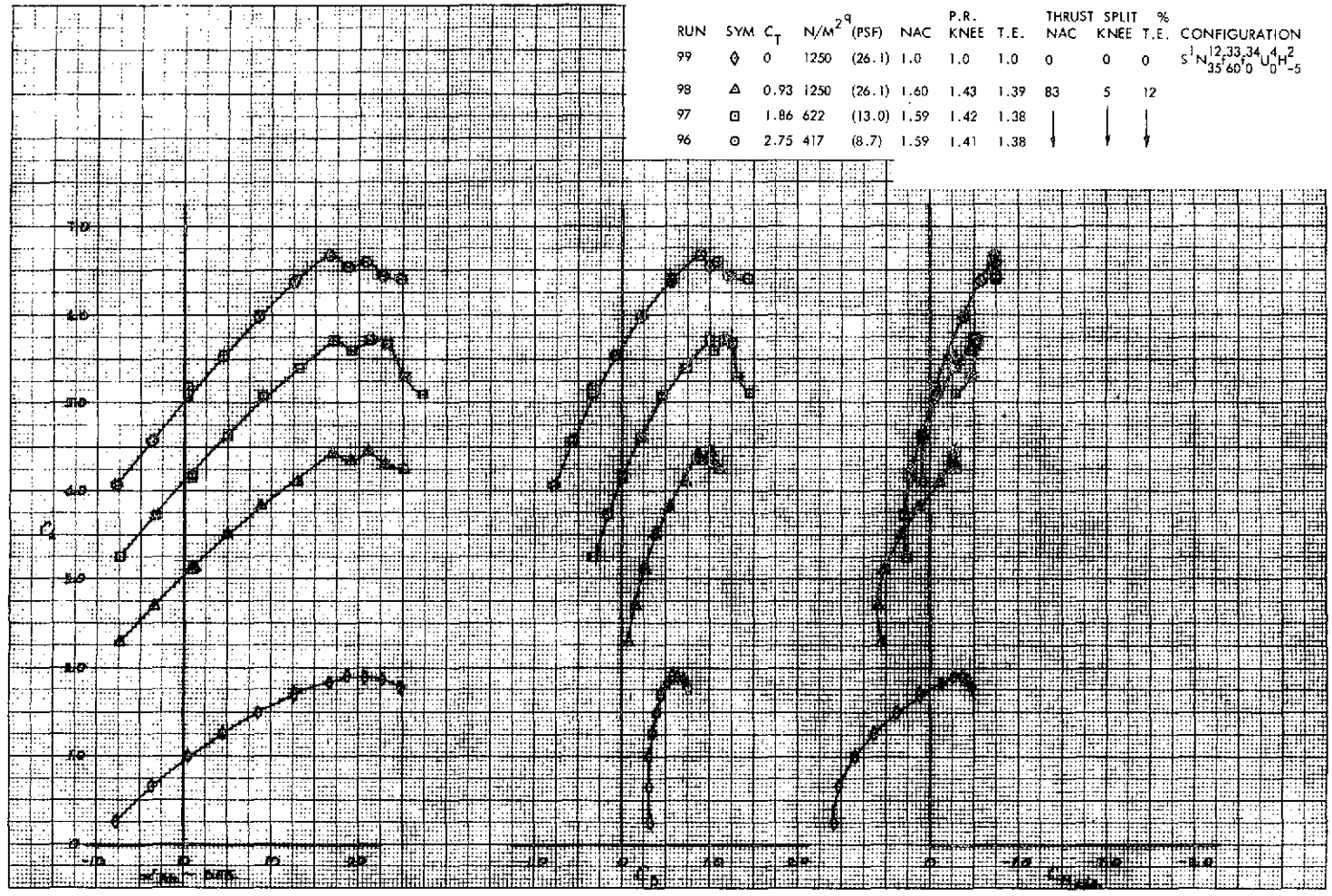

Figure 24. - Longitudinal Characteristics of the Low Wing Model with -5° Horizontal Stabilizer Incidence, 60°/0° J/H Flap, 0° Open Deflector

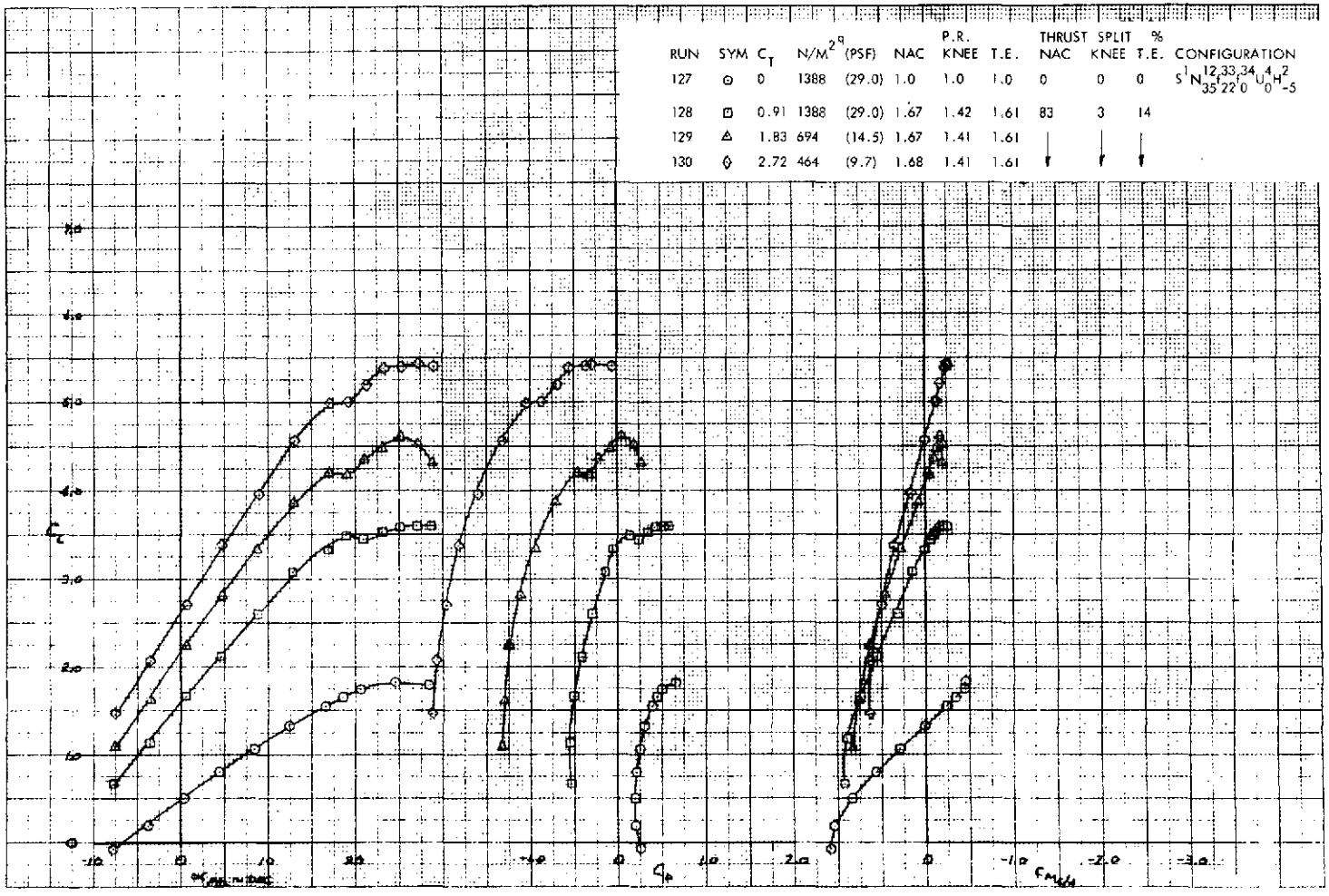

Figure 25. - Longitudinal Characteristics of the Low Wing Model with -5° Horizontal Stabilizer Incidence, 22°/0° J/H Flap, 0° Open Deflector

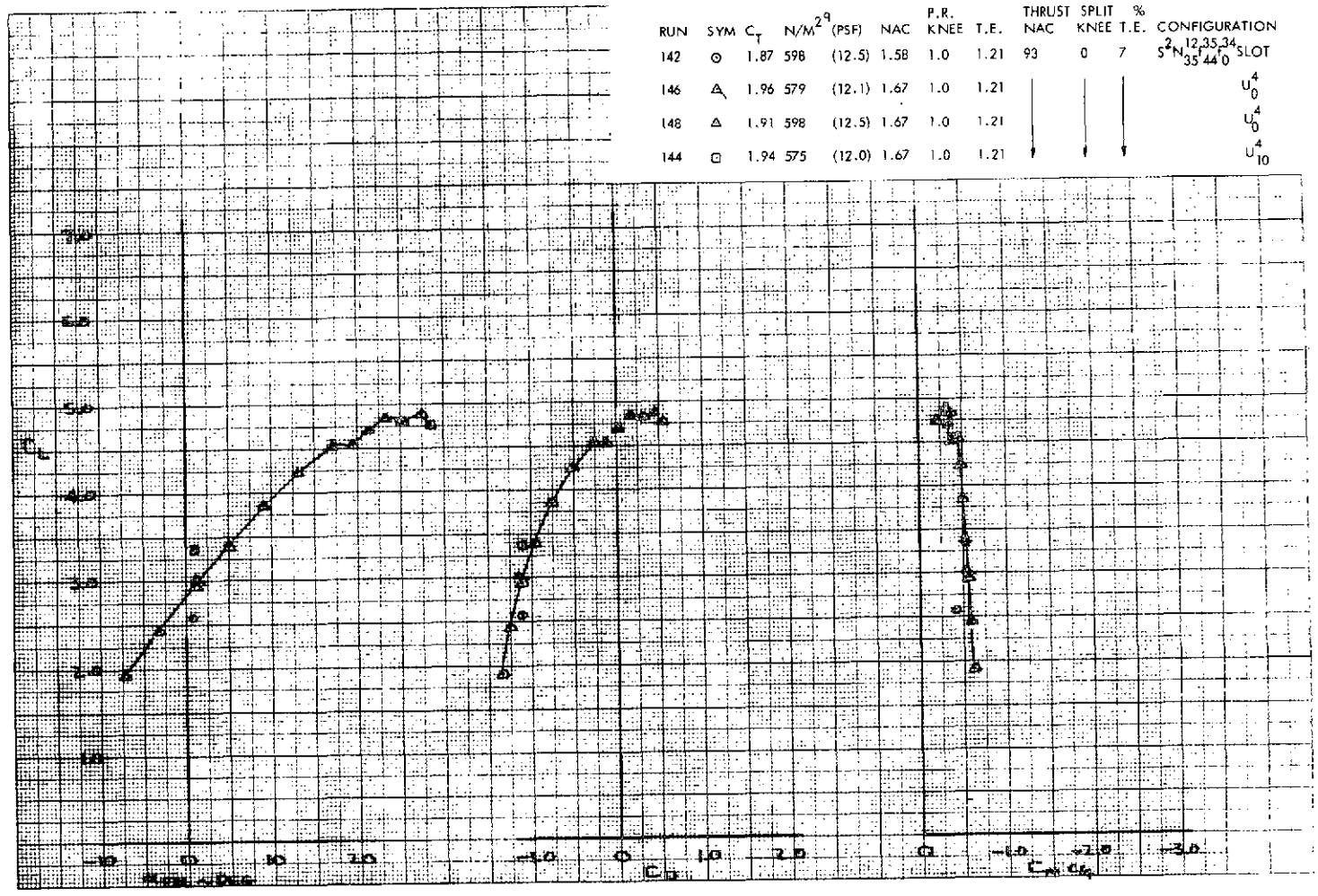

Figure 26. - Longitudinal Characteristics of the Low Wing Model with Various Nacelle Exit Configurations, $44^\circ/0^\circ$ Coanda Flap, Tail Off

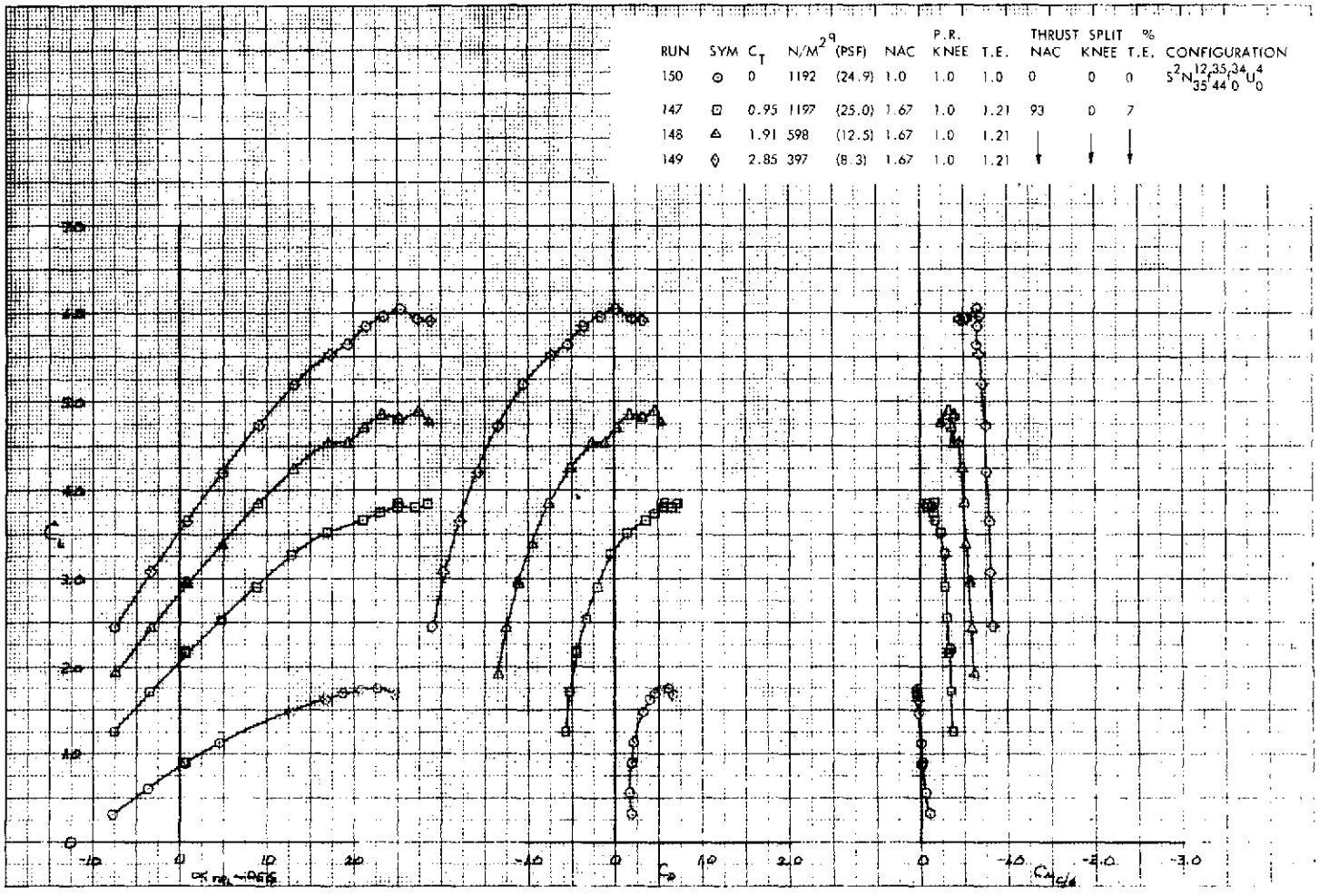

Figure 27. - Longitudinal Characteristics of the Low Wing Model, 44°/0° Coanda Flap, 0° Open Deflector, T-tail Off

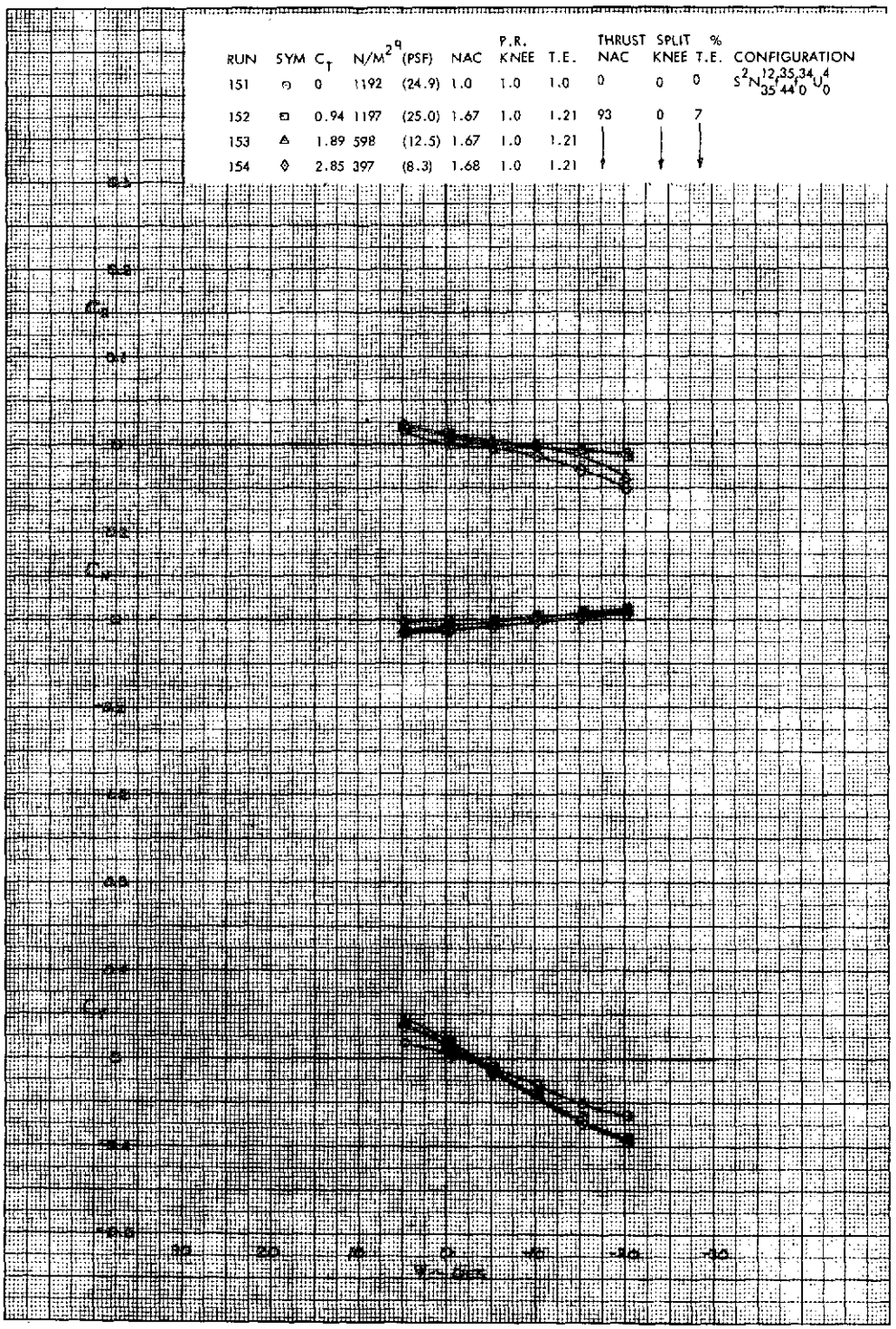

Figure 28. - Lateral-Directional Characteristics of the Low Wing Model, 44°/0° Coanda Flap, 0° Open Deflector, Tail Off

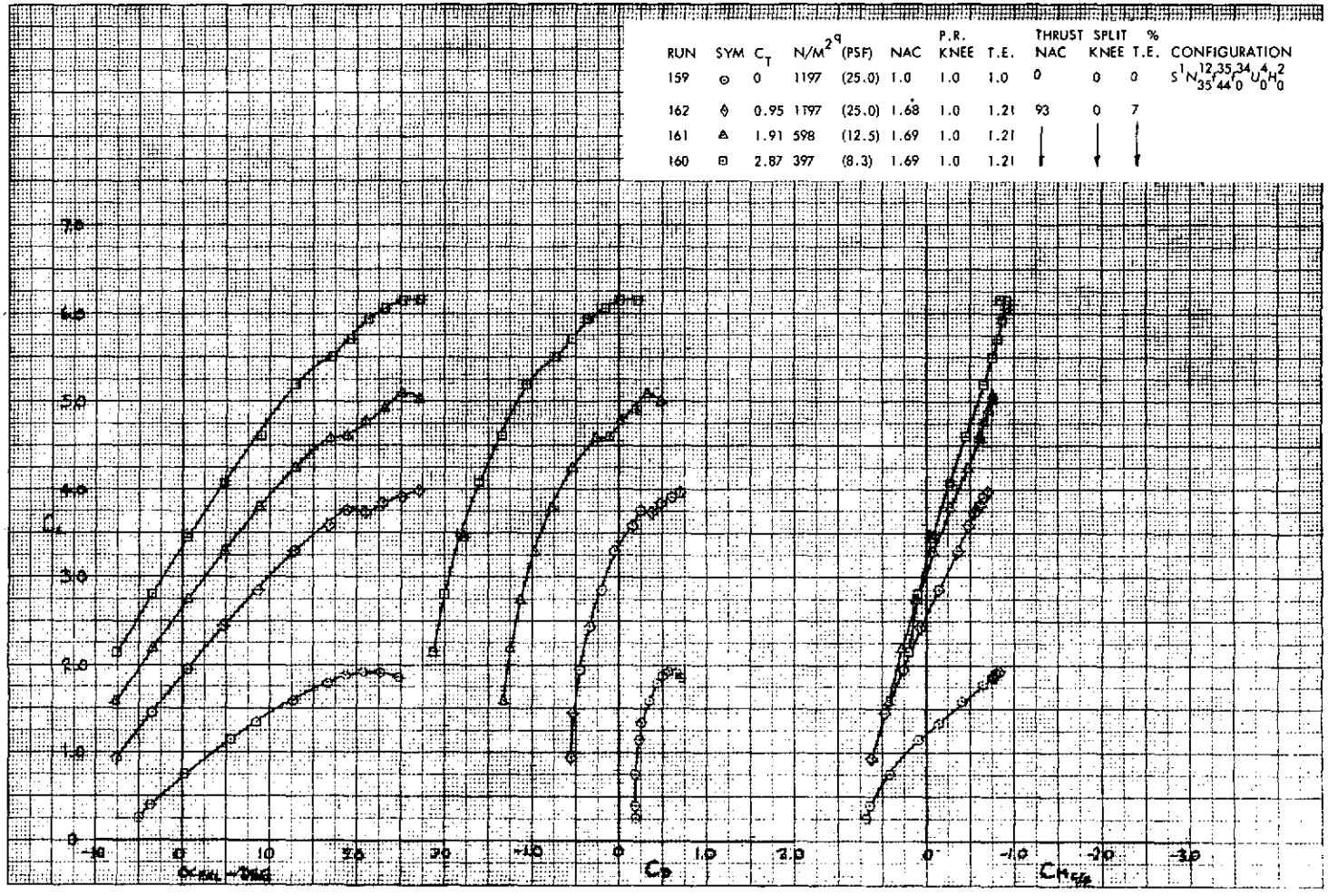

Figure 29. - Longitudinal Characteristics of the Low Wing Model, $44^\circ/0^\circ$ Coanda Flap, 0° Open Deflector, Tail On

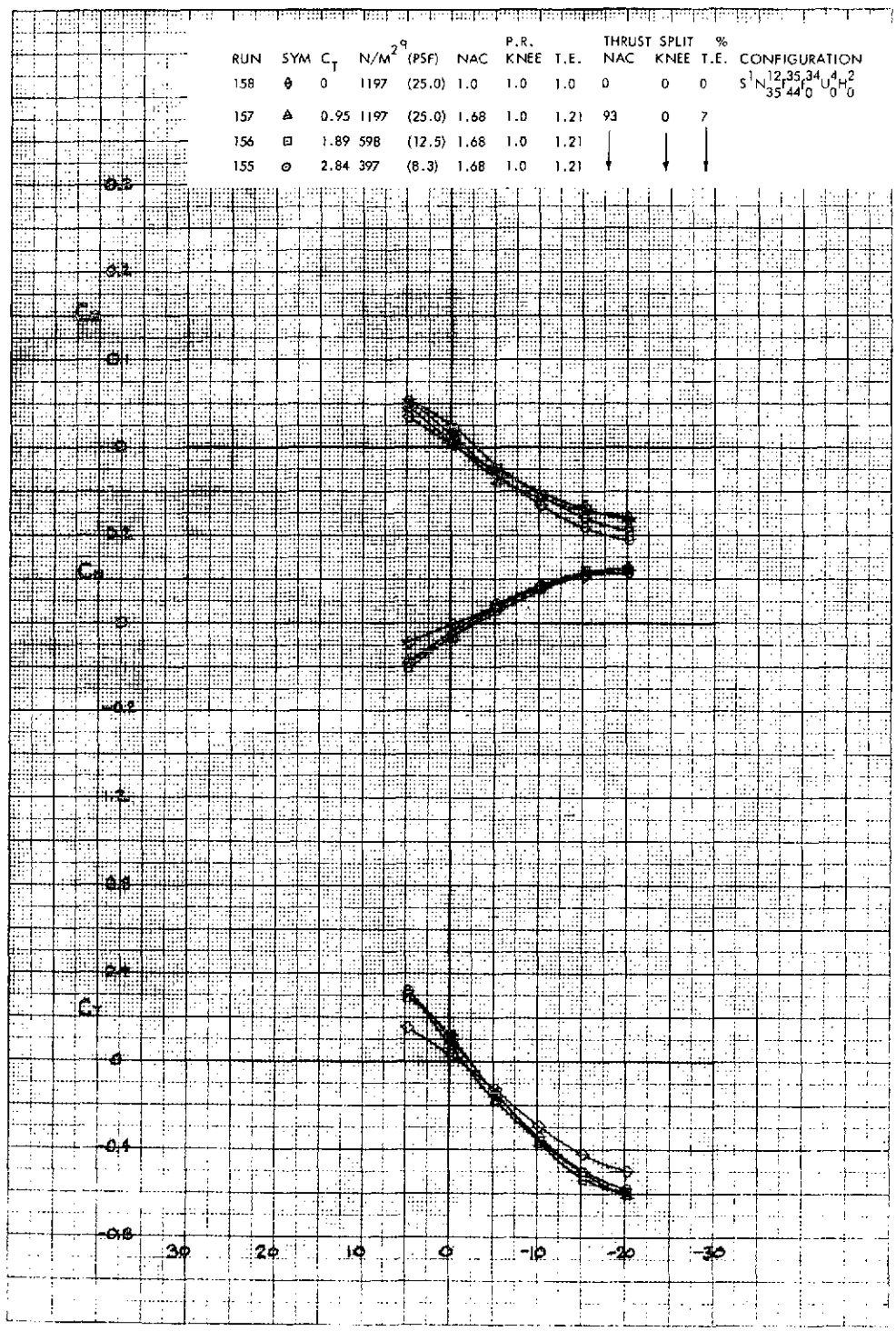

Figure 30. - Lateral-Directional Characteristics of the Low Wing Model, 44°/0° Coanda Flap, 0° Open Deflector, Tail On

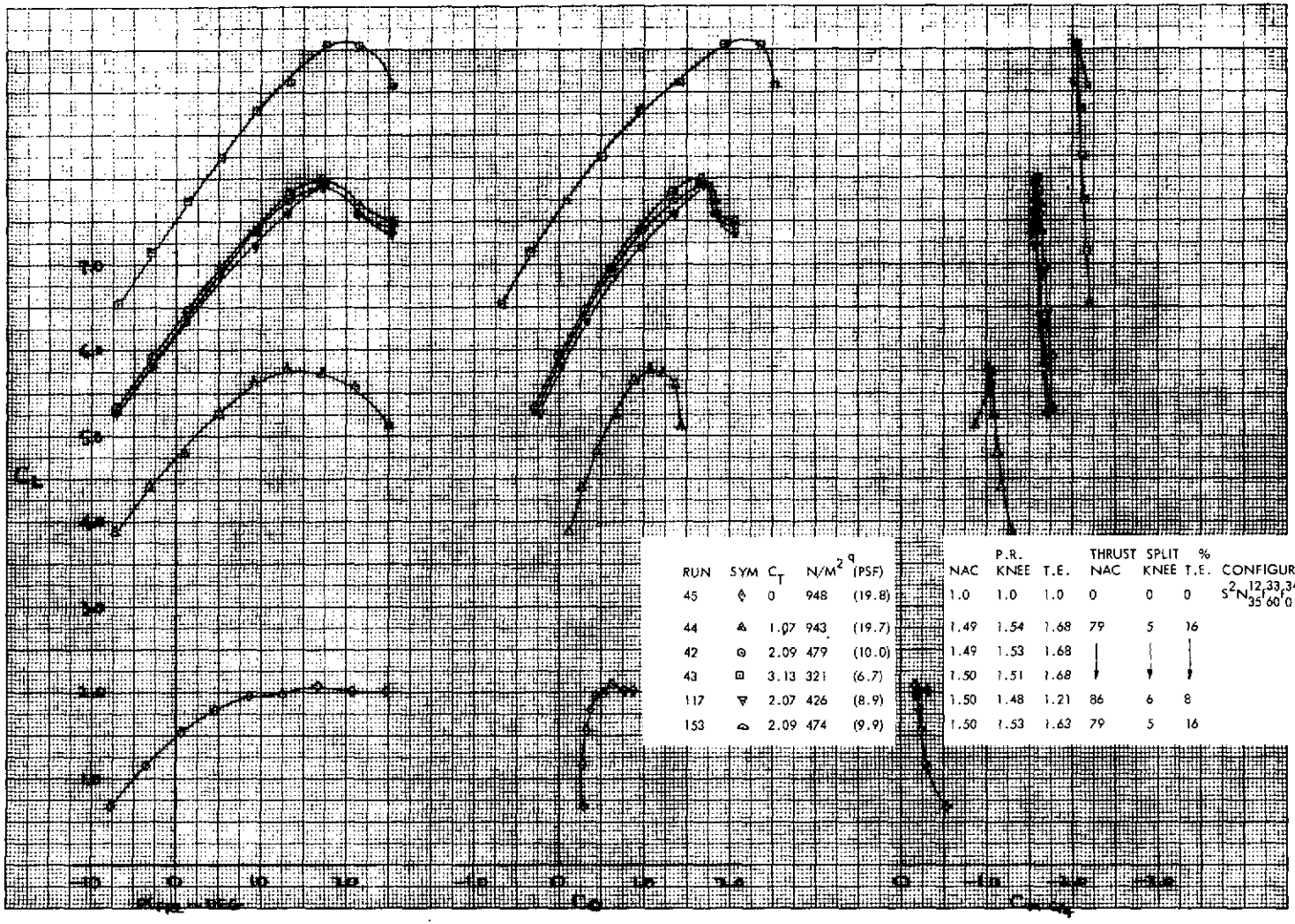

Figure 31. - Longitudinal Characteristics of the High Wing Model, $60^{\circ}/0^{\circ}$ J/H Flap, 10° Open Deflector, Tail Off

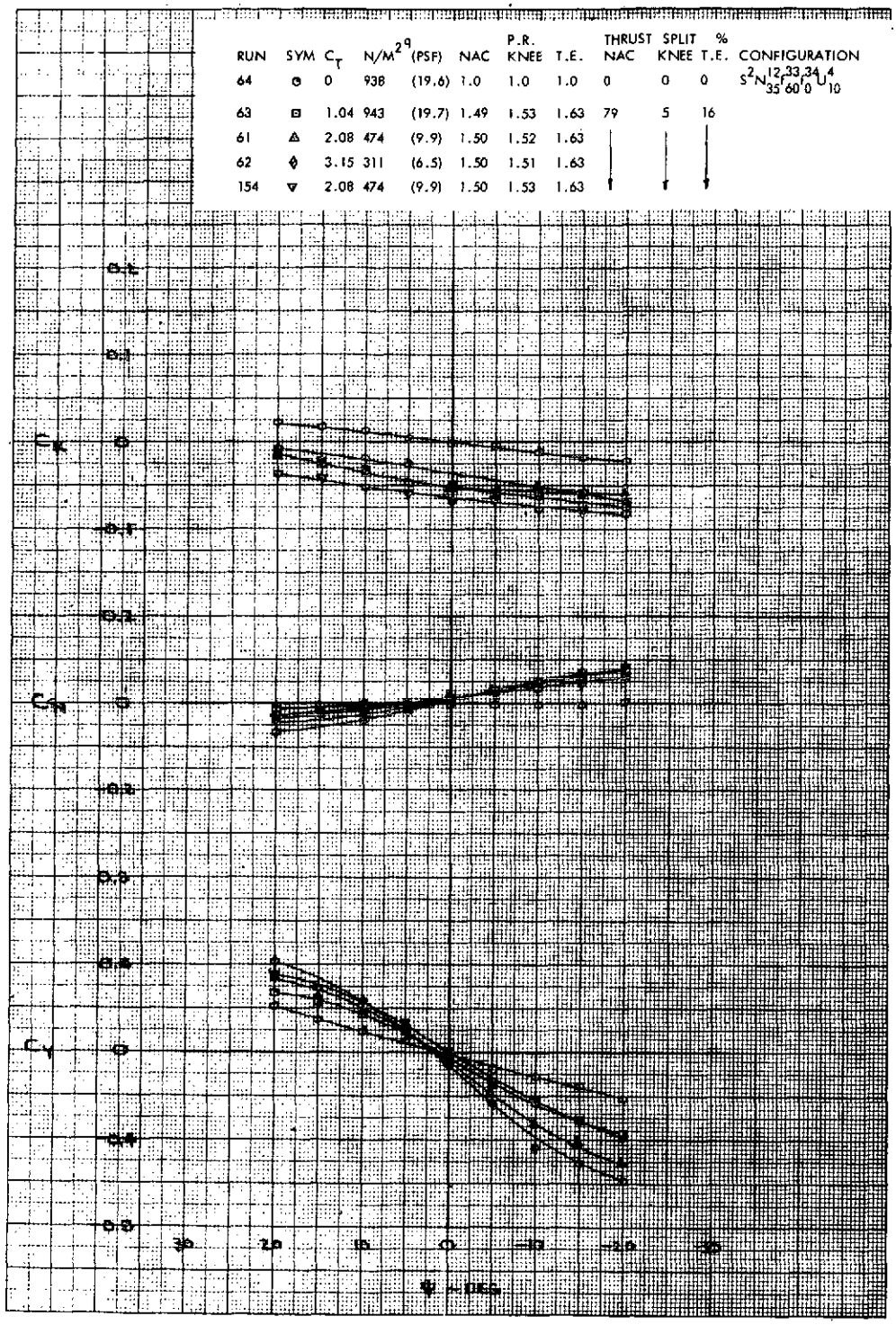

Figure 32. - Lateral-Directional Characteristics of the High Wing Model, $60^\circ/0^\circ$ J/H Flap, 10° Open Deflector, Tail Off

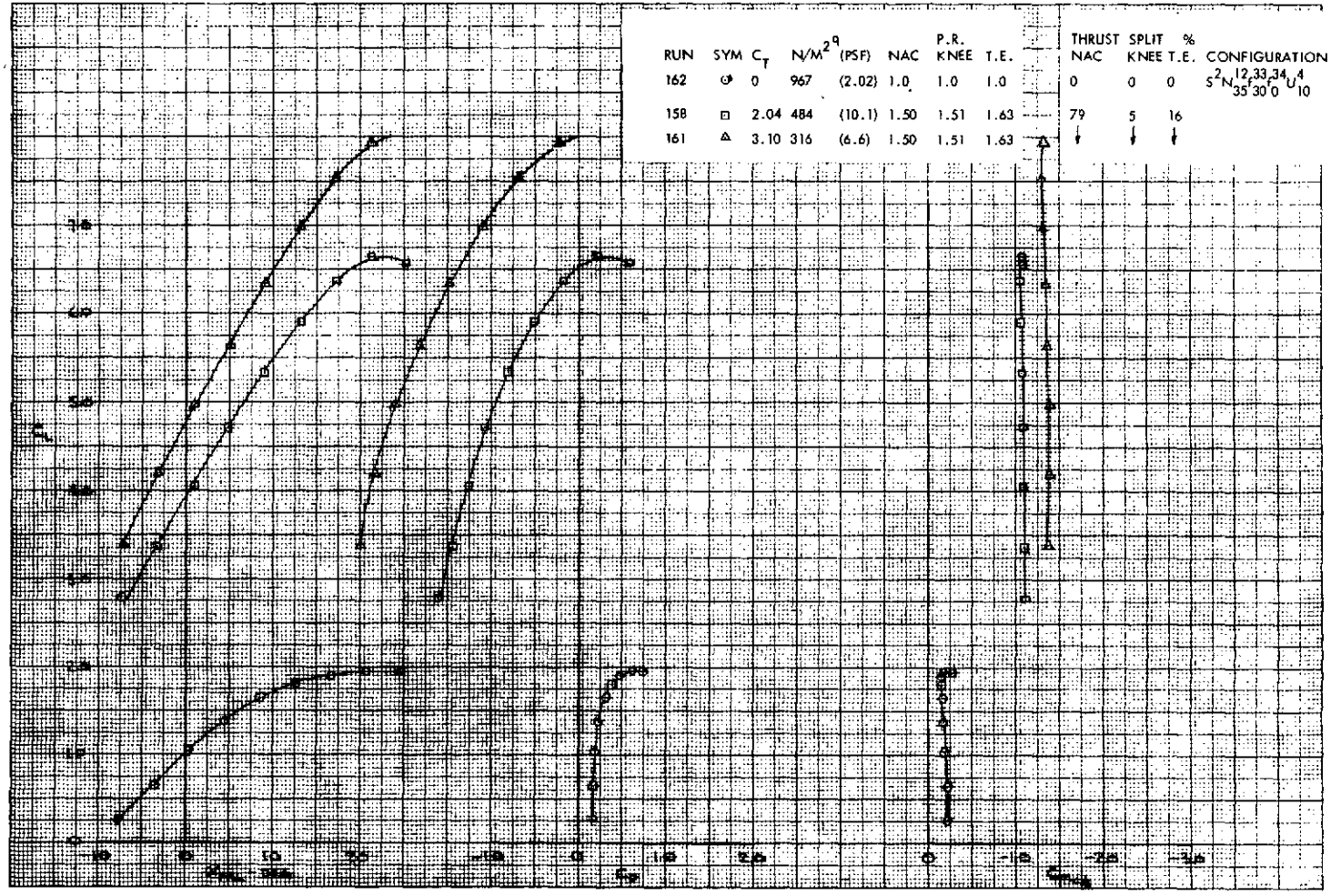

Figure 33. - Longitudinal Characteristics of the High Wing Model, 30°/0° J/H Flap, 10° Open Deflector, Tail Off

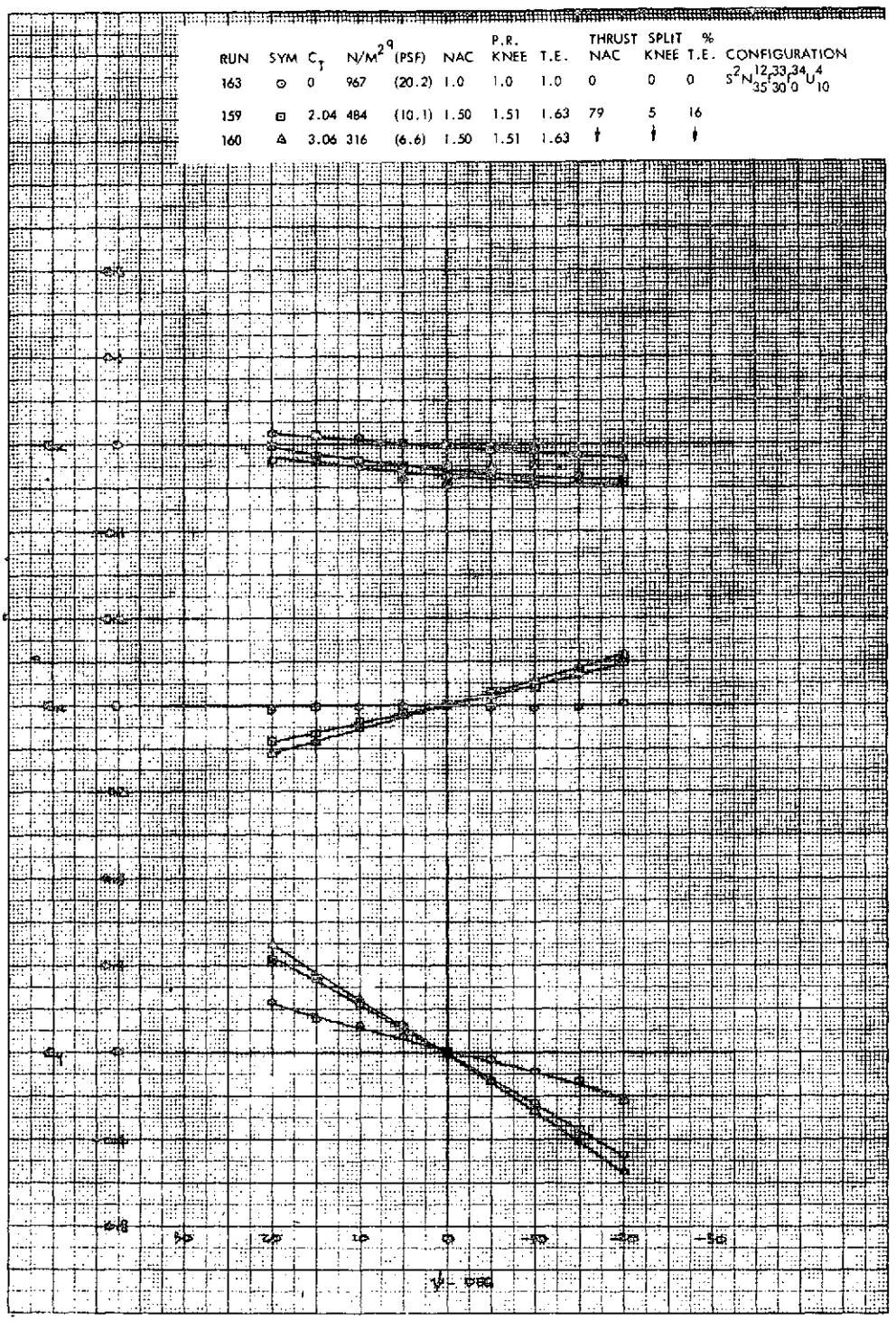

Figure 34. - Lateral-Directional Characteristics of the High Wing Model, 30°/0° J/H Flap, 10° Open Deflector, Tail Off

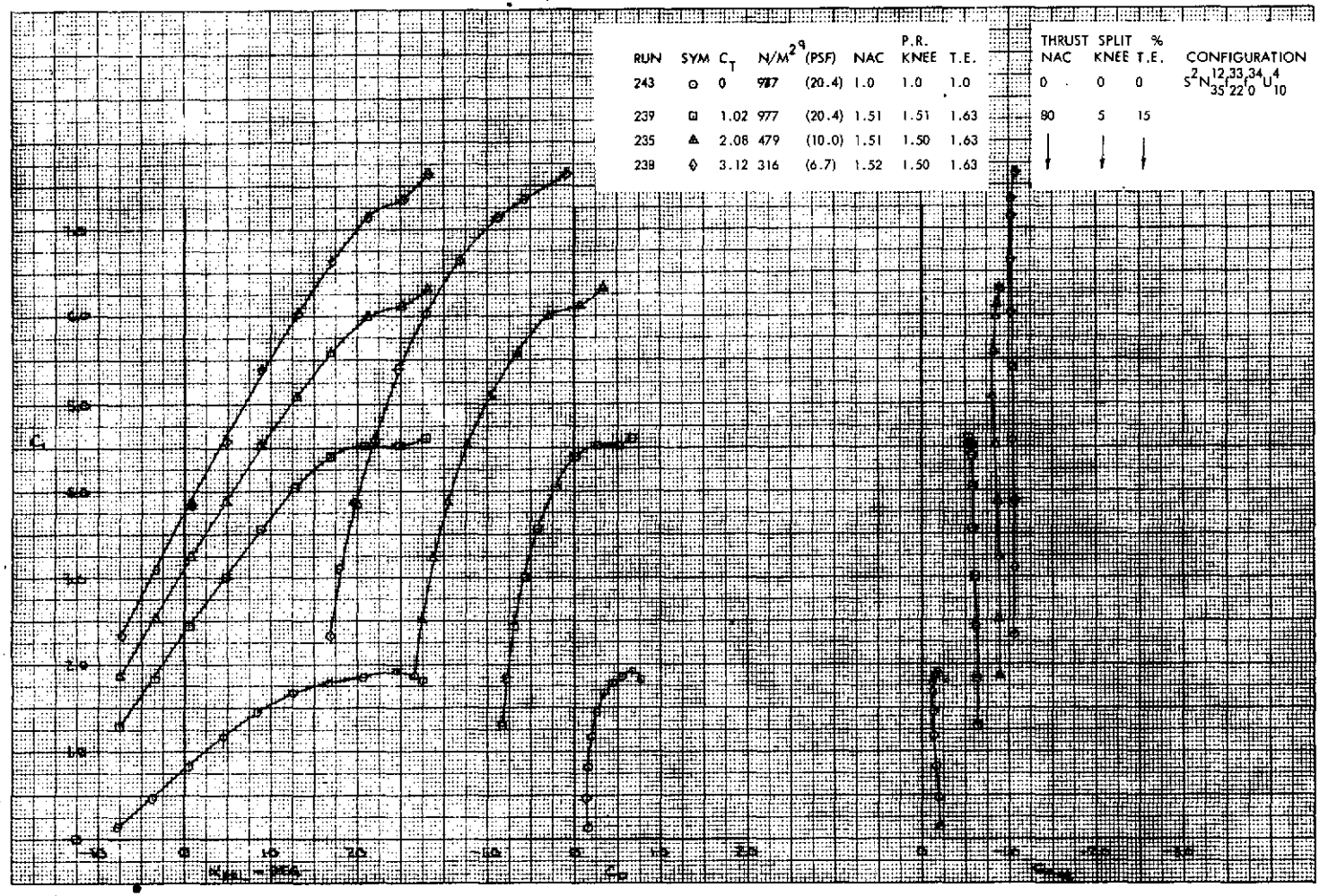

Figure 35. – Longitudinal Characteristics of the High Wing Model, 22°/0° J/H Flap, 10° Open Deflector, Tail Off

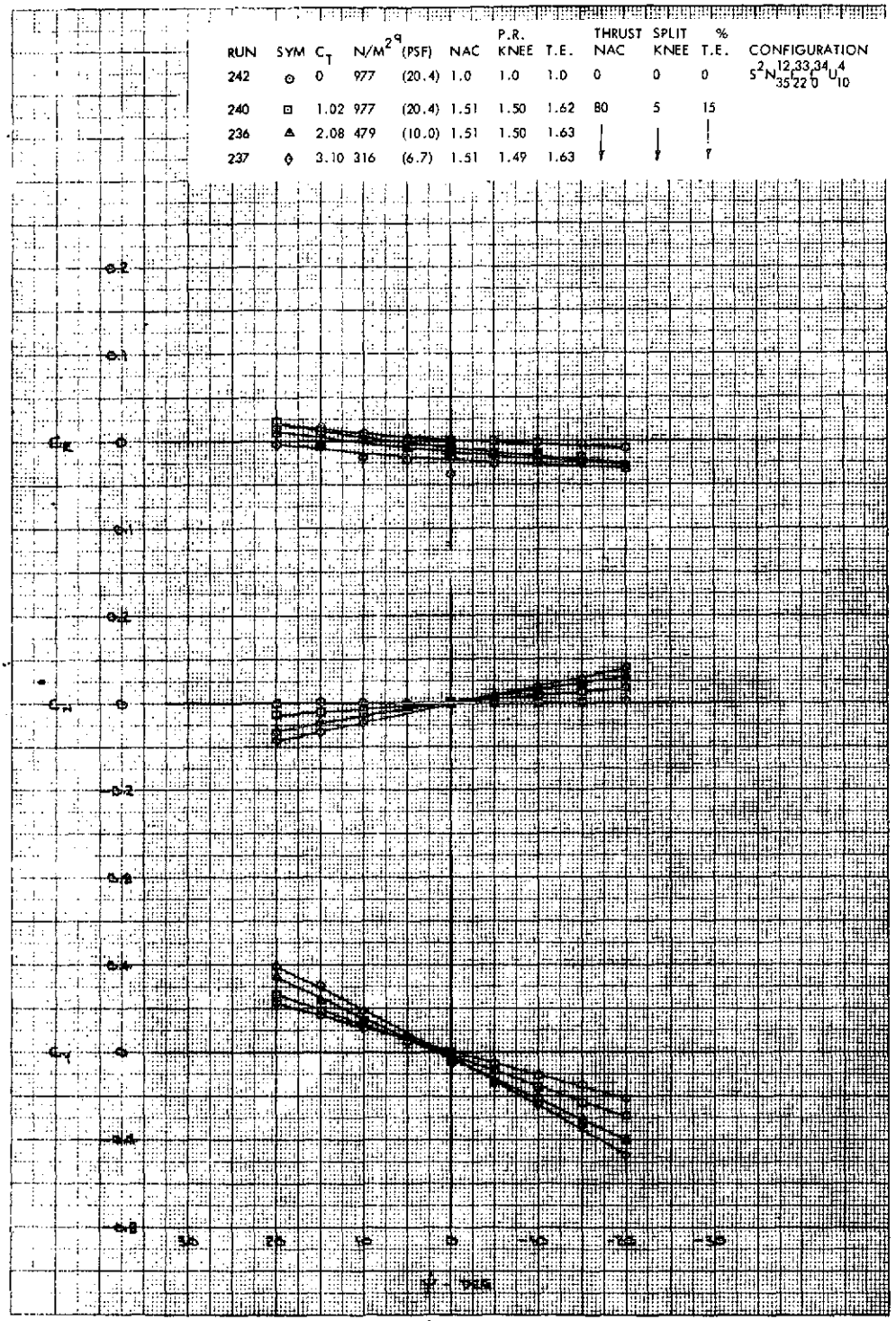

Figure 36. - Lateral-Directional Characteristics of the High Wing Model, $22^\circ/0^\circ$ J/H Flap, 10° Open Deflector, Tail Off

C-2

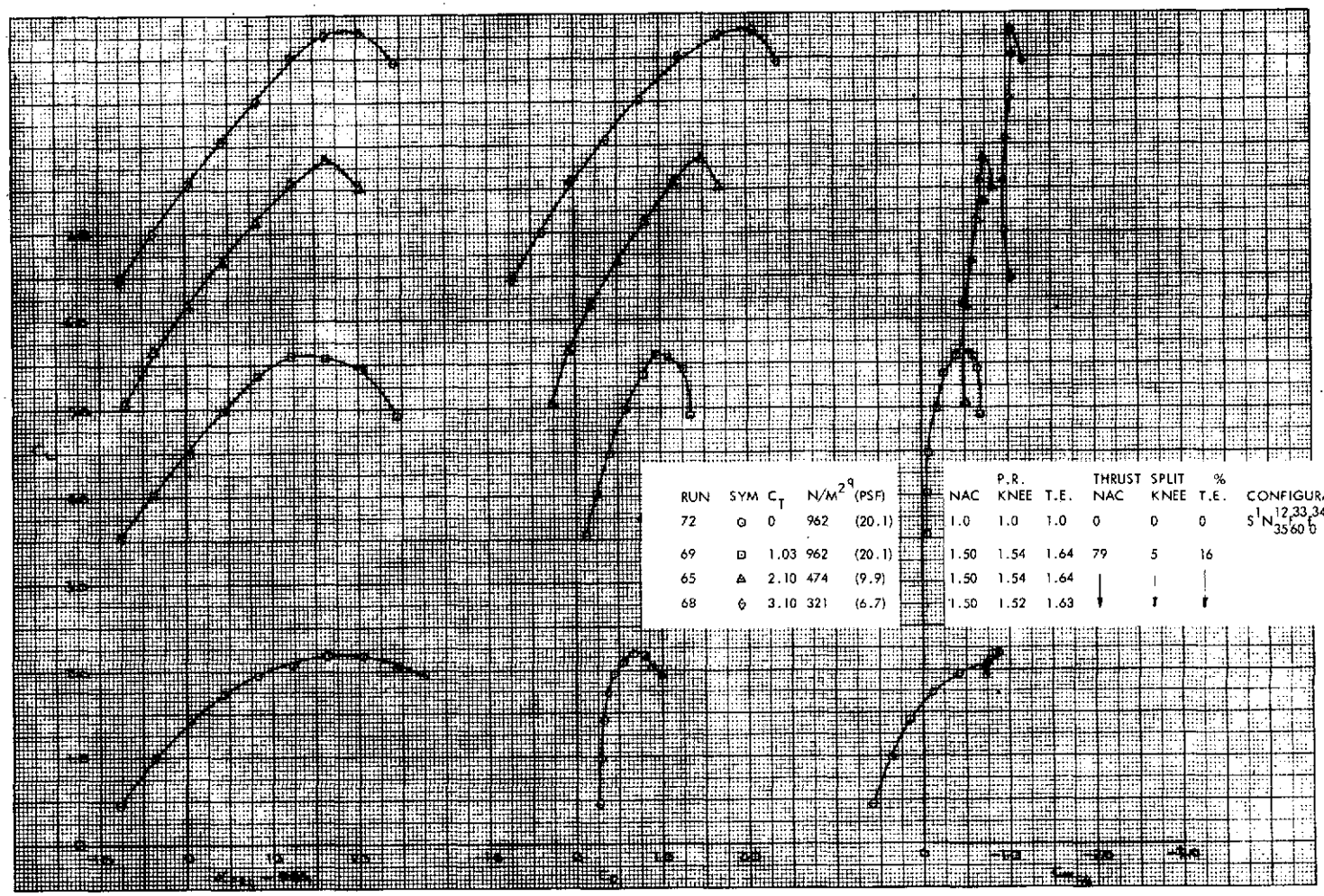

Figure 37. - Longitudinal Characteristics of the High Wing Model, $60°/0°$ J/H Flap, $10°$ Open Deflector, Tail On

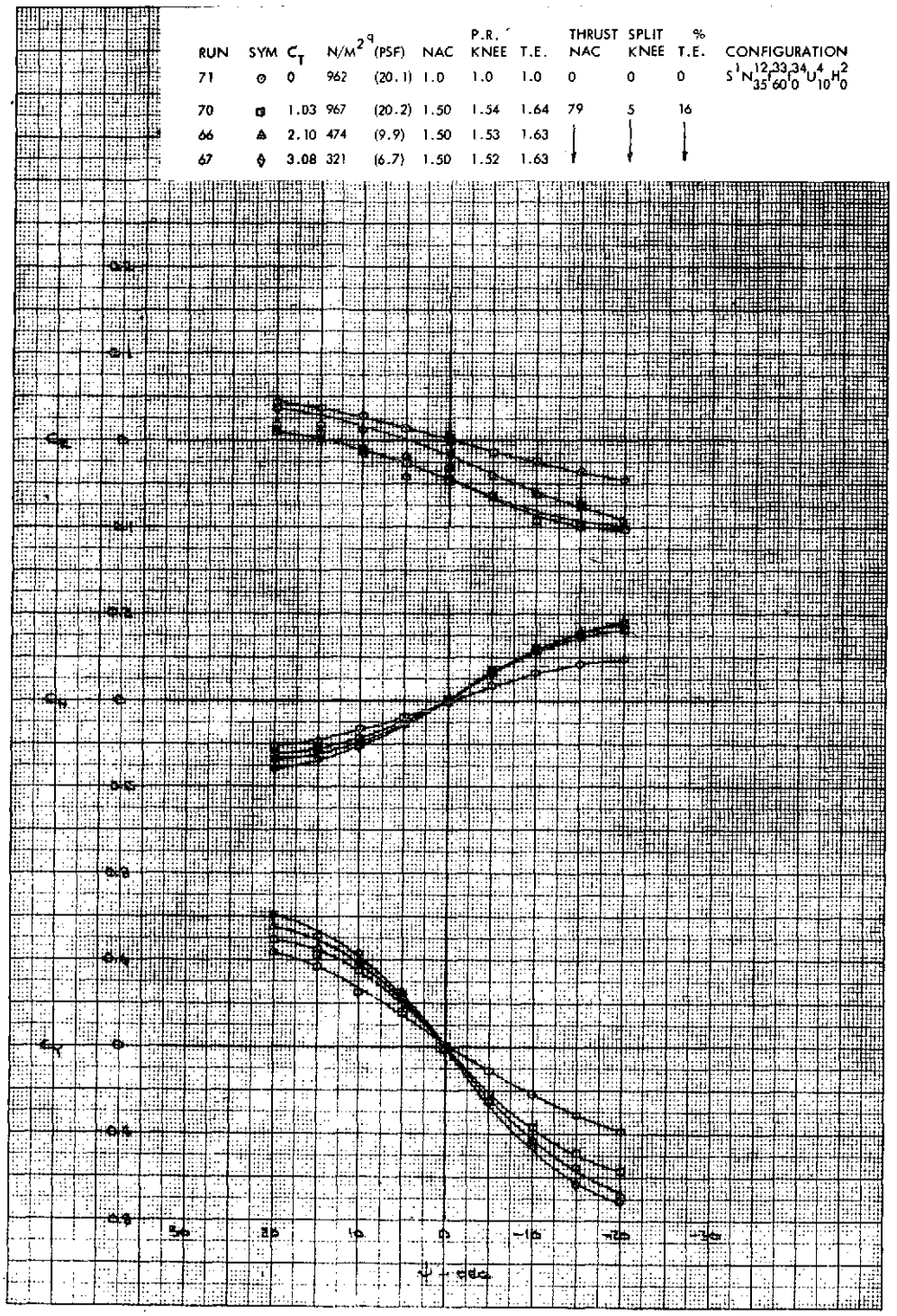

Figure 38. - Lateral-Directional Characteristics of the High Wing Model, 60°/0° J/H Flap, 10° Open Deflector, Tail On

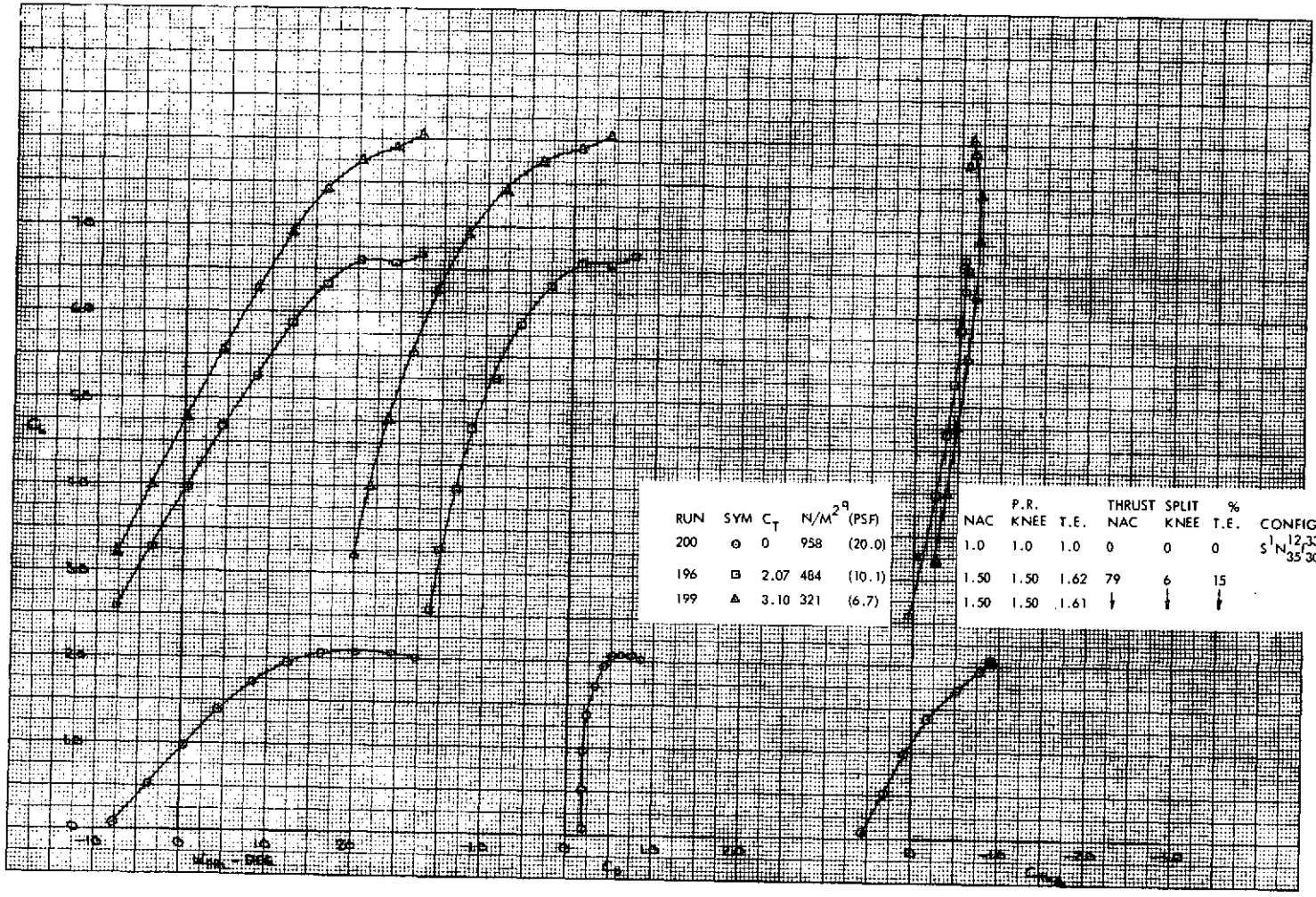

Figure 39. - Longitudinal Characteristics of the High Wing Model, $30°/0°$ J/H Flap, $10°$ Open Deflector, Tail

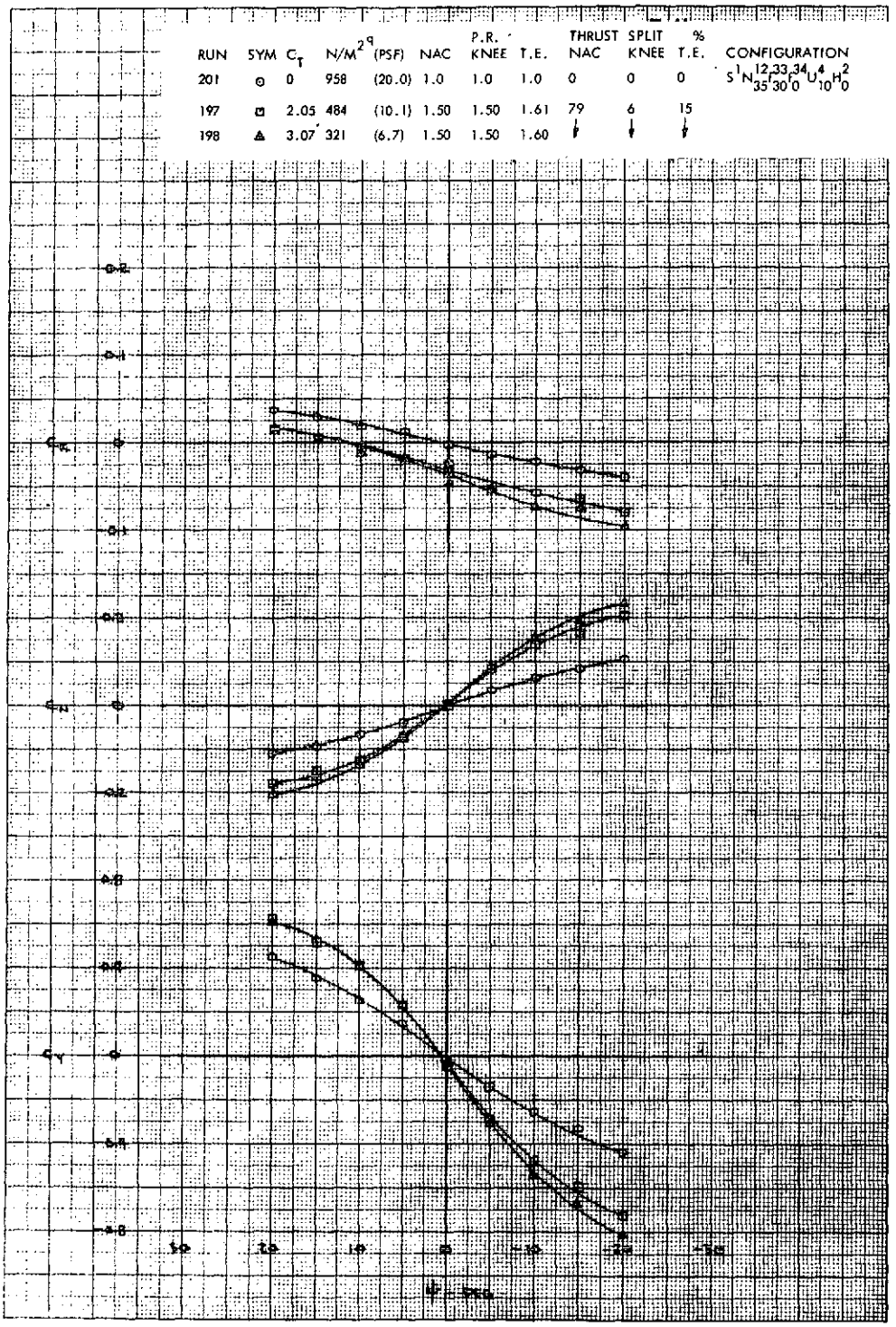

Figure 40. - Lateral-Directional Characteristics of the High Wing Model, 30°/0° J/H Flap, 10° Open Deflector, Tail On

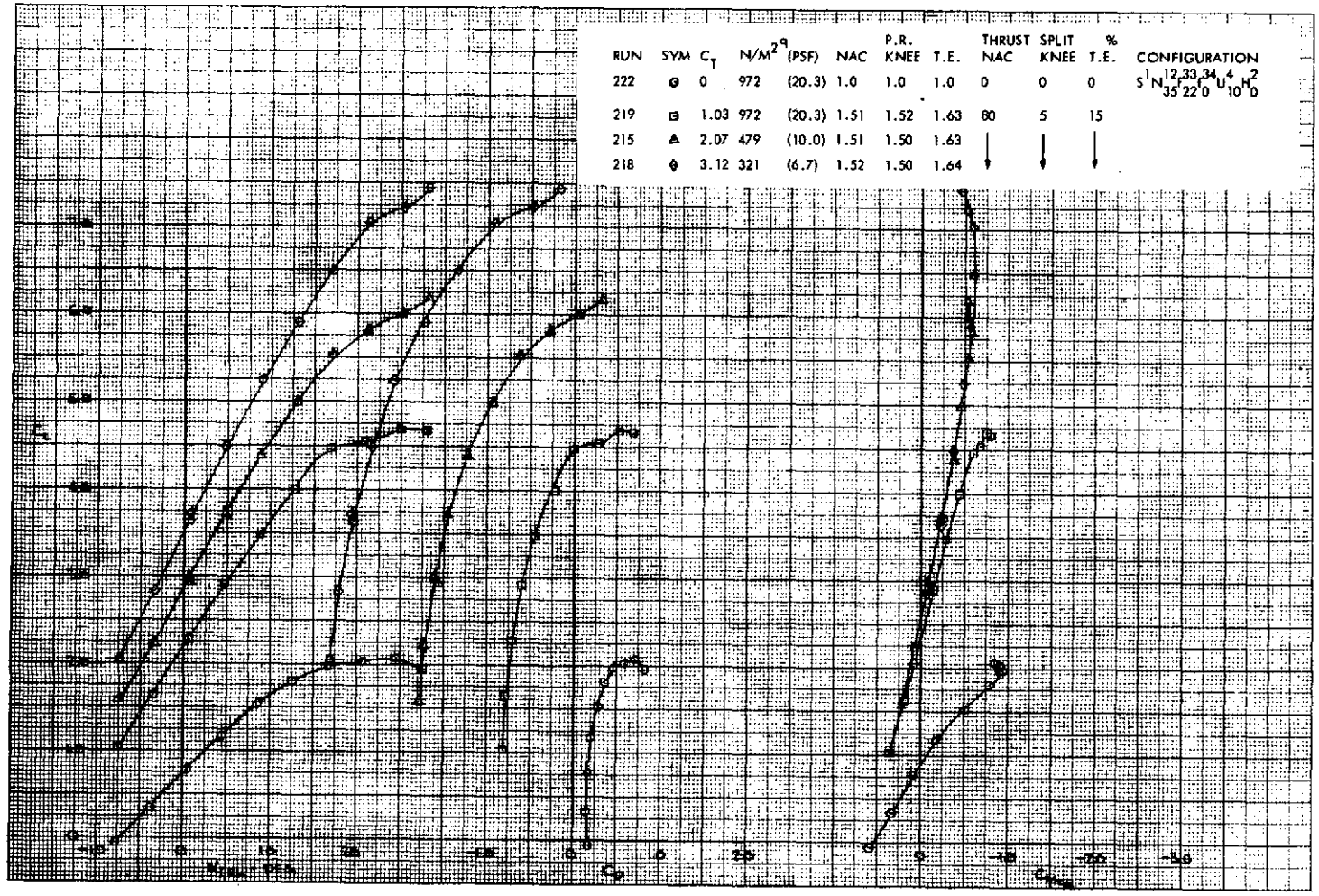

Figure 41. - Lateral-Directional Characteristics of the High Wing Model, 22°/0° J/H Flap, 10° Open Deflector, Tail On

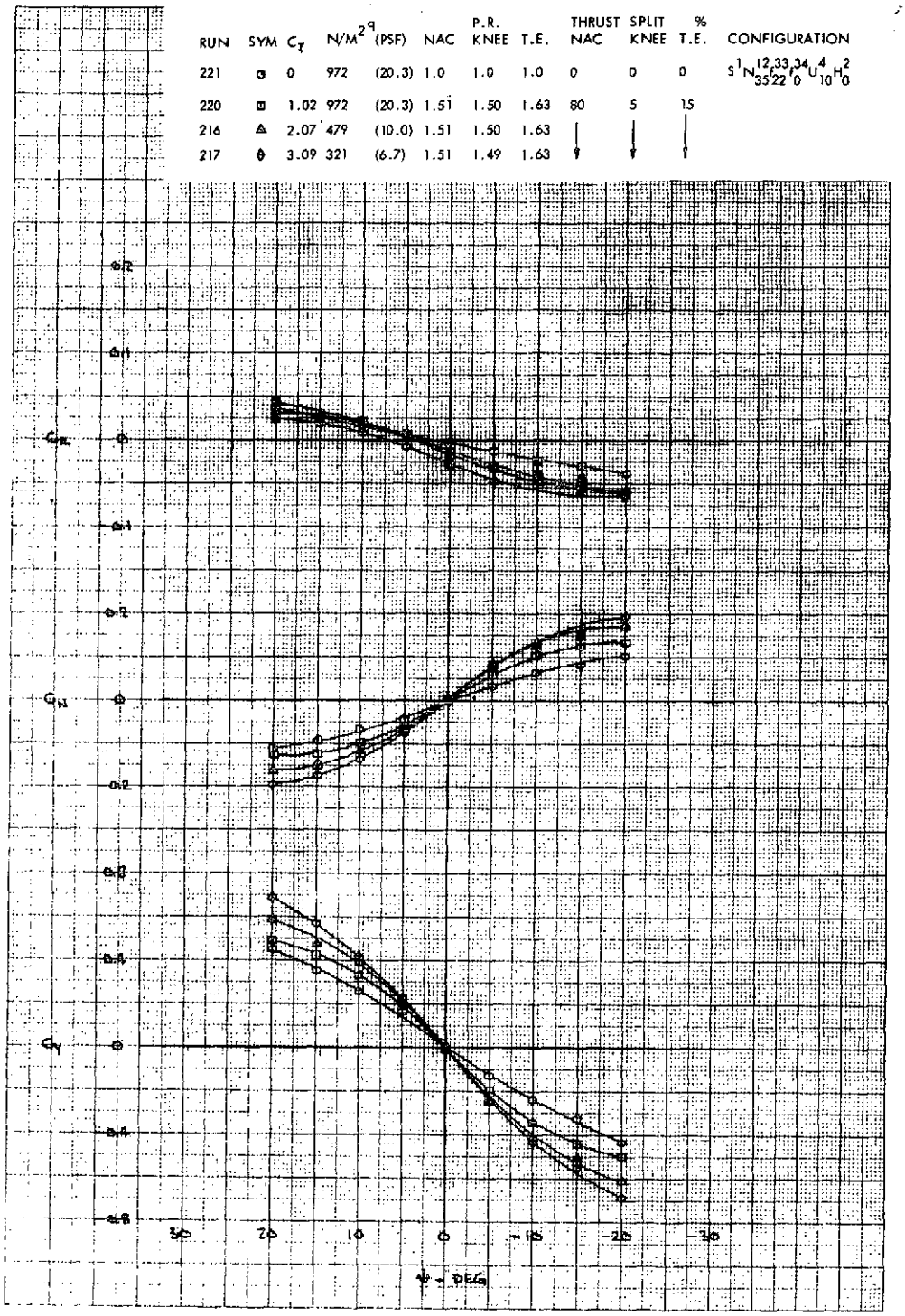

Figure 42. - Lateral-Directional Characteristics of the High Wing Model, 22°/0° J/H Flap, 10° Open Deflector, Tail On

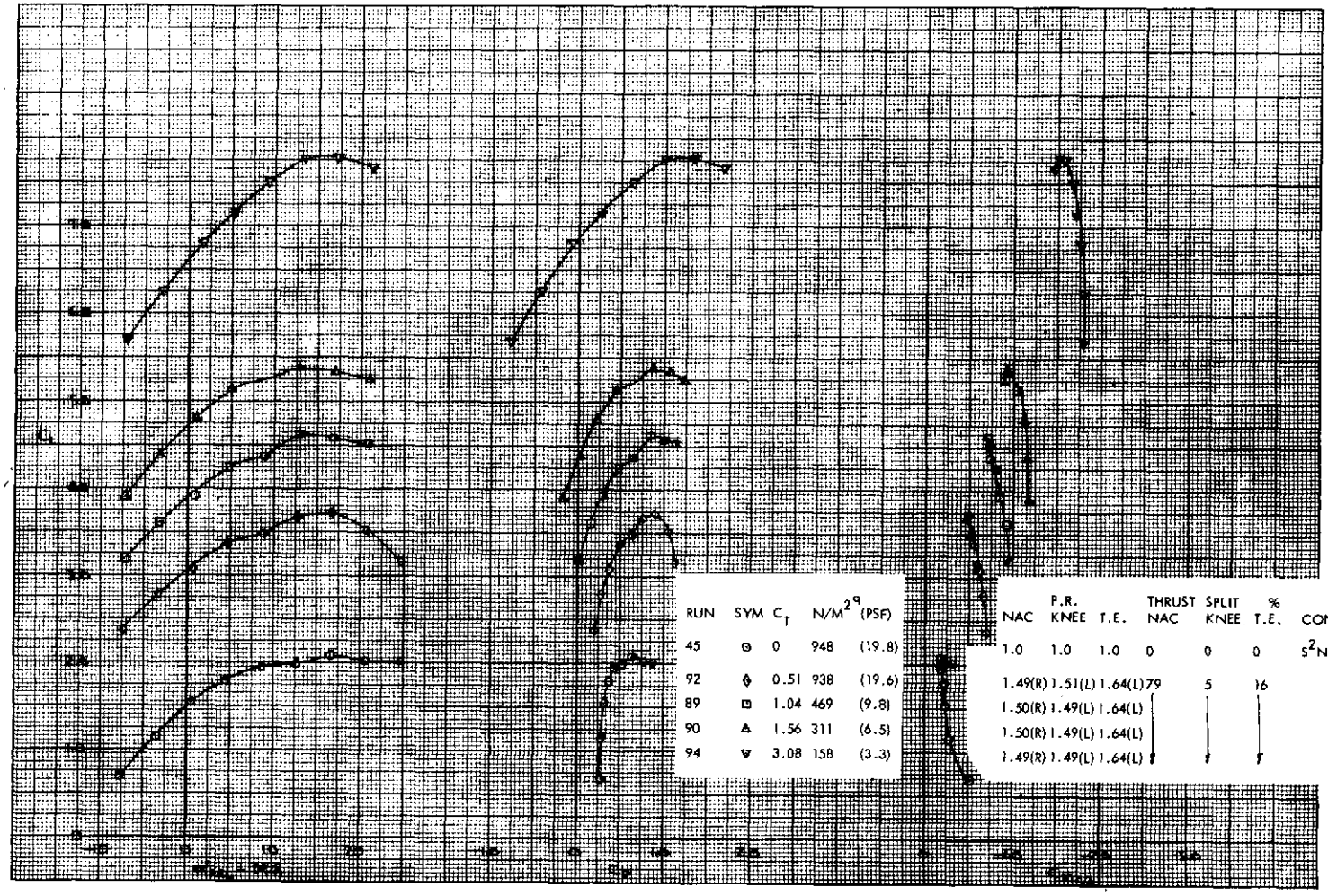

Figure 43. - Longitudinal Characteristics of the High Wing Model with the Left Engine Inoperative, $60^{\circ}/0^{\circ}$ J/H Flap, 10° Open Deflector, Tail Off

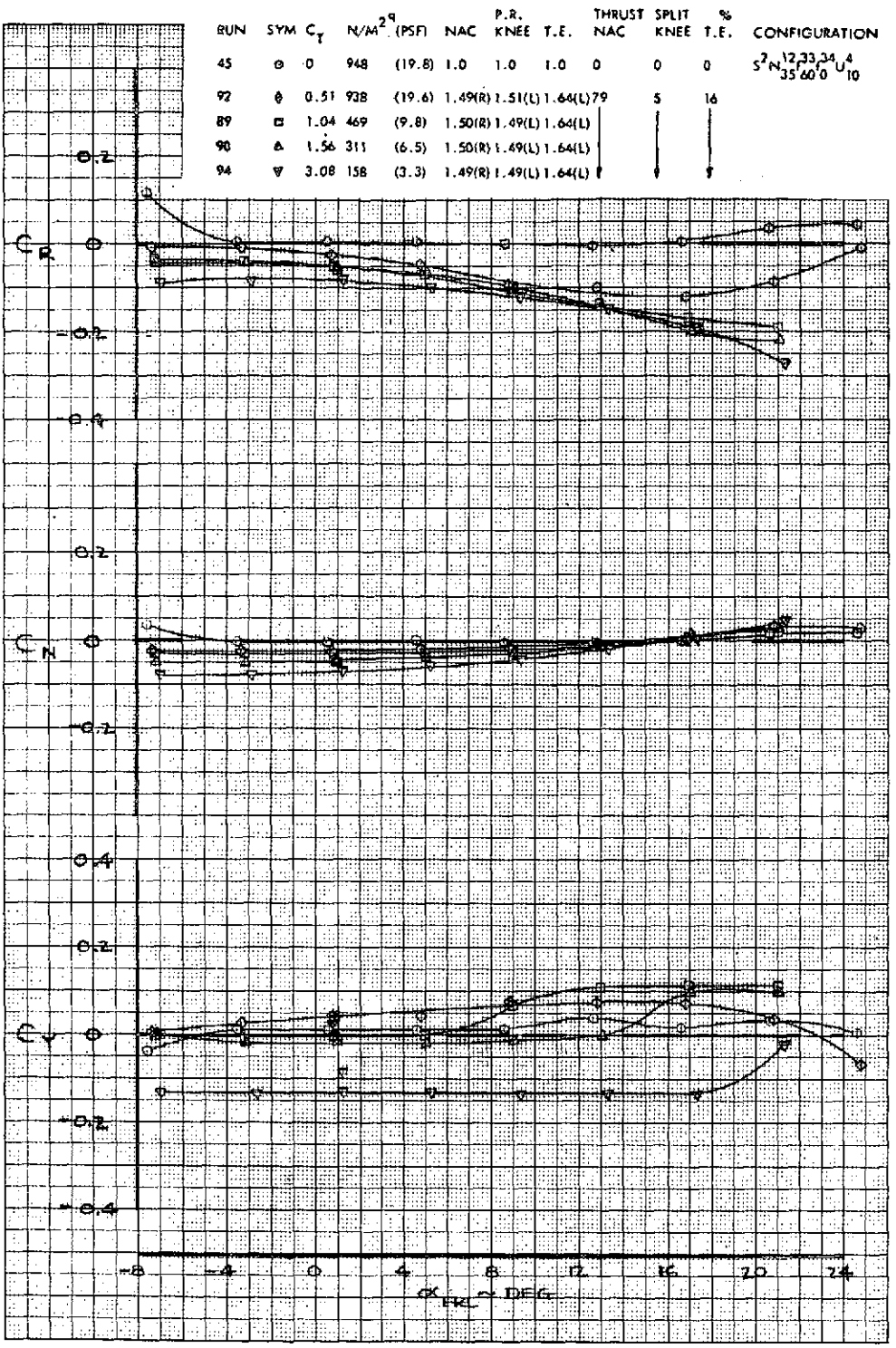

Figure 44. - Effect of Angle-of-Attack on Lateral-Directional Characteristics of the High Wing Model with the Left Engine Inoperative, $60^\circ/0^\circ$ J/H Flap, 10° Open Deflector, Tail Off

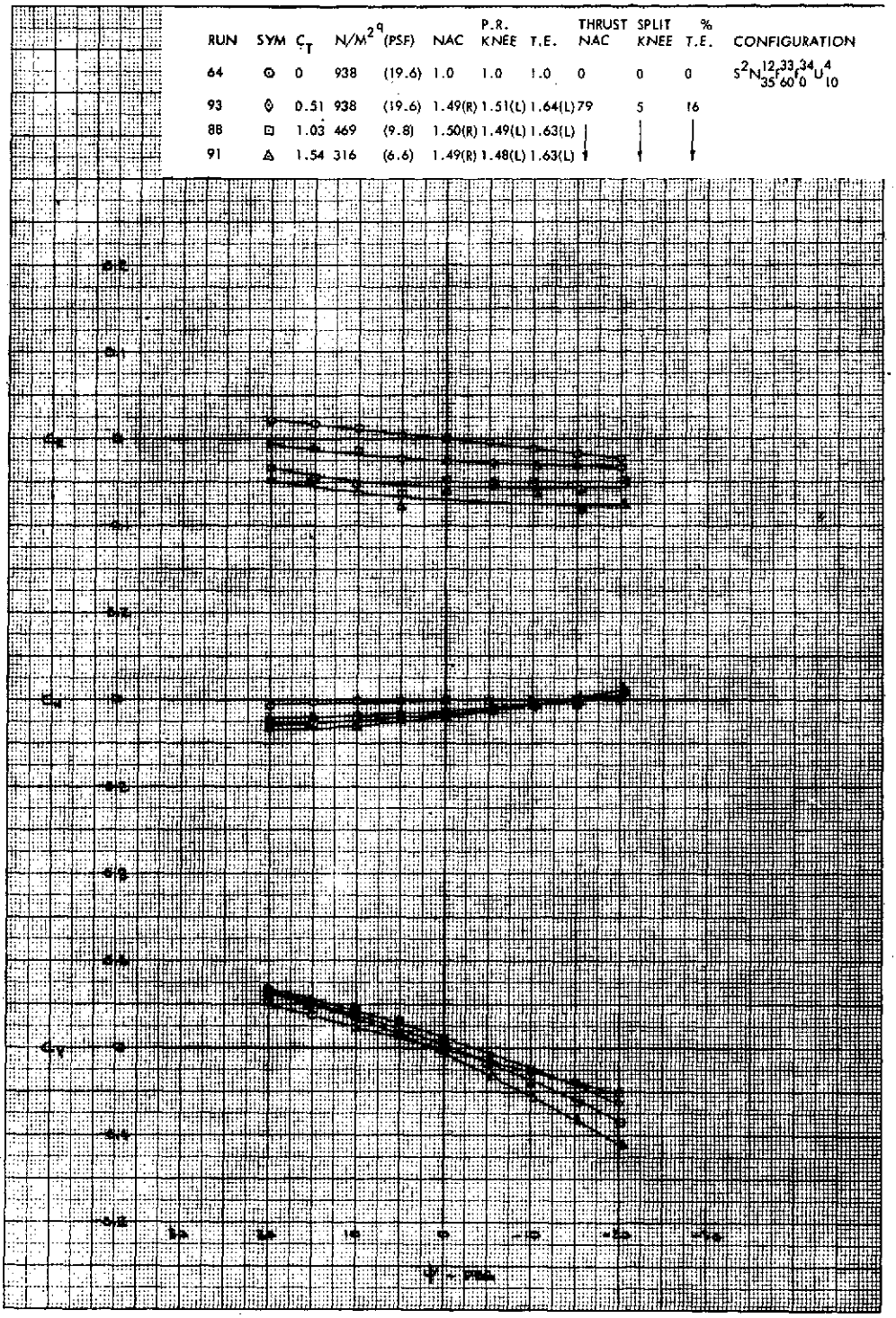

Figure 45. - Lateral-Directional Characteristics of the High Wing Model with the Left Engine Inoperative, $60^\circ/0^\circ$ J/H Flap, 10° Open Deflector, Tail Off

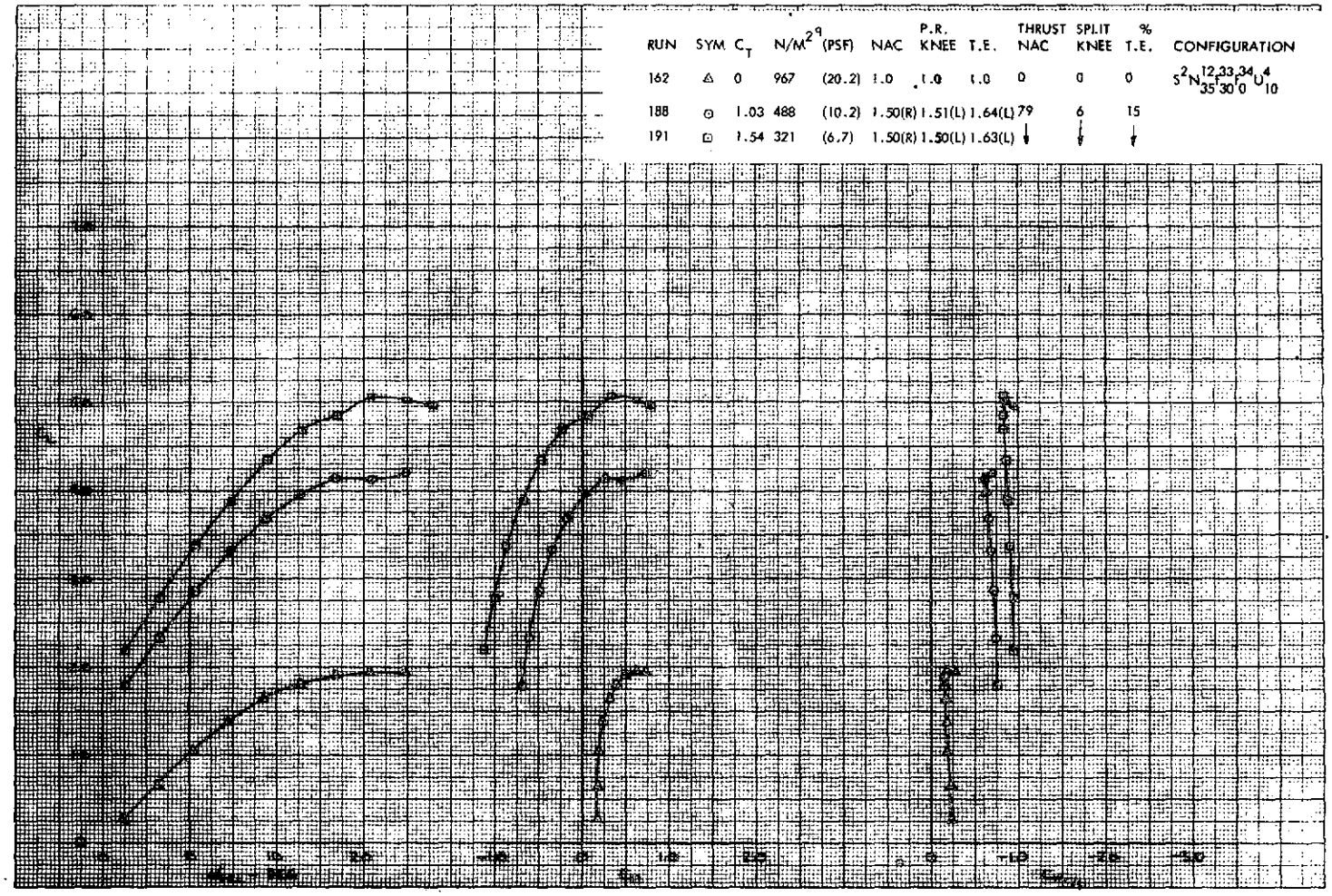

Figure 46. - Longitudinal Characteristics of the High Wing Model with the Left Engine Inoperative, 30°/0° J/H Flap, 10° Open Deflector, Tail Off

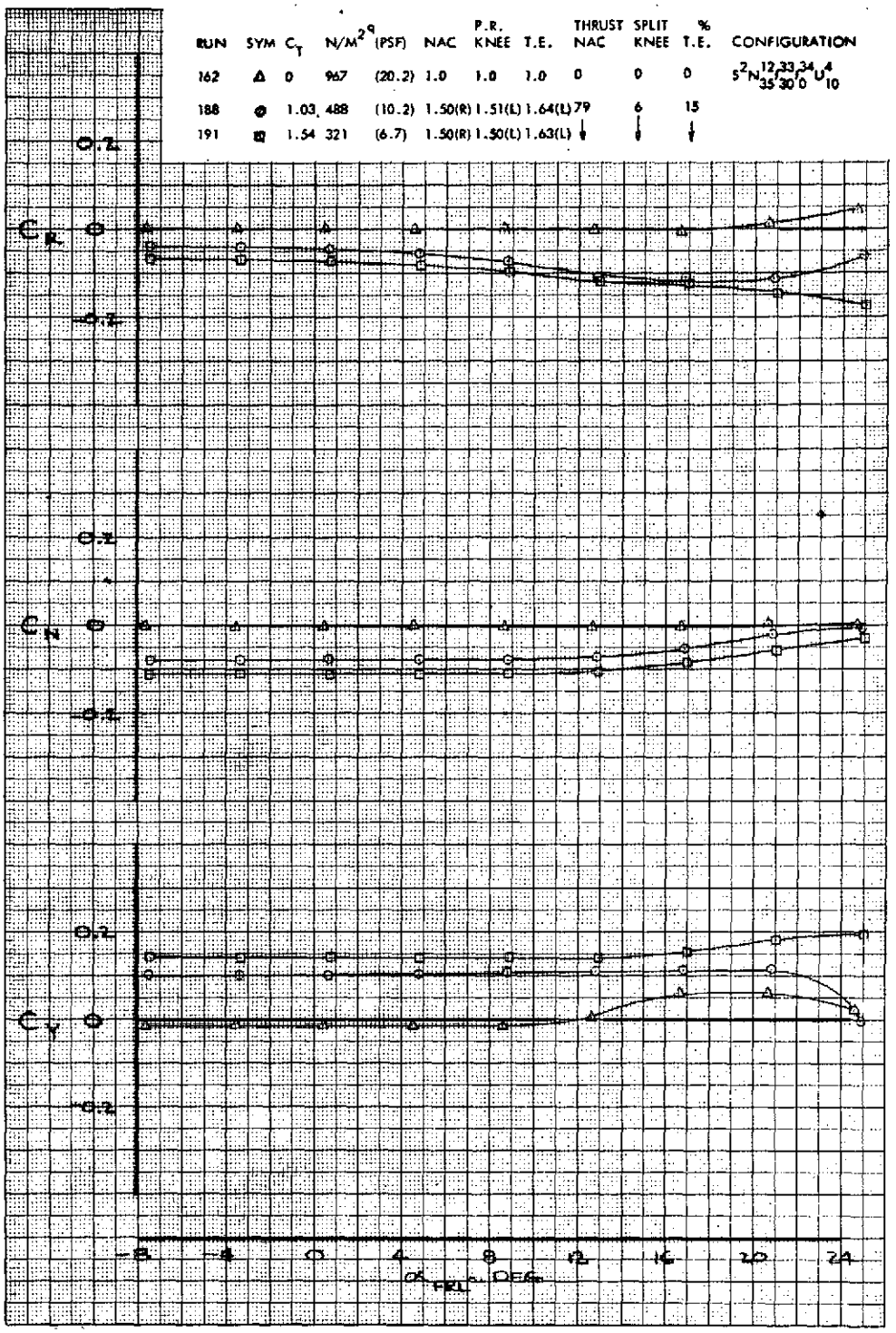

Figure 47. - Effect of Angle-of-Attack on Lateral-Directional Characteristics of the High Wing Model with the Left Engine Inoperative, 30°/0° J/H Flap, 10° Open Deflector, Tail Off

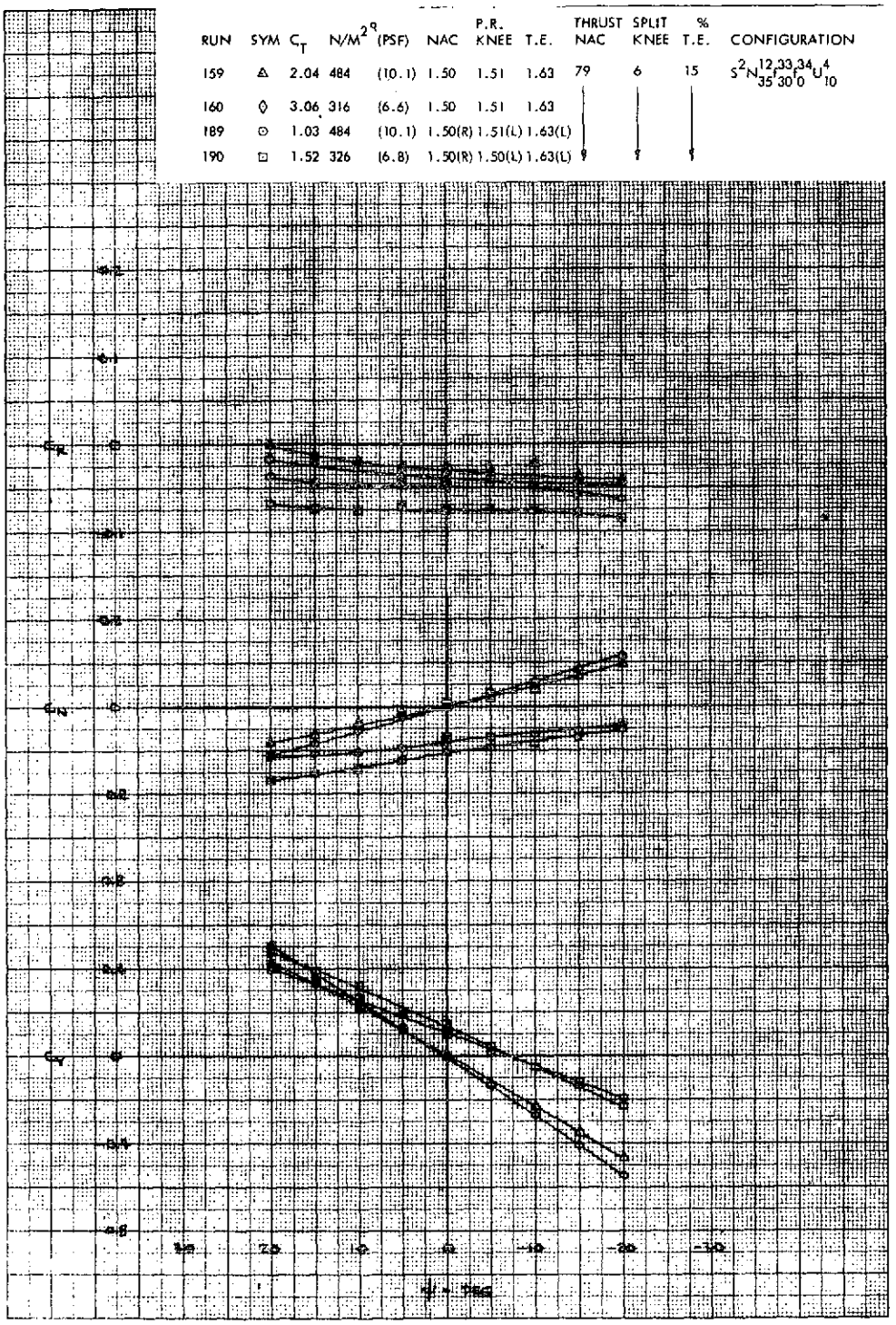

Figure 48. - Lateral-Directional Characteristics of the High Wing Model with Symmetric and Asymmetric Blowing, $30^\circ/0^\circ$ J/H Flap, 10° Open Deflector, Tail Off

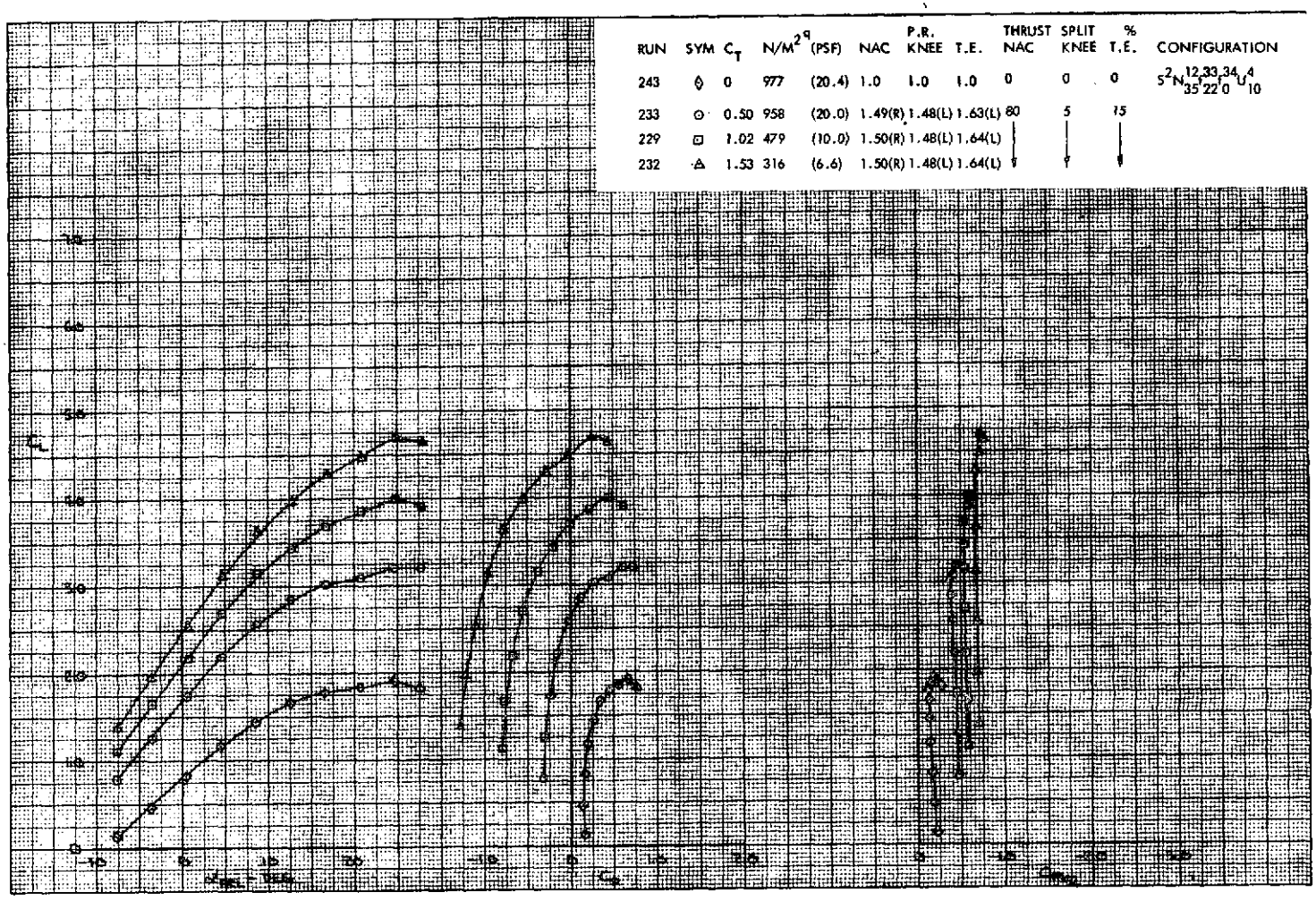

Figure 49. - Longitudinal Characteristics of the High Wing Model with the Left Engine and the Right BLC Systems Inoperative, 22°/0° J/H Flap, 10° Open Deflector, Tail Off

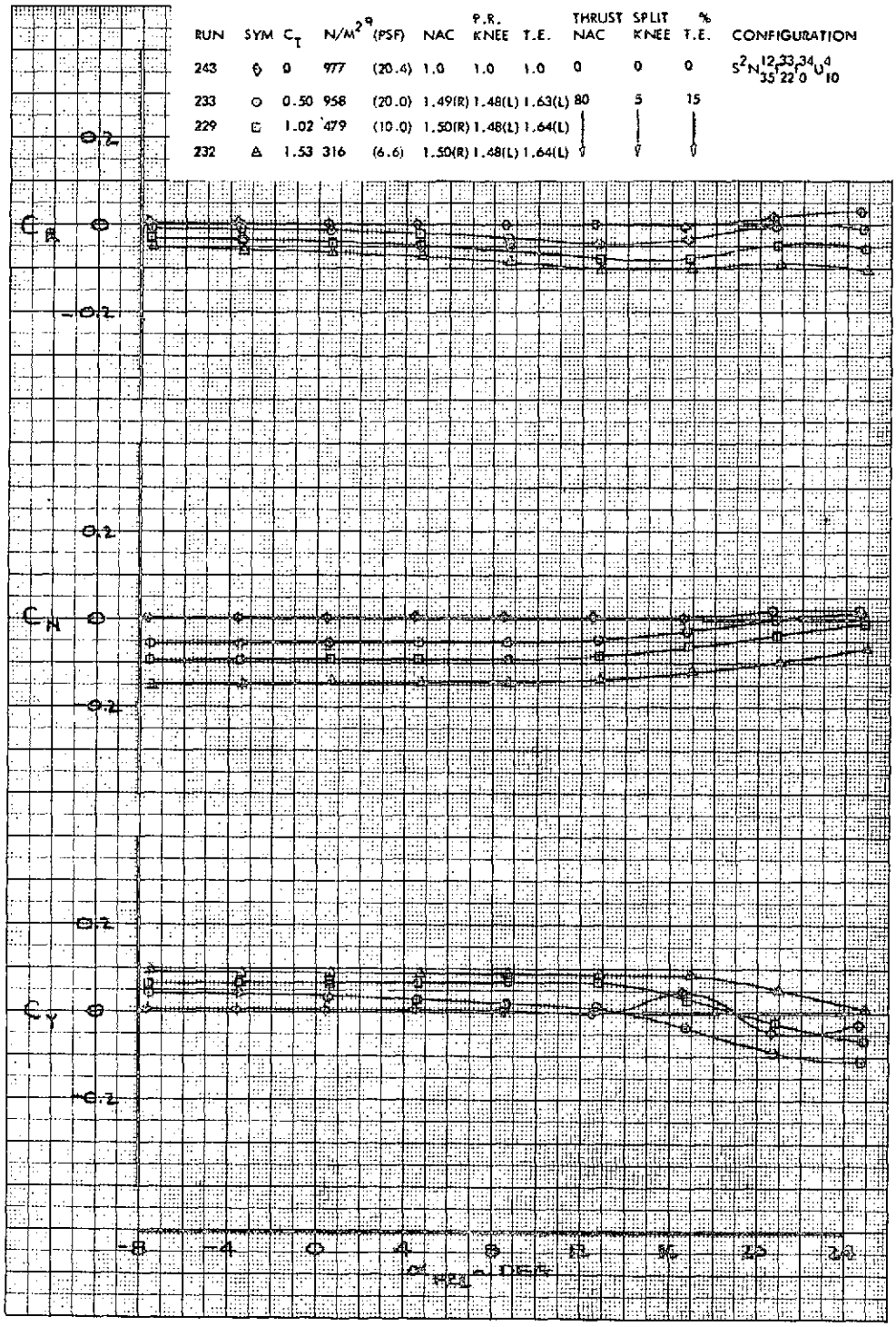

Figure 50. - Effect of Angle-of-Attack on Lateral-Directional Characteristics of the High Wing Model with the Left Engine and the Right BLC Systems Inoperative, 22°/0° J/H Flap, Open Deflector, Tail Off

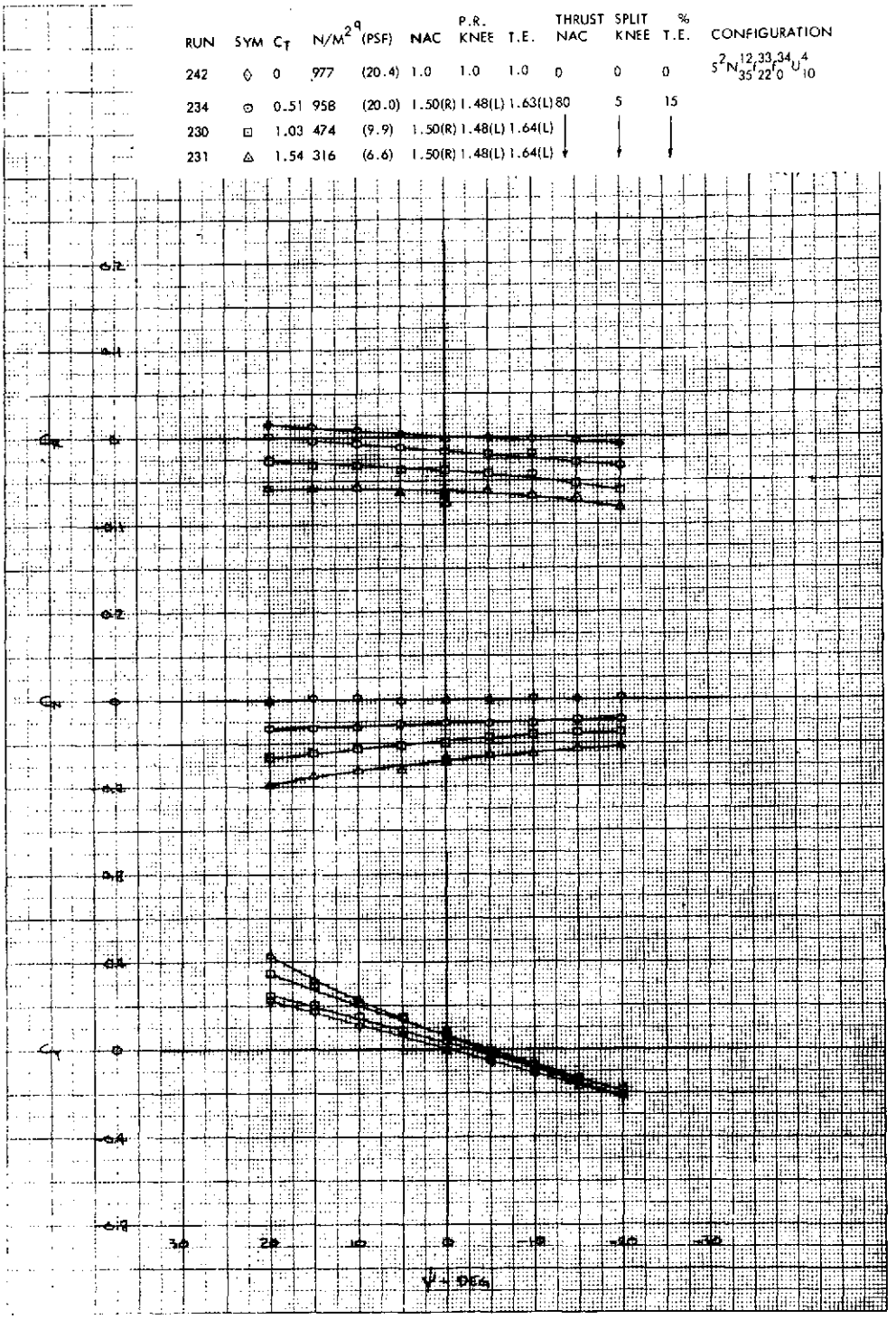

Figure 51. - Lateral-Directional Characteristics of the High Wing Model with the Left Engine and the Right BLC Systems Inoperative, $22^\circ/0^\circ$ J/H Flap, 10° Open Deflector, Tail Off

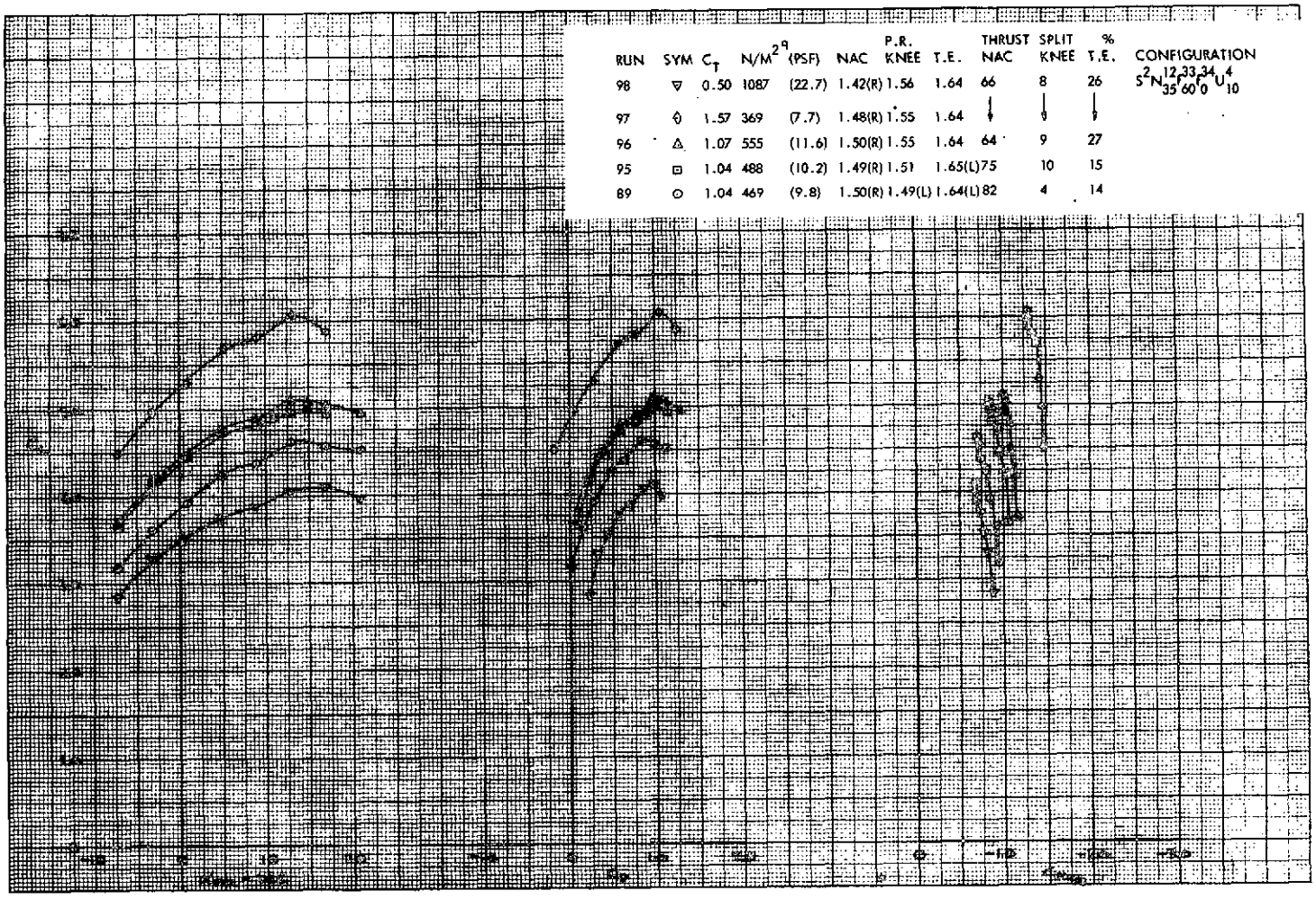

Figure 52. - Longitudinal Characteristics of the High Wing Model with the Left Engine Inoperative and with BLC Variations, $60^\circ/0^\circ$ J/H Flap, 10° Open Deflector, Tail Off

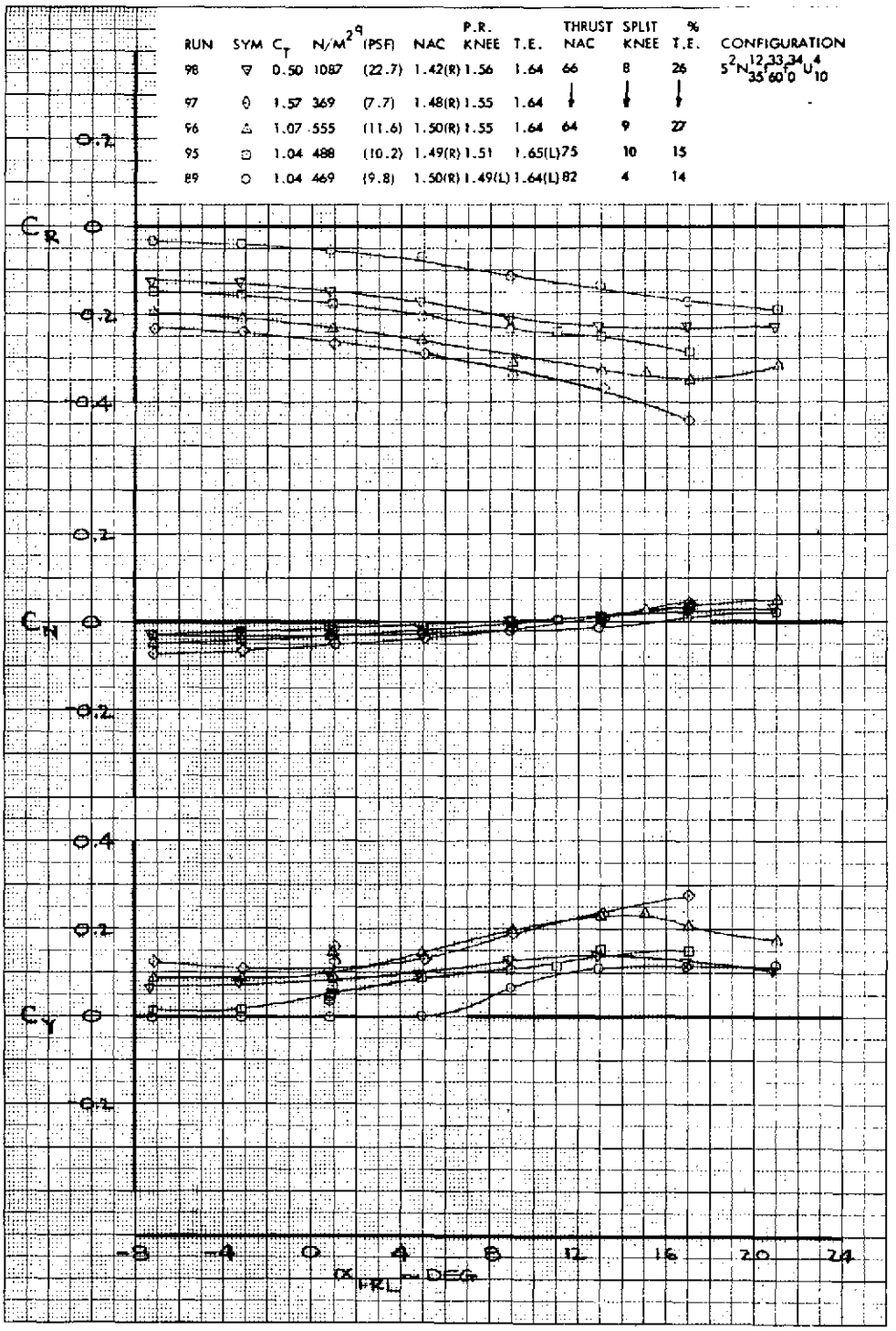

Figure 53. - Effect of Angle-of-Attack on Lateral-Directional Characteristics of the High Wing Model with the Left Engine Inoperative and with BLC Variations, $60^\circ/0^\circ$ J/H Flap, 10° Open Deflector, Tail Off

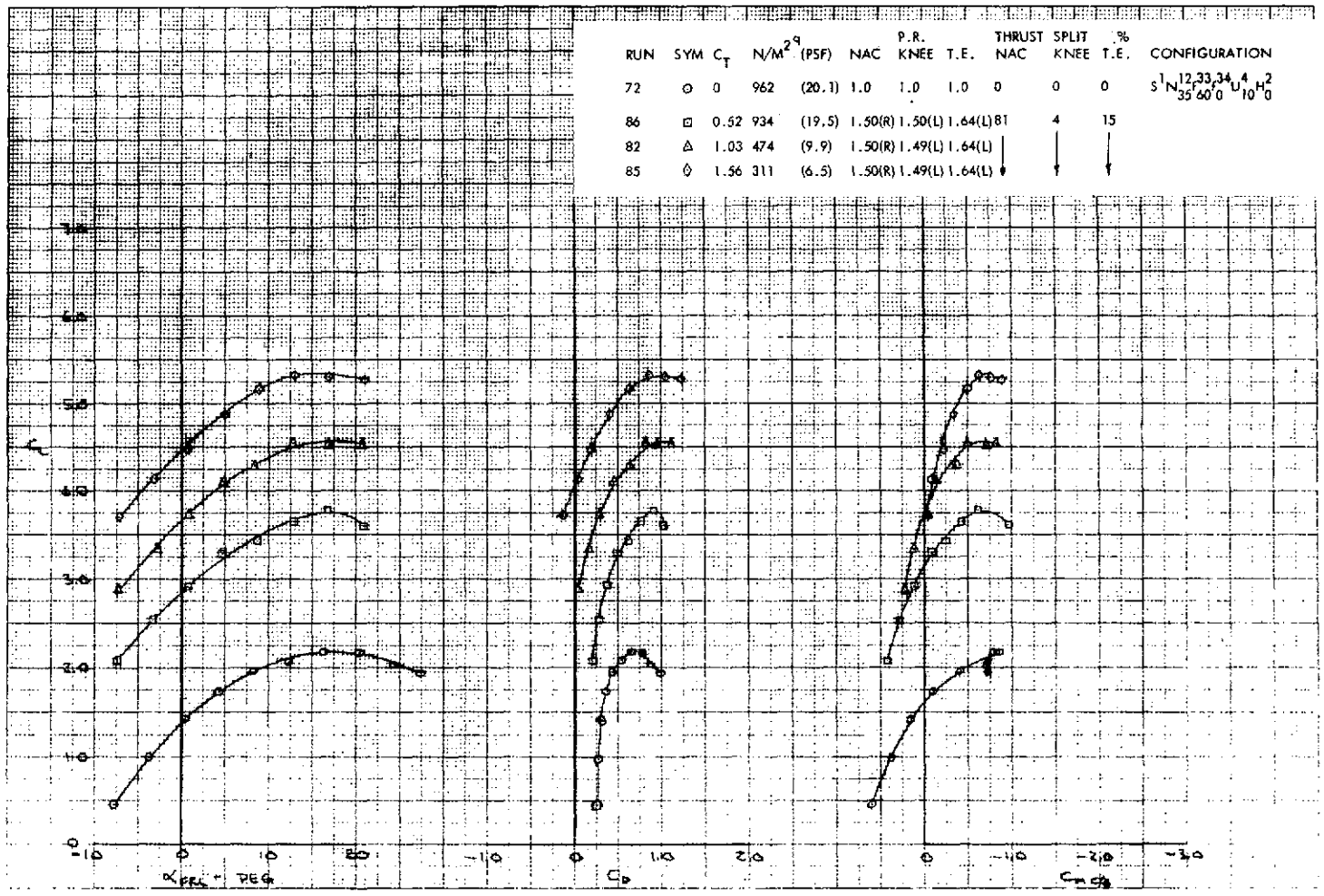

Figure 54. - Longitudinal Characteristics of the High Wing Model with the Left Engine and the Right BLC Systems Inoperative, $60^{\circ}/0^{\circ}$ J/H Flap, 10° Open Deflector Tail On

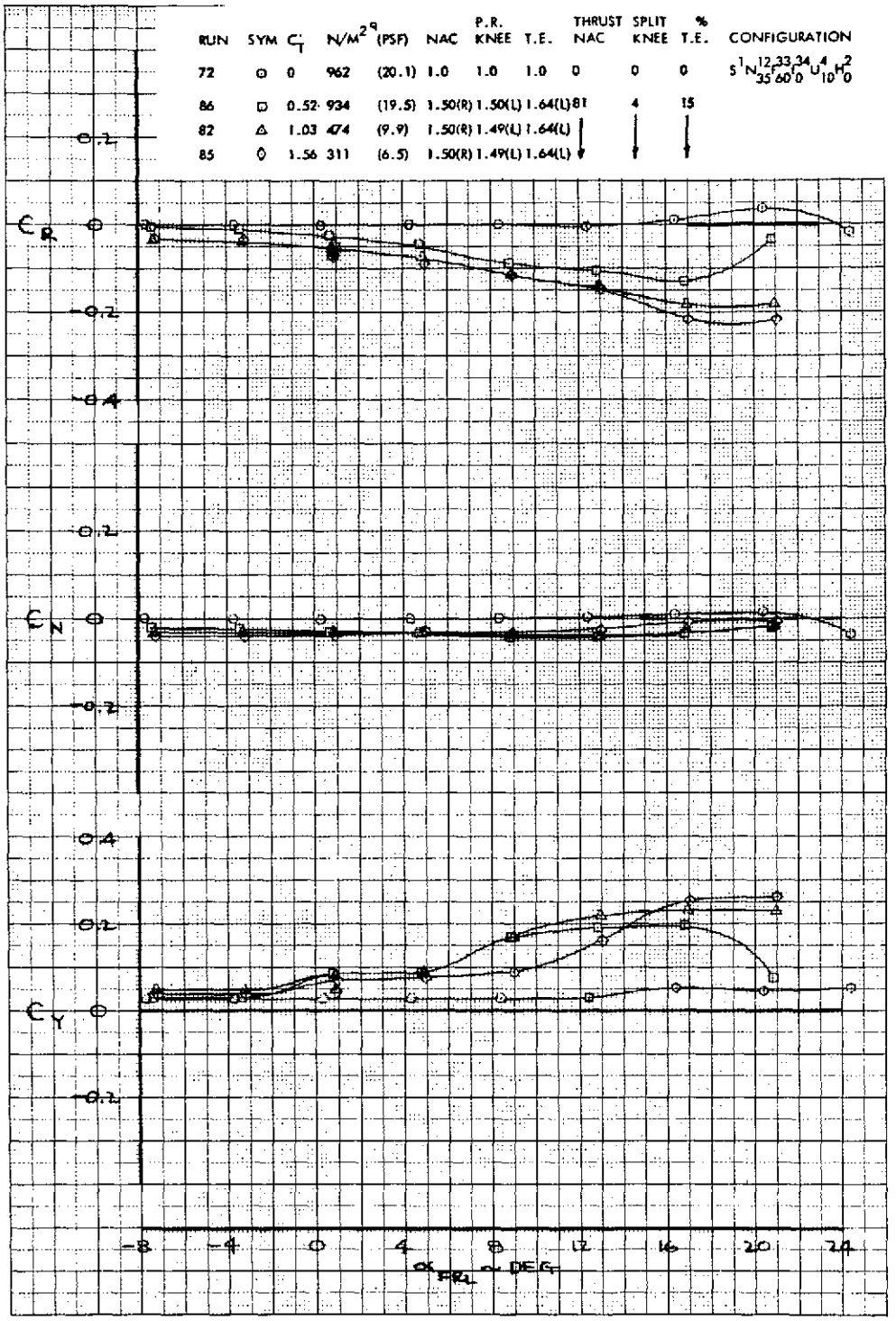

Figure 55. - Effect of Angle-of-Attack on Lateral-Directional Characteristics of the High Wing Model with the Left Engine and the Right BLC Systems Inoperative, 60°/0° J/H Flap, 10° Open Deflector, Tail On

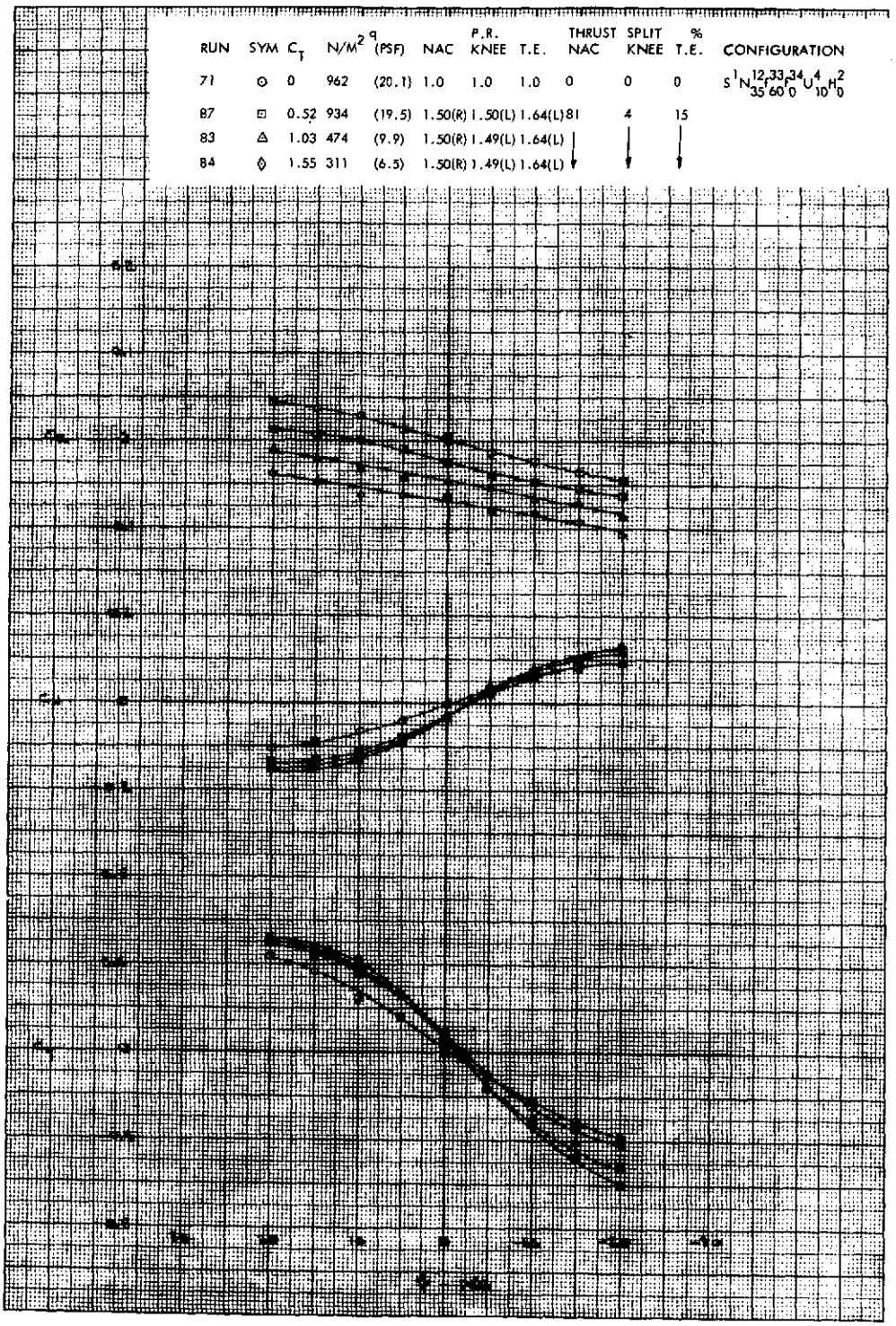

Figure 56. - Lateral Directional Characteristics of the High Wing Model with the Left Engine and the Right BLC Systems Inoperative, $60^{\circ}/0^{\circ}$ J/H Flap, 10° Open Deflector, Tail On

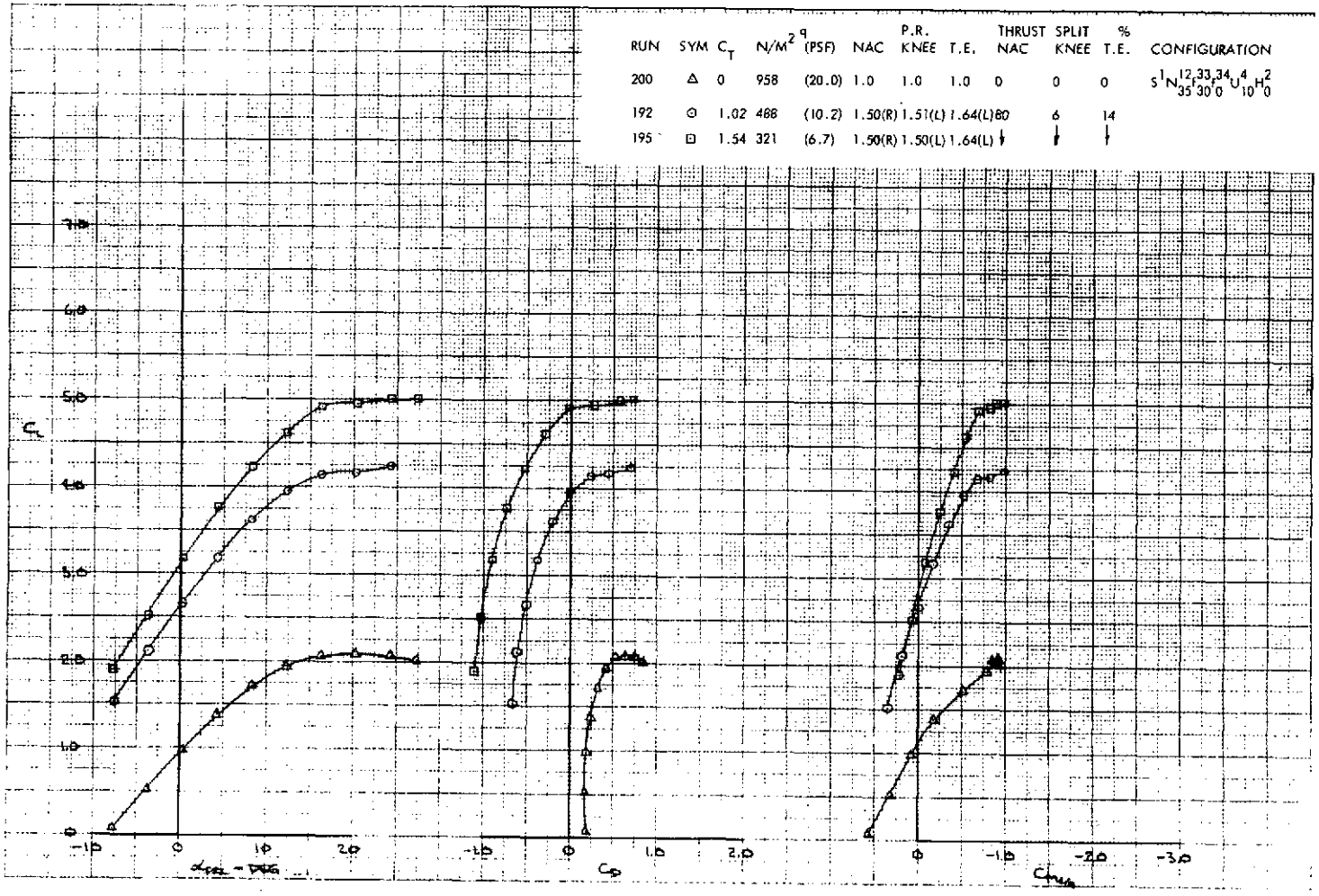

Figure 57. - Longitudinal Characteristics of the High Wing Model with the Left Engine and Right BLC Systems Inoperative, 30°/0° J/H Flap, 10° Open Deflector, Tail On

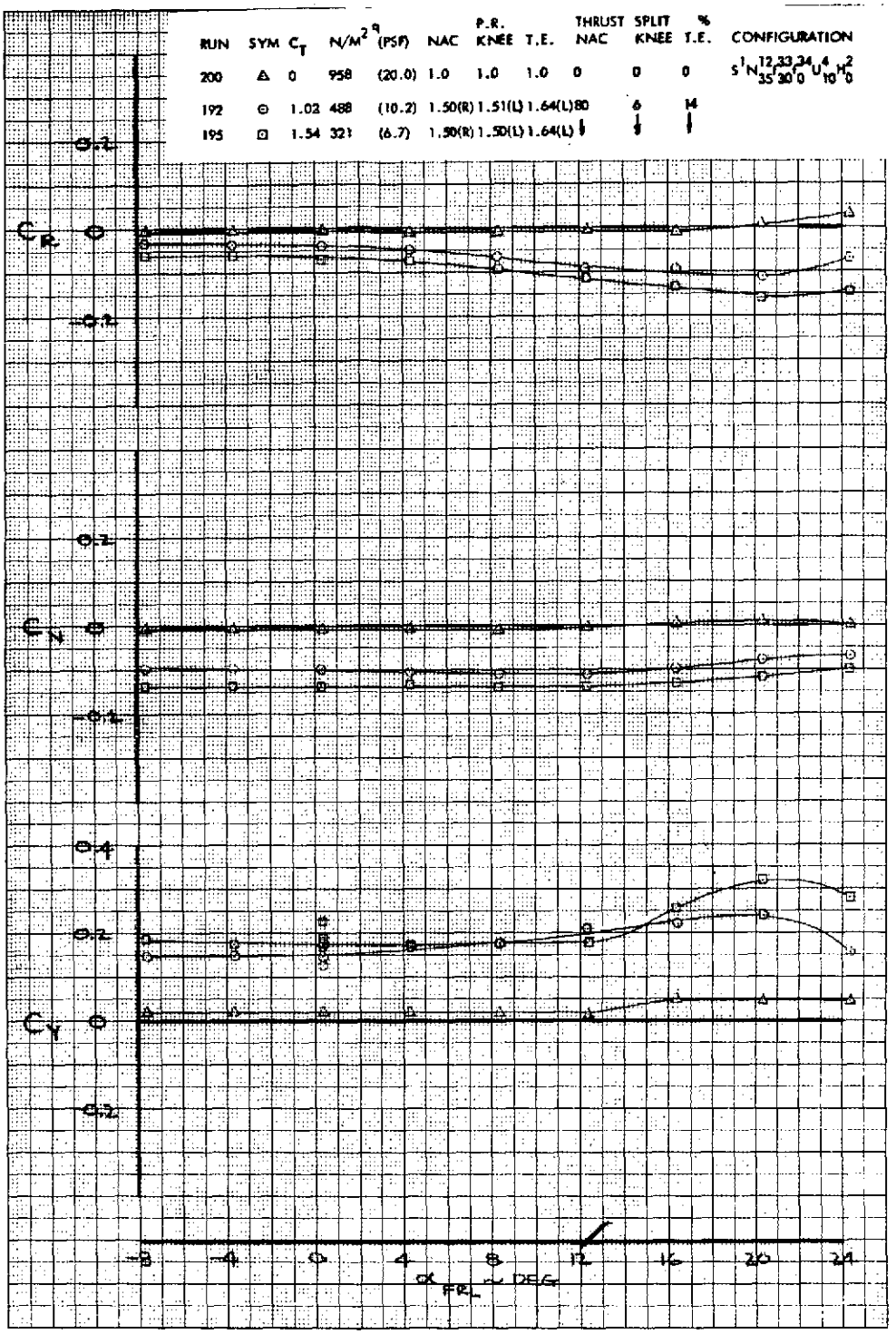

Figure 58. - Effect of Angle-of-Attack on Lateral-Directional Characteristics of the High Wing Model with the Left Engine and Right BLC Systems Inoperative, $30°/0°$ J/H Flap, $10°$ Open Deflector, Tail On

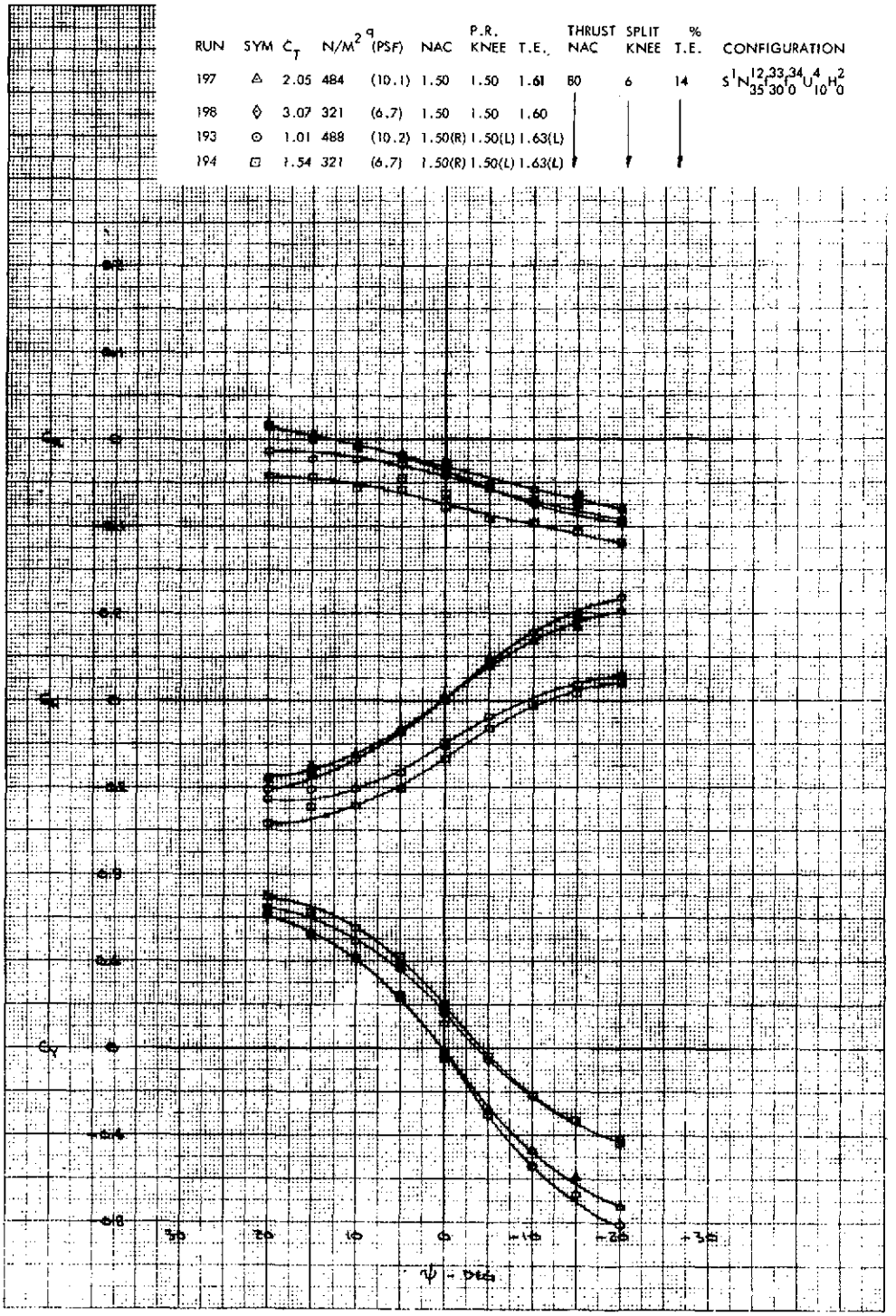

Figure 59. - Lateral-Directional Characteristics of the High Wing Model with Symmetric and Asymmetric Blowing, $30^\circ/0^\circ$ J/H Flap, 10° Open Deflector, Tail On

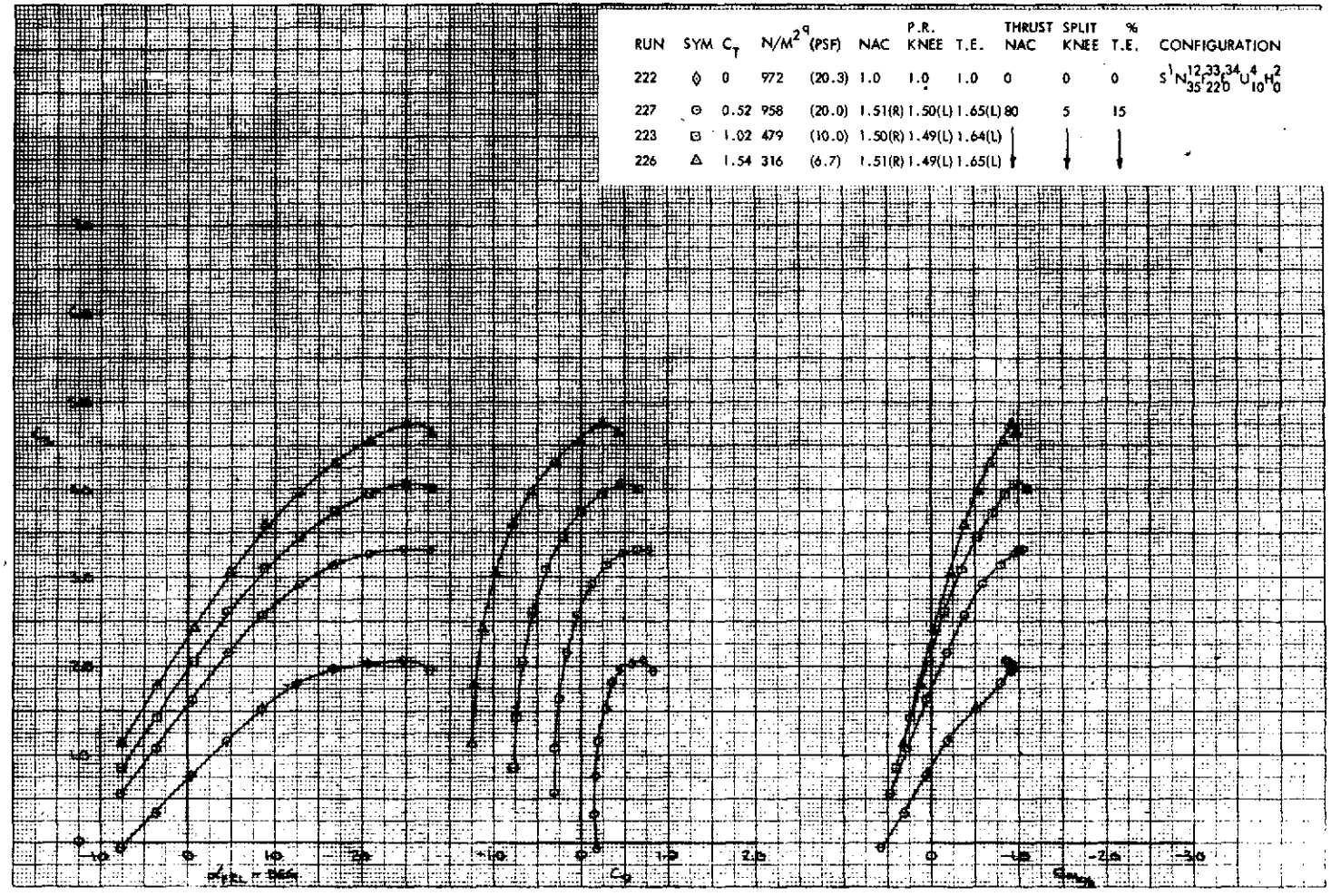

Figure 60. - Longitudinal Characteristics of the High Wing Model with the Left Engine and the Right BLC Systems Inoperative, 22°/0° J/H Flap, 10° Open Deflector, Tail On

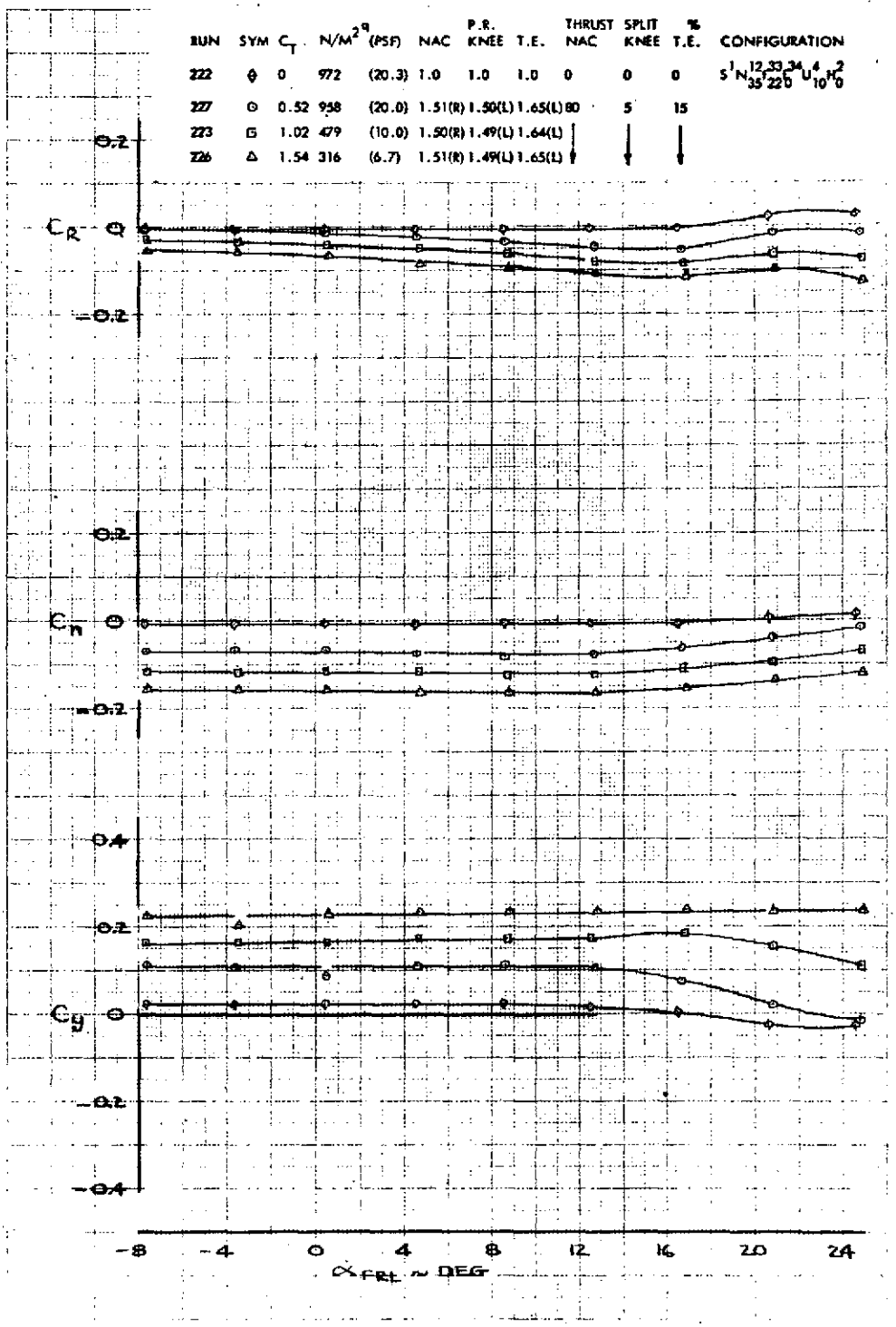

Figure 61. - Effect of Angle-of-Attack on Lateral-Directional Characteristics of the High Wing Model with the Left Engine and Right BLC Systems Inoperative, $22^{\circ}/0^{\circ}$ J/H Flap, 10° Open Deflector, Tail On

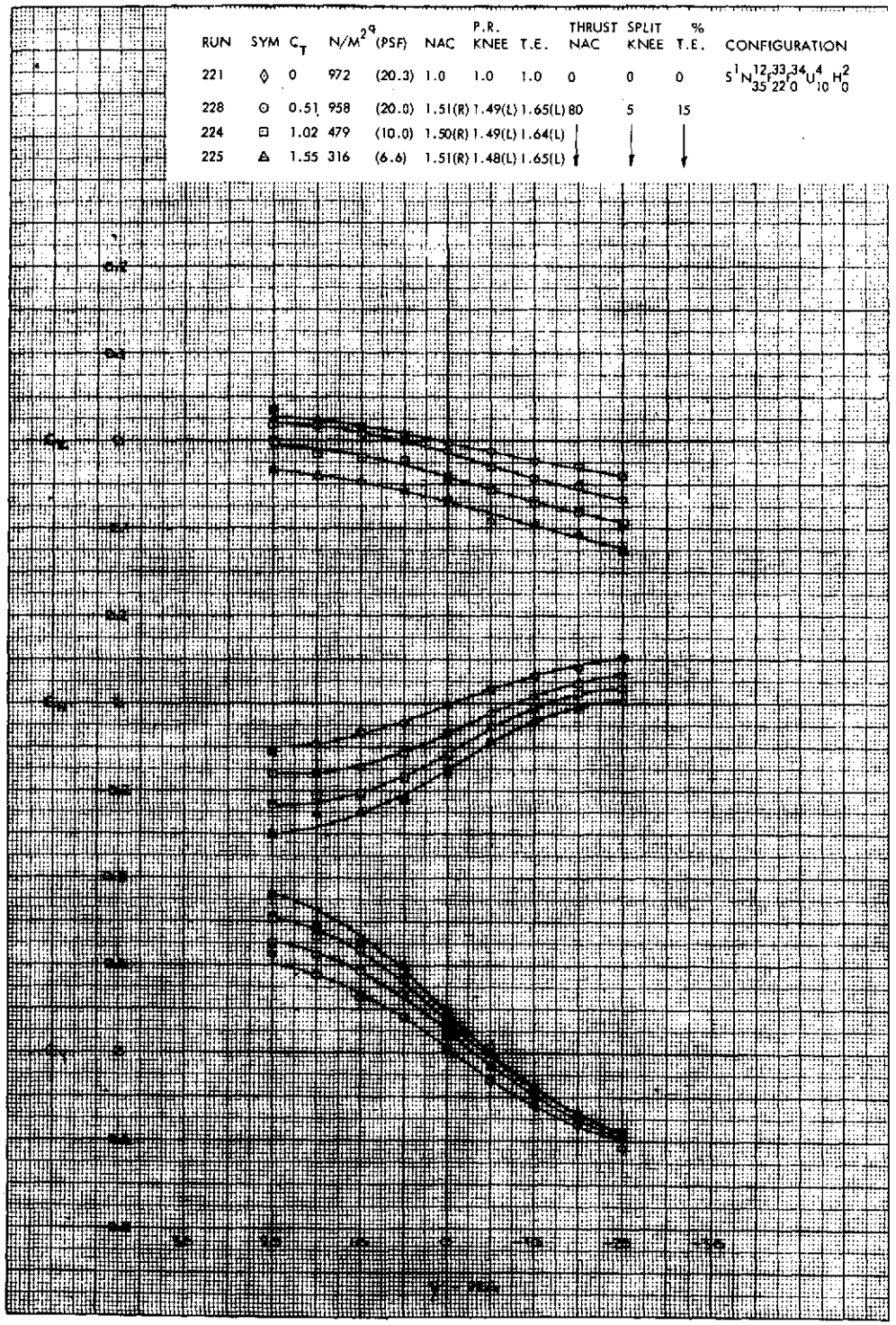

Figure 62. - Lateral-Directional Characteristics of the High Wing Model with the Left Engine and the Right BLC Systems Inoperative, $22^\circ/0^\circ$ J/H Flap, 10° Open Deflector, Tail On

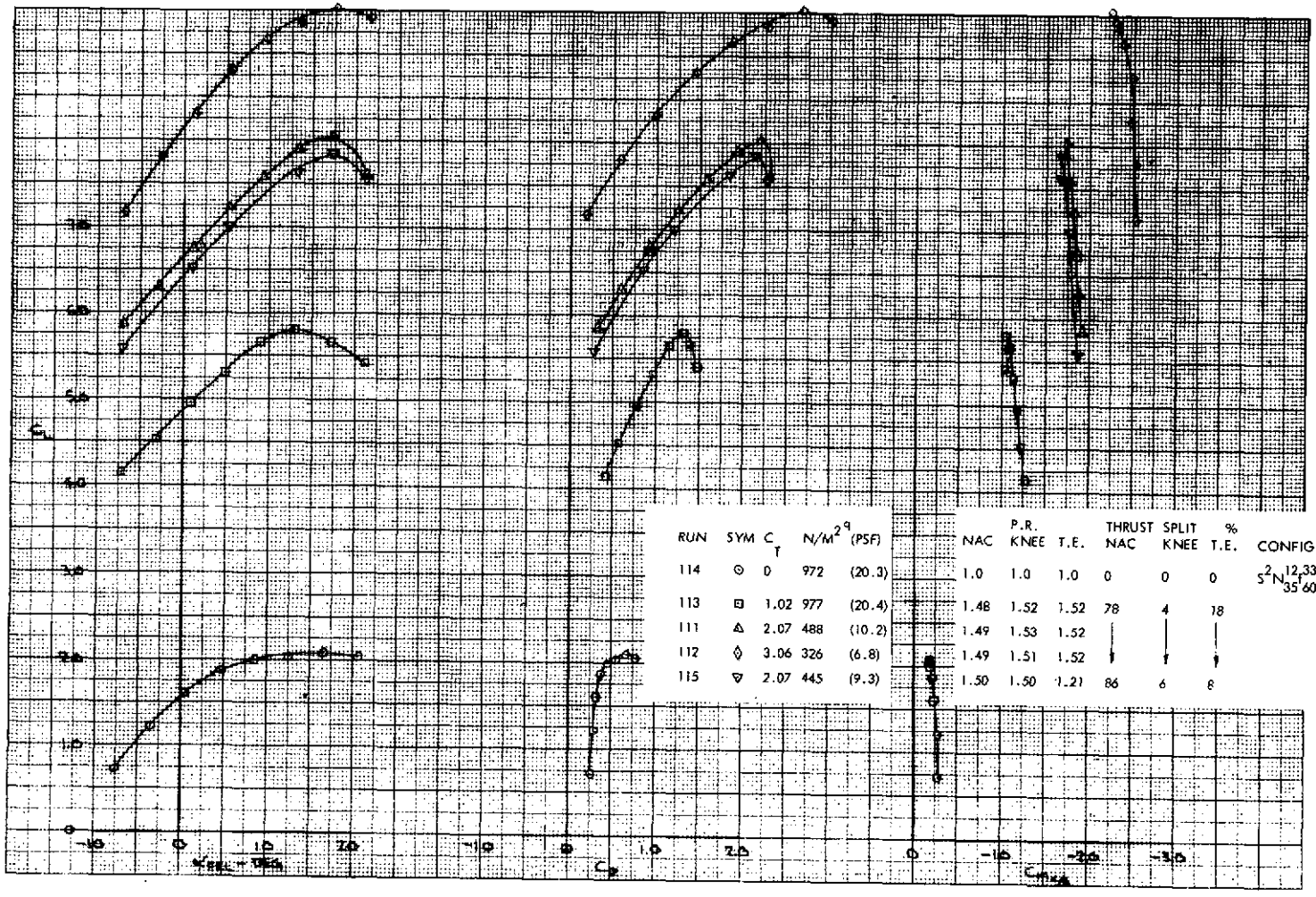

Figure 63. - Longitudinal Characteristics of the High Wing Model, $60^\circ/+15^\circ$ J/H Flap, 10° Open Deflector, Tail Off

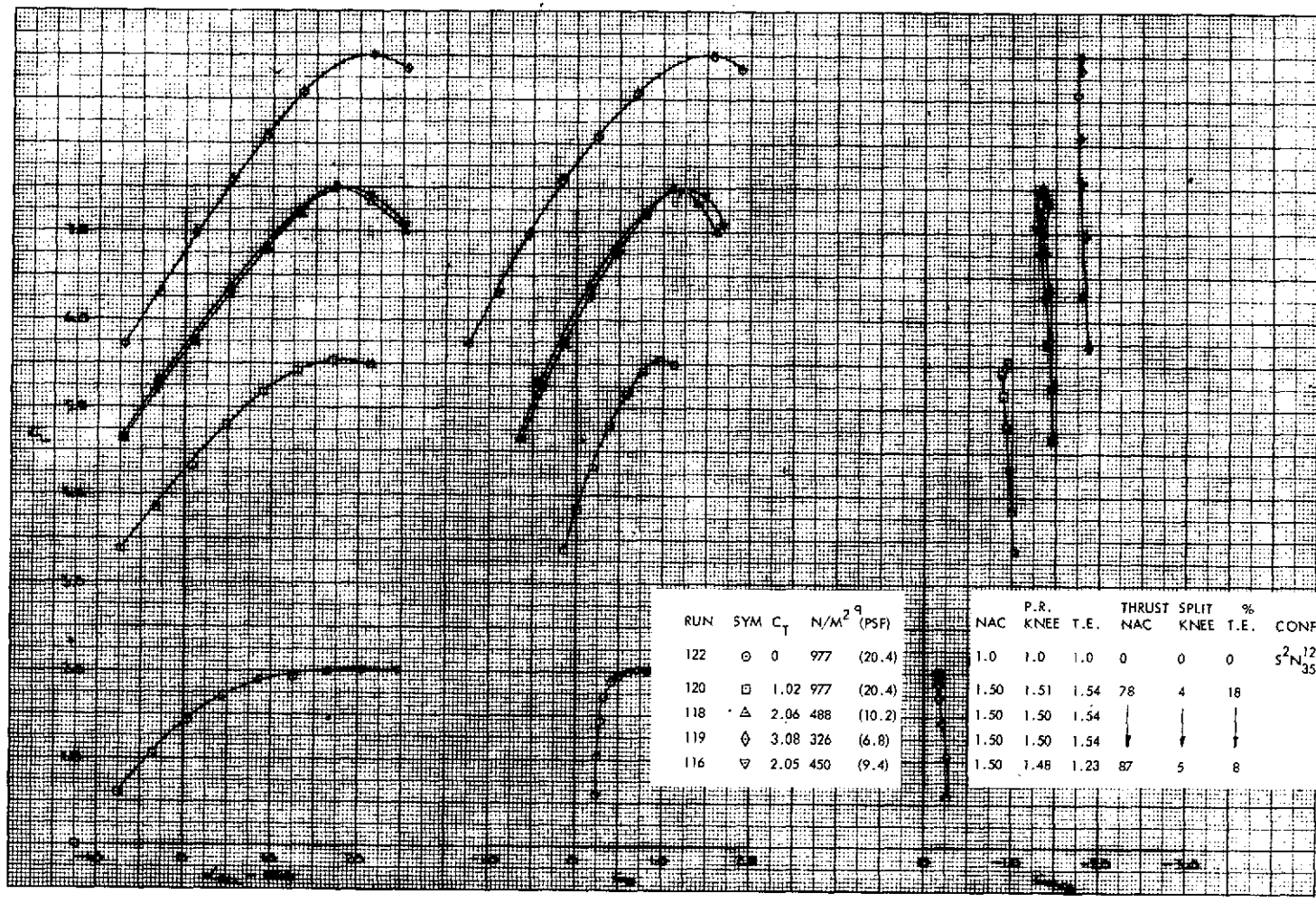

Figure 64. - Longitudinal Characteristics of the High Wing Model, $60^\circ/-15^\circ$ J/H Flap, 10° Open Deflector, Tail Off

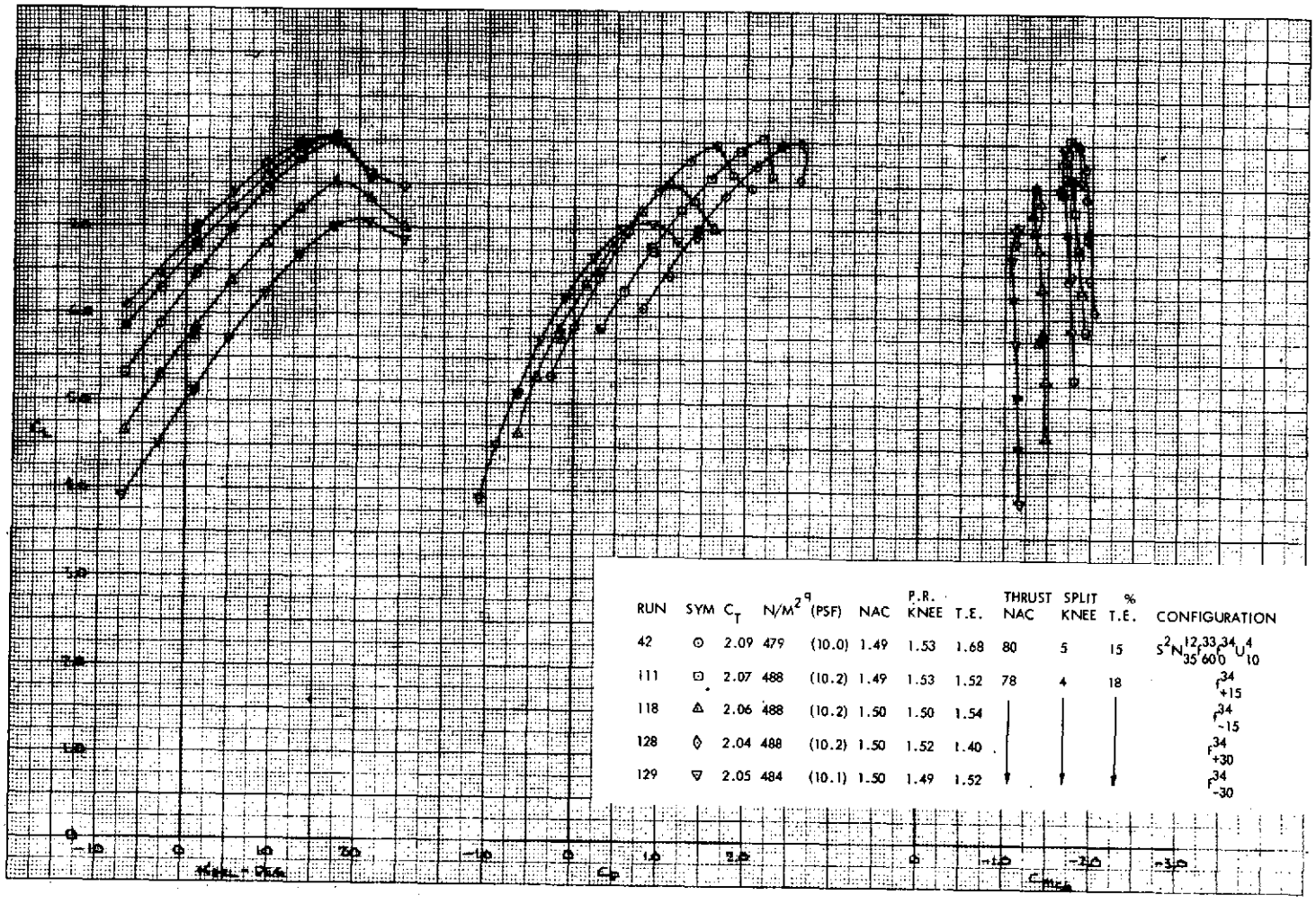

Figure 65. - Longitudinal Characteristics of the High Wing Model, 60° J/H Flap with Symmetric Deflections of the Aft Control Flap from +30° to -30°, 10° Open Deflector, Tail Off

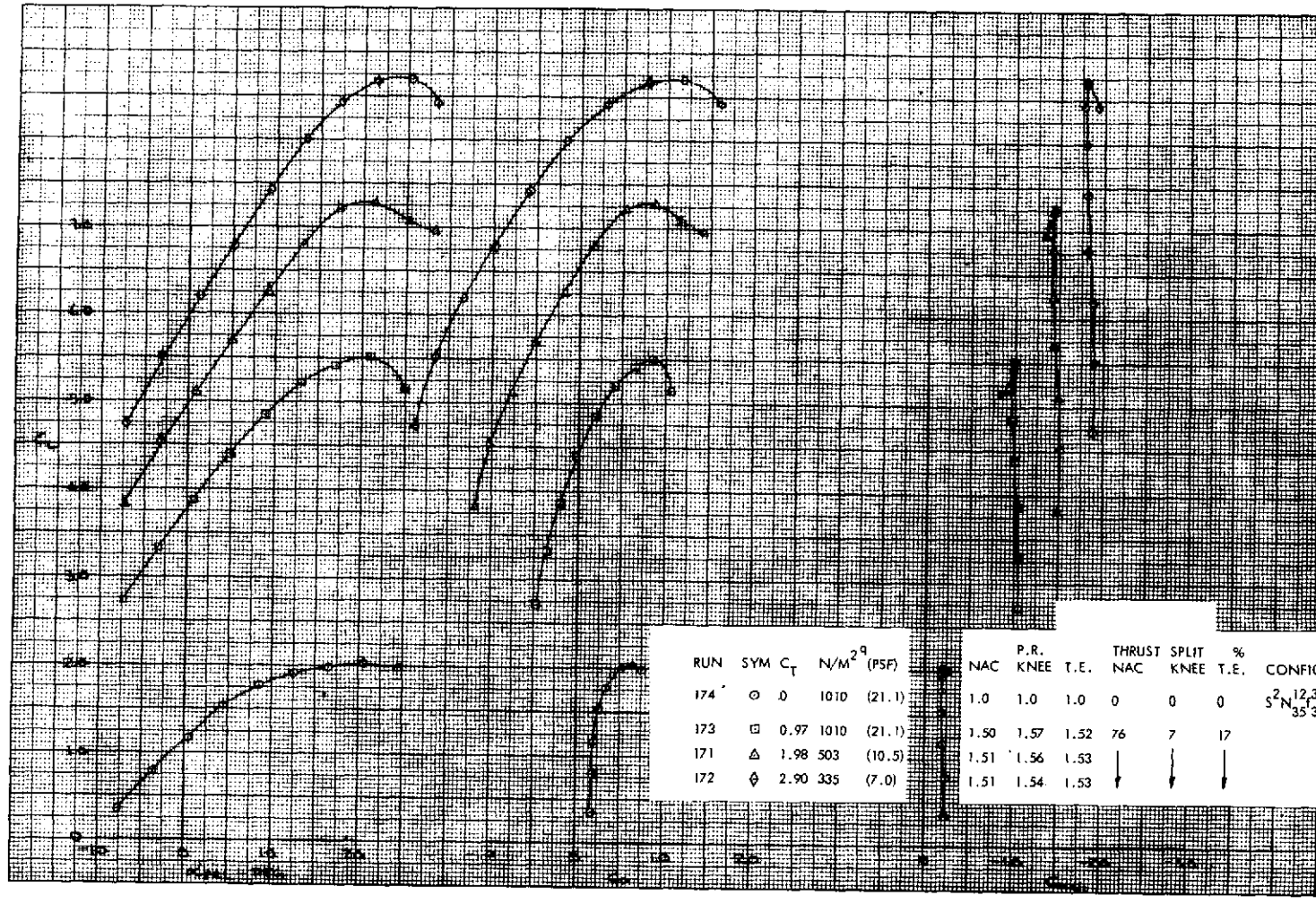

Figure 66. - Longitudinal Characteristics of the High Wing Model, $30^{\circ}/15^{\circ}$ J/H Flap, Open Deflector, Tail Off

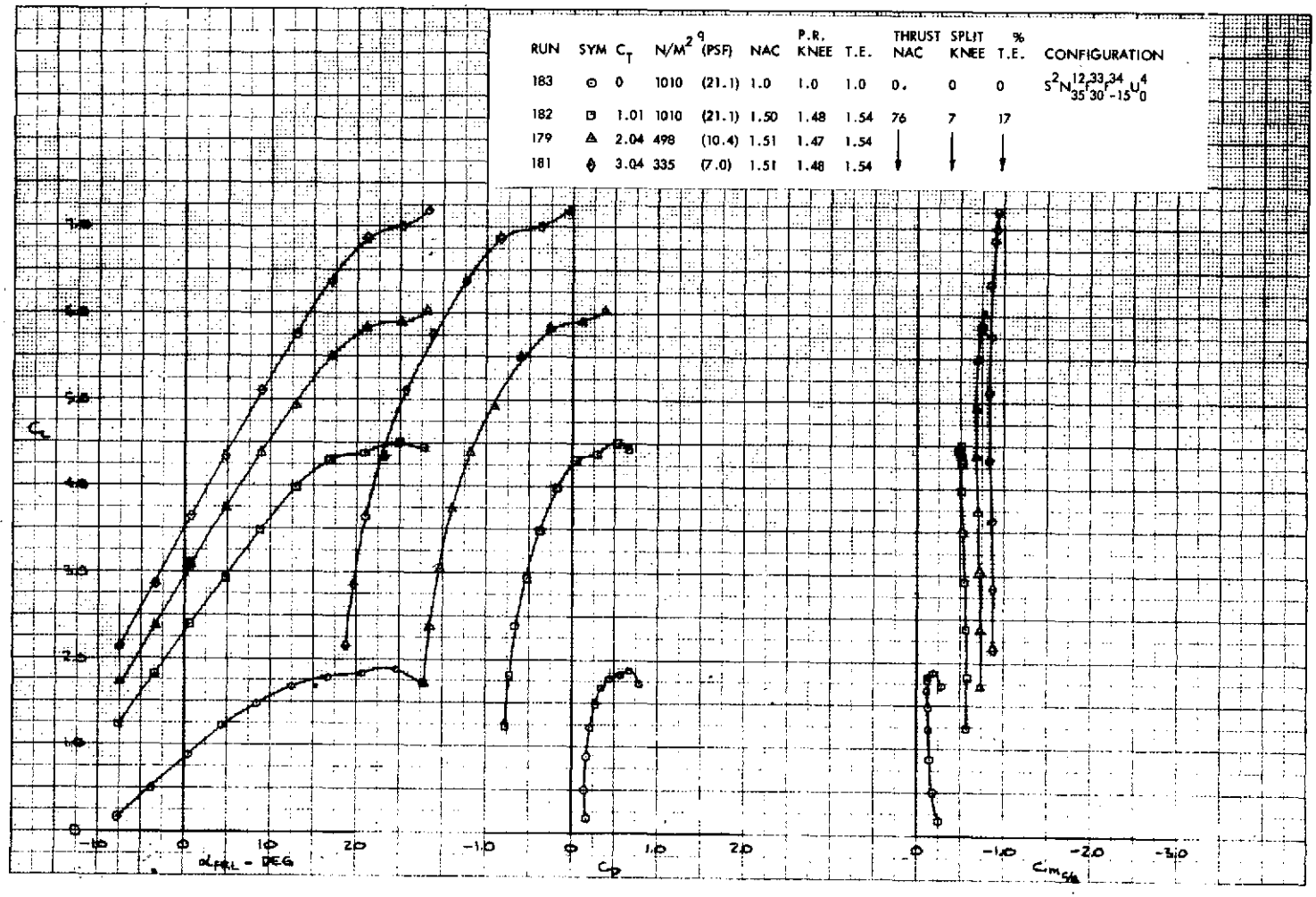

Figure 67. - Longitudinal Characteristics of the High Wing Model, 30°/-15° J/H Flap, 0° Open Deflector, Tail Off

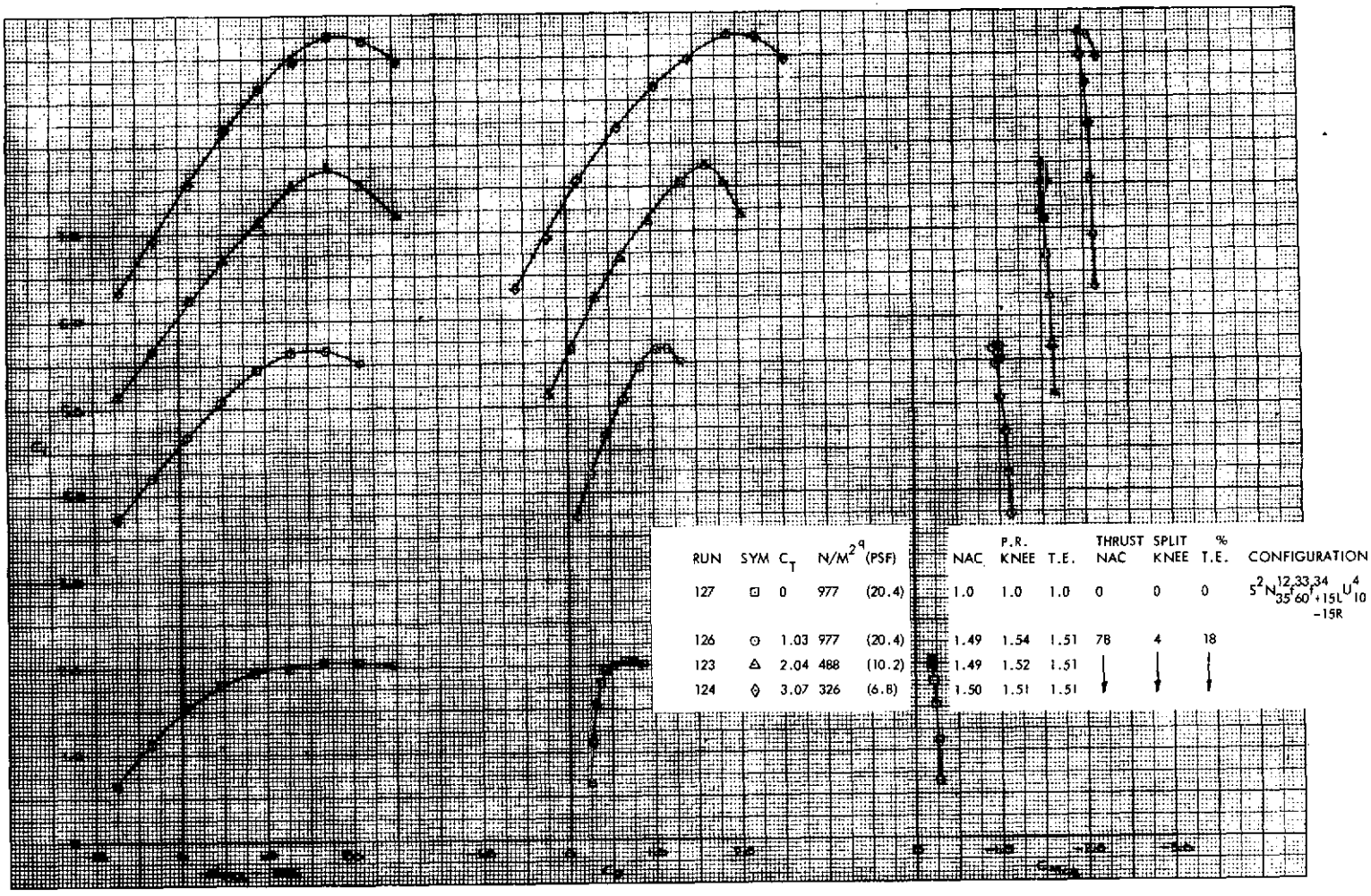

Figure 68. - Longitudinal Charactertistics of the High Wing Model, 60° J/H Flap with +15° Left and -15° Right Aft Flap Deflection, 10° Open Deflector, Tail Off

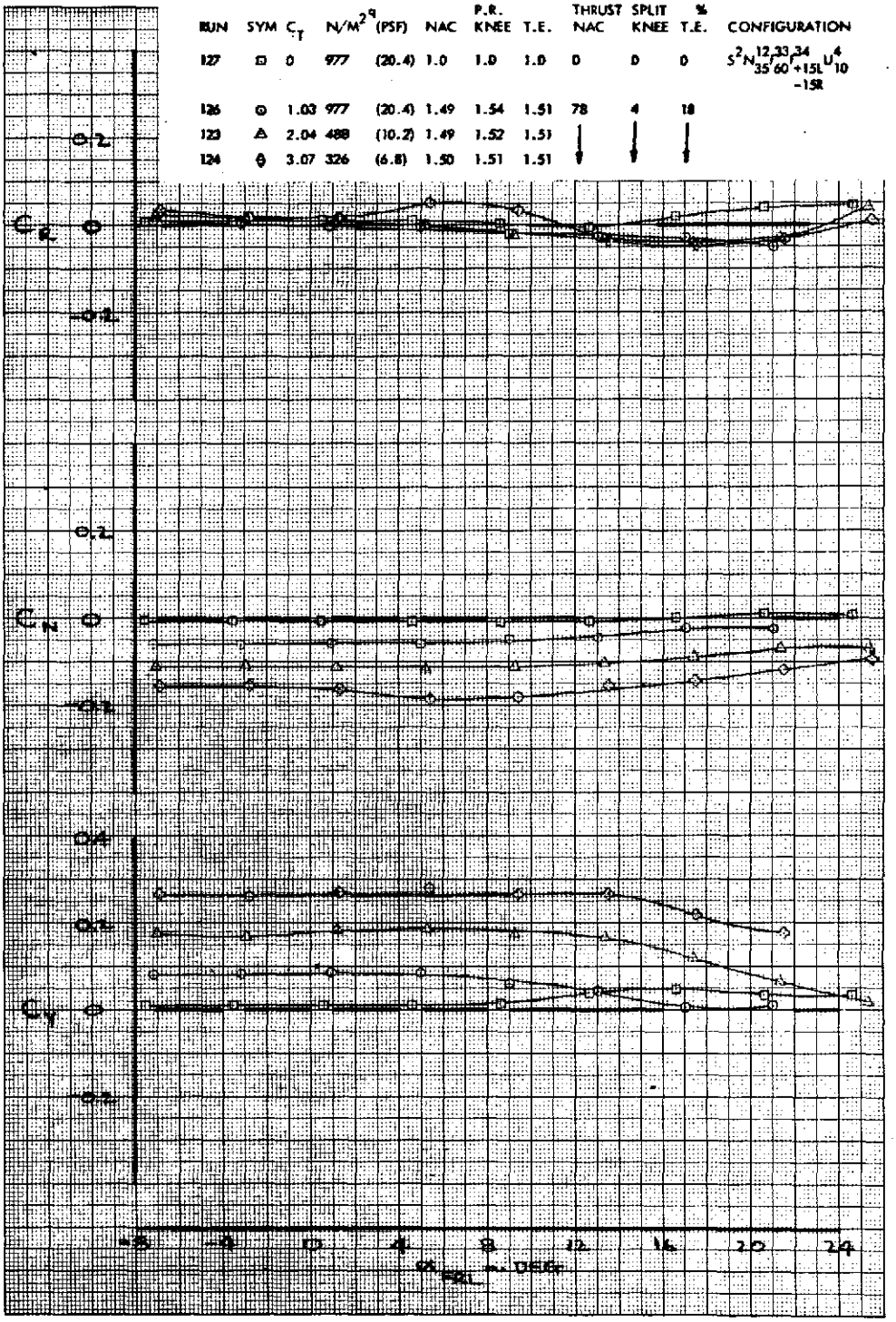

Figure 69. - Effect of Angle-of-Attack on Lateral-Directional Characteristics of the High Wing Model, 60° J/H Flap with +15° Left and -15° Right Aft Flap Deflection, 10° Open Deflector, Tail Off

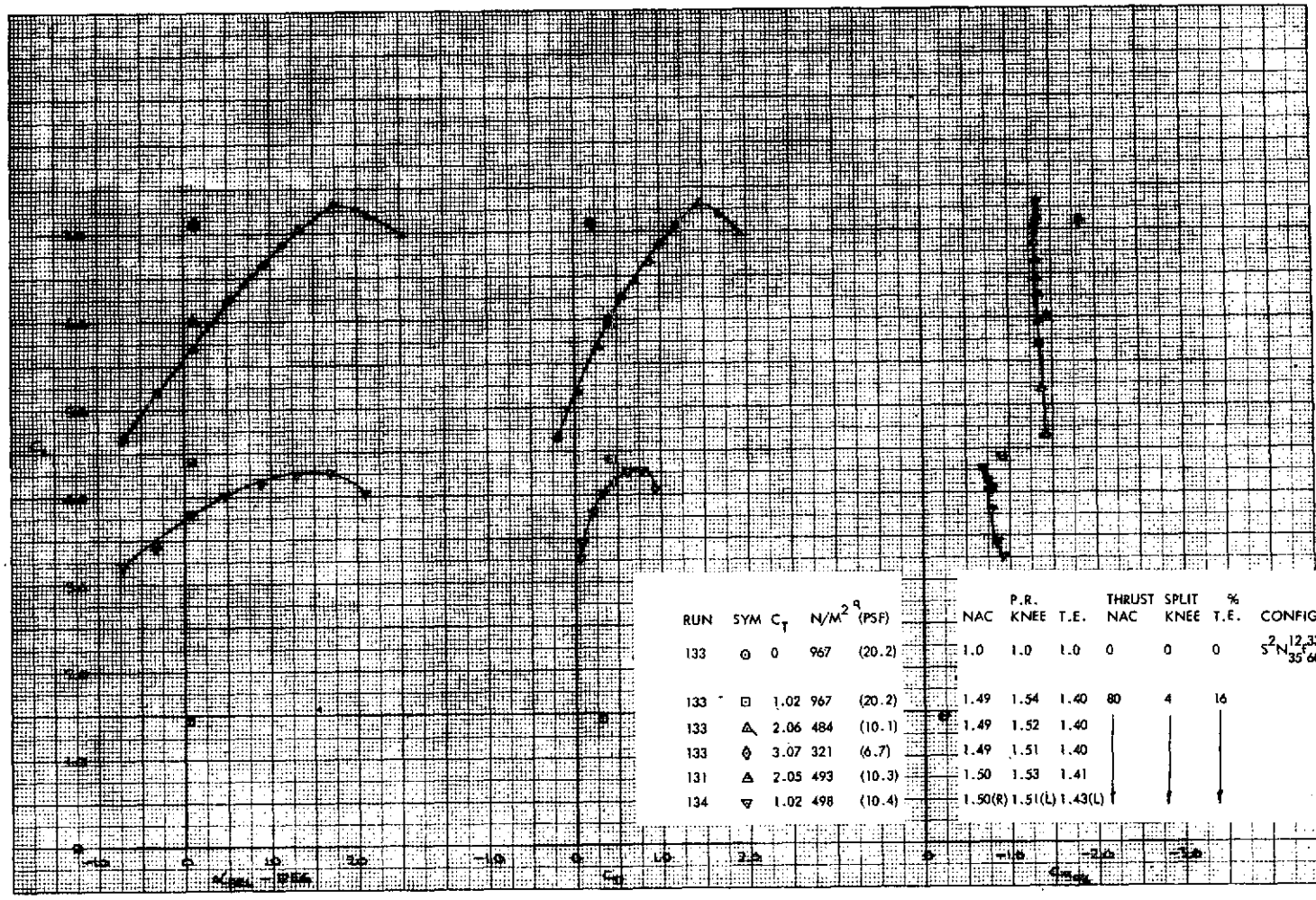

Figure 70. - Longitudinal Characteristics of the High Wing Model, 60° J/H Flap with +30° Left and -30° Right Aft Flap Deflection, 10° Open Deflector, Tail Off

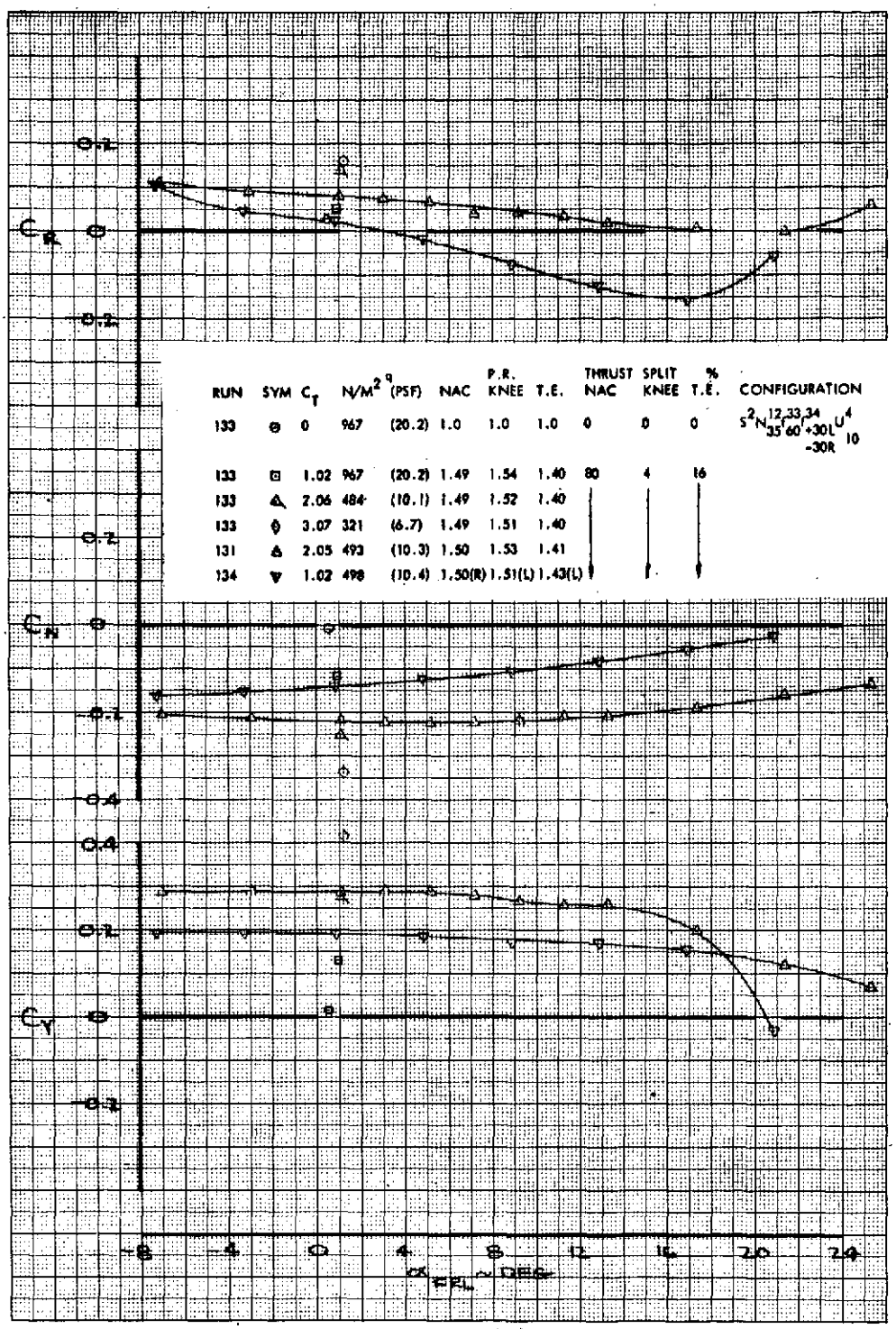

Figure 71. - Effect of Angel-of-Attack on Lateral-Directional Characteristics of the High Wing Model, 60° J/H Flap with +30° Left and -30° Right Aft Flap Deflection, 10° Open Deflector, Tail Off

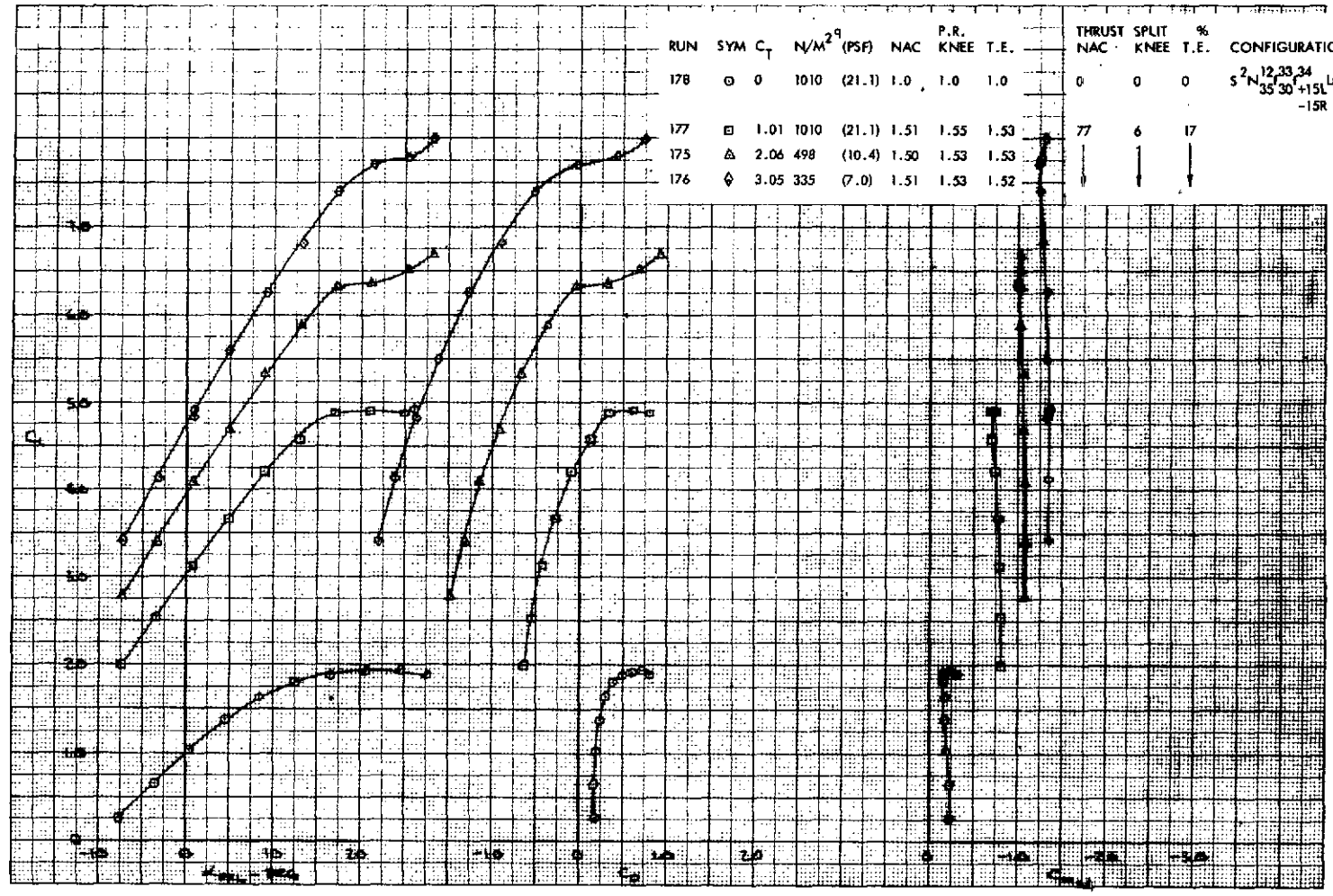

Figure 72. - Longitudinal Characteristics of the High Wing Model, 30° J/H Flap with +15° Left and -15° Right Aft Flap Deflection, 10° Open Deflector, Tail Off

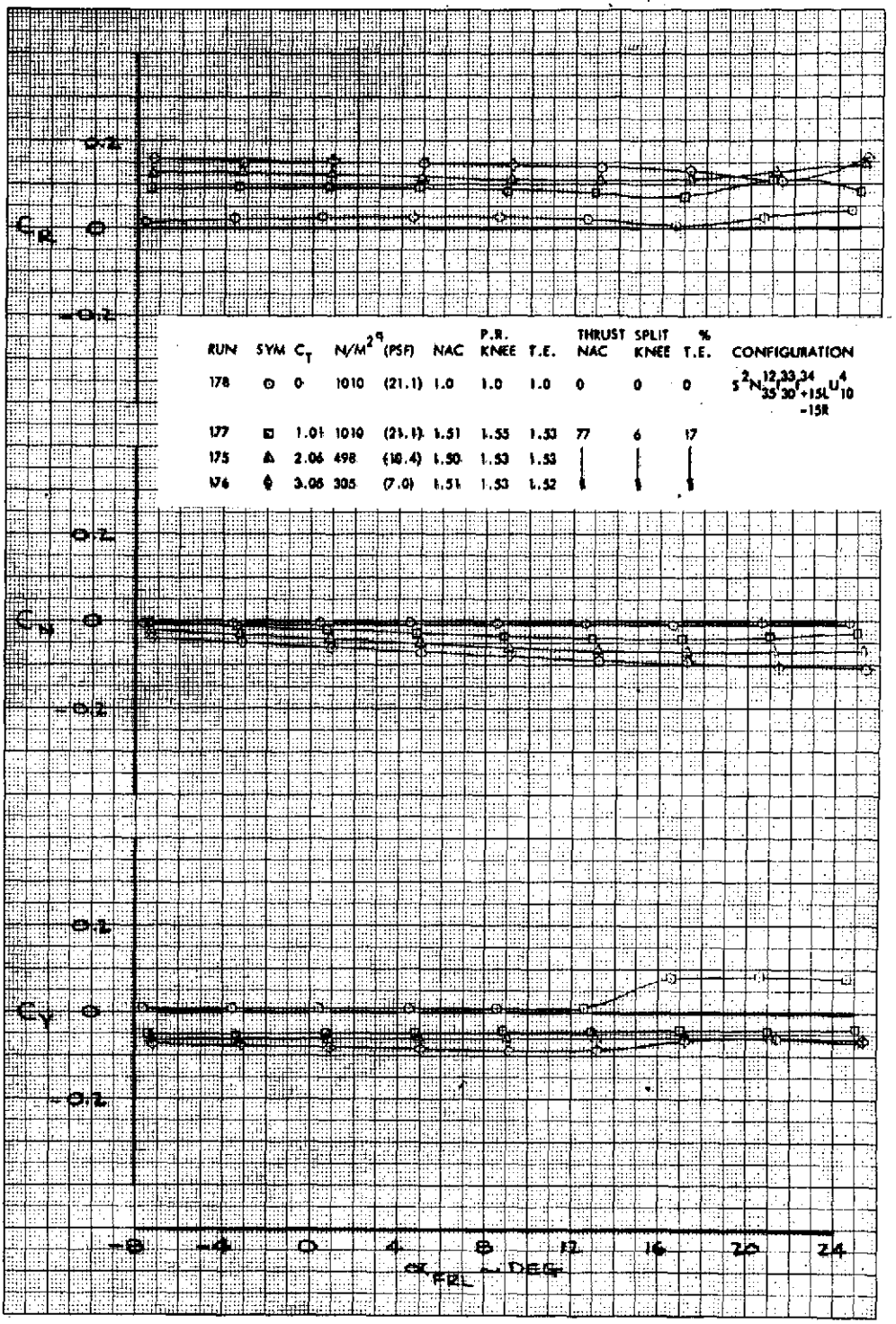

Figure 73. - Effect of Angle-of-Attack on Lateral-Directional Characteristics of the High Wing Model, 30° J/H Flap with +15° Left and -15° Right Aft Flap Deflection, 10° Open Deflector, Tail Off

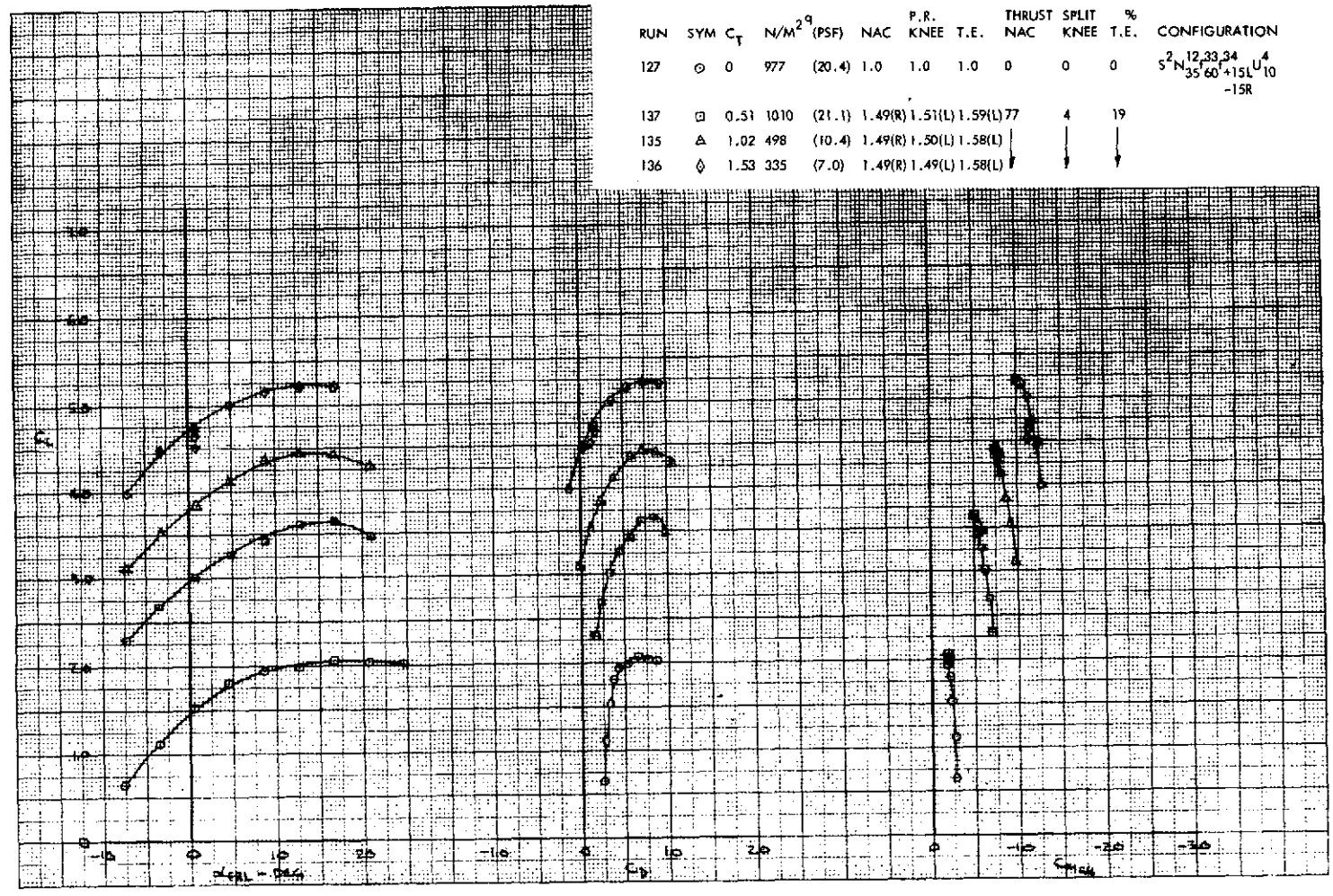

Figure 74. - Longitudinal Characteristics of the High Wing Model with the Left Engine and the Right BLC Systems Inoperative, 60° J/H Flap with +15° Left and -15° Right Aft Flap Deflection, 10° Open Deflector, Tail Off

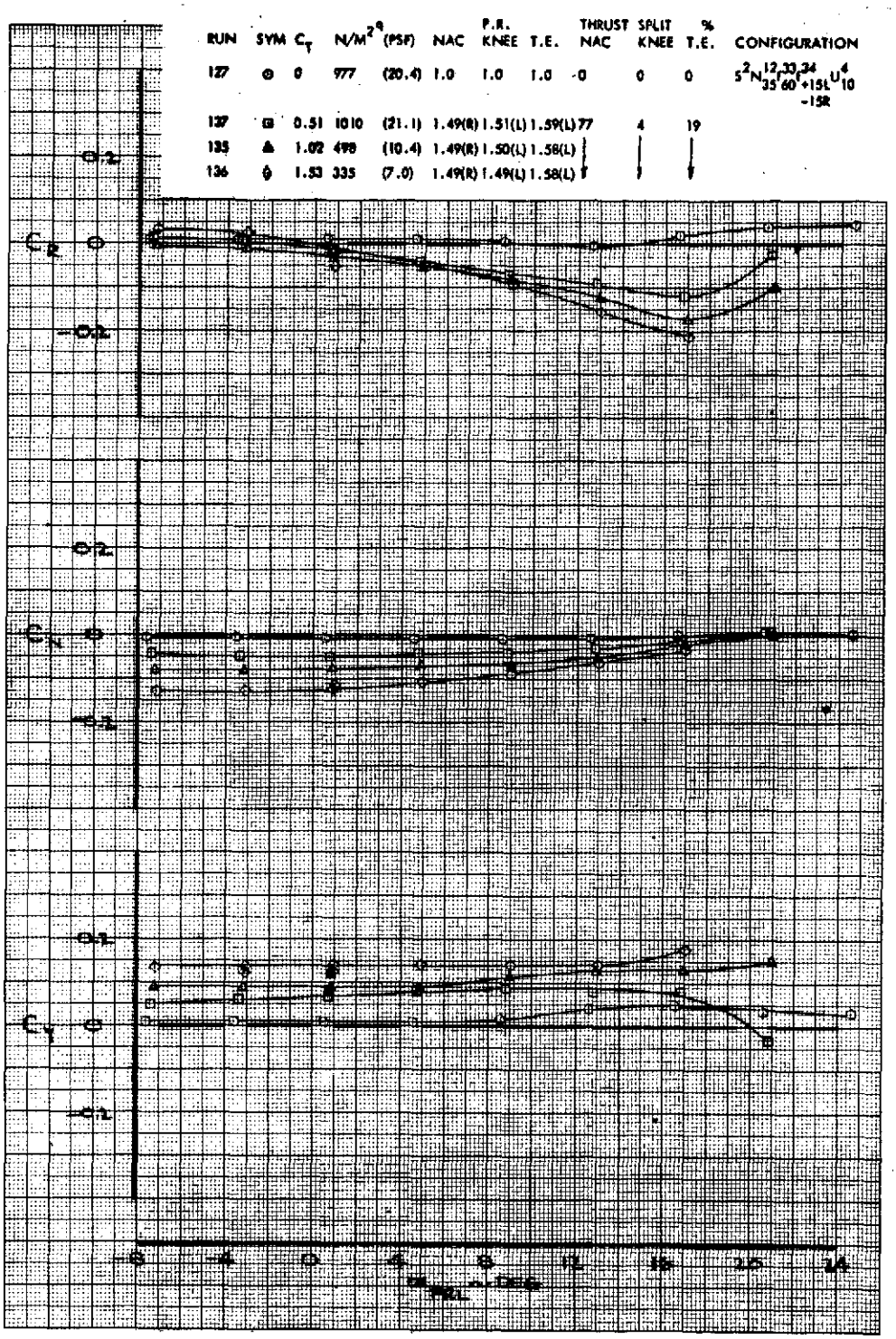

Figure 75. - Effect of Angle-of-Attack on Lateral-Directional Characteristics of the High Wing Model with the Left Engine and the Right BLC Systems Inoperative, 60° J/H Flap with +15° Left and -15° Right Aft Flap Deflection, 10° Open Deflector, Tail Off

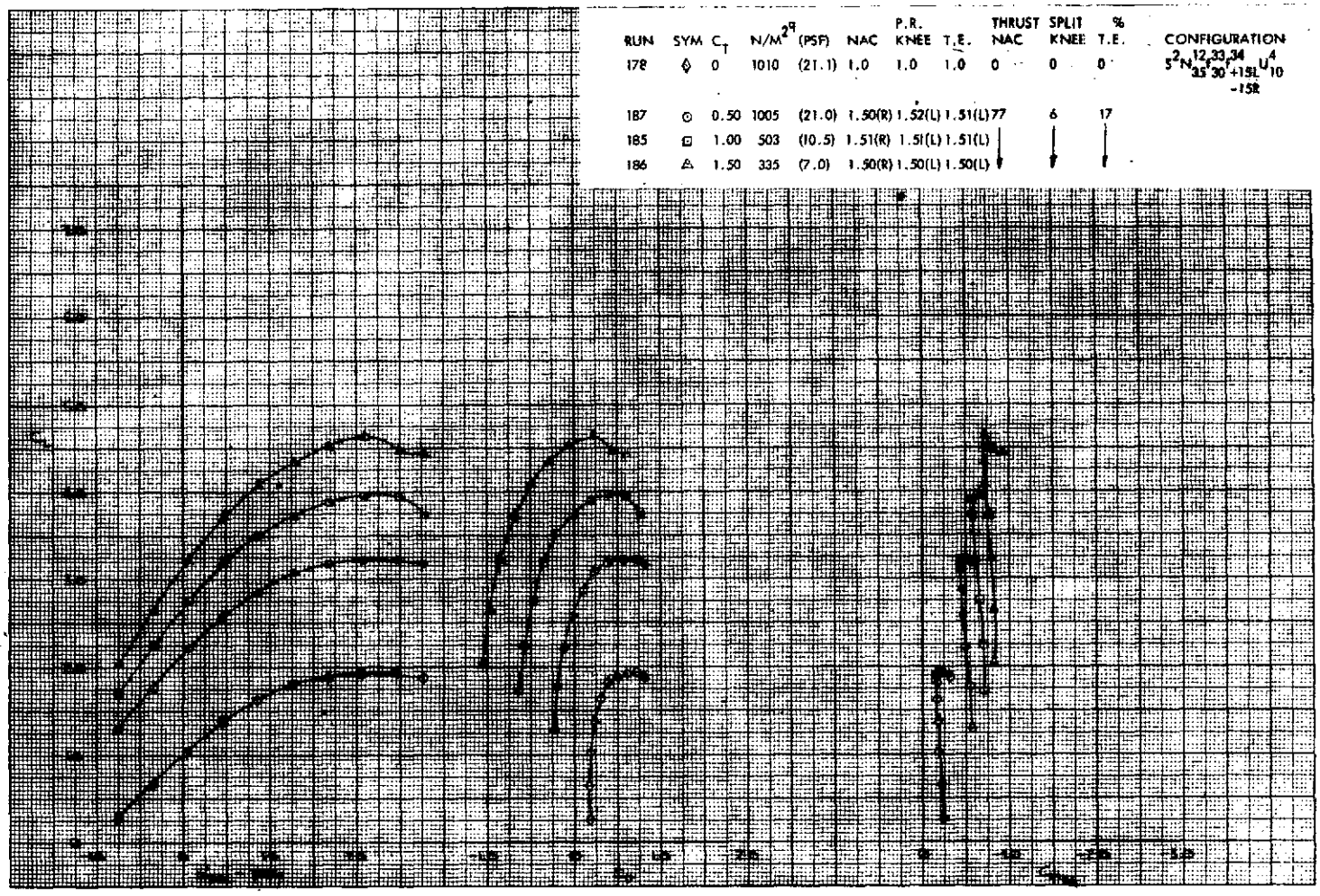

Figure 76. - Longitudinal Characteristics of the High Wing Model with the Left Engine and the Right BLC Systems Inoperative, 30° J/H Flap with +15° Left and -15° Right Aft Flap Deflection, 10° Open Deflector, Tail Off

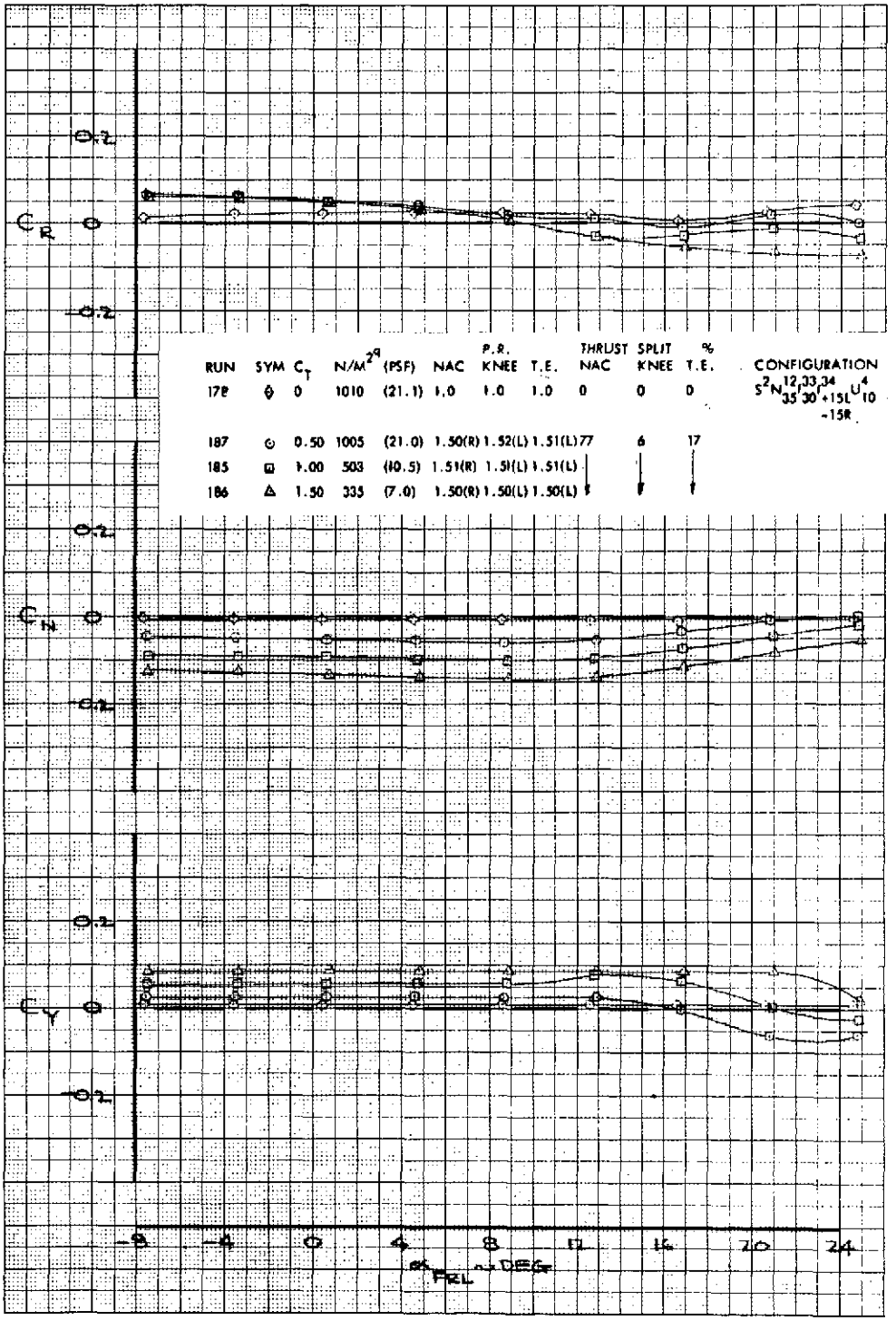

Figure 77. - Effect of Angle-of-Attack on Lateral-Directional Characteristics of the High Wing Model with the Left Engine and the Right BLC Systems Inoperative, 30° J/H Flap with +15° Left and -15° Right Aft Flap Deflection, 10° Open Deflector, Tail Off

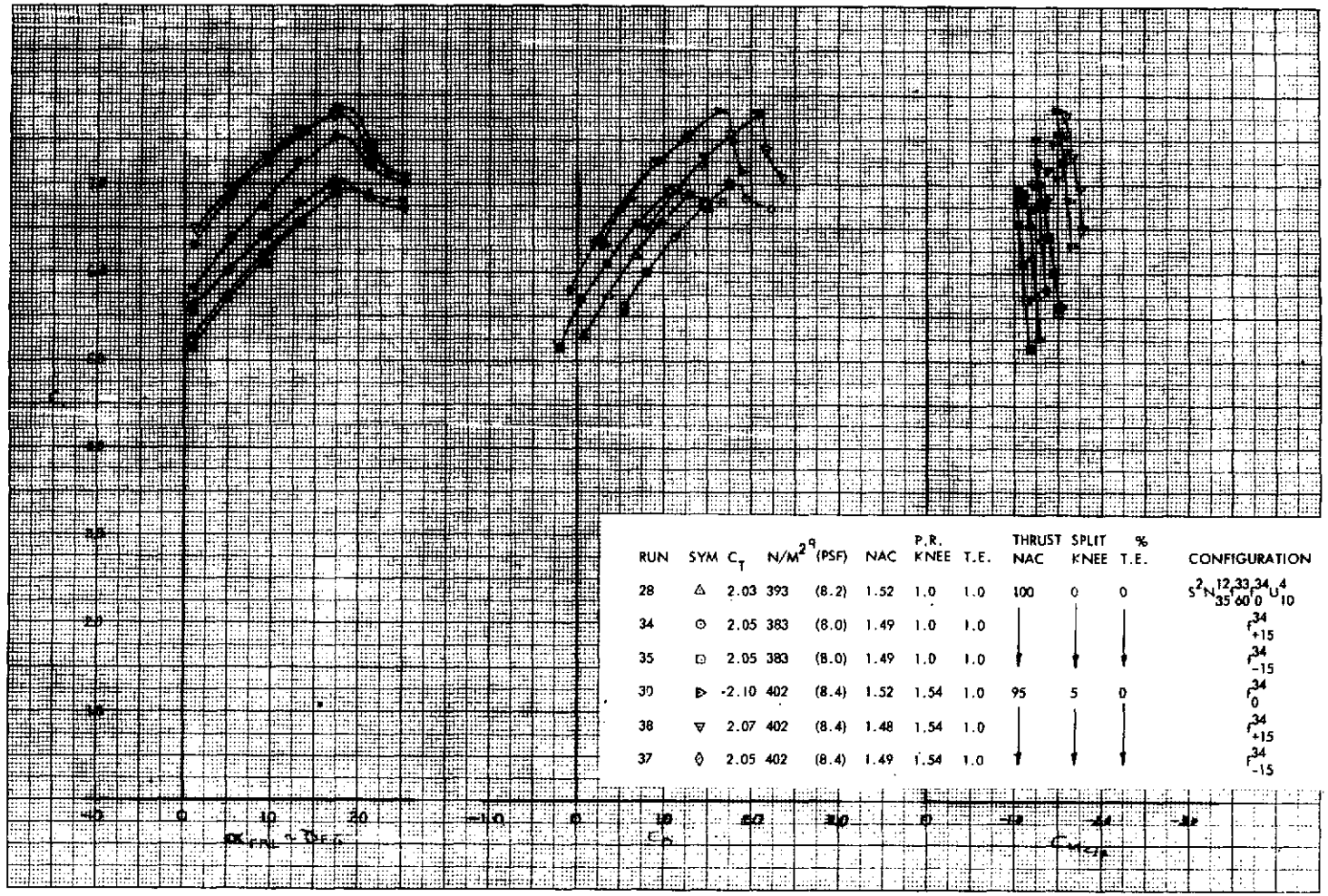

Figure 78. - Longitudinal Characteristics of the High Wing Model with Selected Blowing, 60° J/H Flap θ°, +15° and -15° Symmetric Aft Flap Deflection, 10° Open Deflector, Tail Off

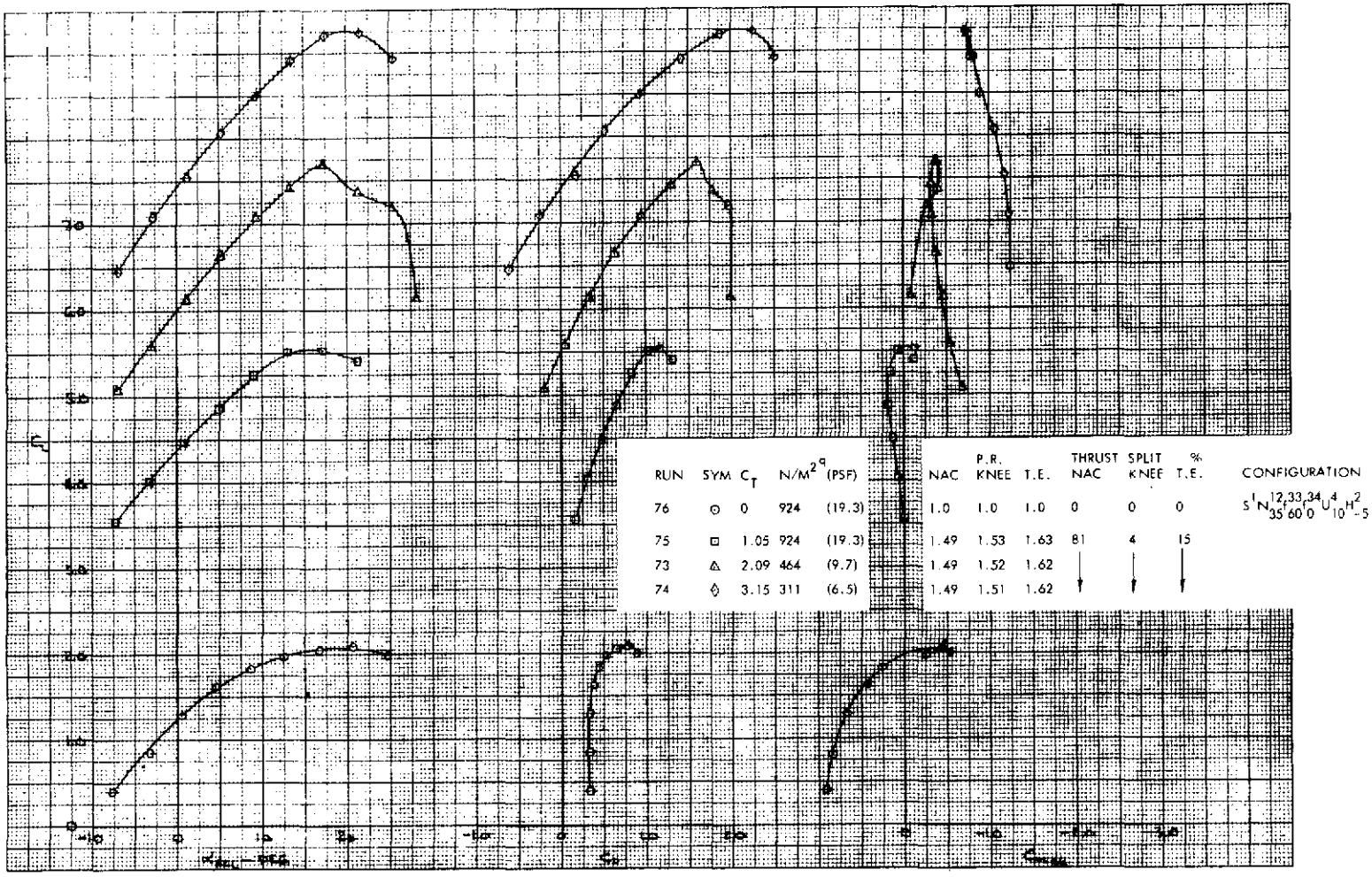

Figure 79. - Longitudinal Characteristics of the High Wing Model, $60^\circ/0^\circ$ J/H Flap, -5° Horizontal Stabilizer Incidence, 10° Open Deflector

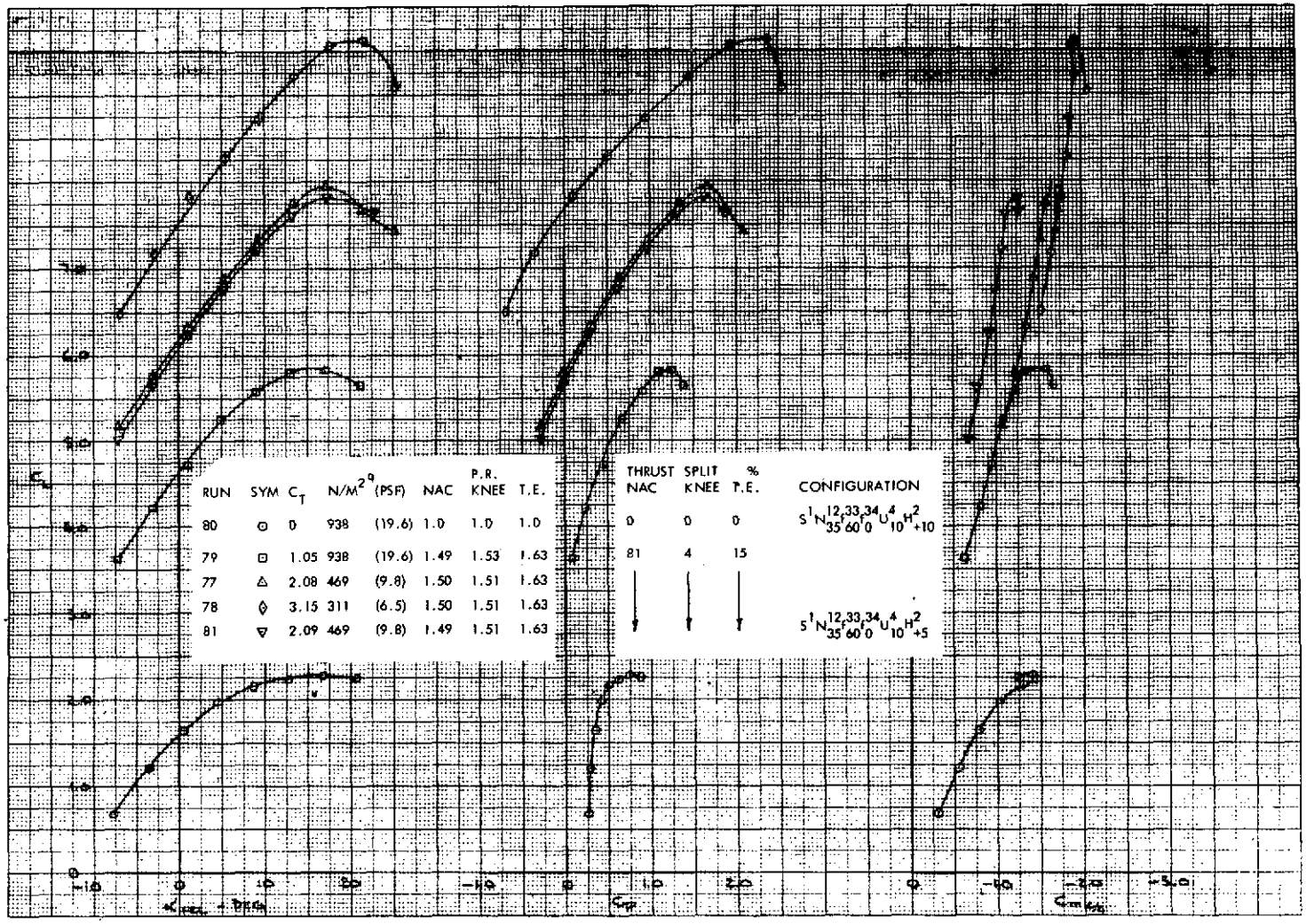

Figure 80. - Longitudinal Characteristics of the High Wing Model, $60^\circ/0^\circ$ J/H Flap, $+5^\circ$ and $+10^\circ$ Horizontal Stabilizer Incidence, 10° Open Deflector

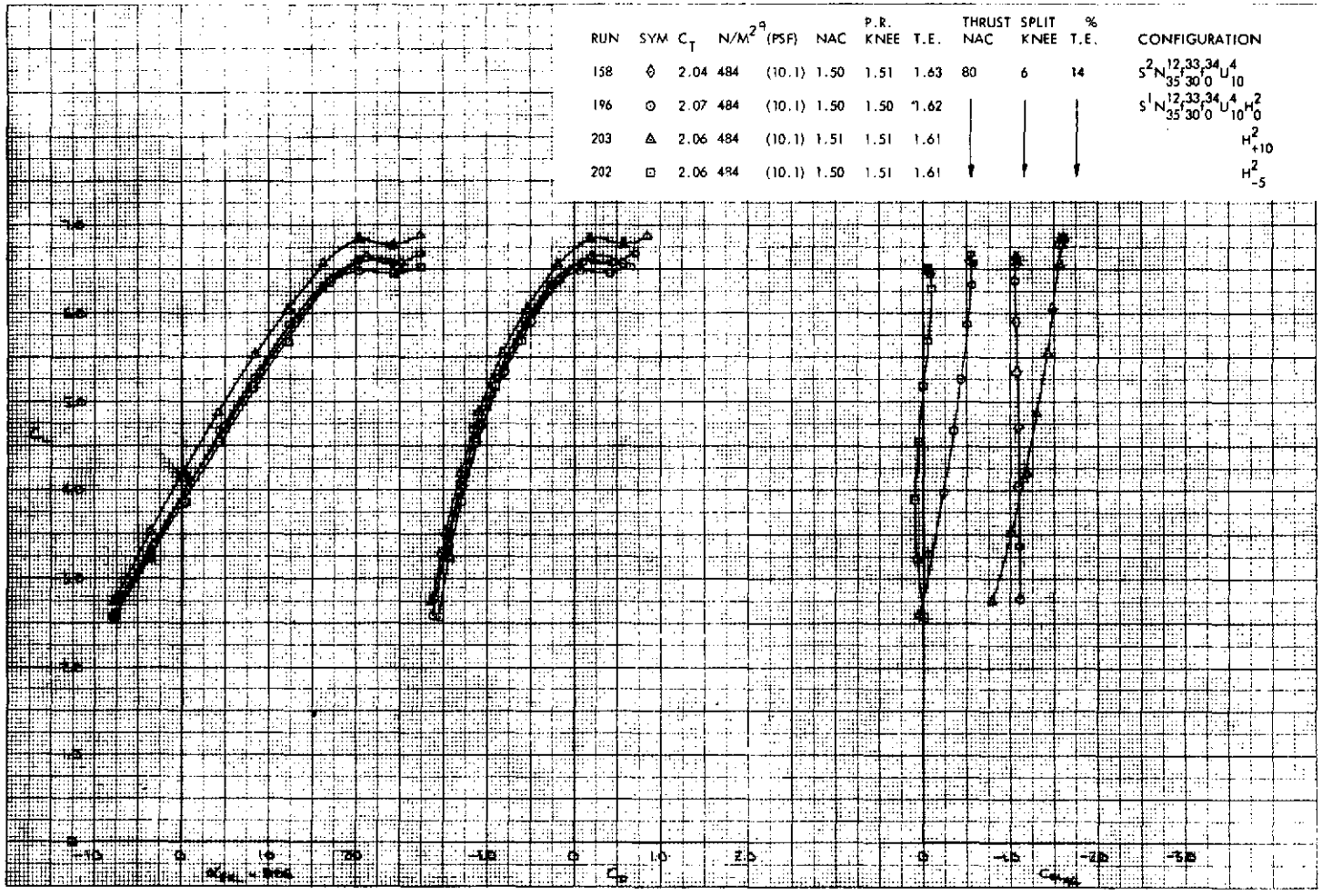

Figure 81. - Longitudinal Characteristics of the High Wing Model, $30^\circ/0^\circ$ J/H Flap, -5°, 0°, and $+10^\circ$ Horizontal Stabilizer Incidence, 10° Open Deflector

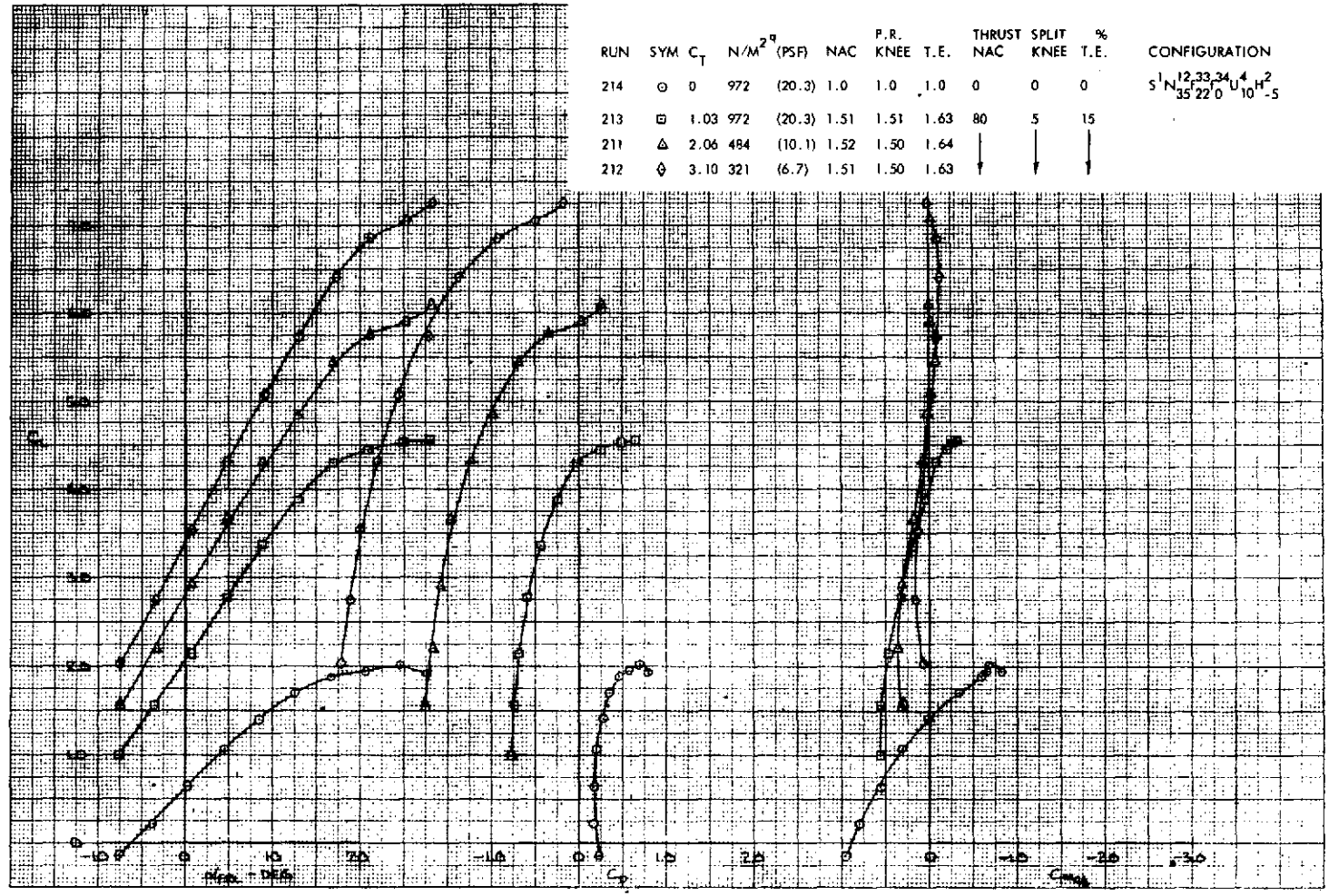

Figure 82. - Longitudinal Characteristics of the High Wing Model, $22^\circ/0^\circ$ J/H Flap, -5° Horizontal Stabilizer Incidence, 10° Open Deflector

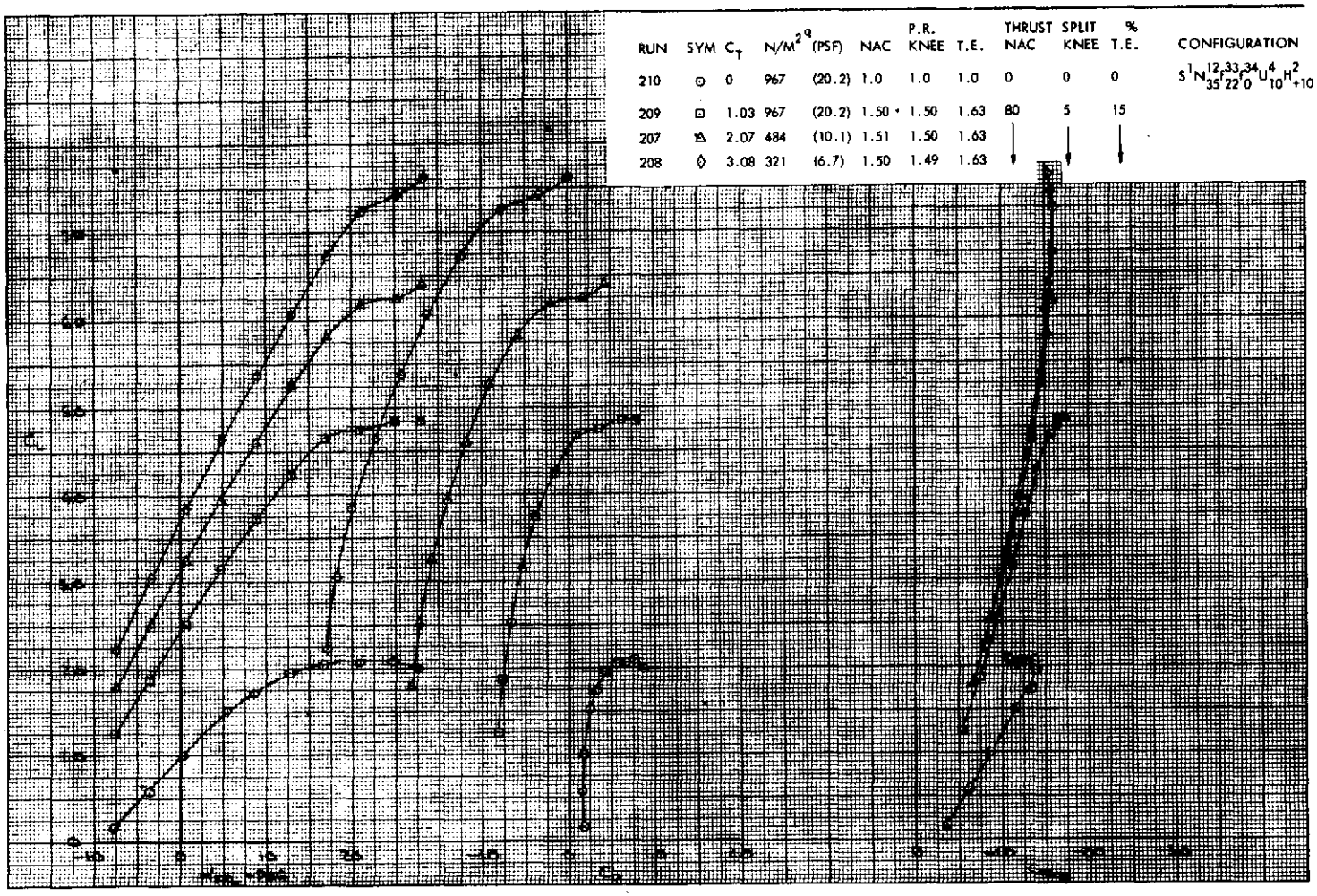

Figure 83. - Longitudinal Characteristics of the High Wing Model, $22^\circ/0^\circ$ J/H Flap, $+10^\circ$ Horizontal Stabilizer Incidence, 10° Open Deflector

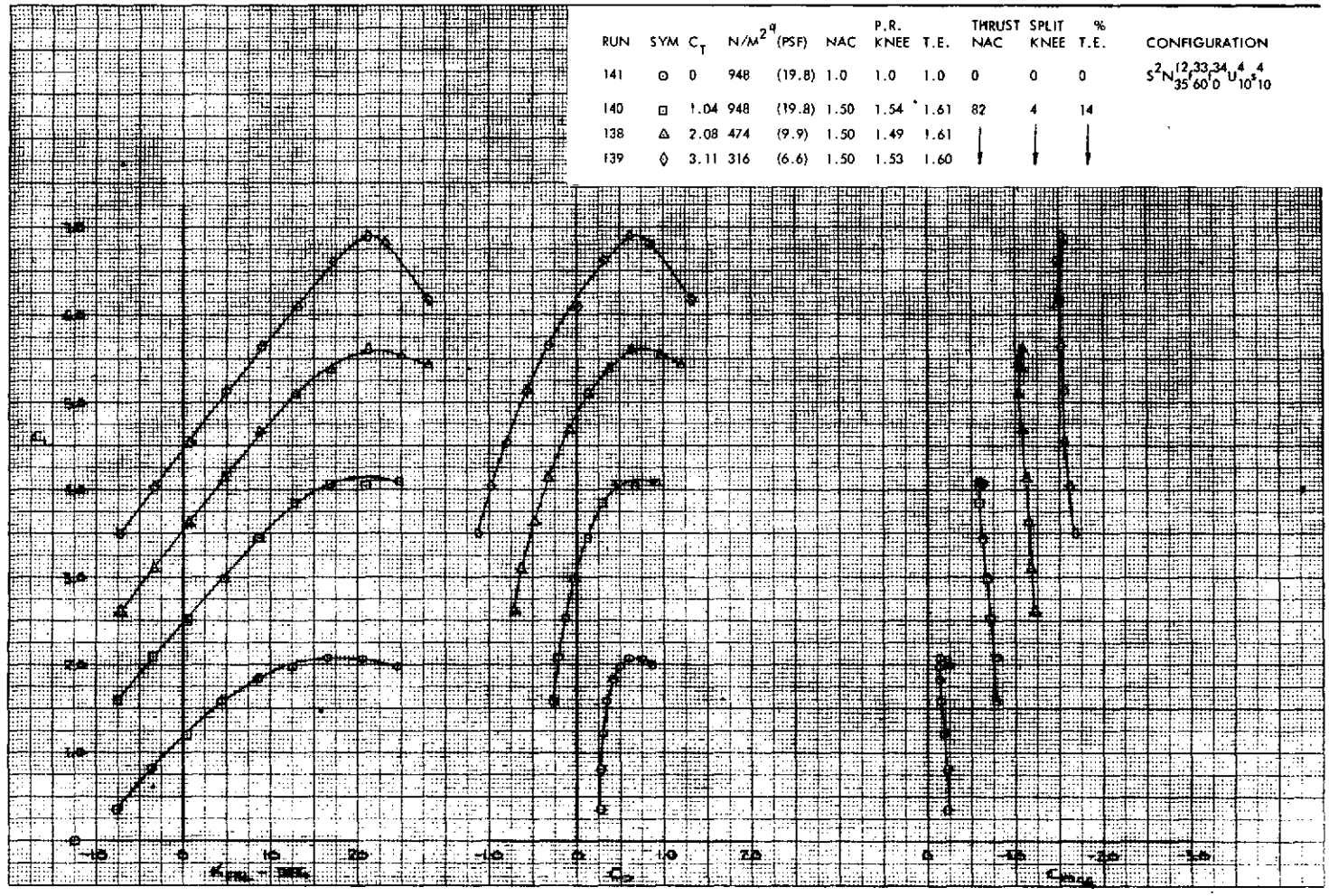

Figure 84. - Longitudinal Characteristics of the High Wing Model, $60^\circ/0^\circ$ J/H Flap, 10° Full Flap Span Solid Spoiler, 10° Open Deflector, Tail Off

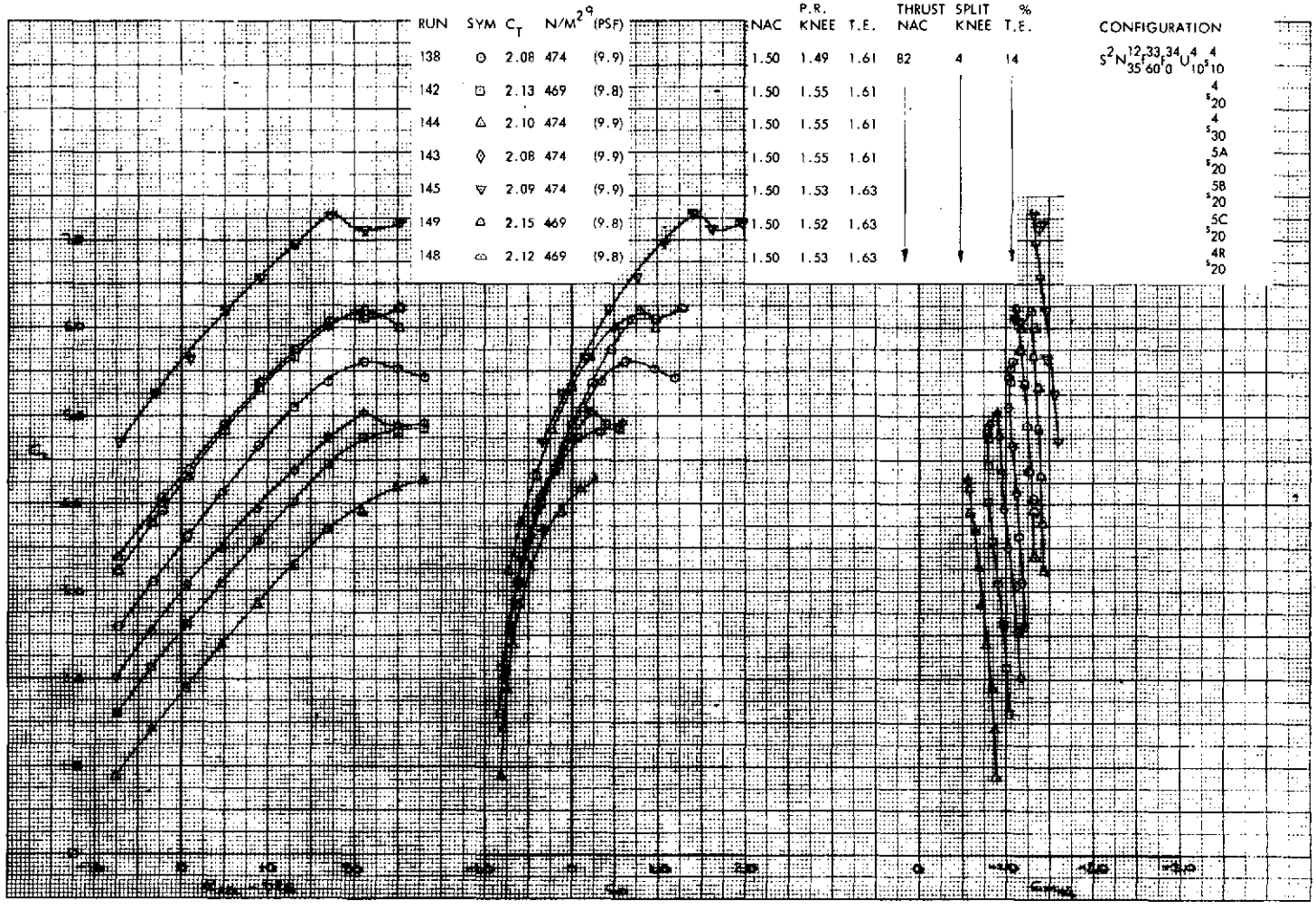

Figure 85. - Longitudinal Characteristics of the High Wing Model, $60^\circ/0^\circ$ J/H Flap, Various Spoilers, 10° Open Deflector, Tail Off

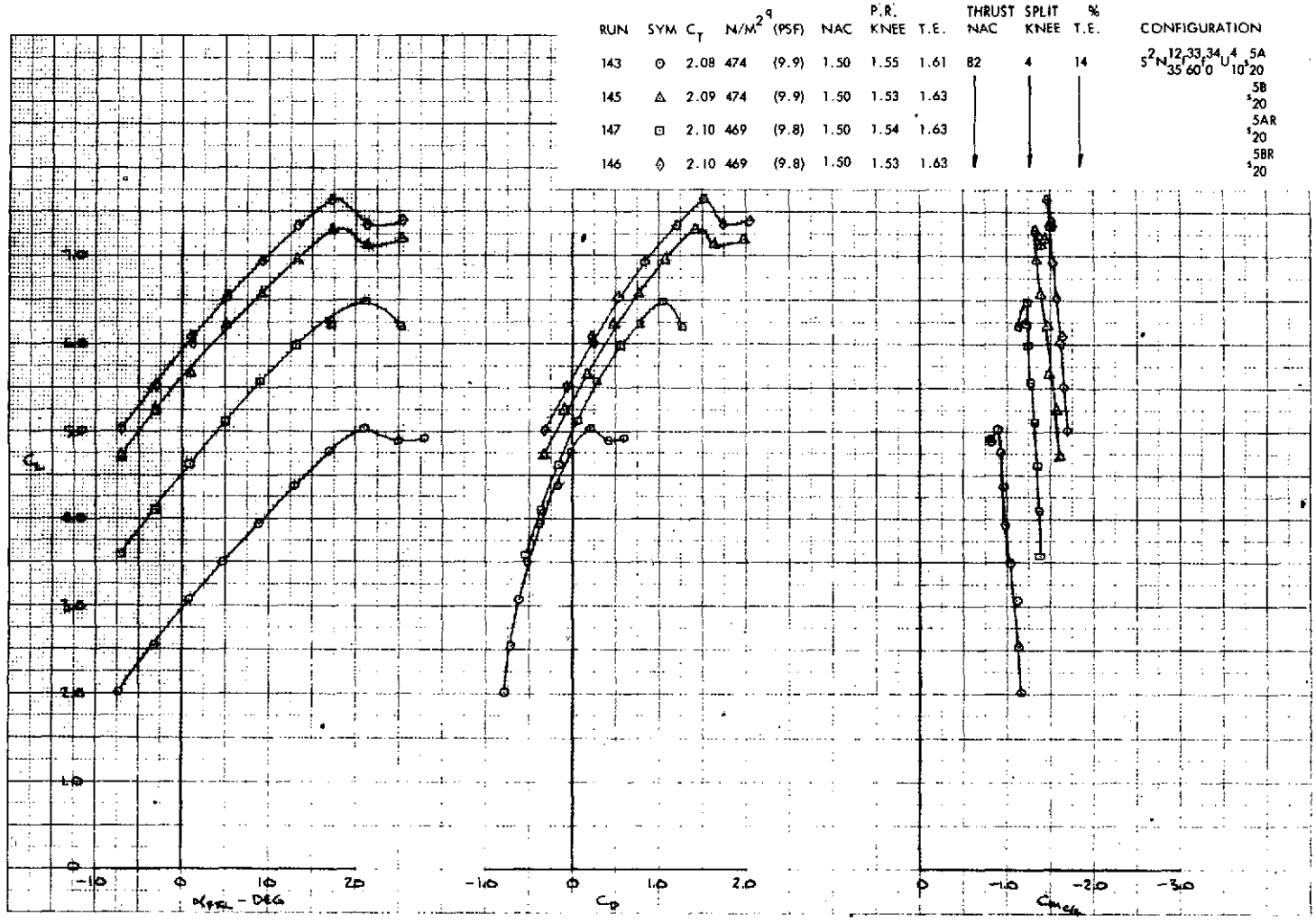

Figure 86. - Longitudinal Characteristics of the High Wing Model, 60°/0° J/H Flap, Part Span Symmetric and Asymmetric 20° Spoiler Comparison, 10° Open Reflector, Tail Off

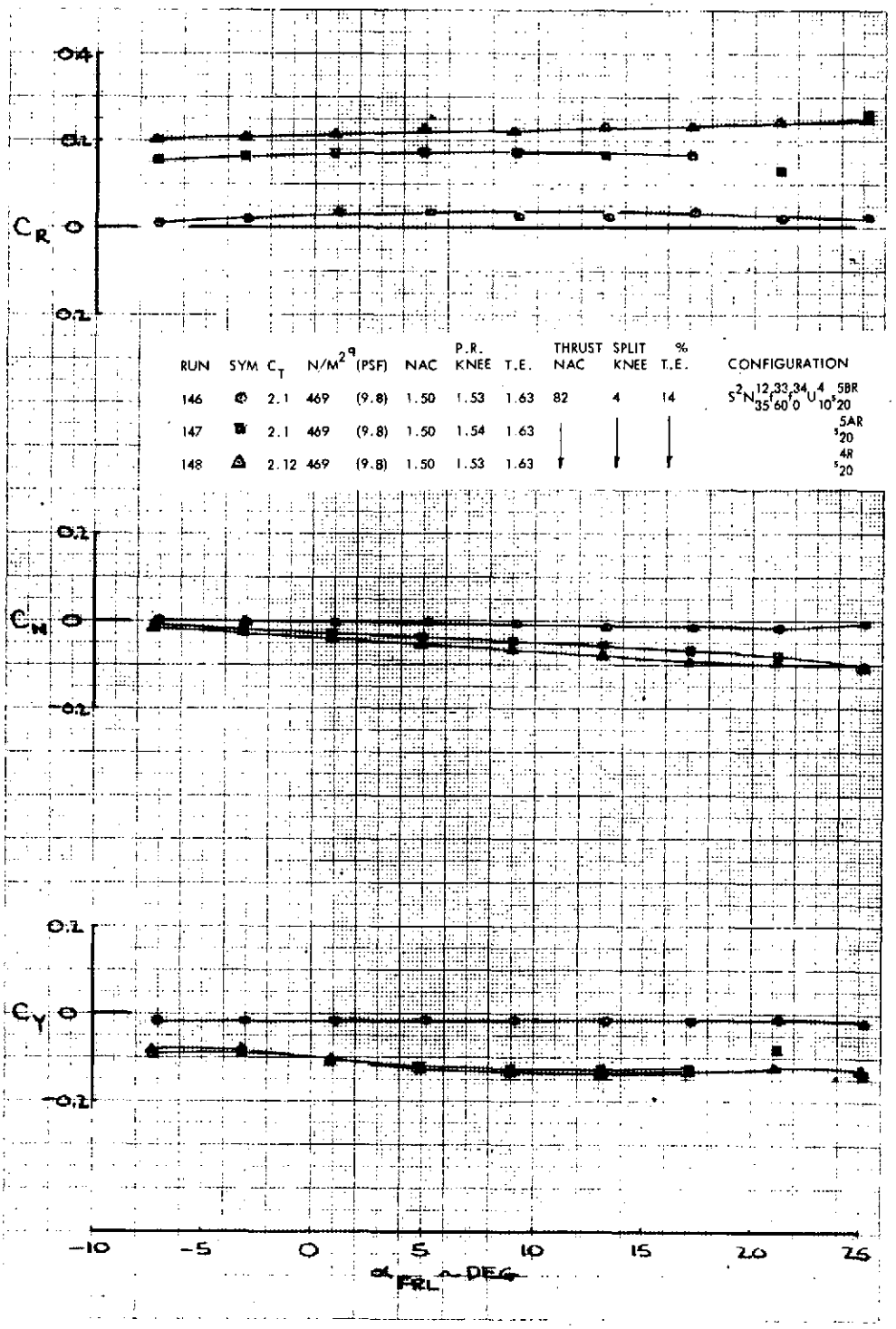

Figure 87. - Effect of Angle-of-Attack on Lateral-Directional Characteristics of the High Wing Model, $60^\circ/0^\circ$ J/H Flap, Part Span Asymmetric 20° Spoiler Comparison, 10° Open Deflector, Tail Off

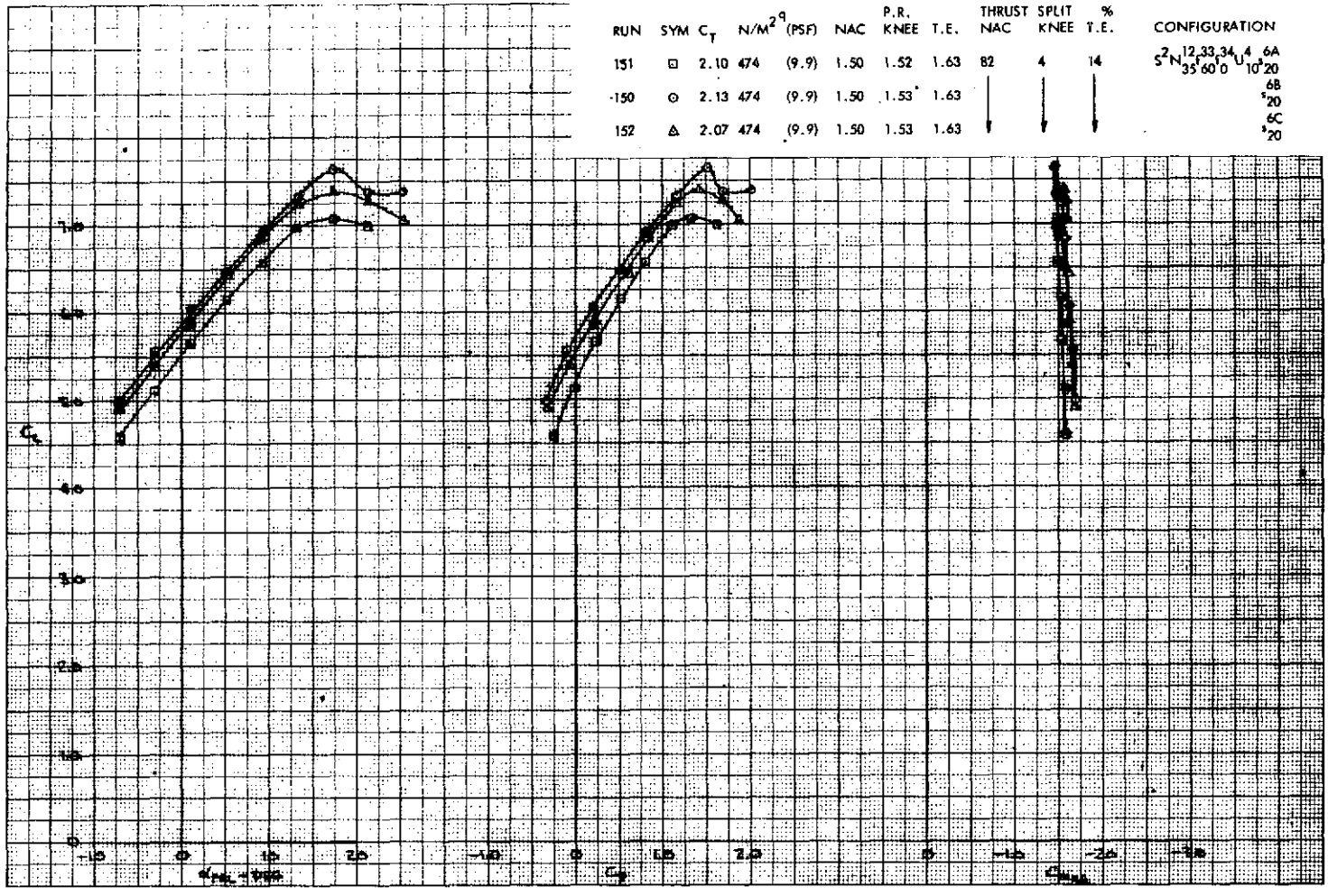

Figure 88. - Longitudinal Characteristics of the High Wing Model, 60°/0° J/H Flap, Part Span 20° Porous Spoilers, 10° Open Deflector, Tail Off

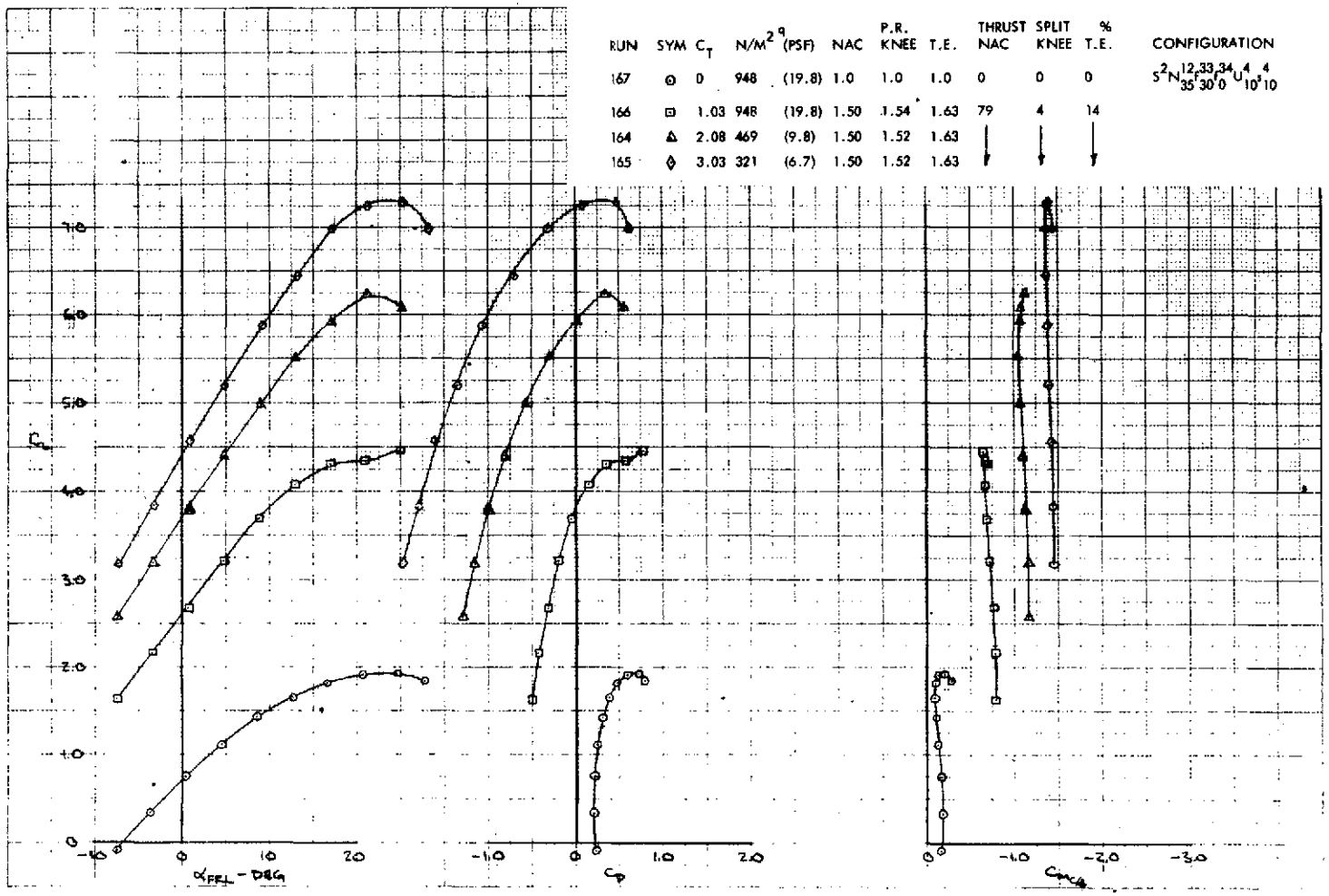

Figure 89. - Longitudinal Characteristics of the High Wing Model, 30°/0° J/H Flap, Full Span 10° Solid Spoilers 10° Open Deflector, Tail Off

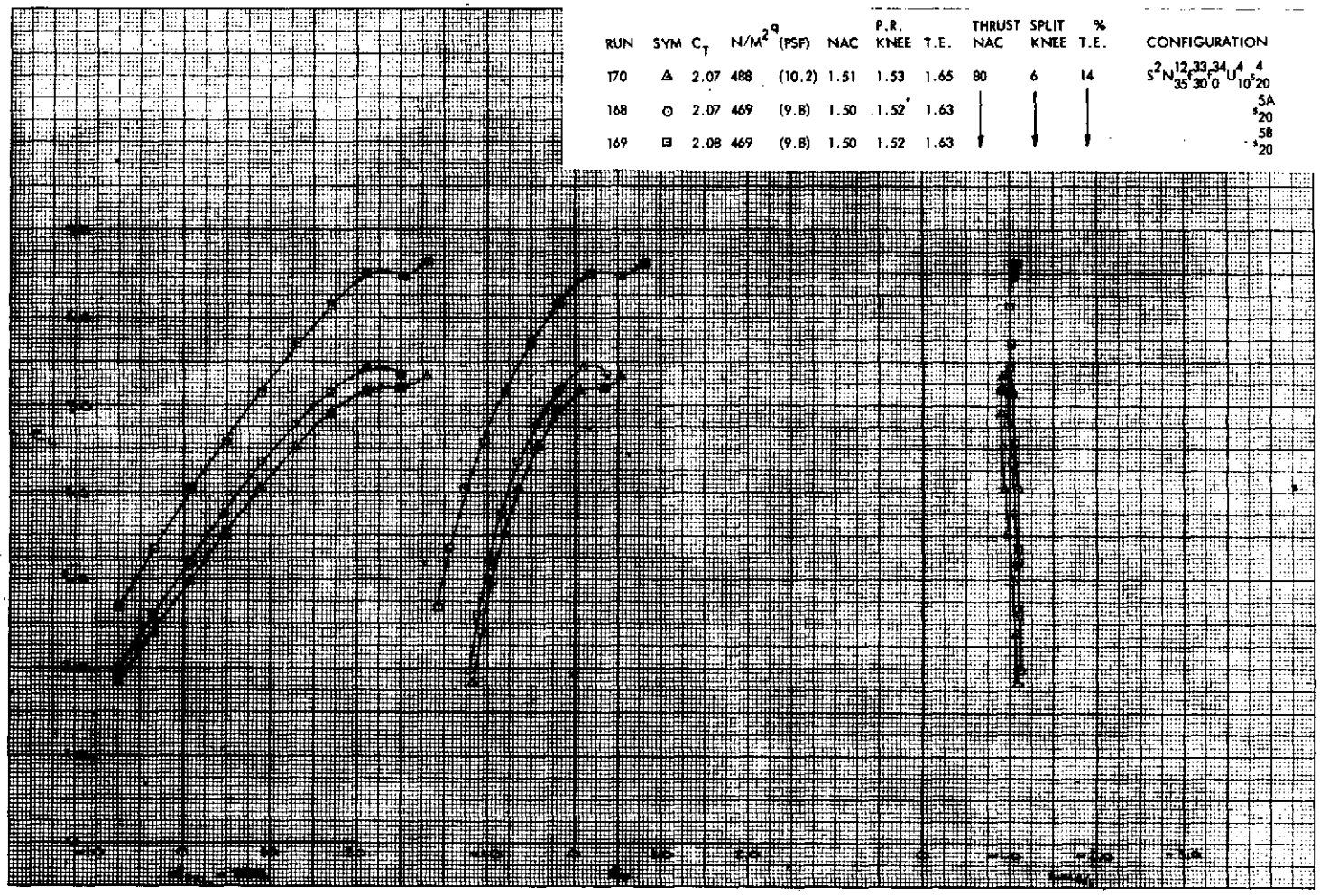

Figure 90. – Longitudinal Characteristics of the High Wing Model, $30^{\circ}/0^{\circ}$ J/H Flap, Symmetric Solid Full and Part Span 20° Spoilers, 10° Open Deflector, Tail Off

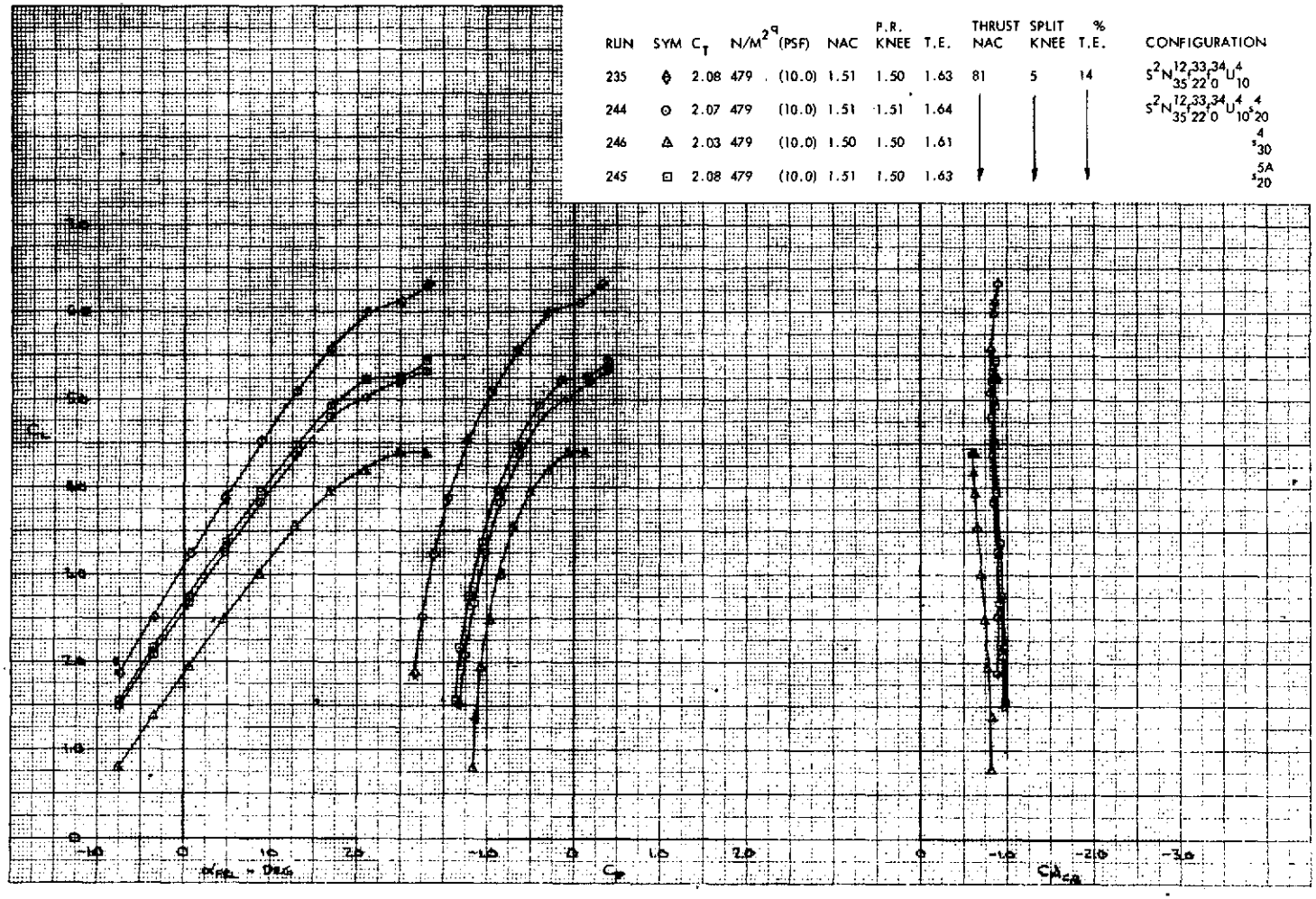

Figure 91. - Longitudinal Characteristics of the High Wing Model, 30°/0° J/H Flap, Symmetric Solid Spoilers, 10° Open Deflector, Tail Off

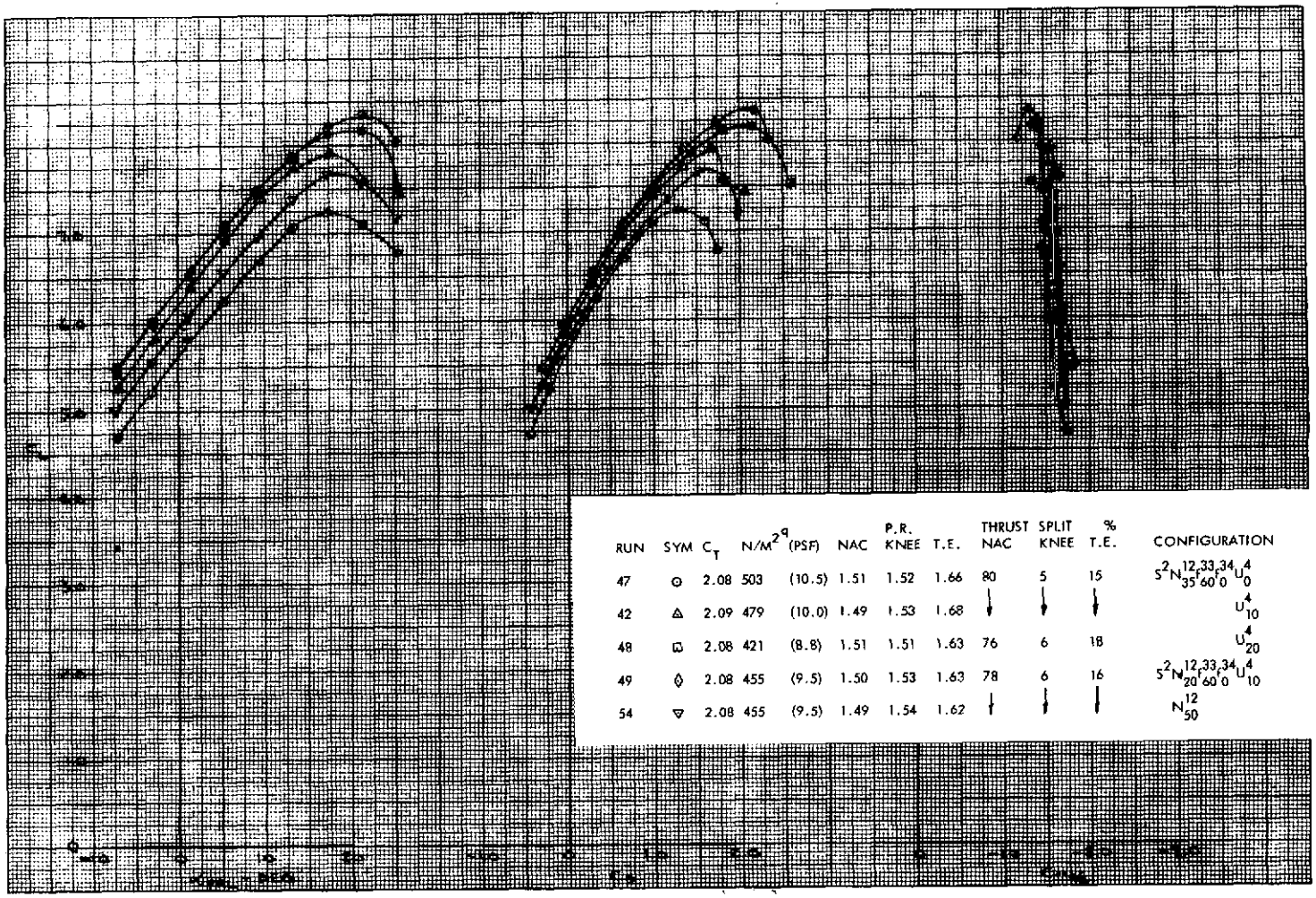

Figure 92. - Longitudinal Characteristics of the High Wing Model, $60^\circ/0^\circ$ J/H Flap, Variations in Nacelle Open Deflectors and Chordwise Exit Locations, Tail Off

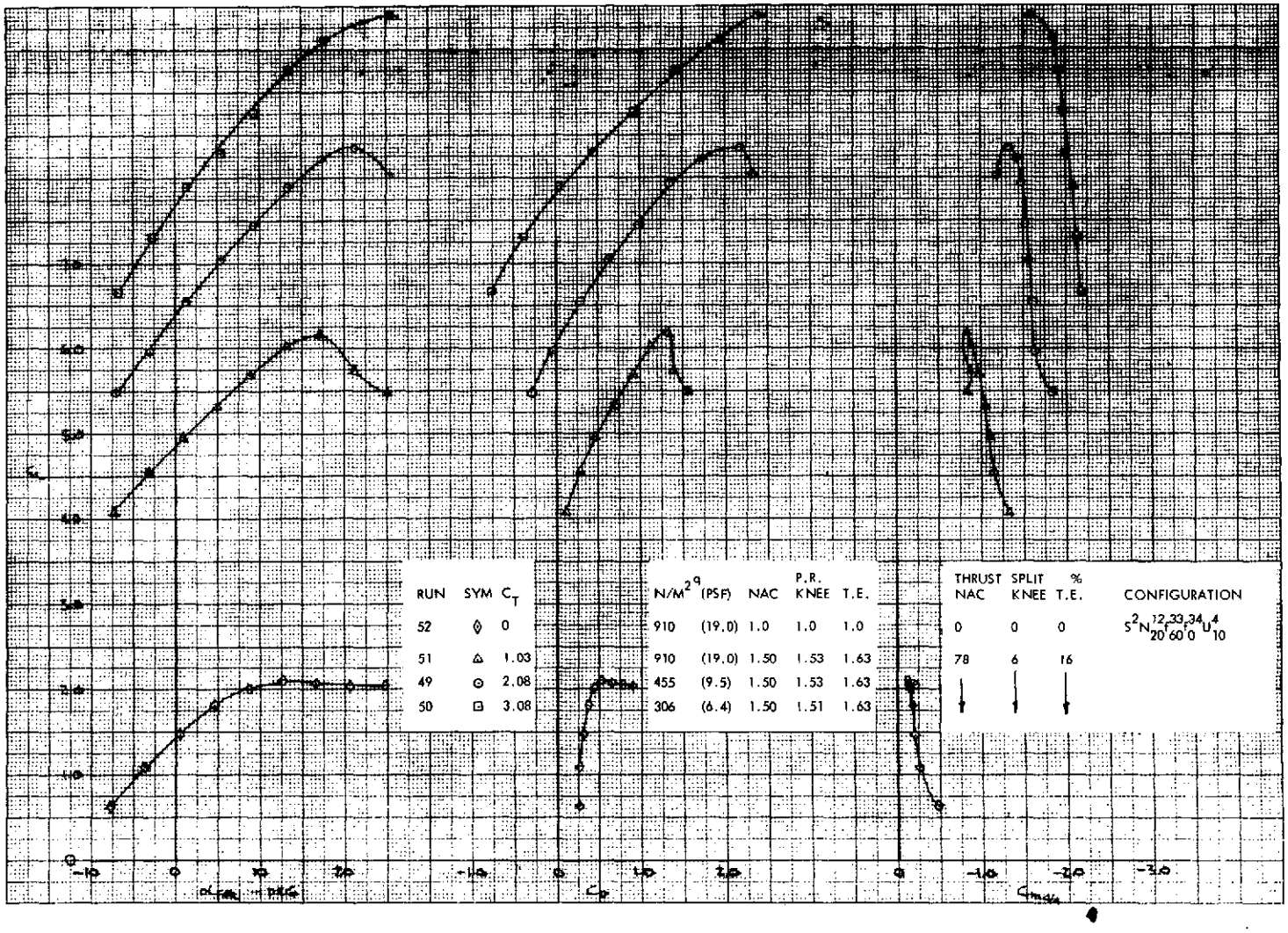

Figure 93. - Longitudinal Characteristics of the High Wing Model, $60^\circ/0^\circ$ J/H Flap, 10° Open Deflector, Nozzle Exit at 20% Chord, Tail Off

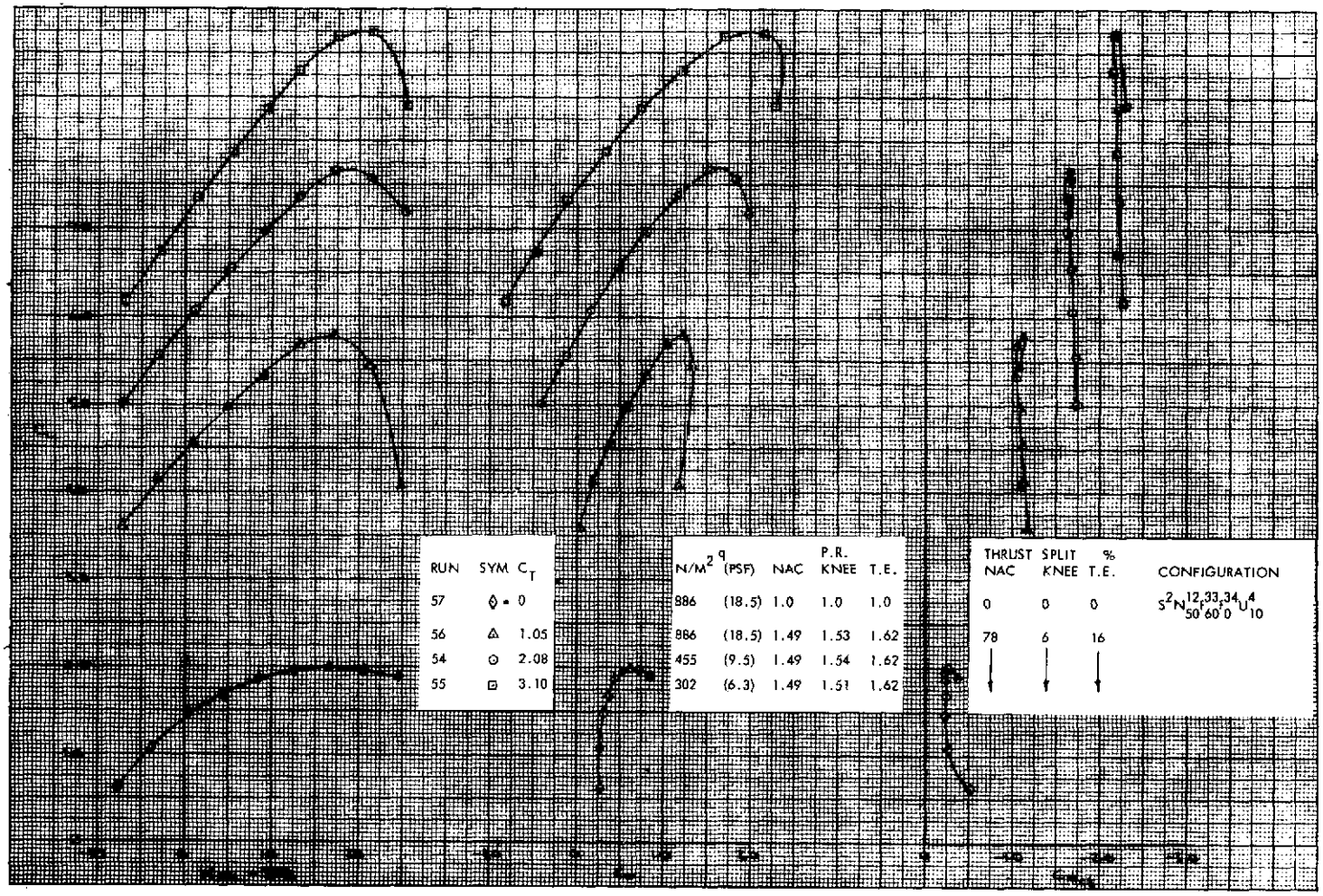

Figure 94. - Longitudinal Characteristics of the High Wing Model, $60^{\circ}/0^{\circ}$ J/H Flap, 10° Open Deflector, Nozzle Exit at 50% Chord, Tail Off

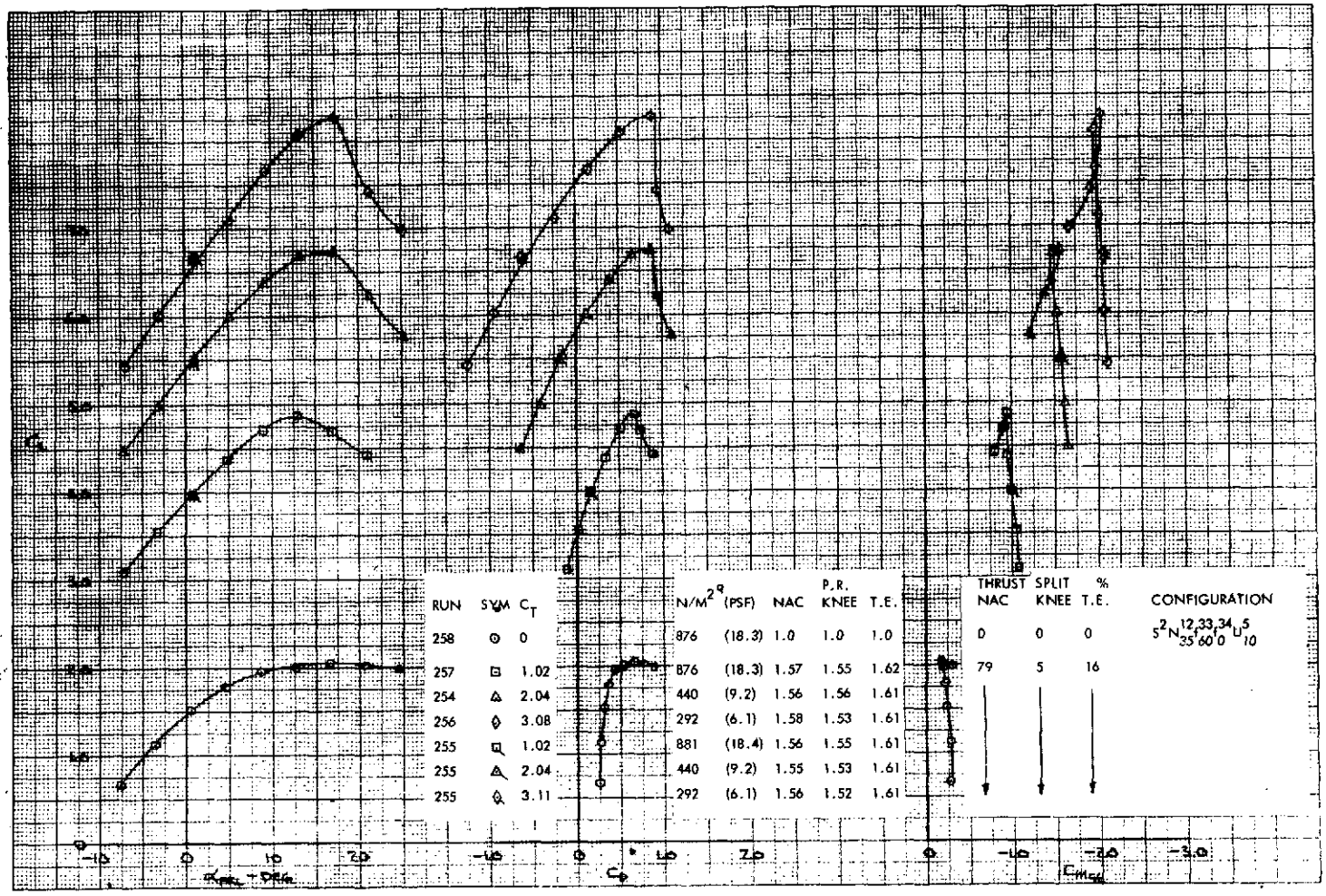

Figure 95. - Longitudinal Characteristics of the High Wing Model, $60^{\circ}/0^{\circ}$ J/H Flap, 10° Closed Deflector, Nozzle Exit at 35% Chord, Tail Off

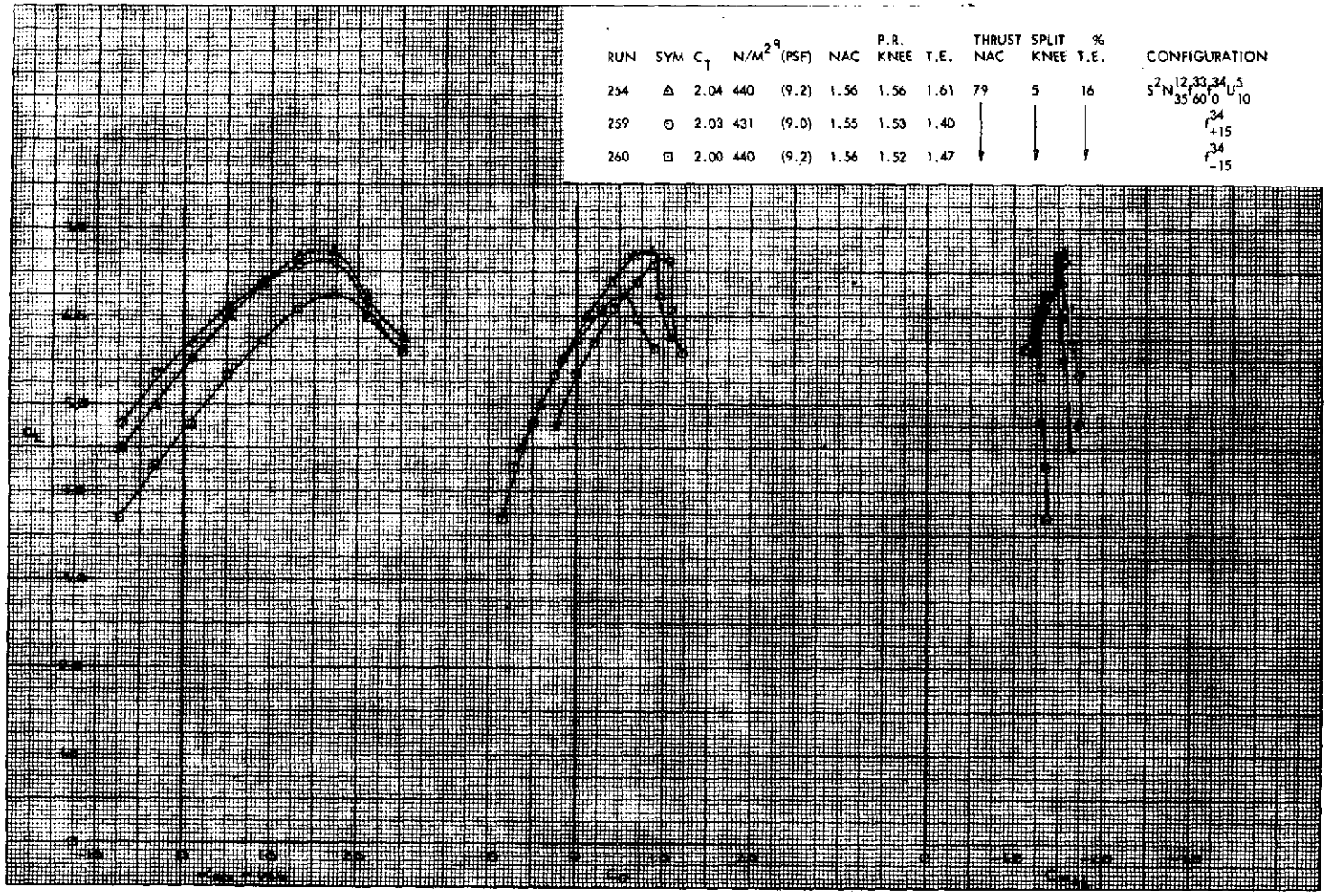

Figure 96. - Longitudinal Characteristics of the High Wing Model, 60° J/H Flap with Symmetric Deflection of the Aft Flap from +15° to -15°, 10° Closed Deflector, Tail Off

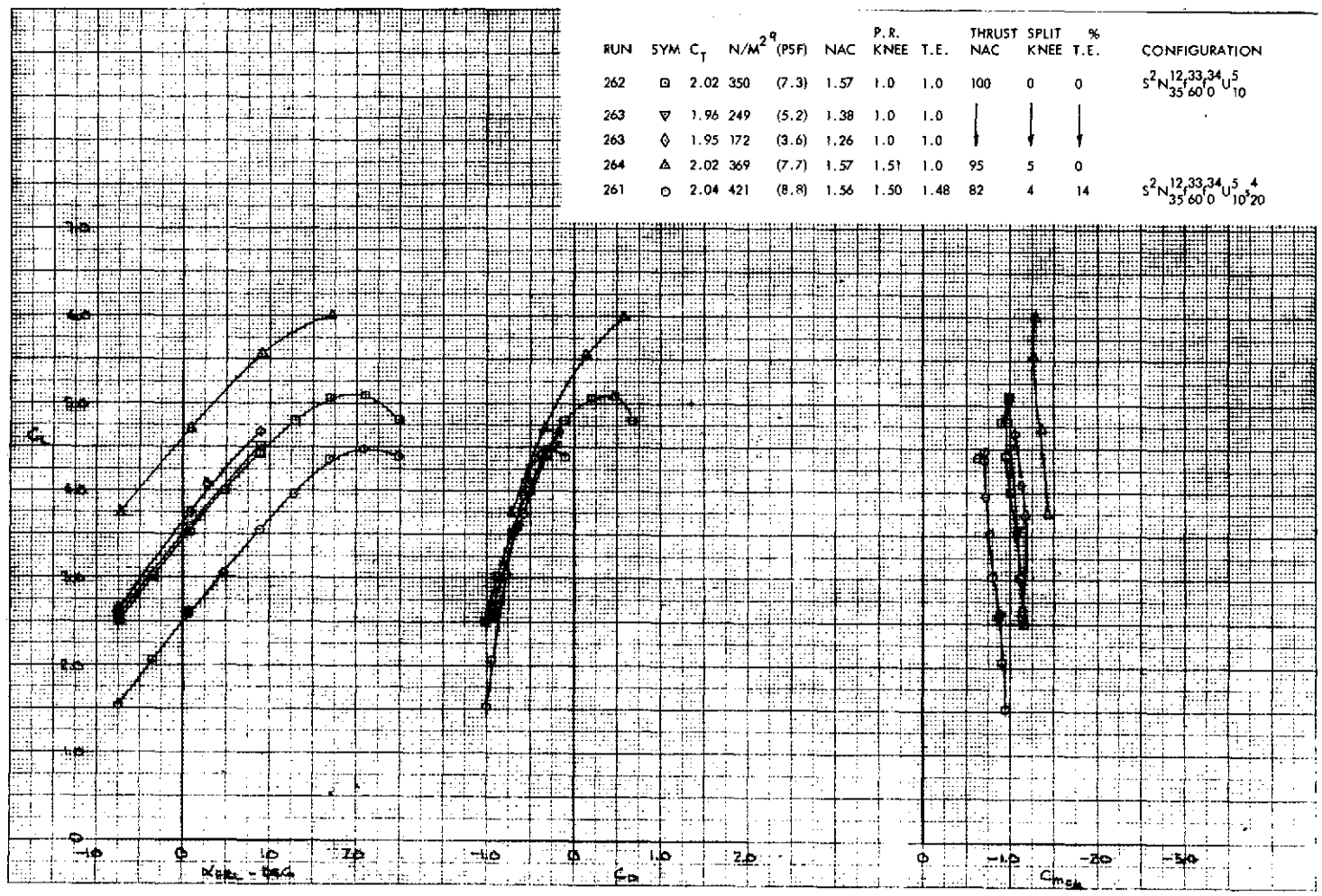

Figure 97. - Longitudinal Characteristics of the High Wing Model, $60^\circ/0^\circ$ J/H Flap, Selected Spoiler and Blowing Variations, 10° Closed Deflector, Tail Off

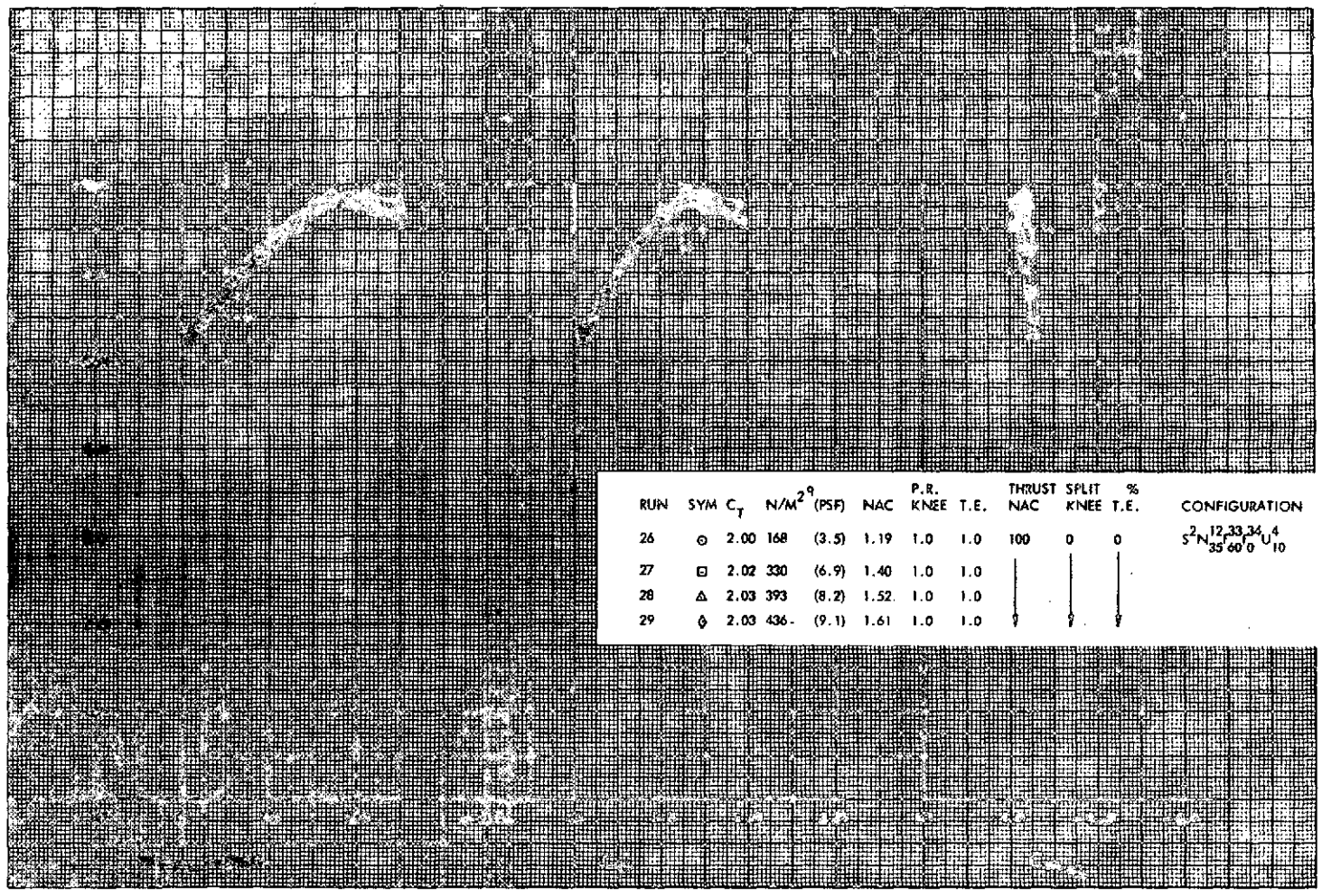

Figure 98. – Longitudinal Characteristics of the High Wing Model, $60^{\circ}/0^{\circ}$ J/H Flap, Pressure Ratio Effects with Nacelle Blowing Only, 10° Open Deflector, Tail Off

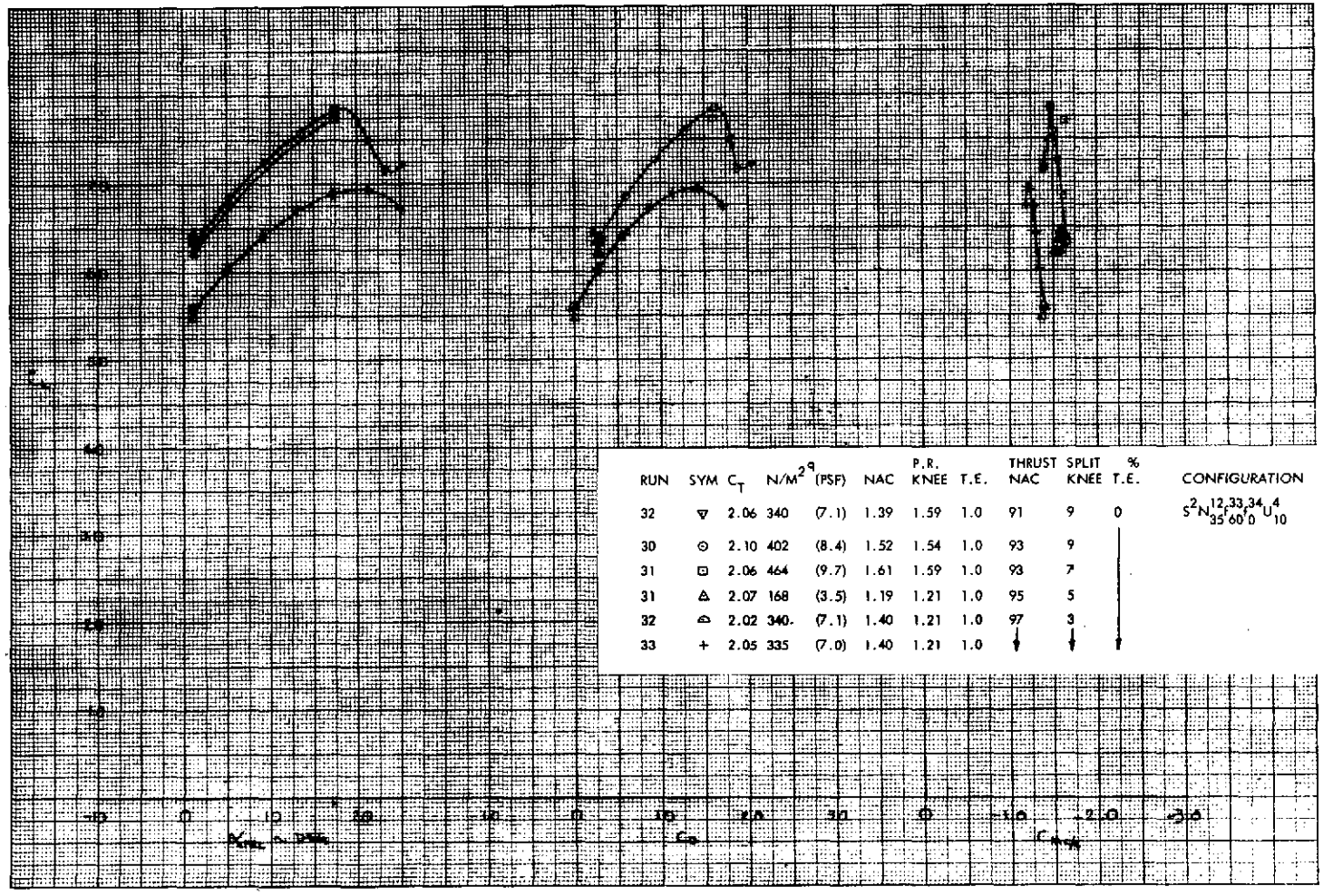

Figure 99. - Longitudinal Characteristics of the High Wing Model, $60^\circ/0^\circ$ J/H Flap, Pressure Ratio Effects with Nacelle and Knee Blowing Only, 10° Open Deflector, Tail Off

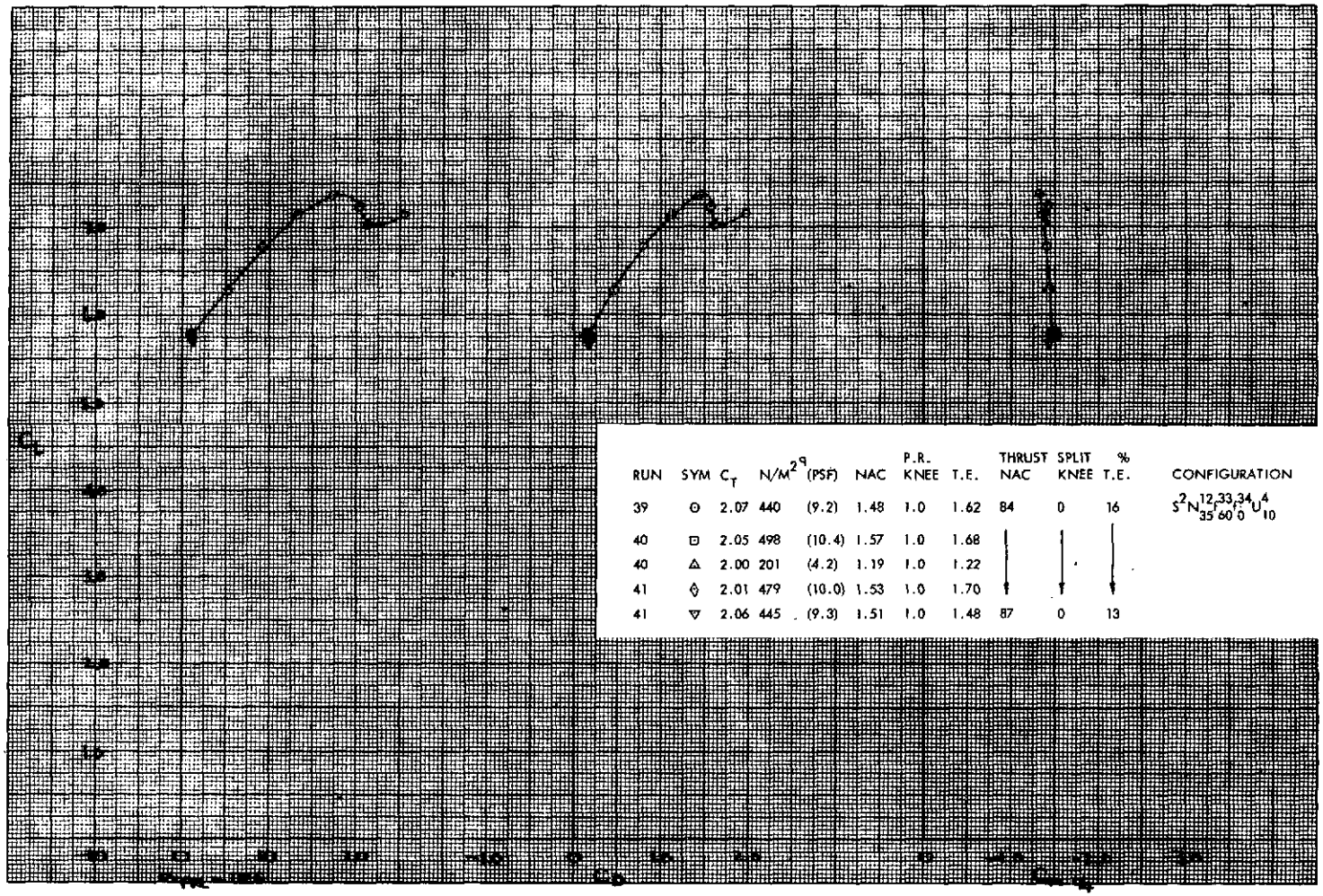

Figure 100. - Longitudinal Characteristics of the High Wing Model, $60^\circ/0^\circ$ J/H Flap, Pressure Ratio Effects with Nacelle and Aft Flap Blowing Only, 10° Open Deflector, Tail Off

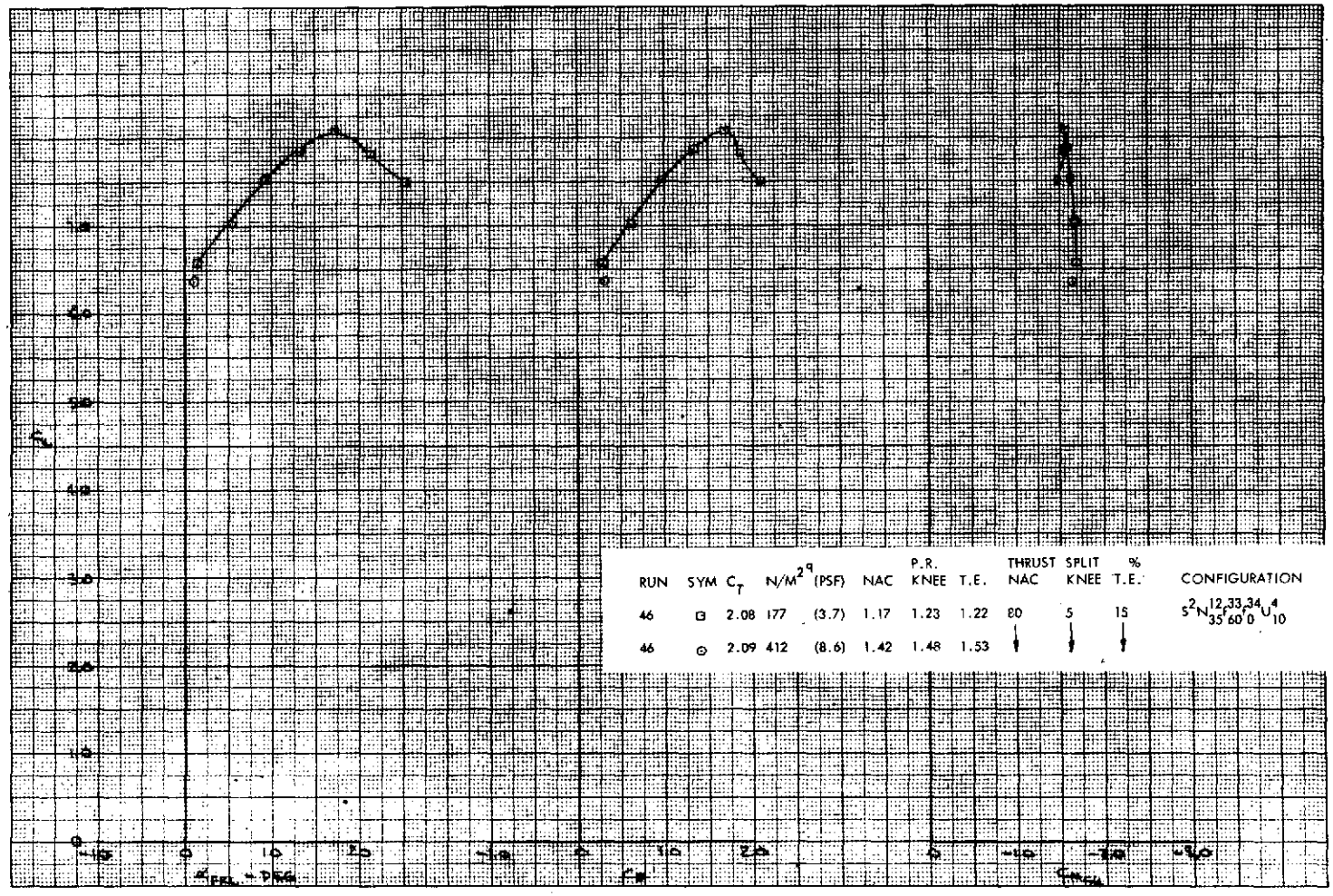

Figure 101. - Longitudinal Characteristics of the High Wing Model, $60^{\circ}/0^{\circ}$ J/H Flap, Pressure Ratio Effect with Nacelle, Knee, and Aft Flap Blowing, 10° Open Deflector, Tail Off

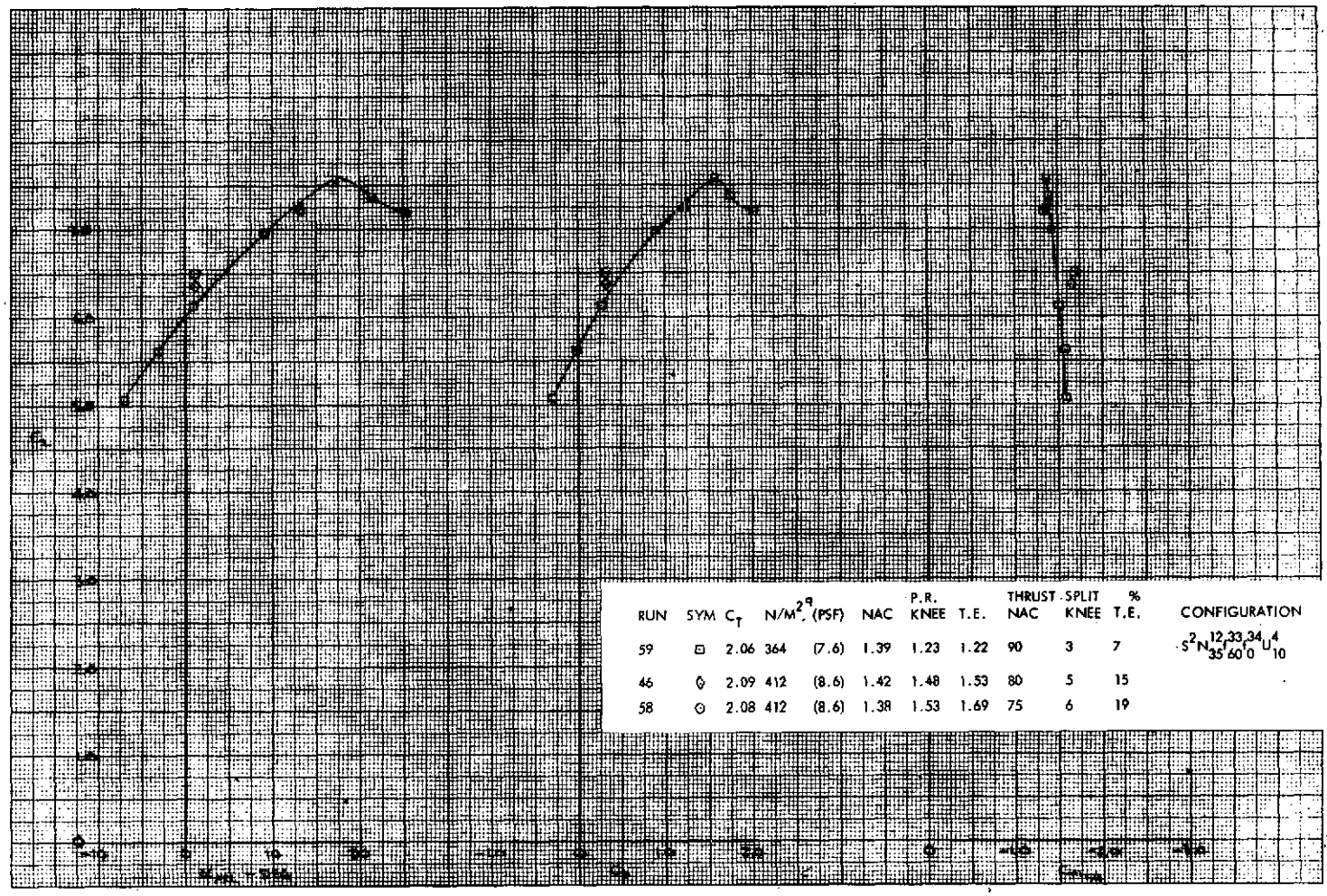

Figure 102. - Longitudinal Characteristics of the High Wing Model, $60^\circ/0^\circ$ J/H Flap, Pressure Ratio Differential Between Nacelle and BLC Systems Effects, 10° Open Deflector, Tail Off

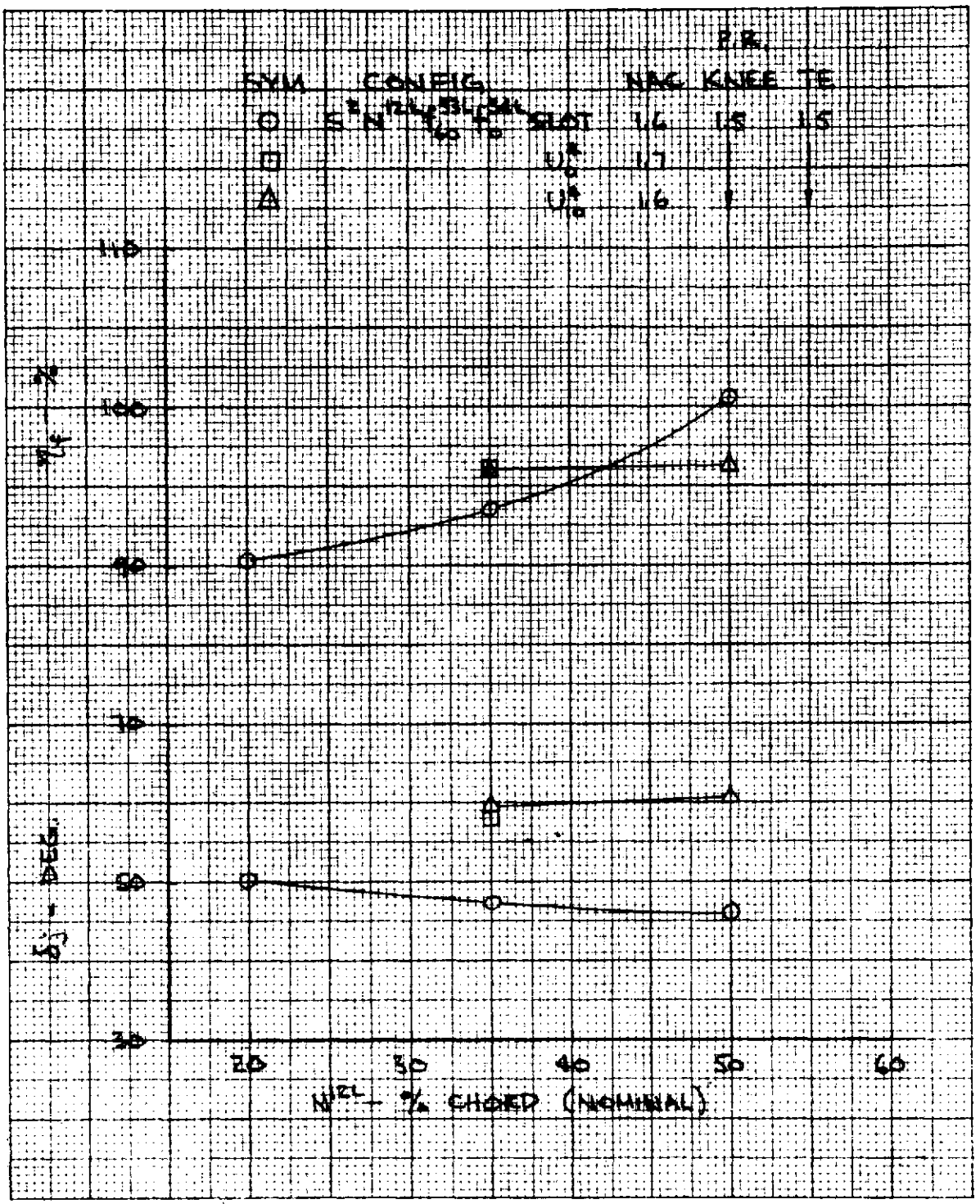

Figure 103. – Static Jet Angle and Turning Efficiency of the Low Wing Model, 60°/0° J/H Flap, Nacelle Exit Configuration and Location Effects

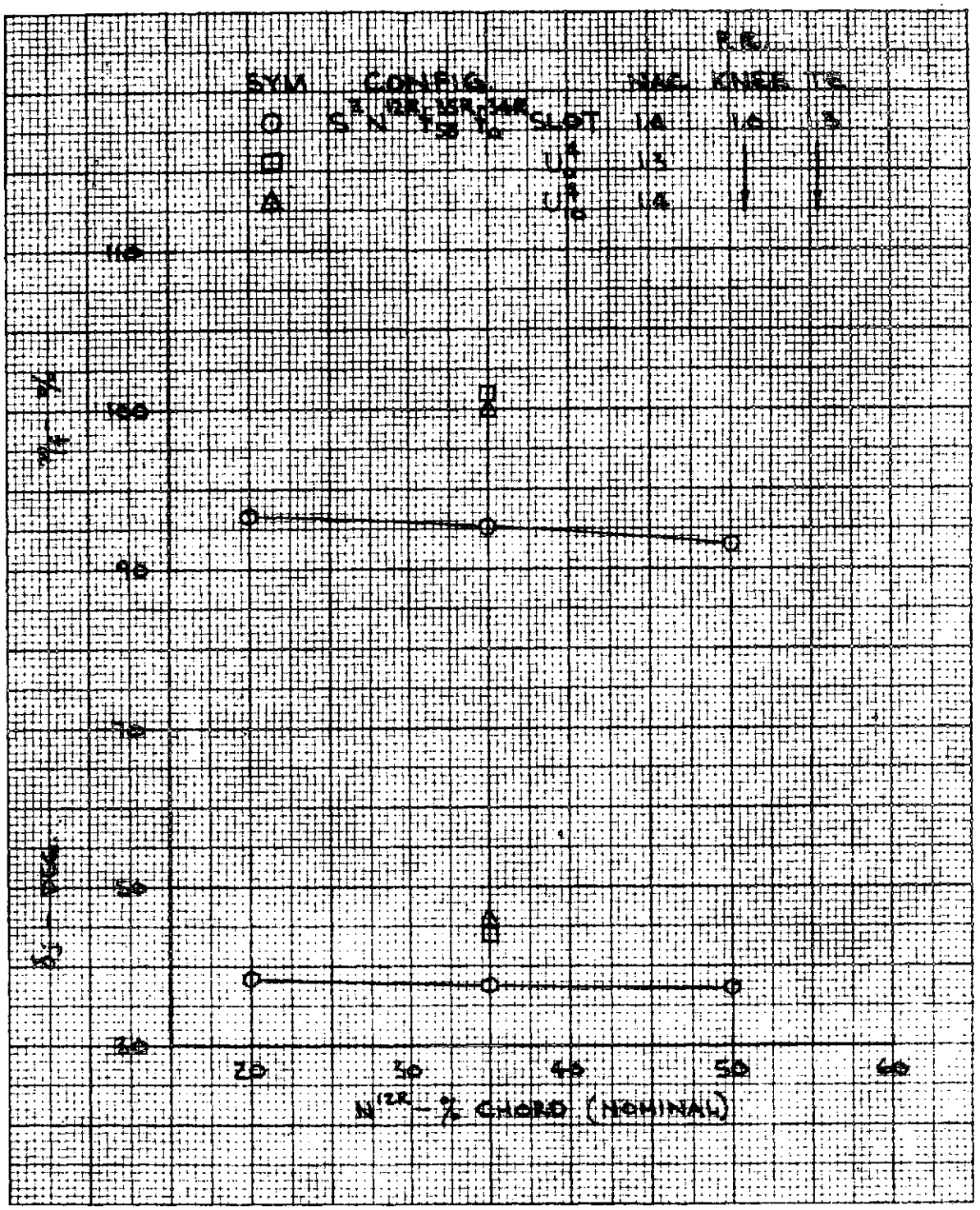

Figure 104. - Static Jet Angle and Turning Efficiency of the Low Wing Model, 58°/0° Coanda Flap, Nacelle Exit Configuration and Location Effects

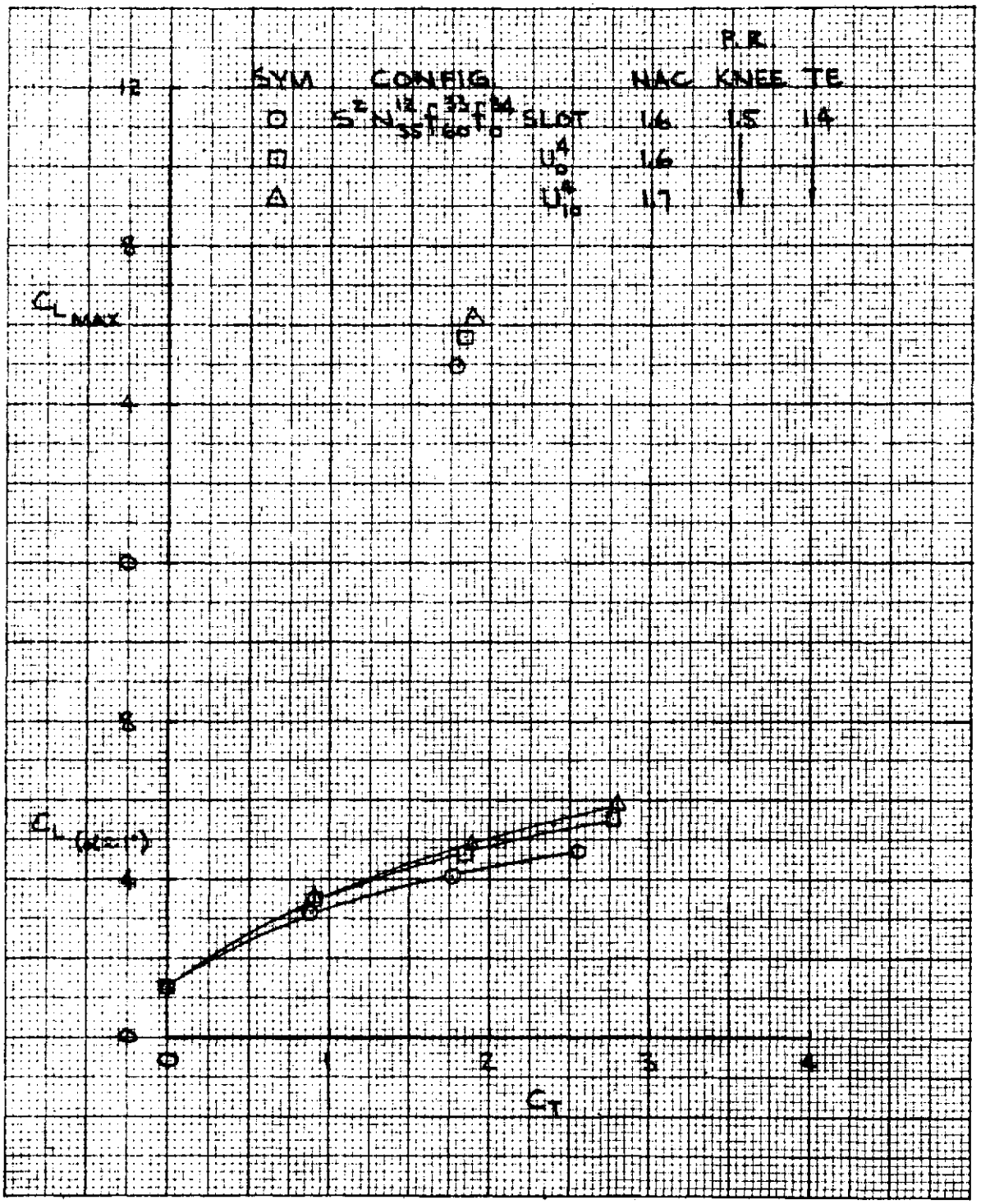

Figure 105. - Lift Variation with C_T and Nacelle Exit Configuration on the Low Wing Model, $60^\circ/0^\circ$ J/H Flap, Tail Off

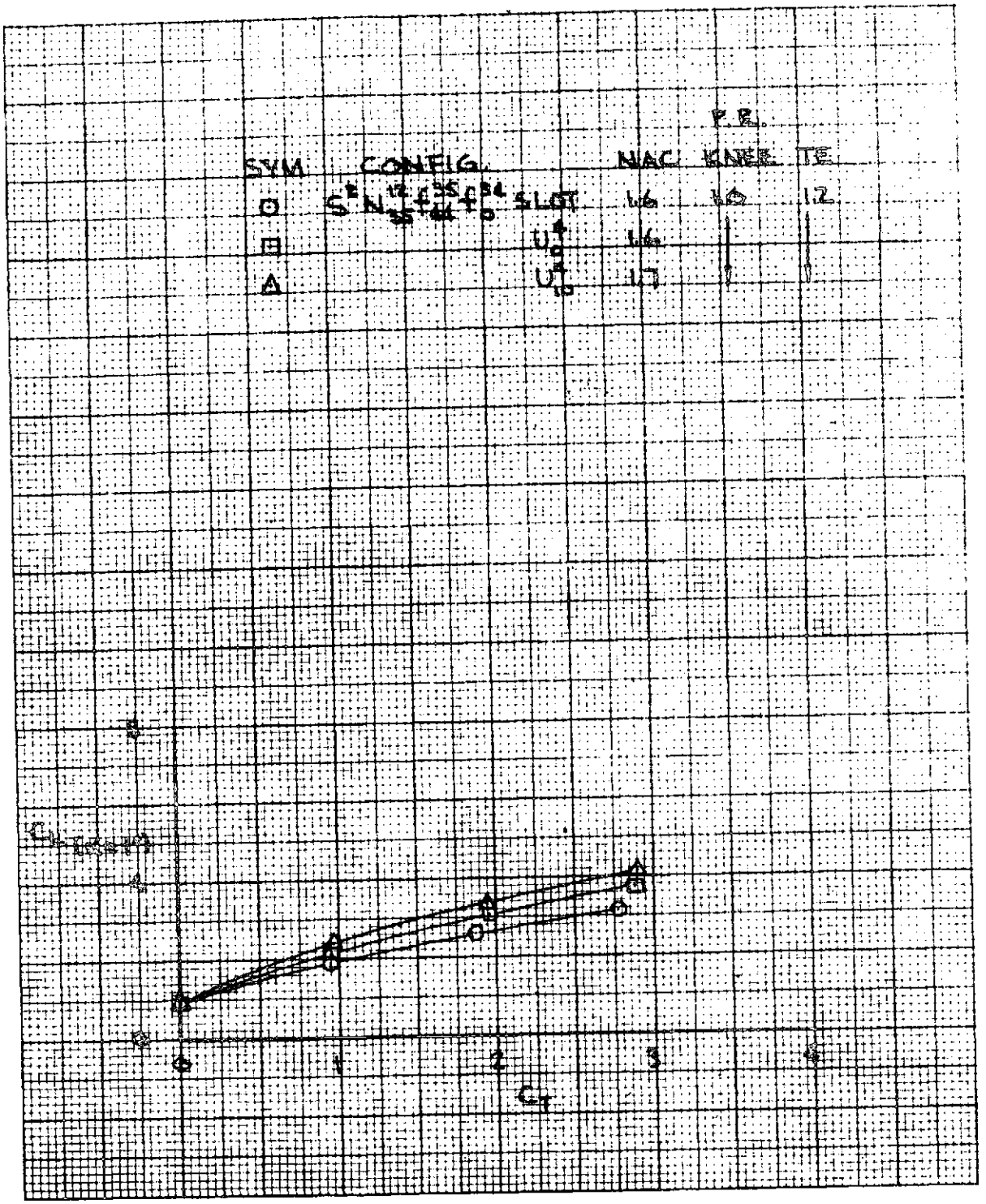

Figure 106. - Lift Variation with C_T and Nacelle Exit Configuration on the Low Wing Model, $44^\circ/0^\circ$ Coanda Flap, Tail Off

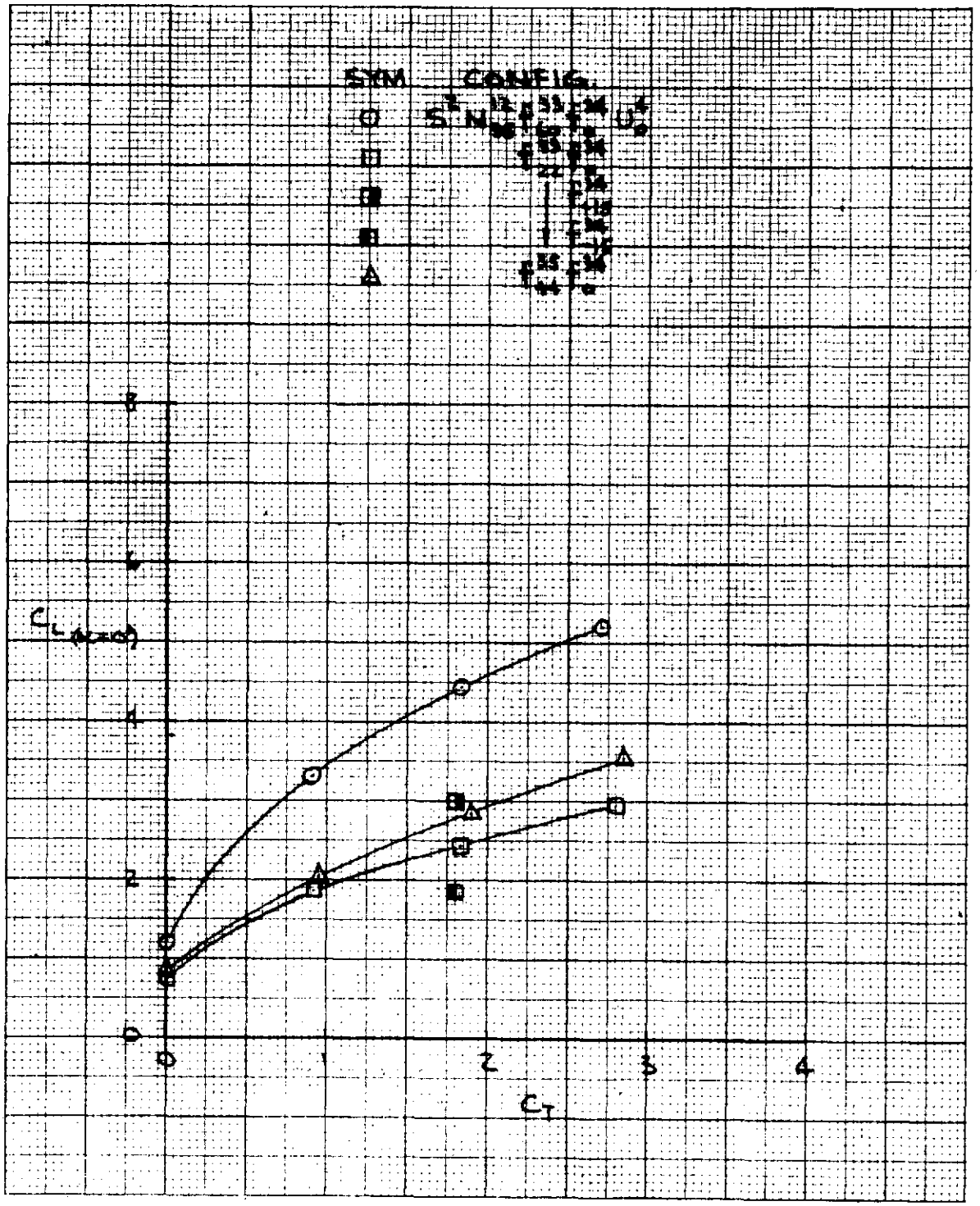

Figure 107. - Lift Variation with C_T and Flap Configuration on the Low Wing Model, 0^o Open Deflector, Tail Off

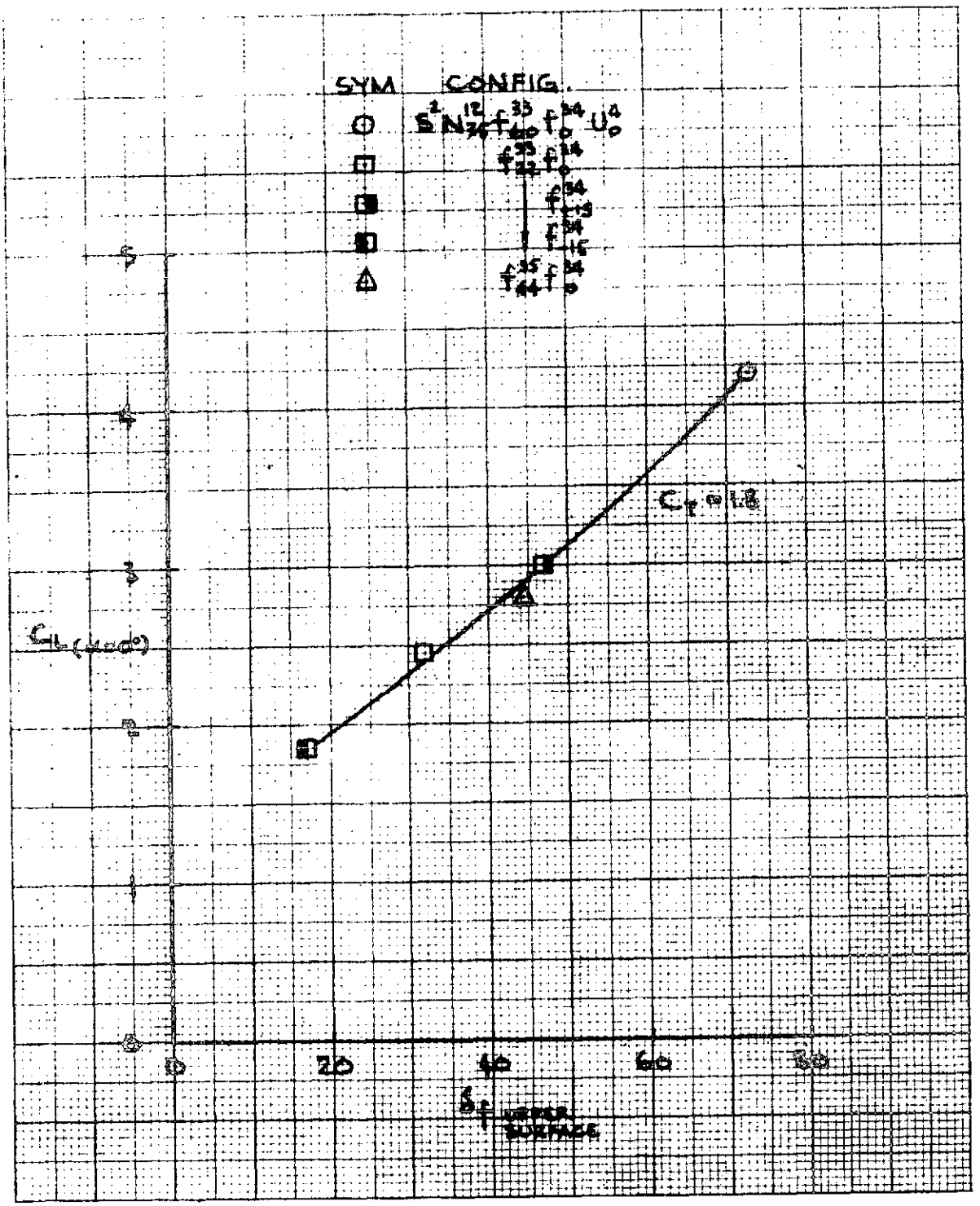

Figure 108. - Lift Variation with Aft Flap Upper Surface Angle on the Low Wing Model, J/H and Coanda Flaps, 0° Open Deflector, Tail Off

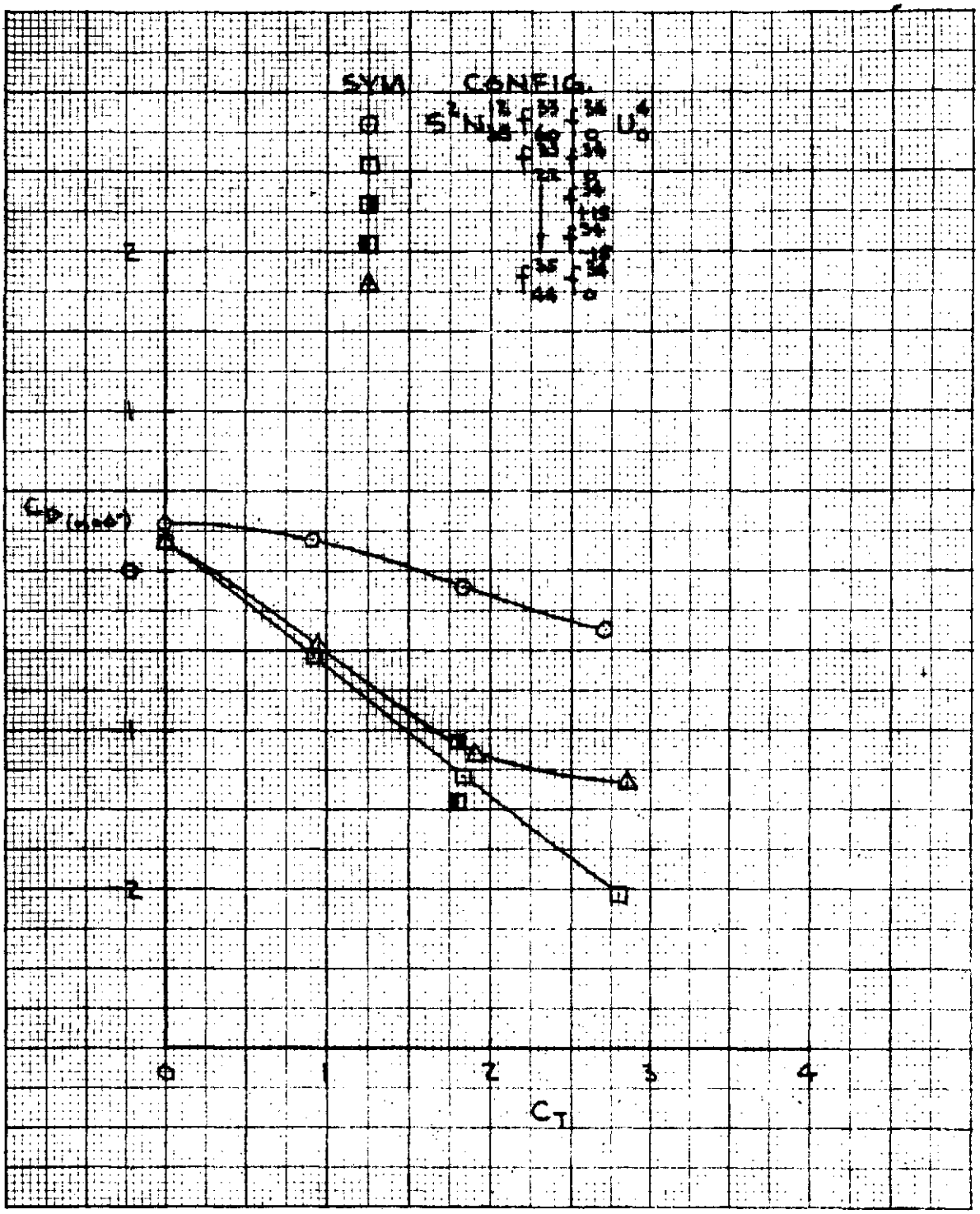

Figure 109. - Drag Variation with C_T and Flap Configuration on the Low Wing Model, 0° Open Deflector, Tail Off

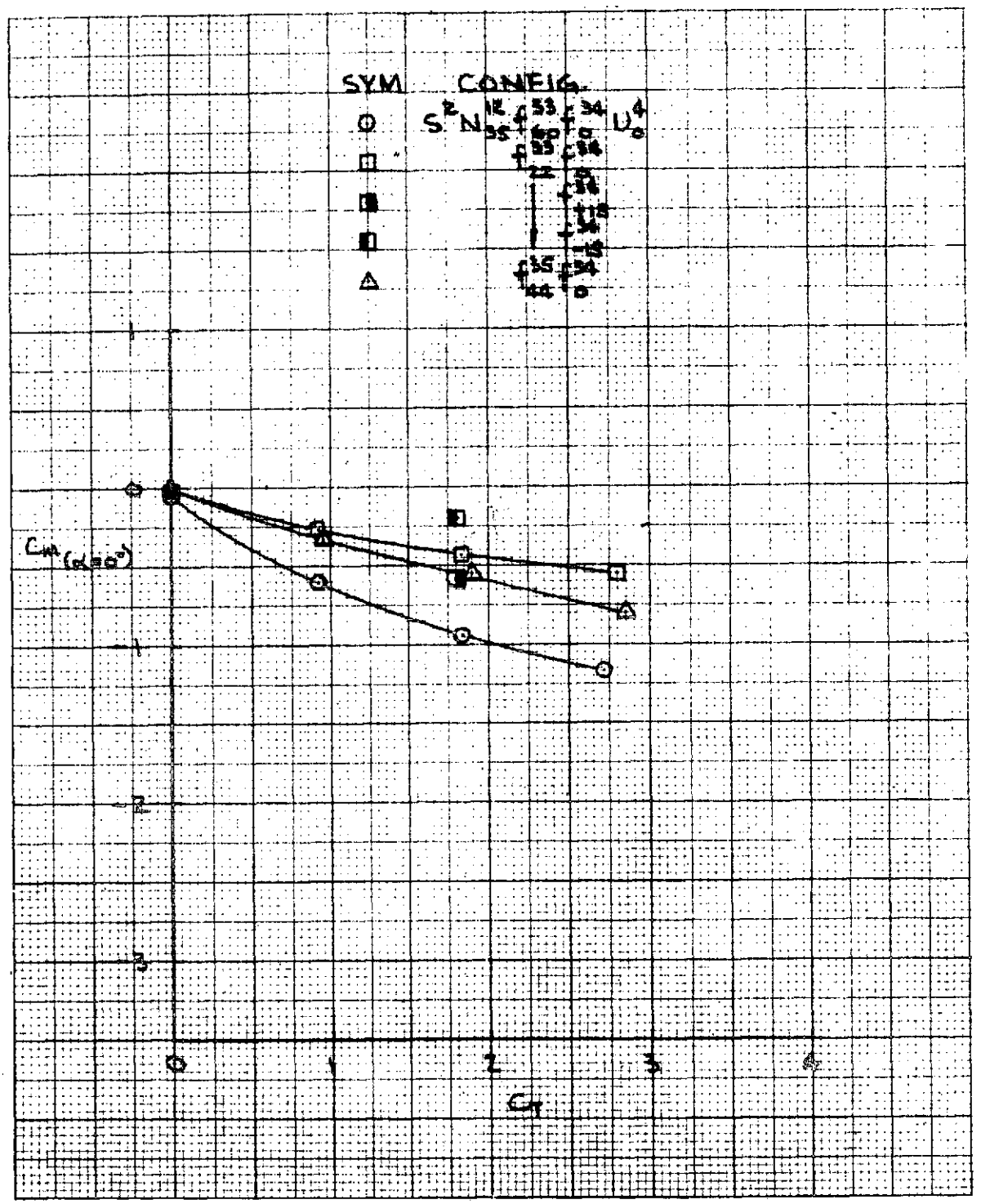

Figure 110. - Pitching Moment Variation with C_T and Flap Configuration on the Low Wing Model, 0° Open Deflector, Tail Off

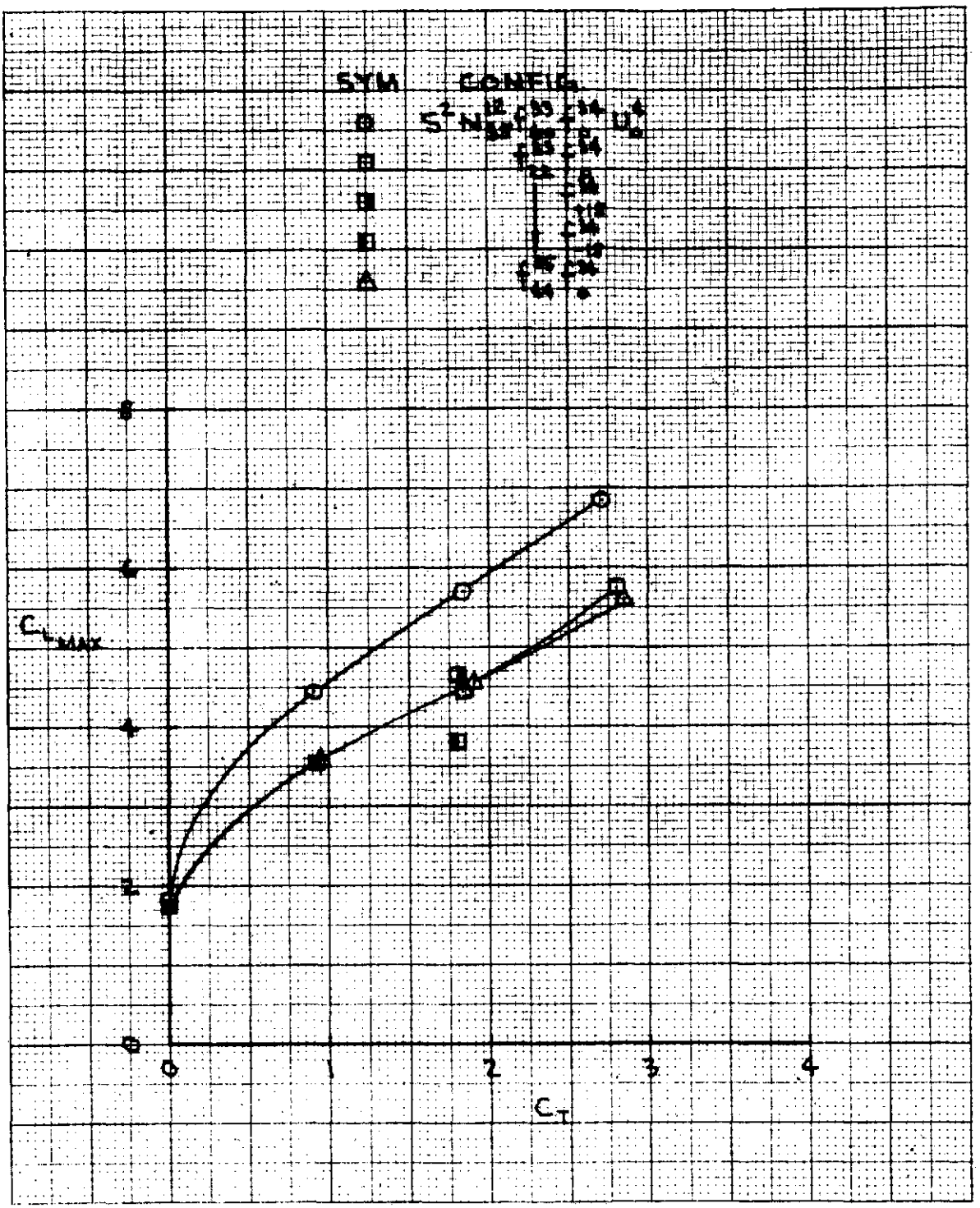

Figure 111. - Maximum Lift Variation with C_T and Flap Configuration on the Low Wing Model, 0^o Open Deflector, Tail Off

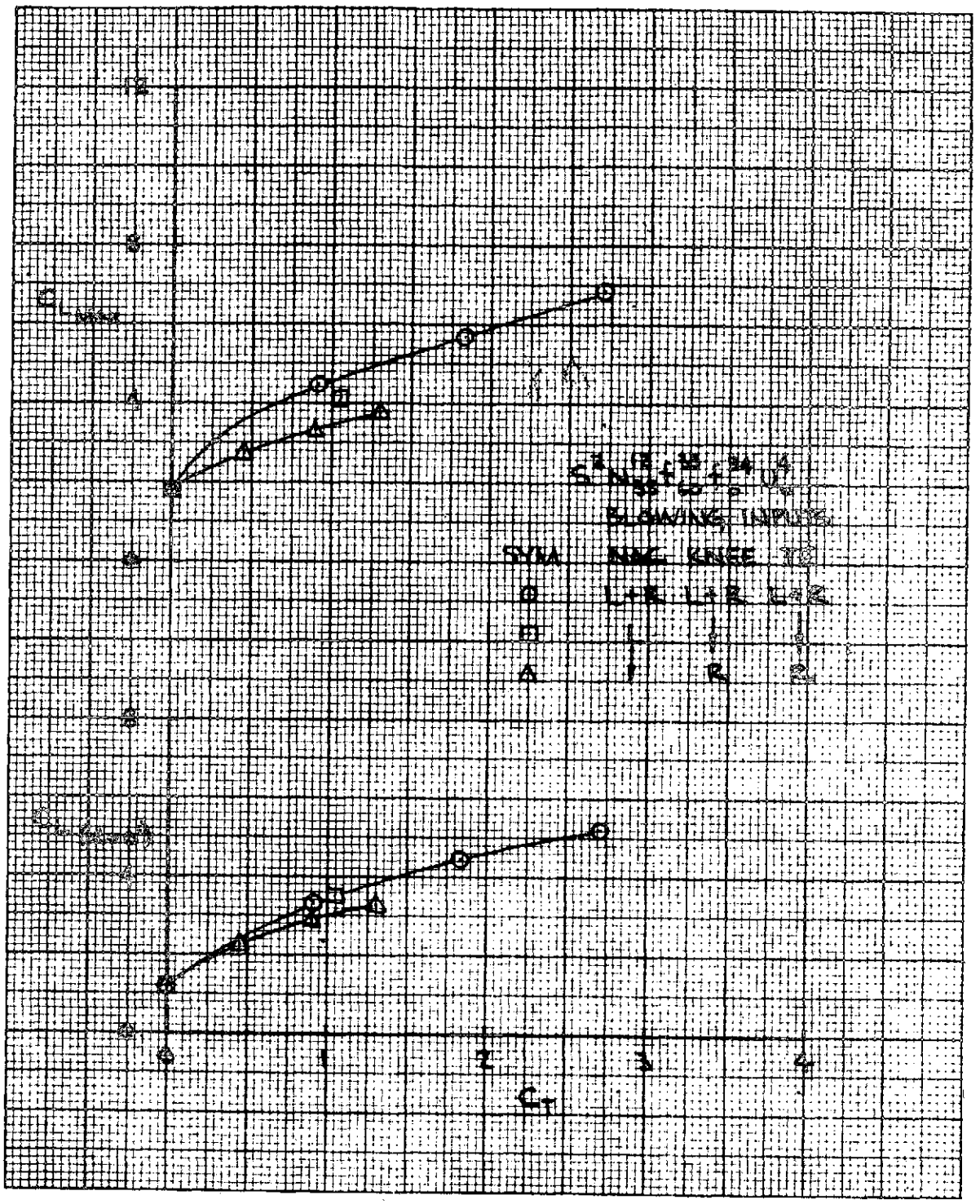

Figure 112. - Lift Variation with C_T and Various Blowing Inputs on the Low Wing Mode, 60°/0° J/H Flap, 0° Open Deflector, Tail Off

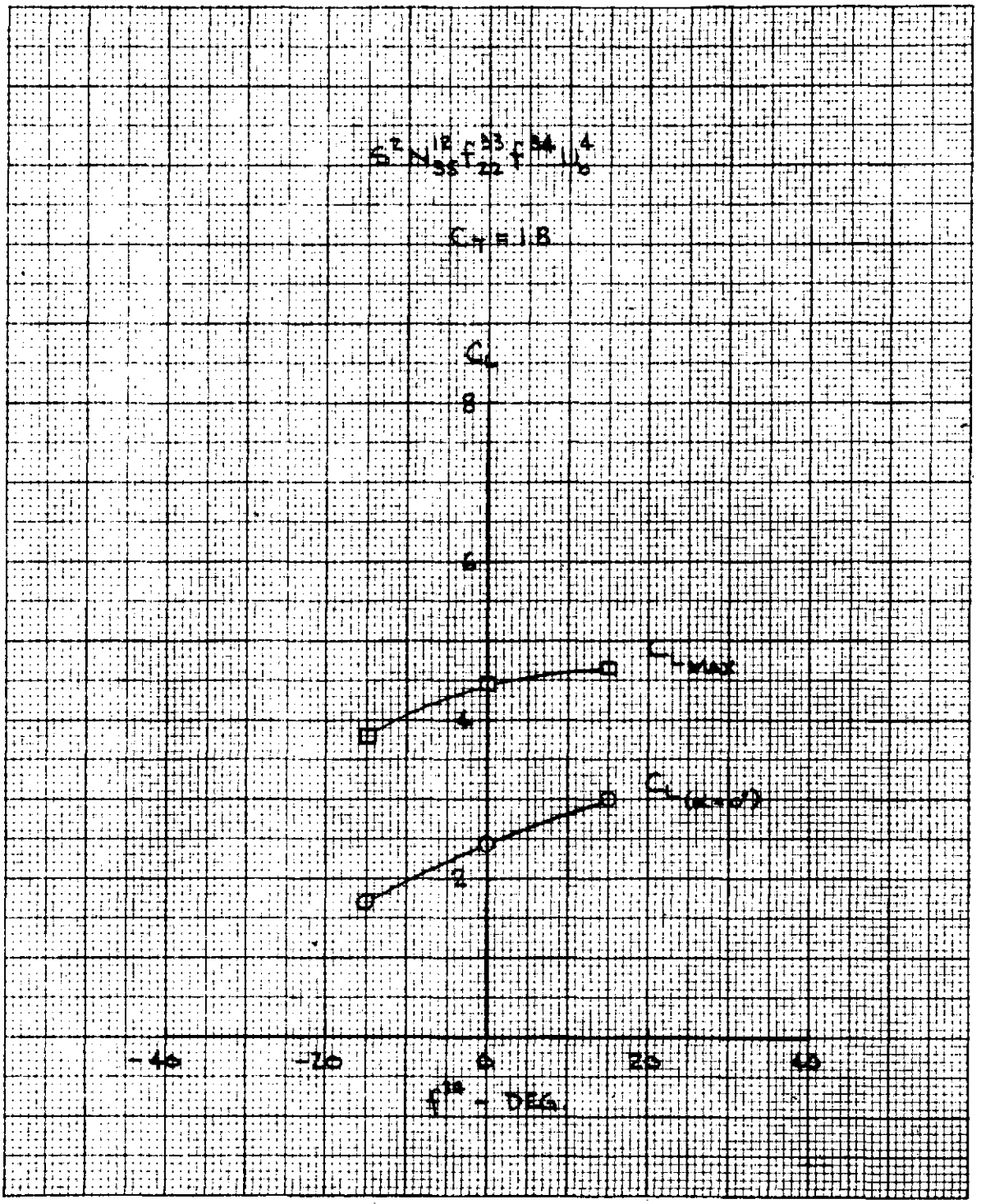

Figure 113. - Aft Flap Effectiveness on the Low Wing Model, 22° J/H Flap, 0° Open Deflector, Tail Off

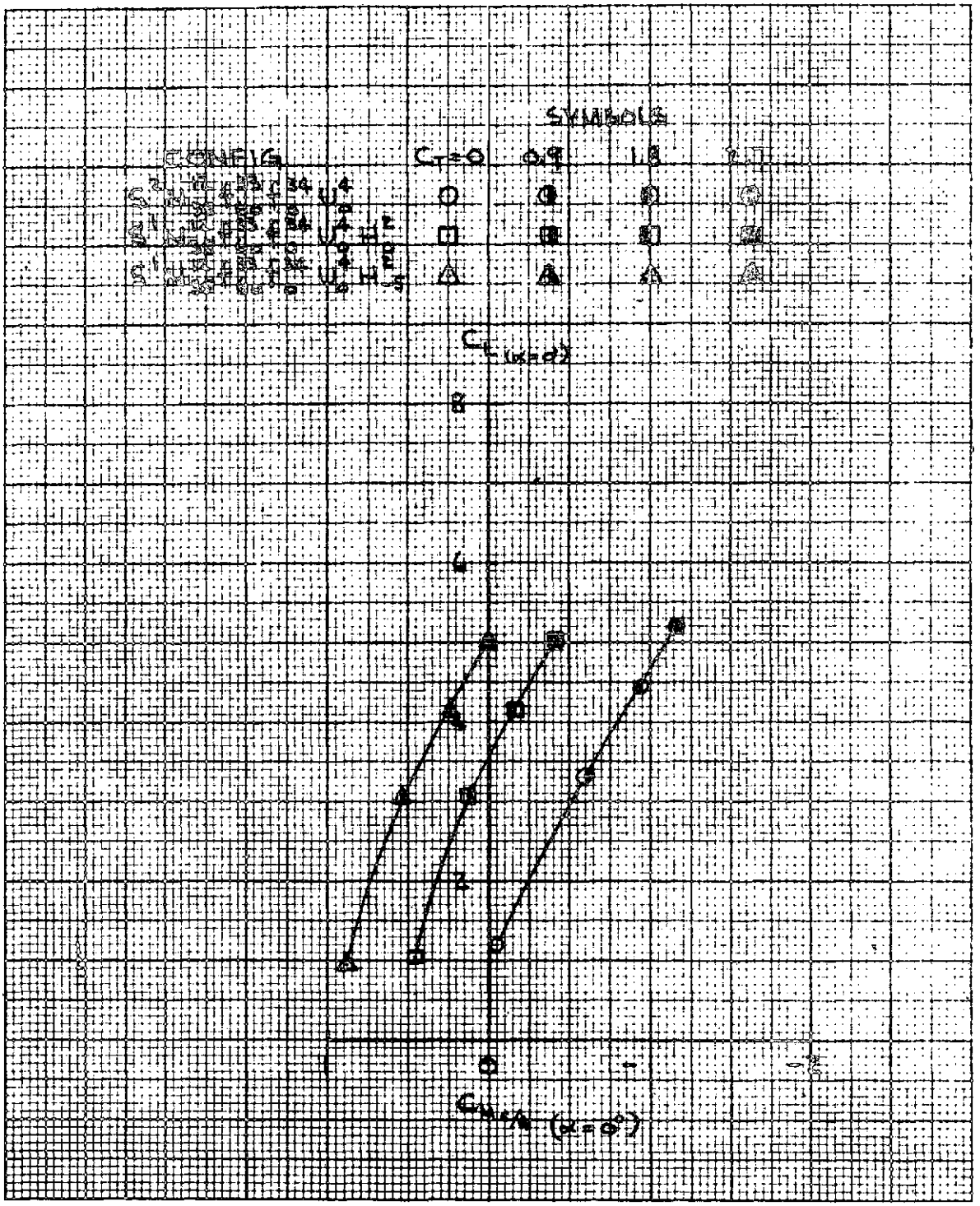

Figure 114. - Horizontal Tail Effectiveness on the Low Wing Model, 60°/0° J/H Flap, 0° Open Deflector

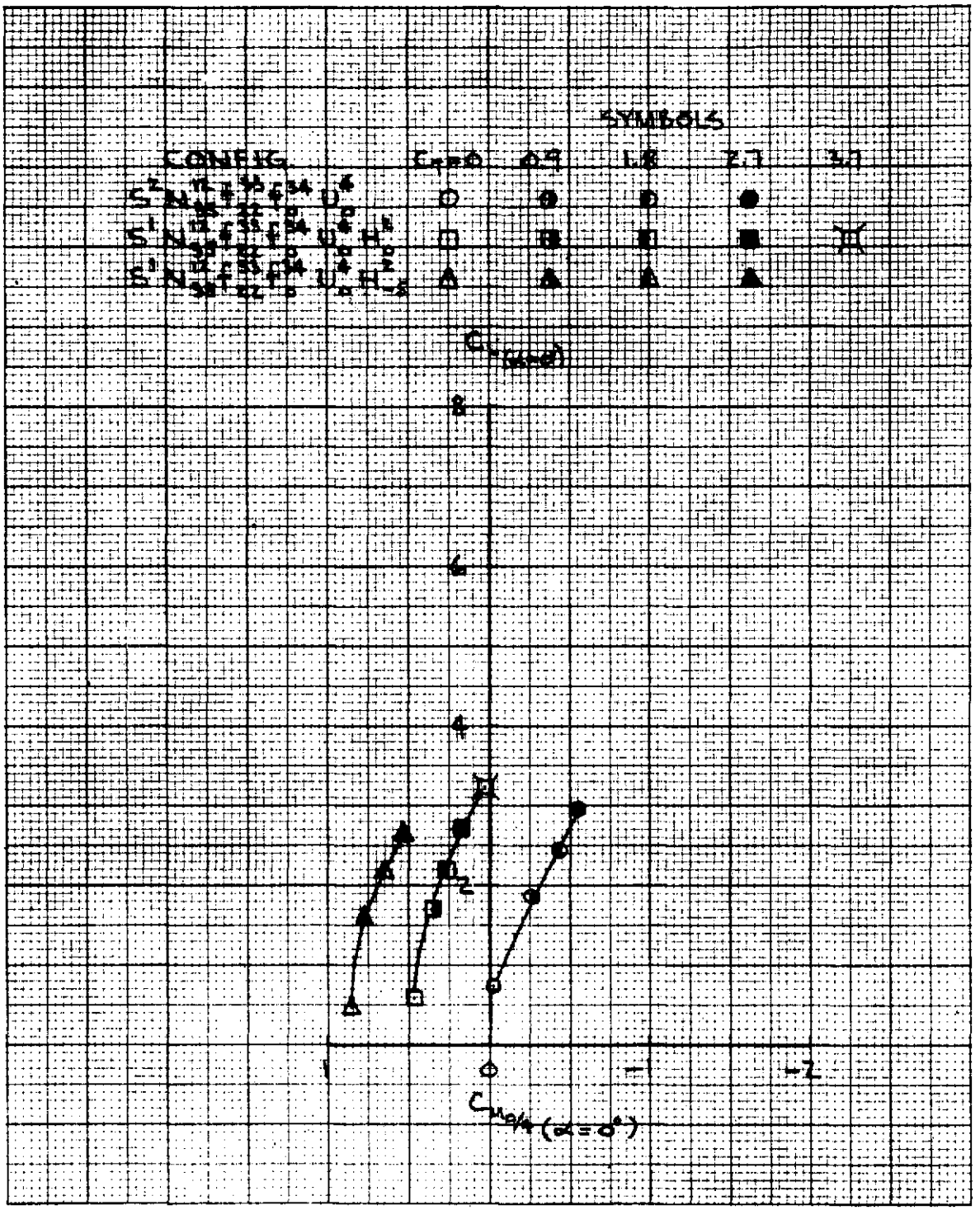

Figure 115. - Horizontal Tail Effectiveness on the Low Wing Model, 22°/0° J/H Flap, 0° Open Deflector

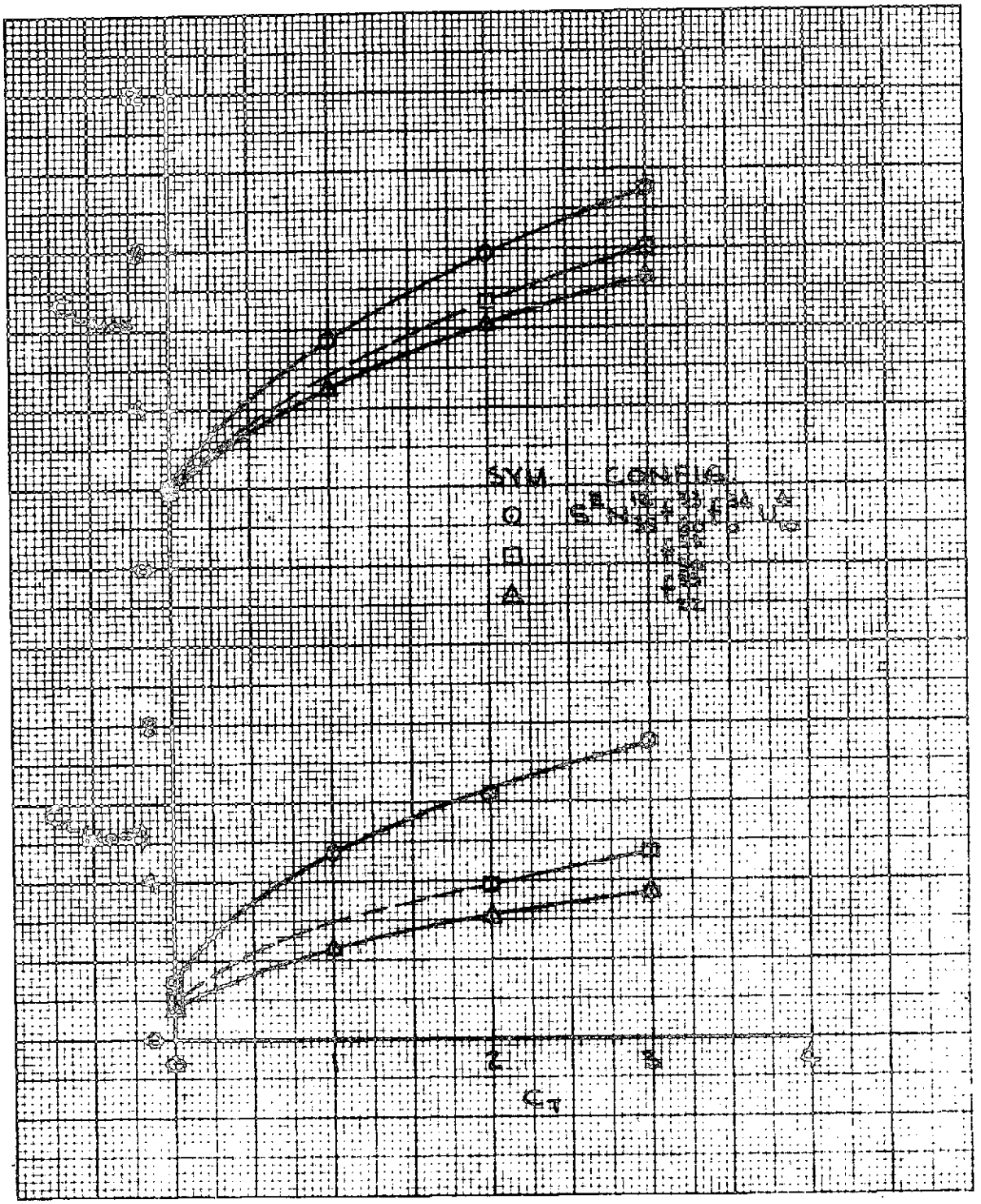

Figure 116. – Lift Variation with C_T and Flap Deflection on the High Wing Model, J/H Flap at 60°/0°, 30°/0°, and 22°/0°, 10° Open Deflector, Tail Off

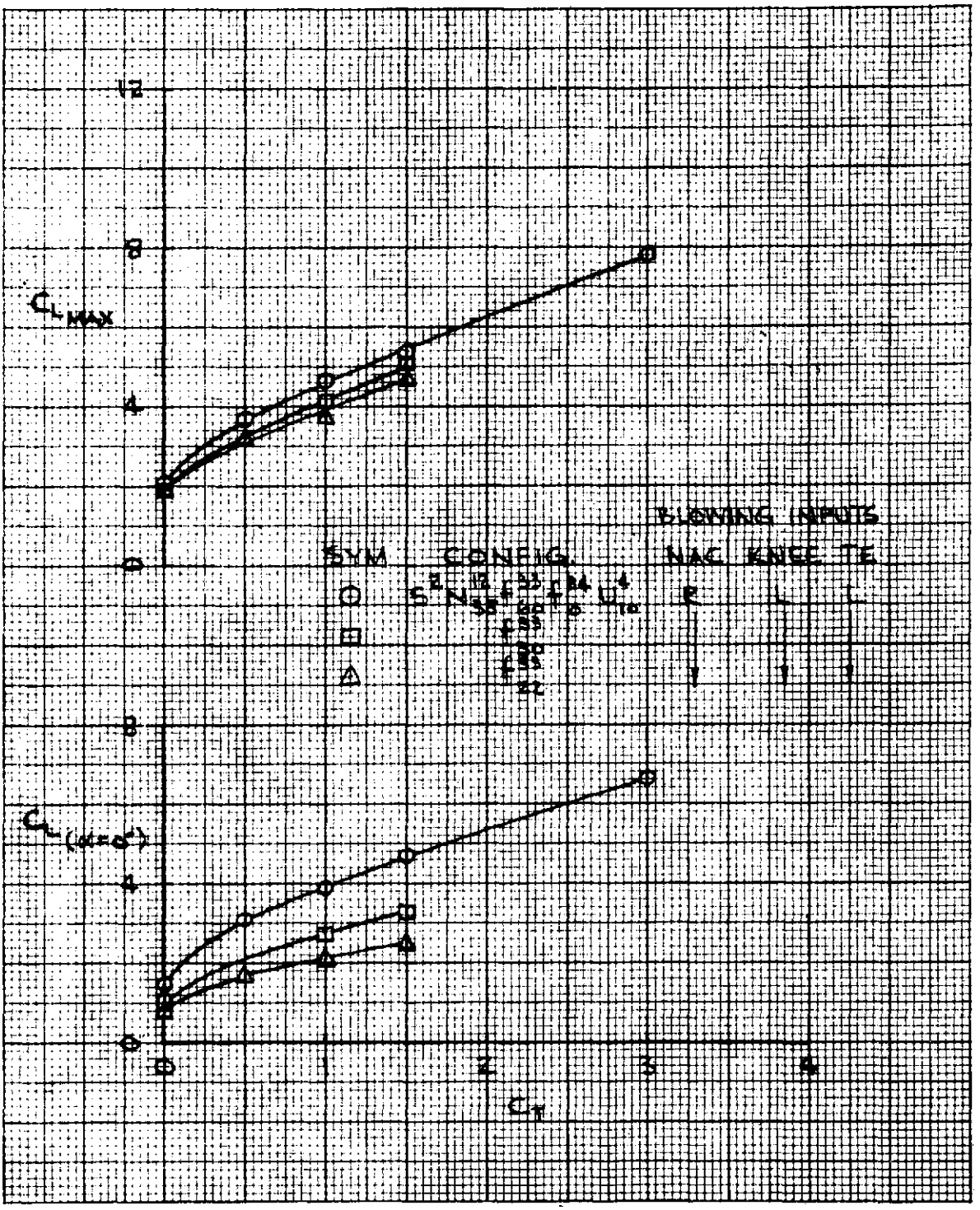

Figure 117. - Lift Variation on the High Wing Model with the Left Engine and the Right BLC Systems Inoperative, J/H Flap at $60^\circ/0^\circ$, $30^\circ/0^\circ$, and $22^\circ/0^\circ$, 10° Open Deflector, Tail Off

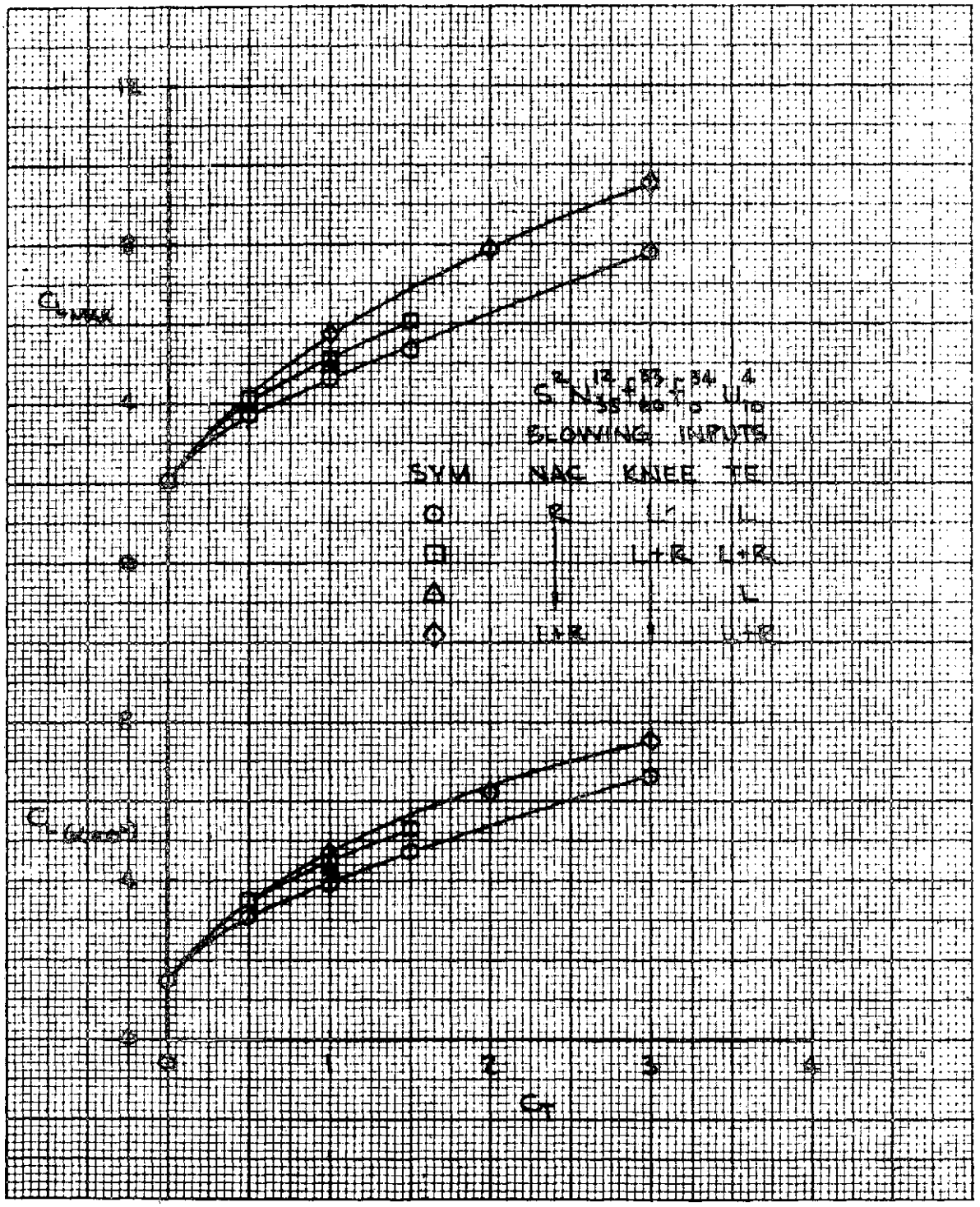

Figure 118. - Lift Variation with C_T and Selected Blowing Inputs on the High Wing Model, 60°/0° J/H Flap, 10° Open Deflector, Tail Off

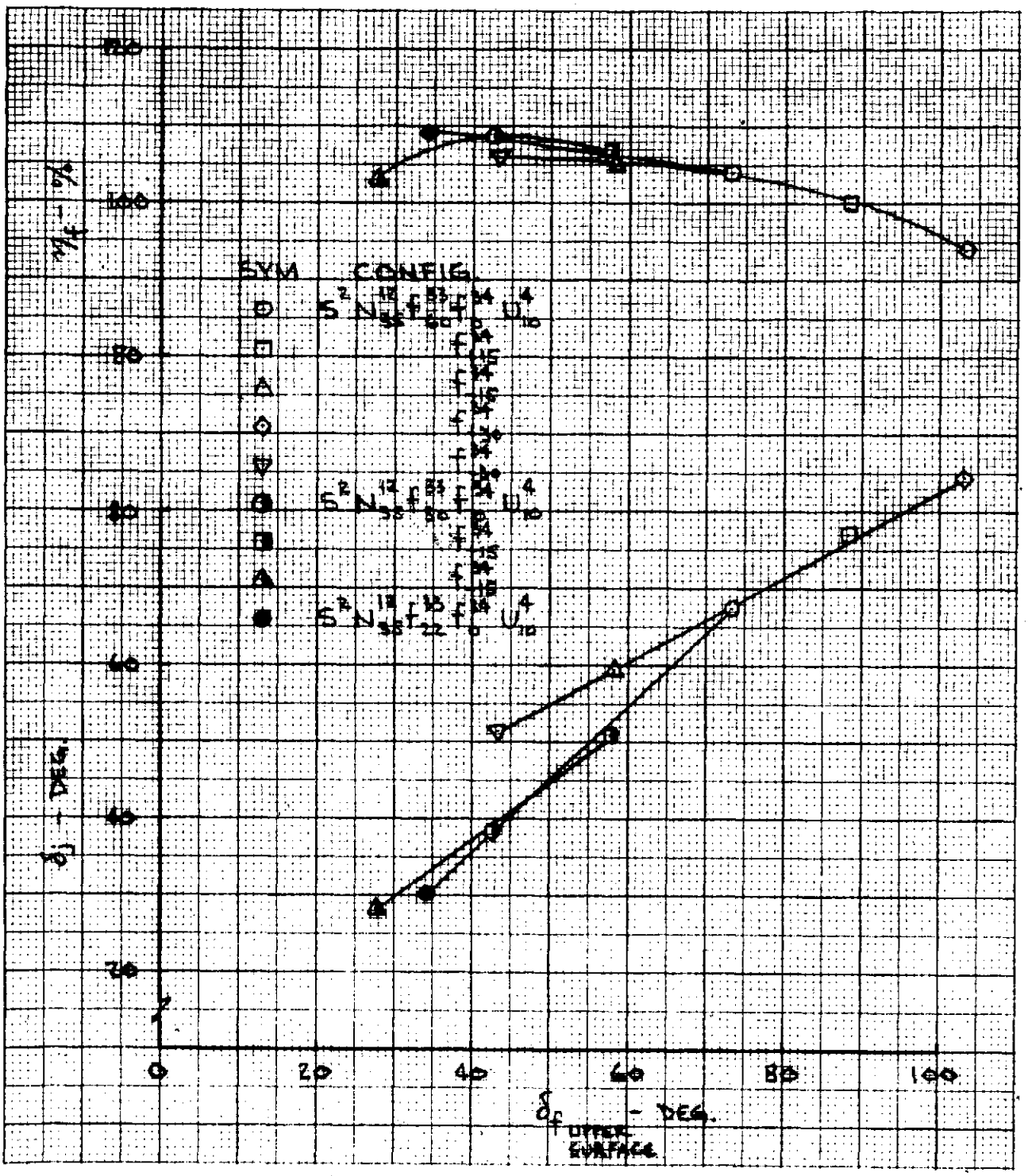

Figure 119. - Static Jet Angle and Turning Efficiency of the High Wing Model, Various J/H Flap Deflections, 10° Open Deflector

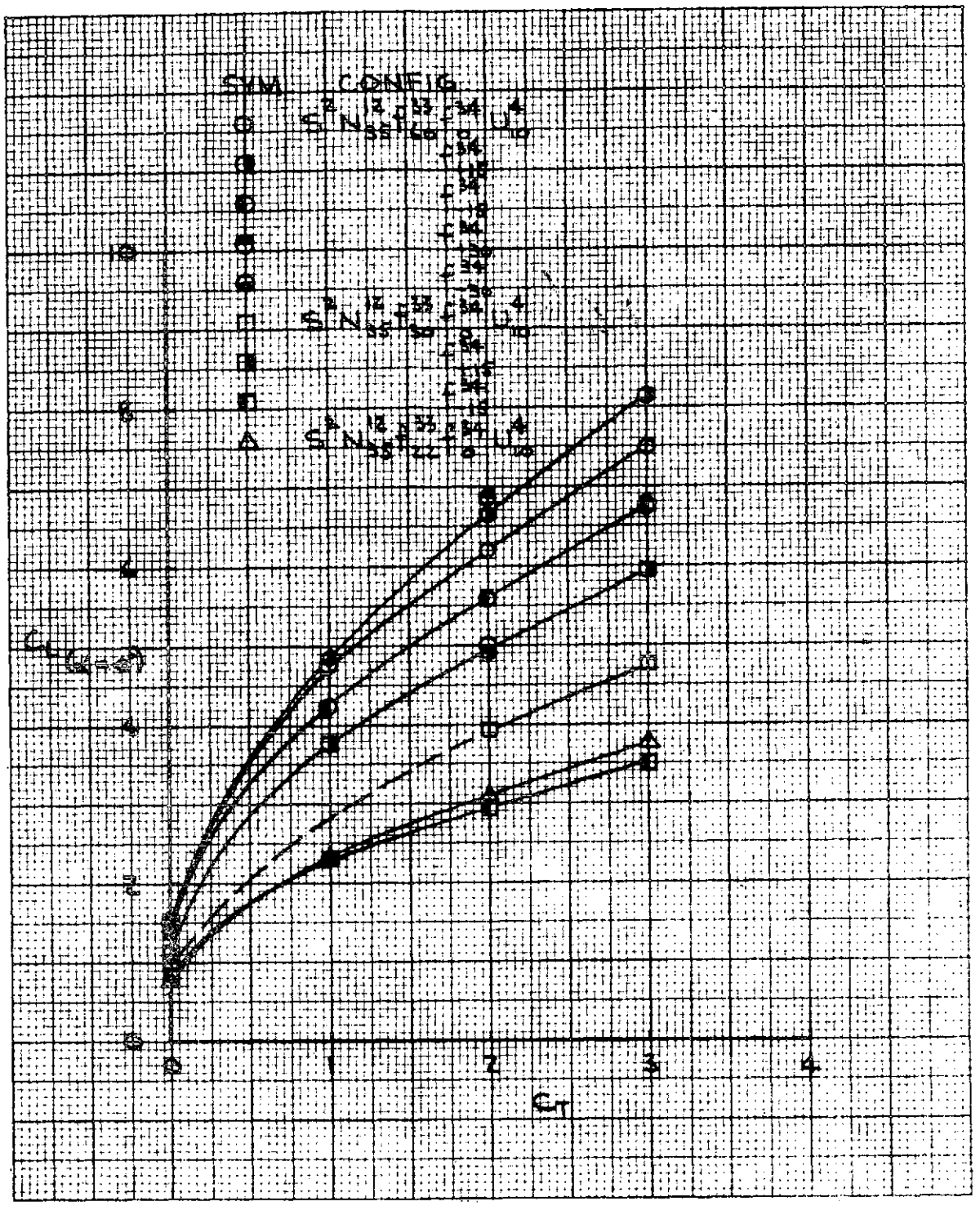

Figure 120. - Lift Variation with C_T and J/H Flap Deflection on the High Wing Model, 10° Open Deflector, Tail Off

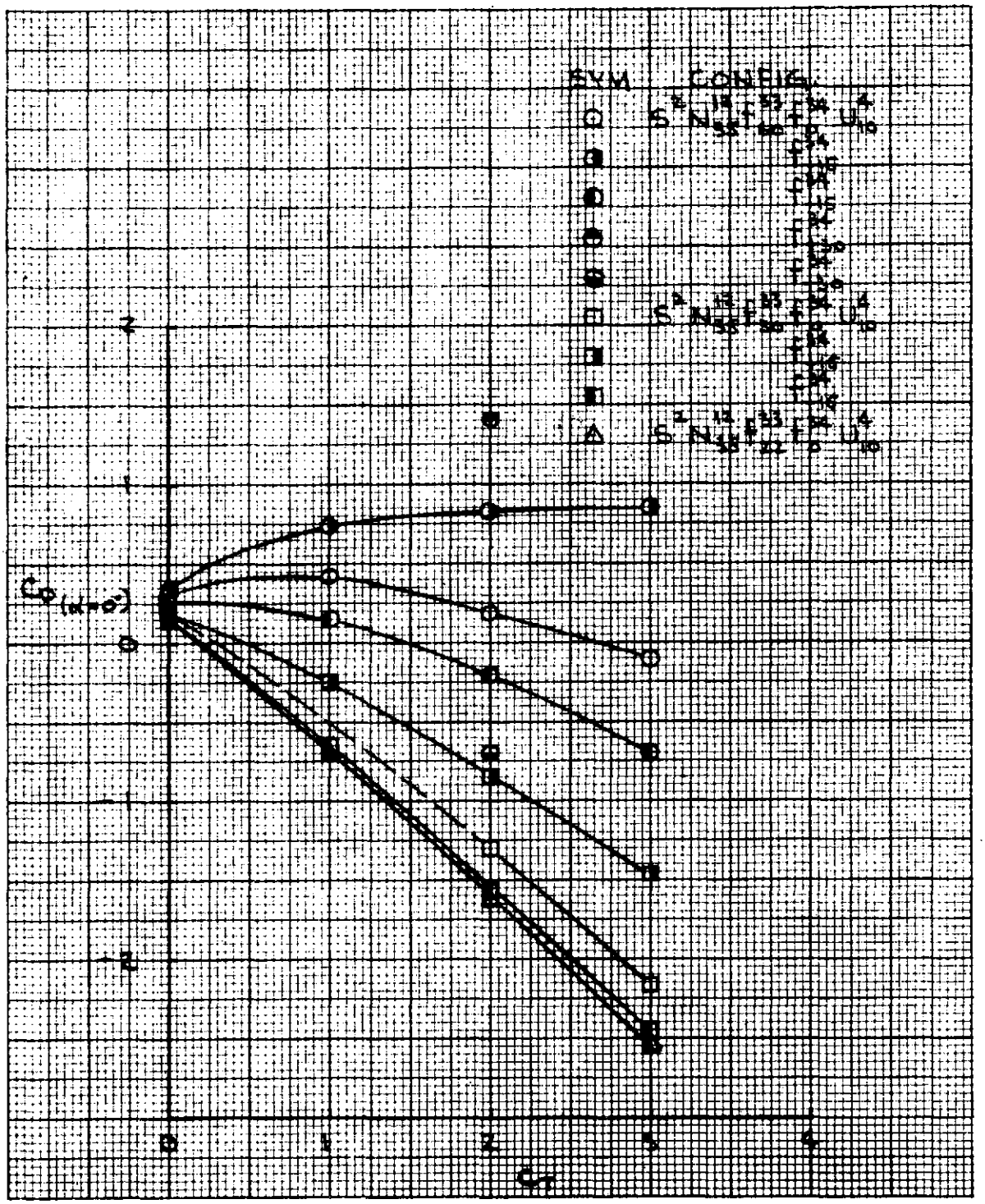

Figure 121. - Drag Variation with C_T and J/H Flap Deflection on the High Wing Model, 10° Open Deflector, Tail Off

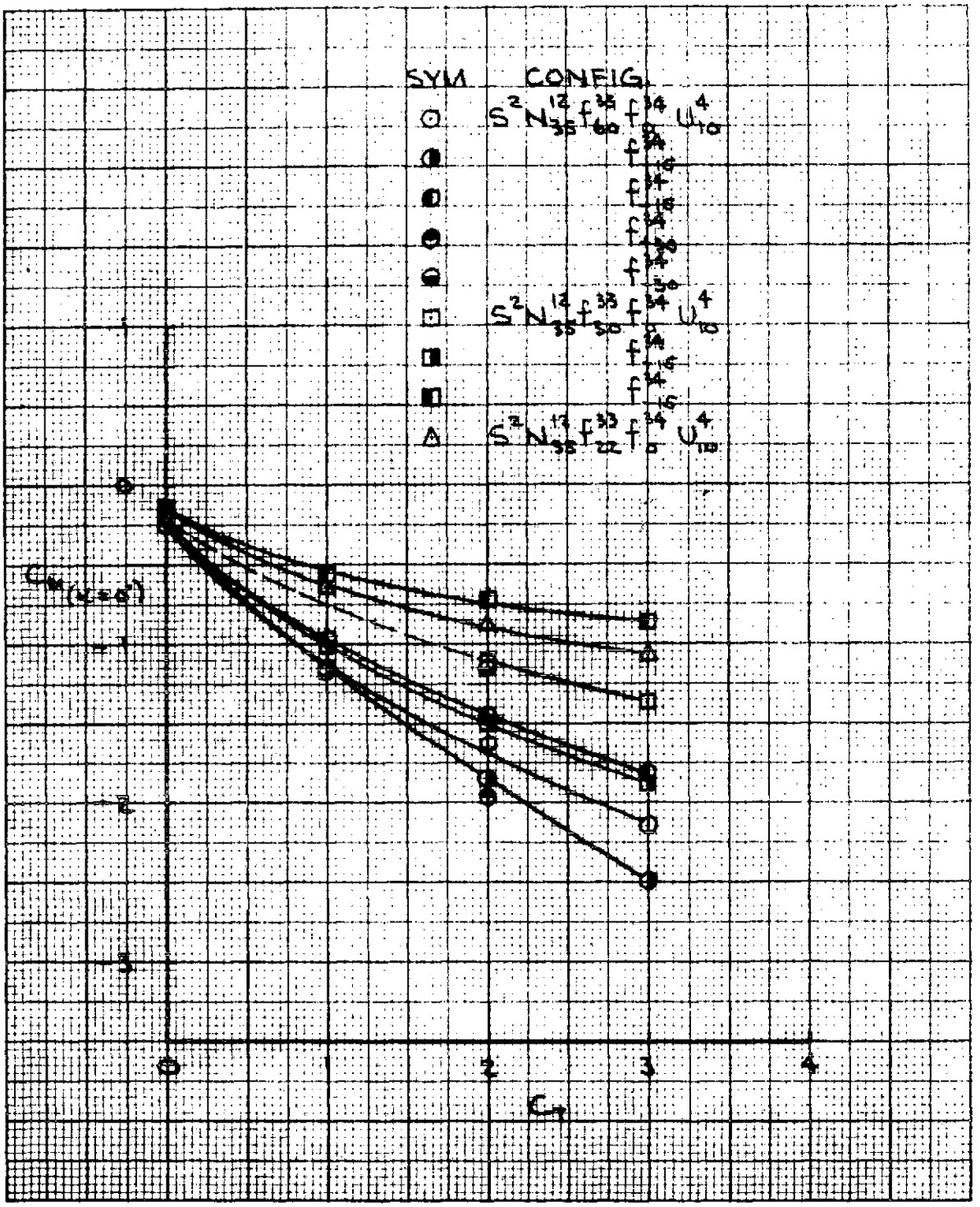

Figure 122. - Pitching Moment Variation with C_T and J/H Flap Deflection on the High Wing Model, 10° Open Deflector, Tail Off

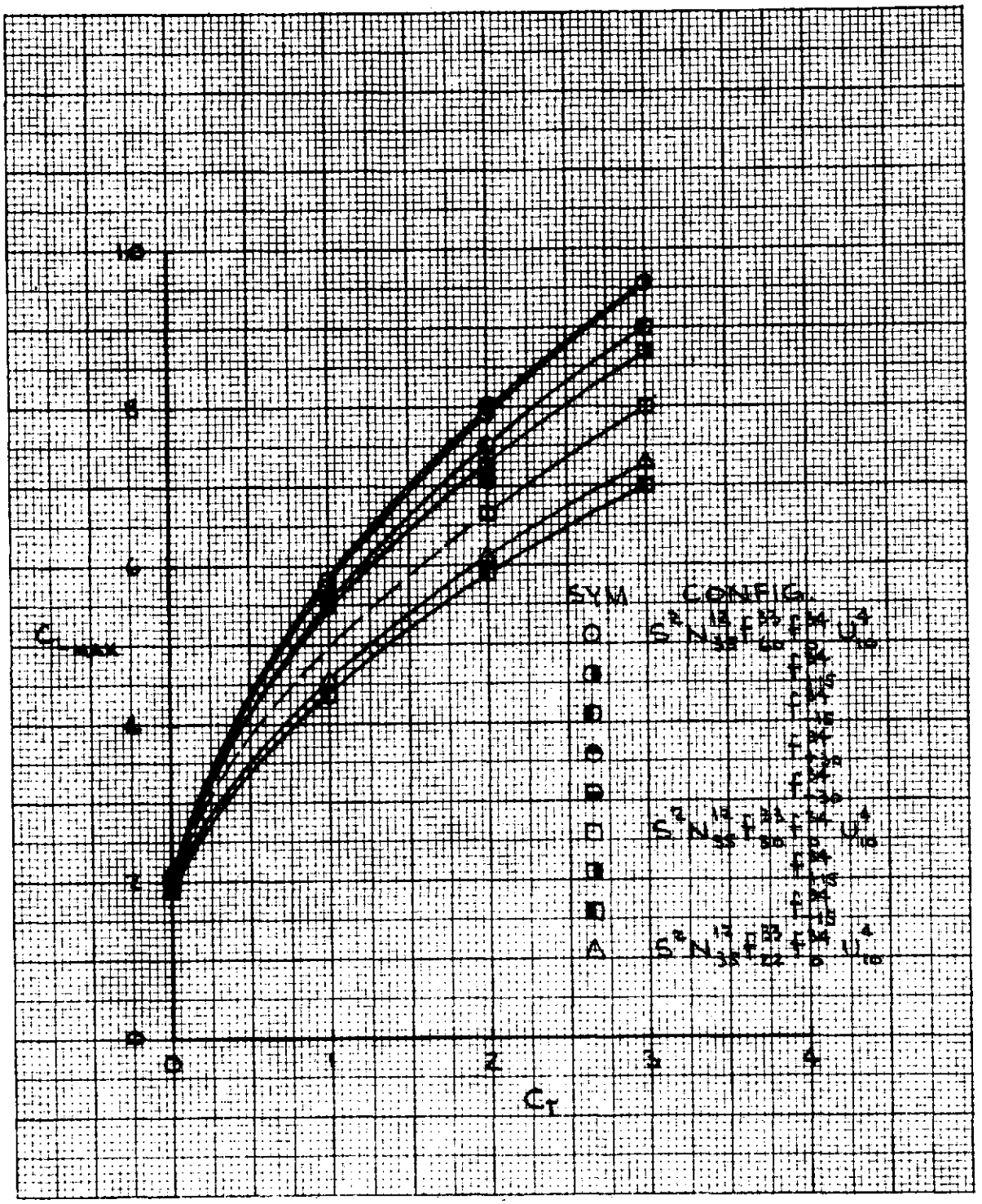

Figure 123. - Maximum Lift Variation with C_T and J/H Flap Deflection on the High Wing Model, 10^0 Open Deflector, Tail Off

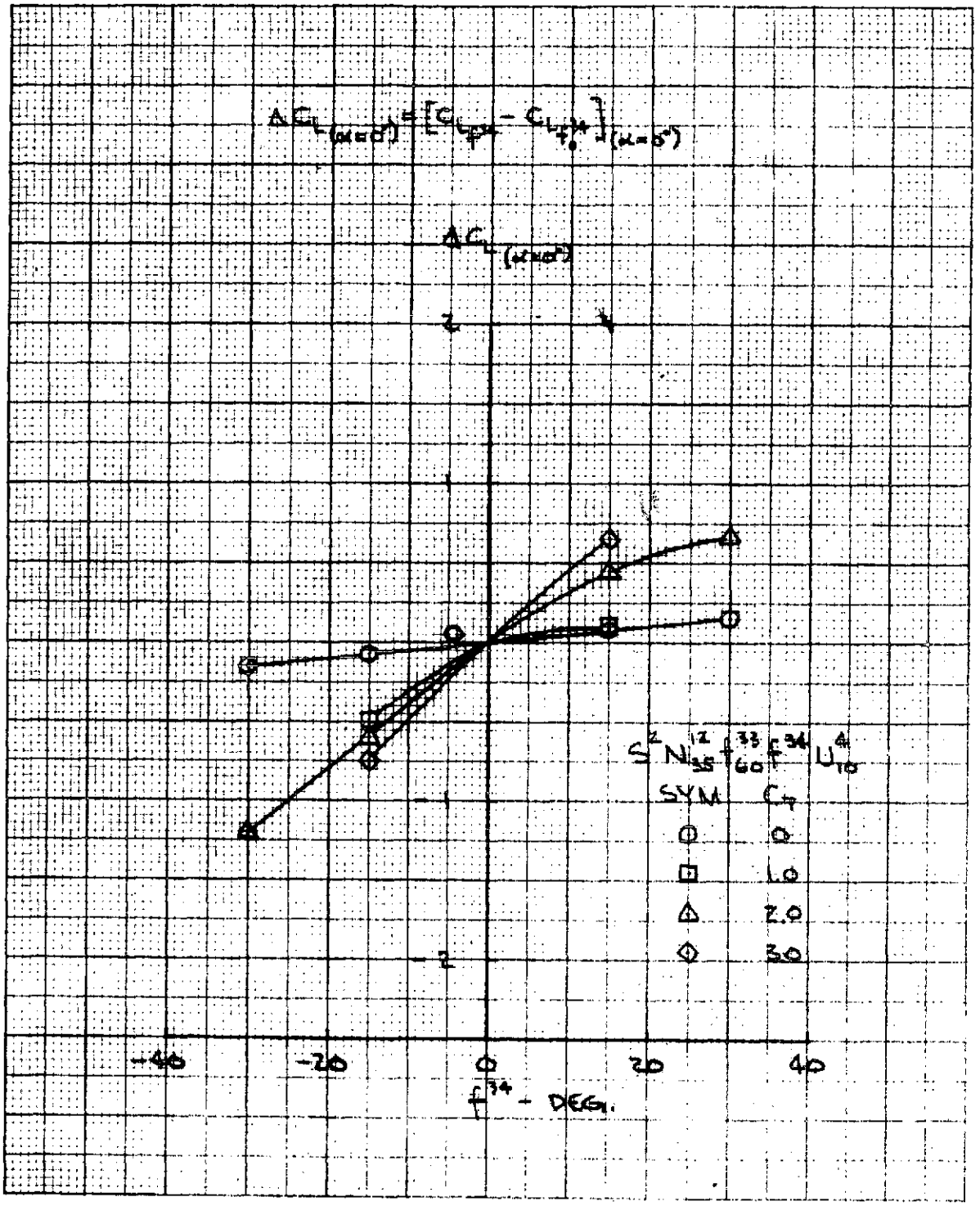

Figure 124. - Lift Change with Aft Flap Deflection on the High Wing Model, 60° J/H Flap, 10° Open Deflector, Tail Off

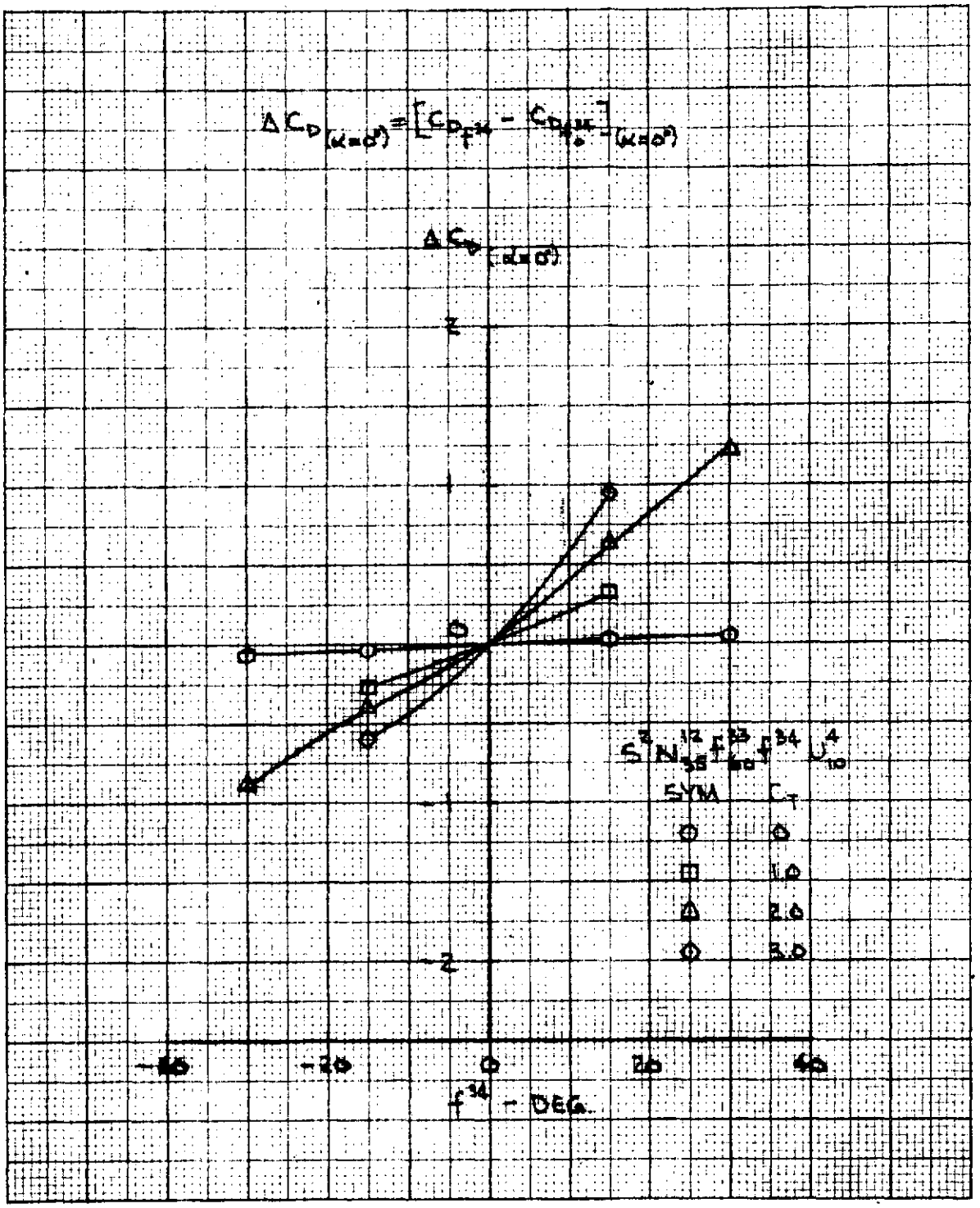

Figure 125. - Drag Change with Aft Flap Deflection on the High Wing Model, 60° J/H Flap, 10° Open Deflector, Tail Off

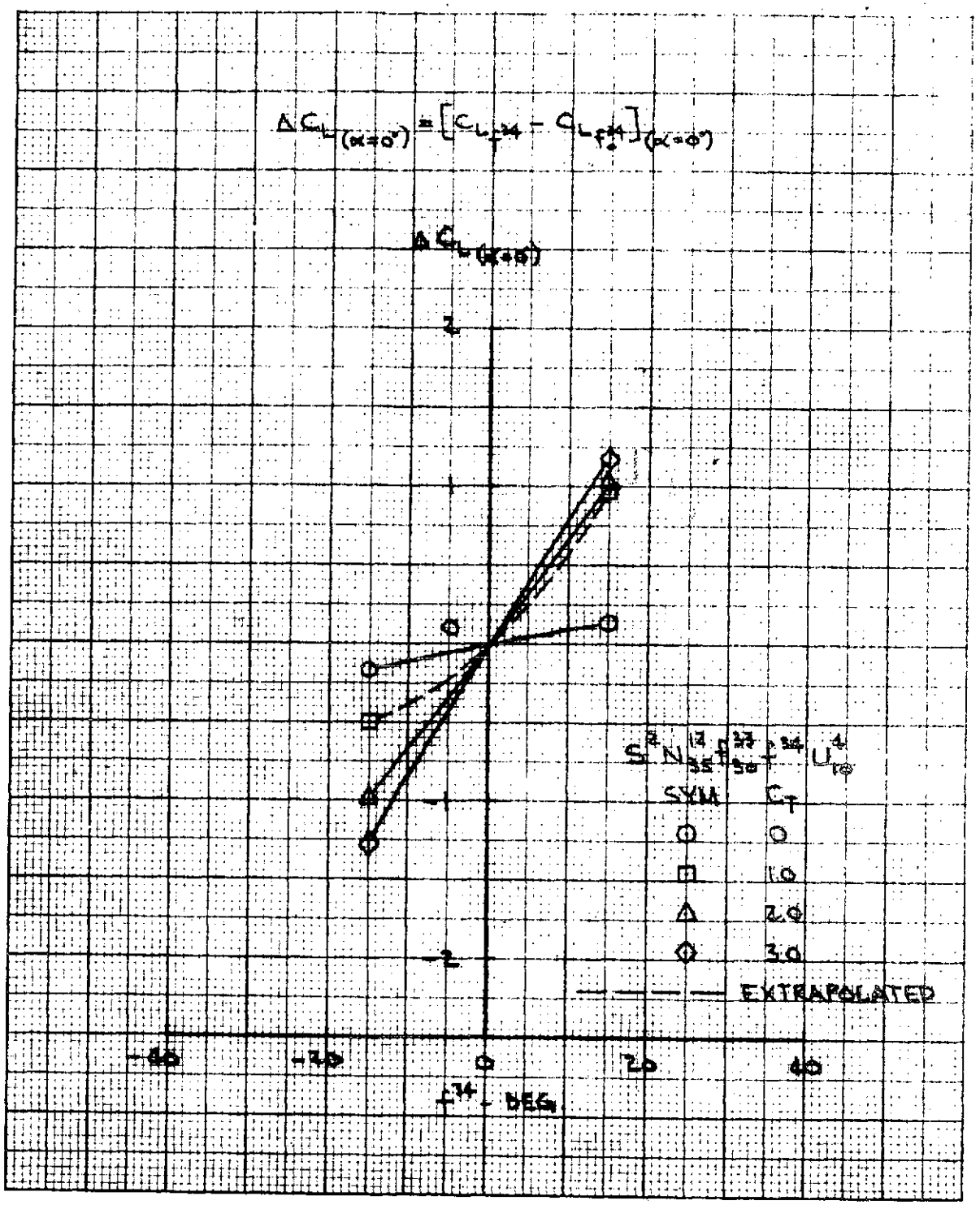

Figure 126. - Lift Change with Aft Flap Deflection on the High Wing Model, 30° J/H Flap, 10° Open Deflector, Tail Off

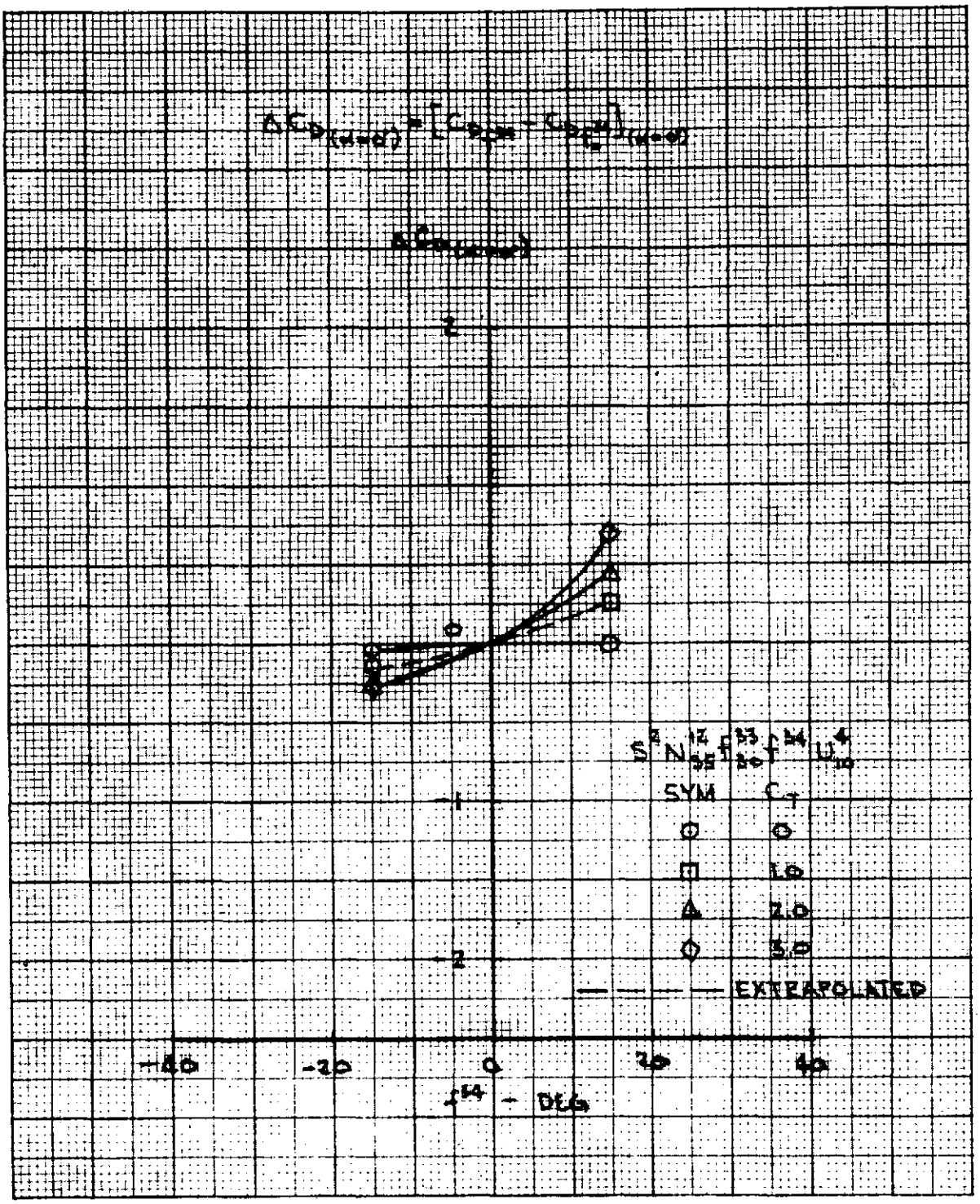

Figure 127. - Drag Change with Aft Flap Deflection on the High Wing Model, 30° J/H Flap, 10° Open Deflector, Tail Off

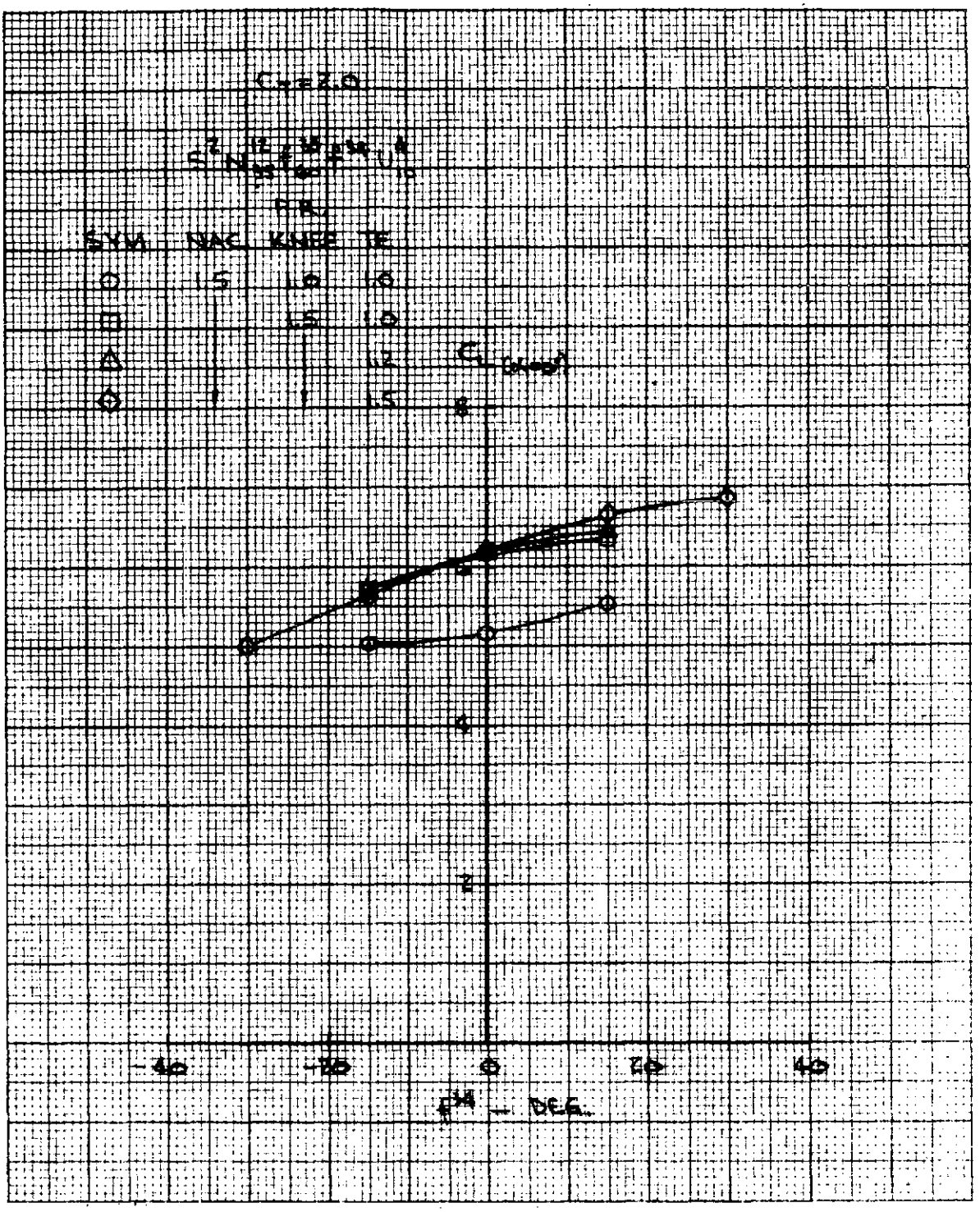

Figure 128. - Aft Flap Effectiveness with Various Blowing Inputs on the High Wing Model, 60° J/H Flap, 10° Open Deflector, Tail Off

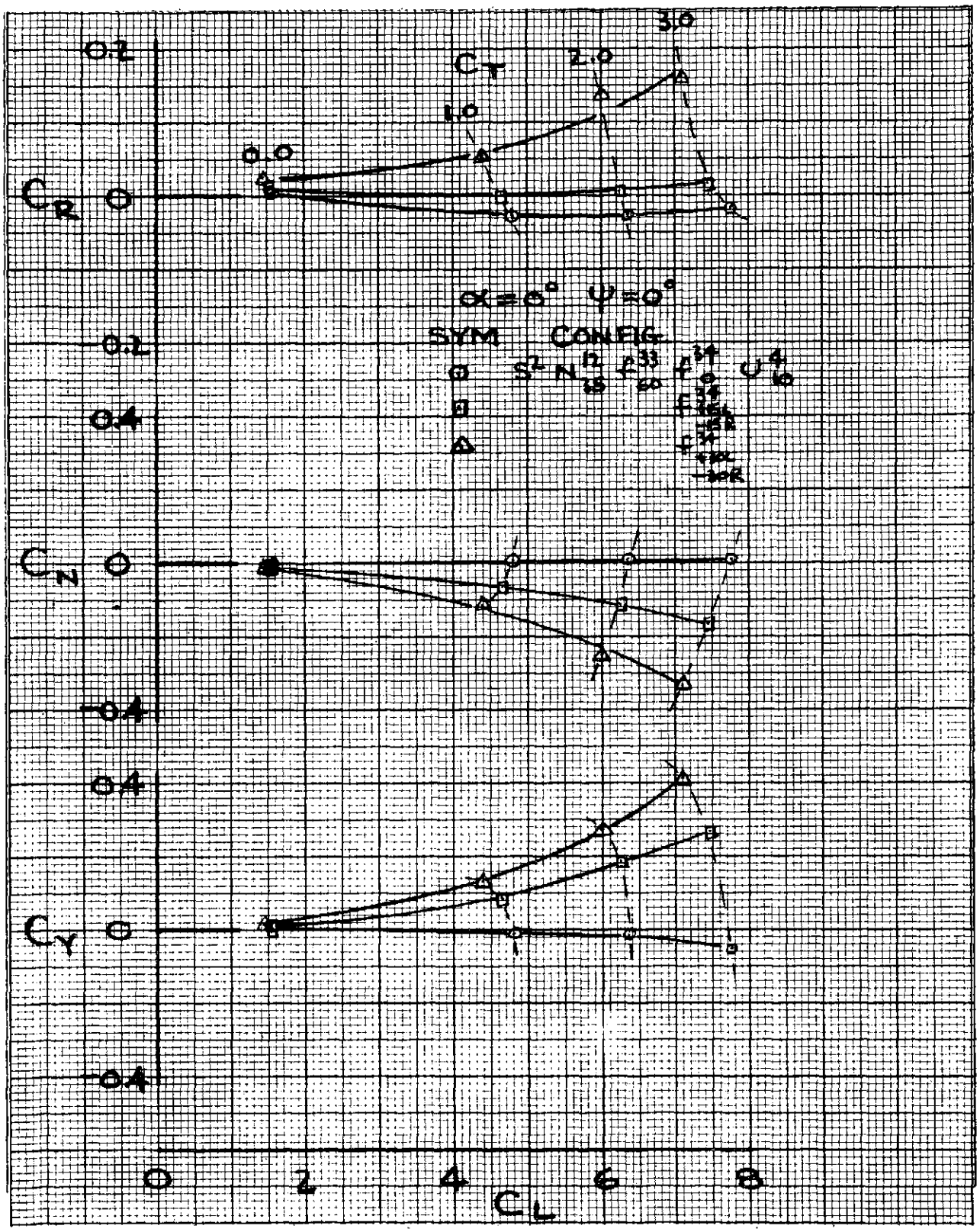

Figure 129. - Effect of Asymmetric Aft Flap Deflection on Lateral-Directional Characteristics of the High Wing Model, 60° J/H Flap, 10° Open Deflector, Tail Off

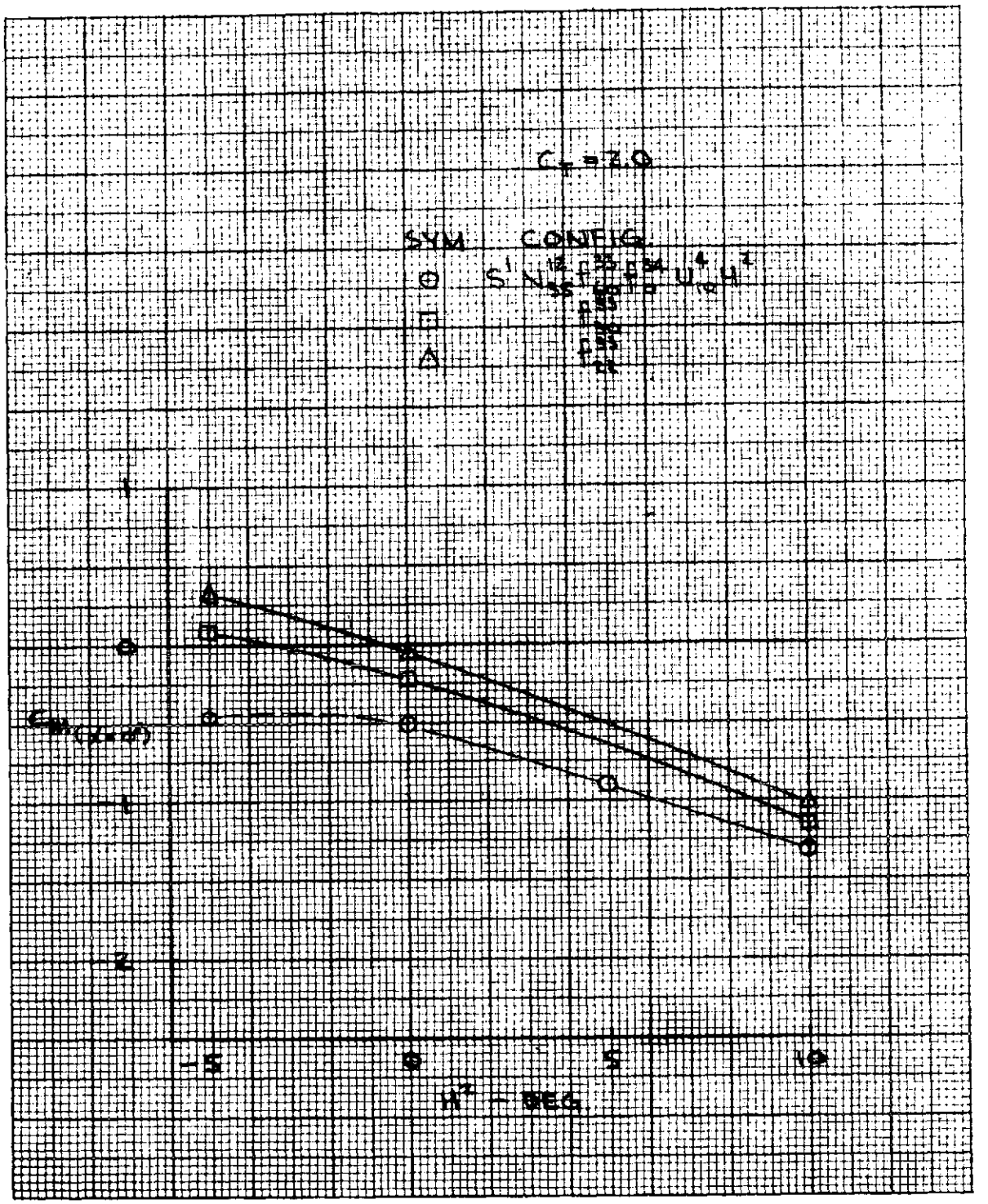

Figure 130. - Effect of Horizontal Tail Incidence and Flap Deflection on Pitching Moment of the High Wing Model, J/H Flap, 10° Open Deflector

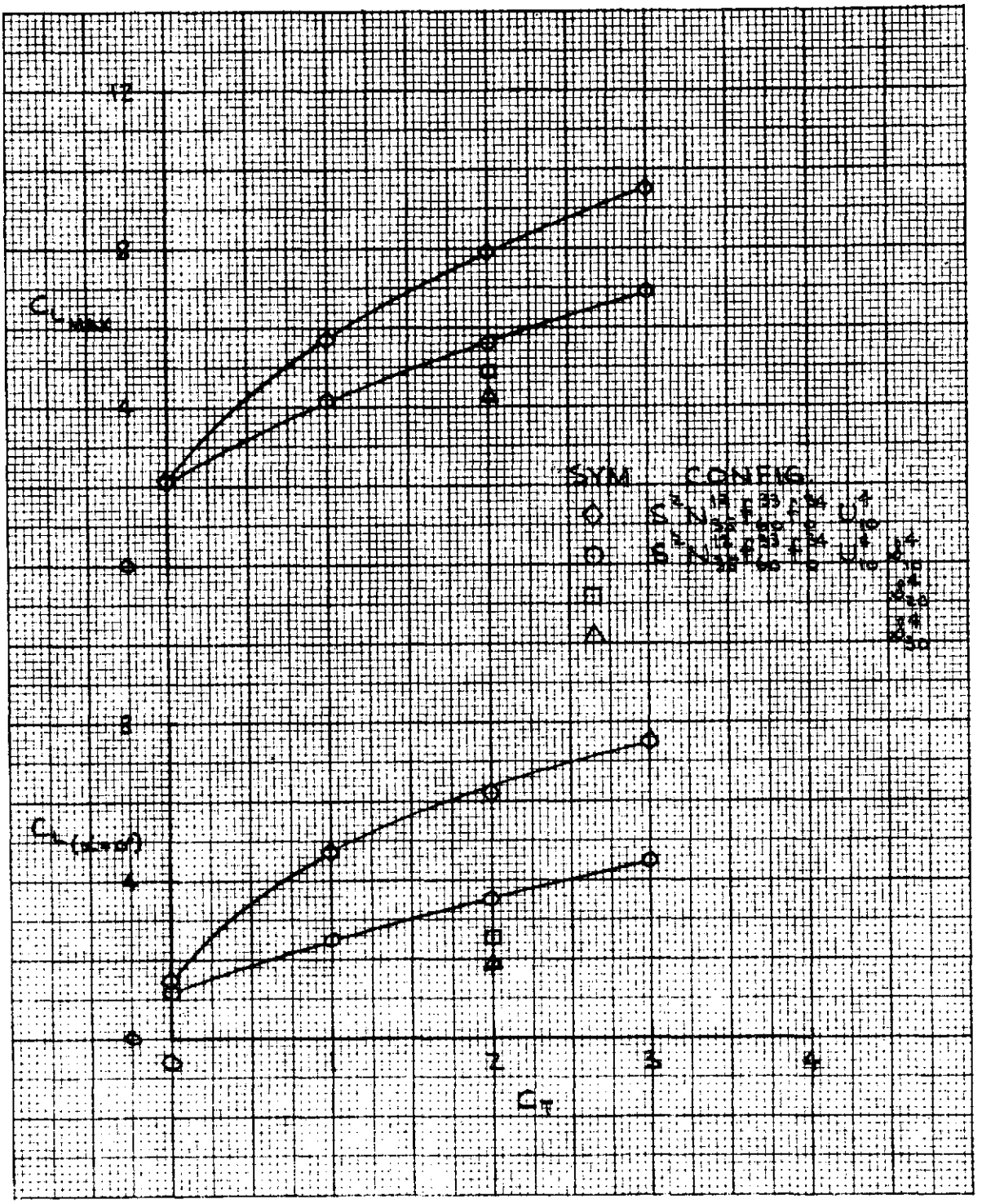

Figure 131. - Lift Variation with C_T and Full Flap-Span Solid Spoiler Deflection on the High Wing Model, 60°/0° J/H Flap, 10° Open Deflector, Tail Off

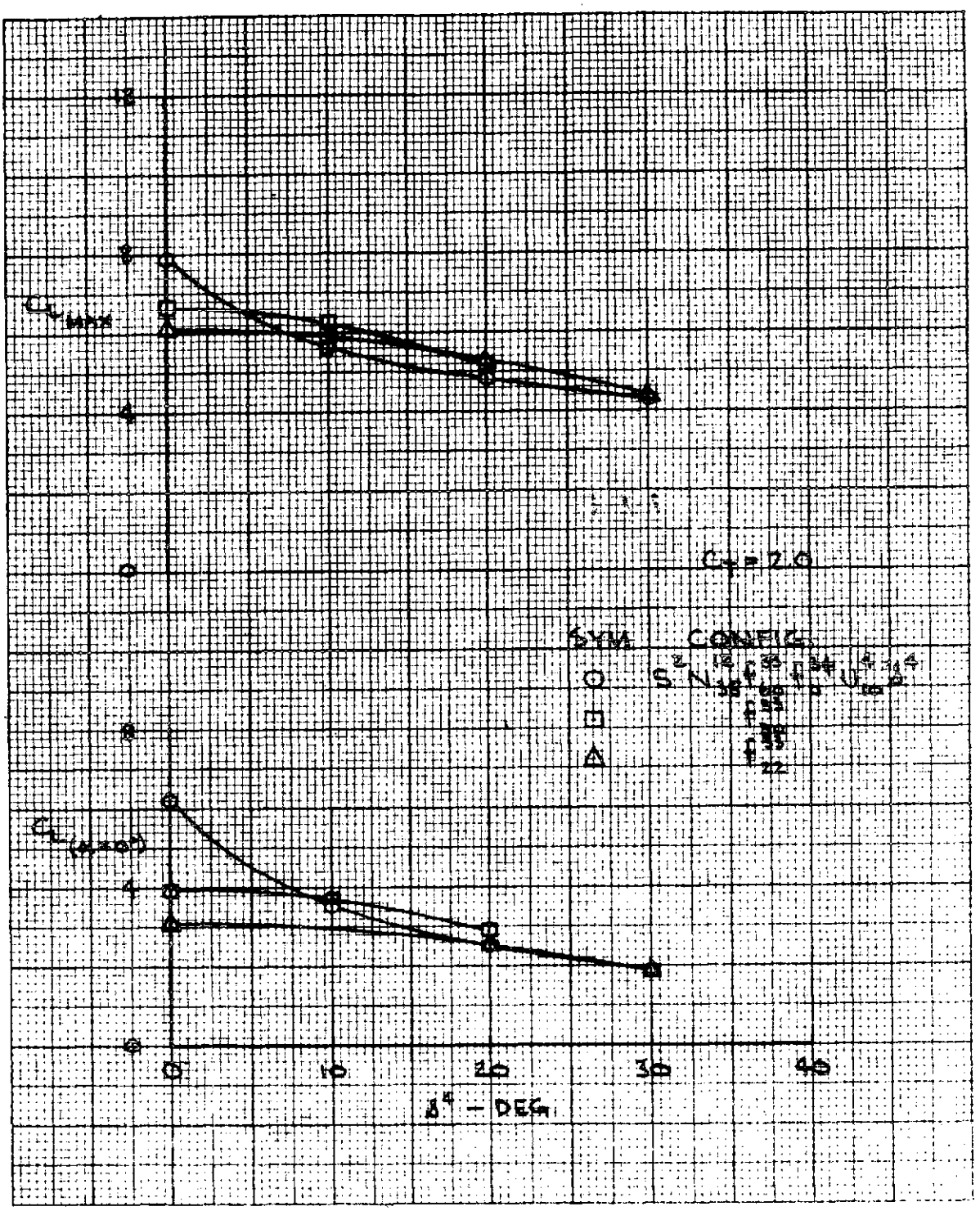

Figure 132. – Lift Variation with Full Flap-Span Solid Spoiler Deflection on the High Wing Model, J/H Flap, 10° Open Deflector, Tail Off

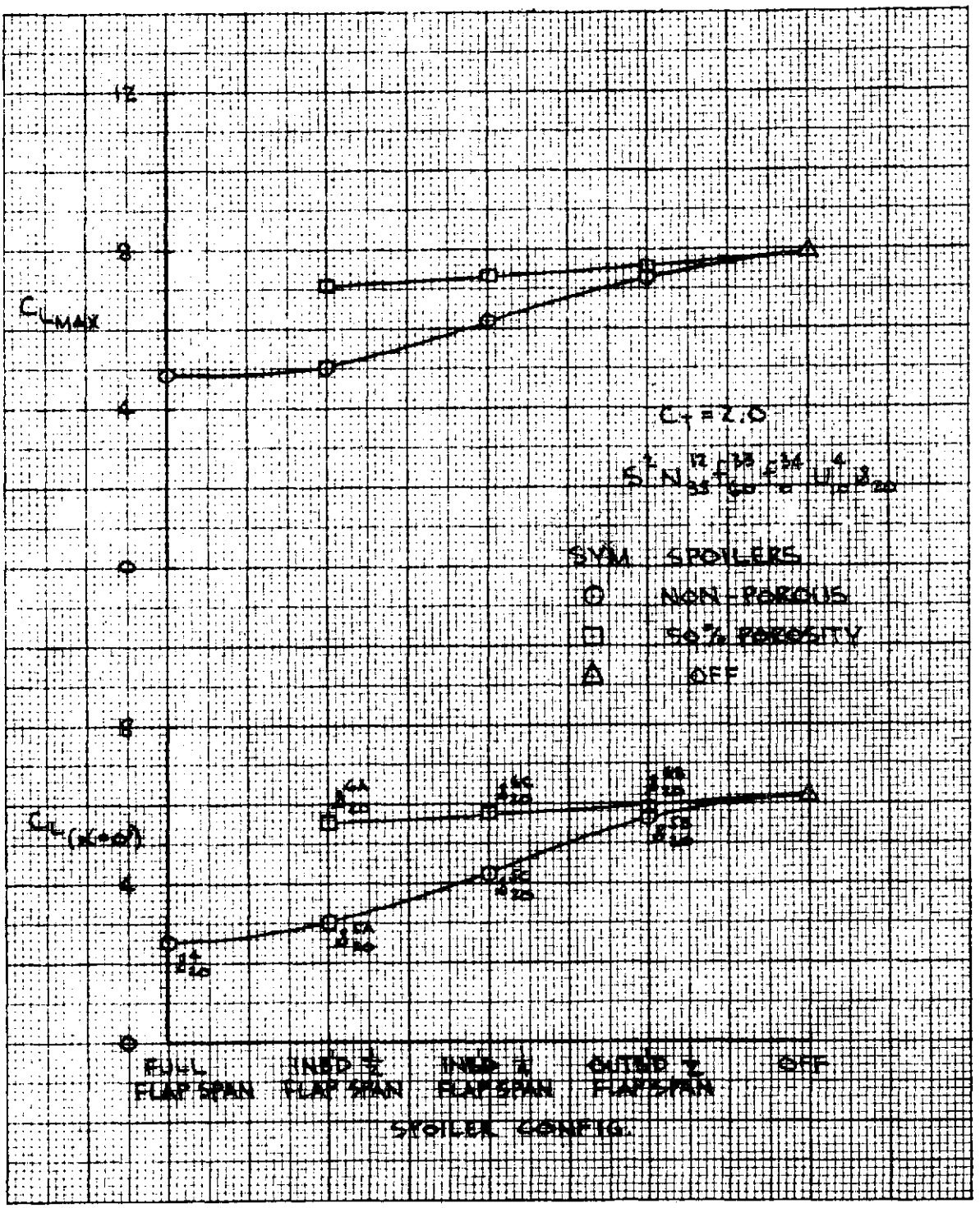

Figure 133. - Lift Variation with 20° Spoiler Configuration on the High Wing Model, 60°/0° J/H Flap, 10° Open Deflector, Tail Off

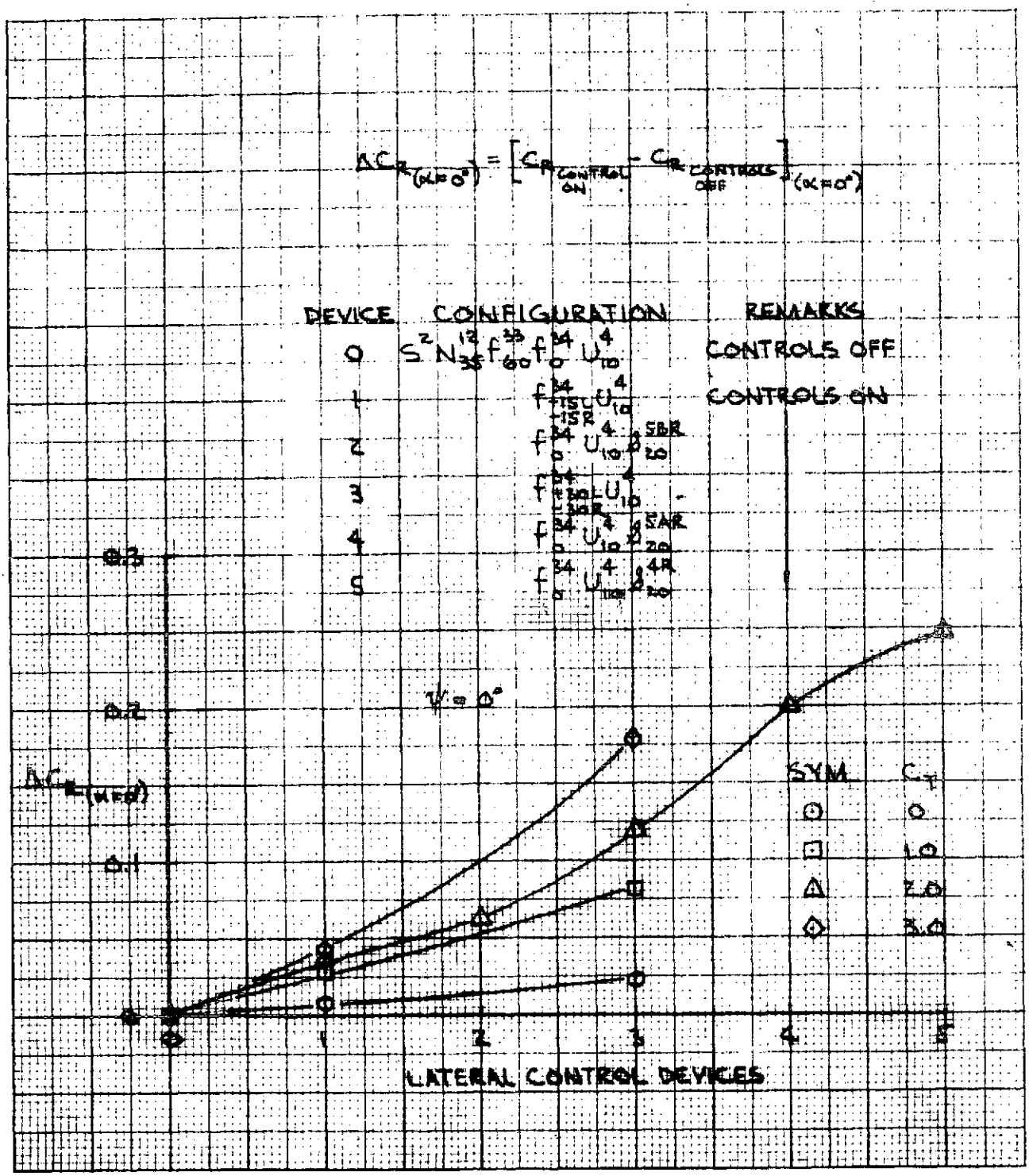

Figure 134. - Roll Control Power of Various Lateral Control Devices on the High Wing Model, 60° J/H Flap, 10° Open Deflector, Tail Off

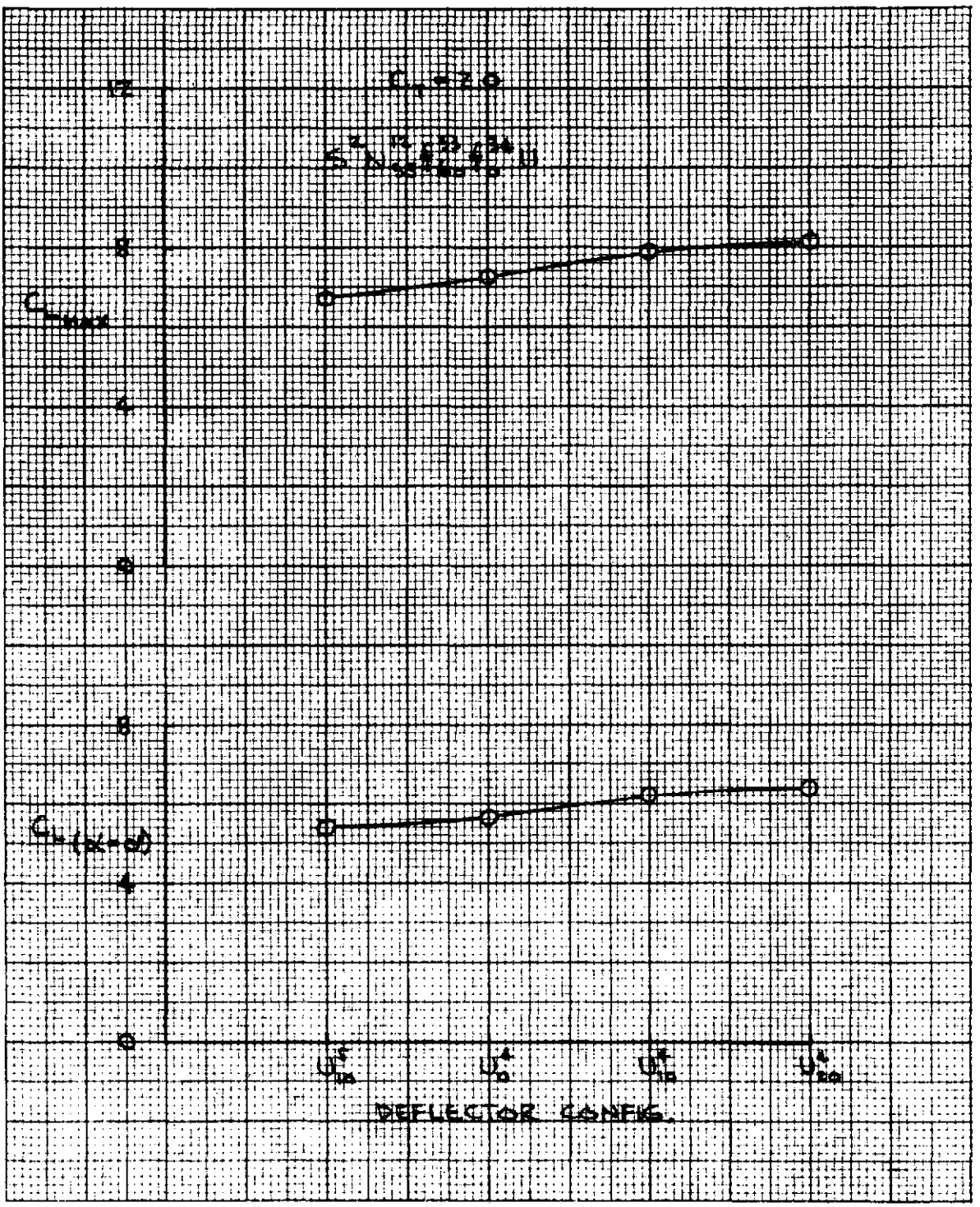

Figure 135. - Lift Variation with Nacelle Exit Configuration on the High Wing Model, 60°/0° J/H Flap, Tail Off

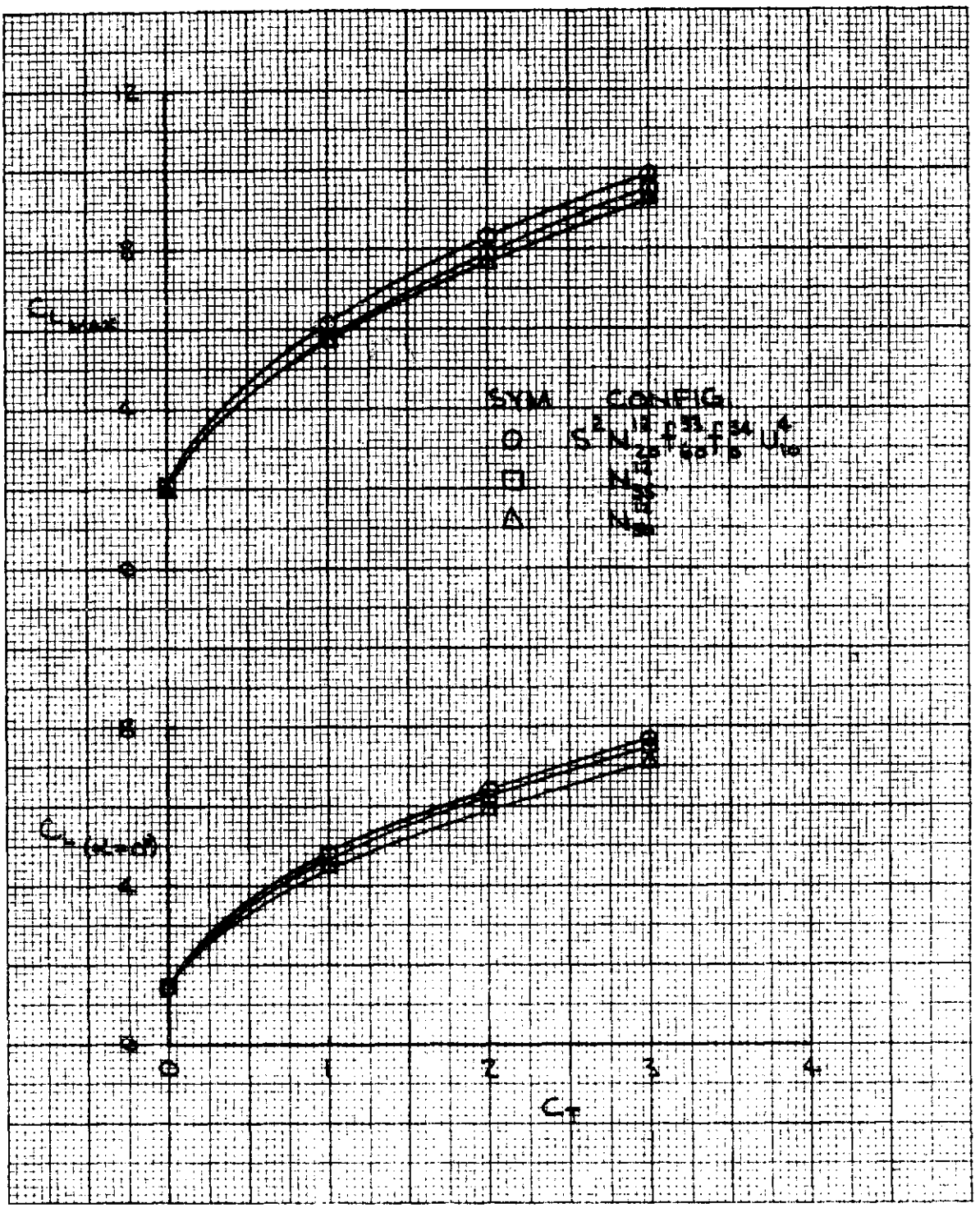

Figure 136. - Lift Variation with C_T and Nozzle Exit Chordwise Position on the High Wing Model, 60°/0° J/H Flap, 10° Open Deflector, Tail Off

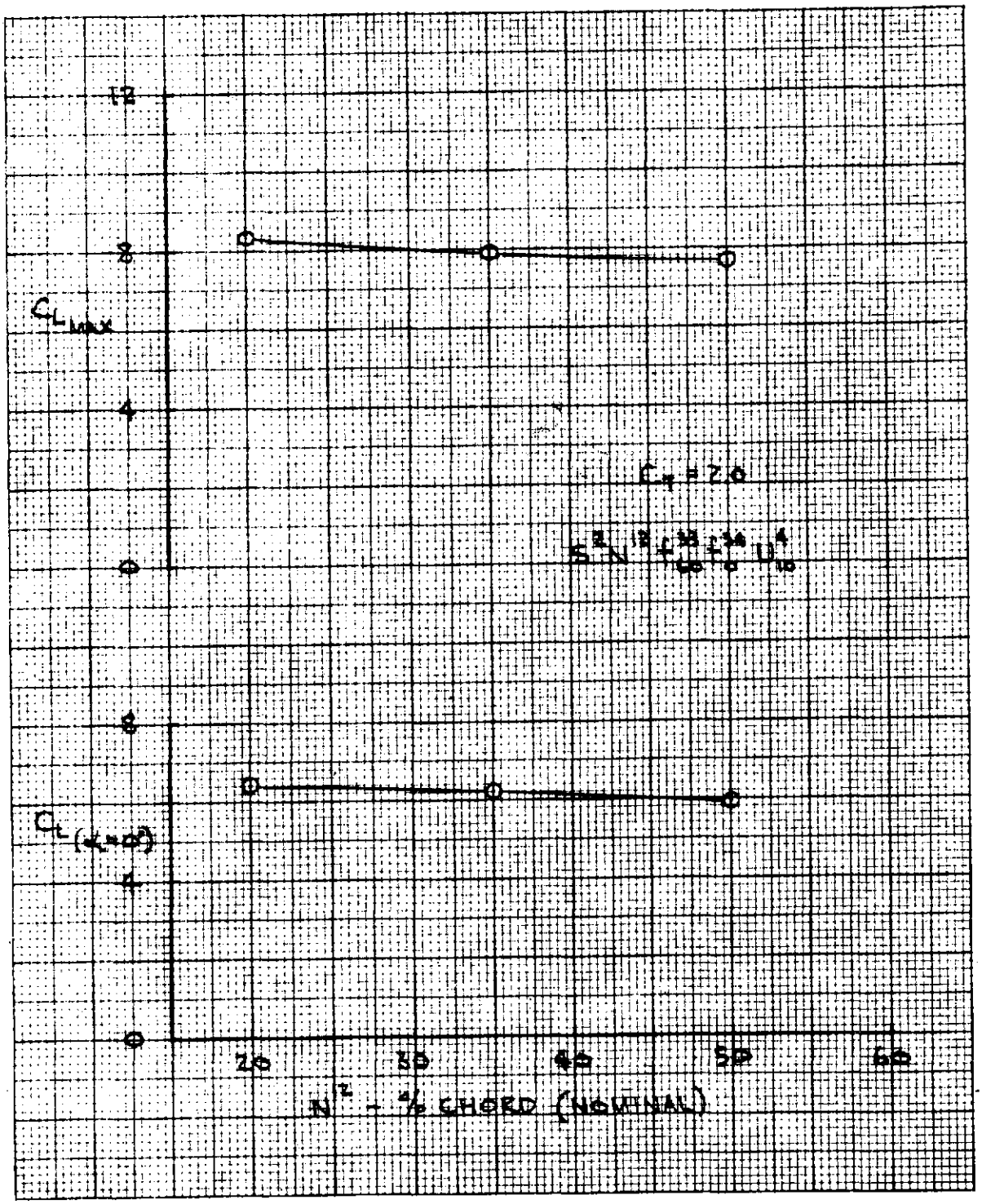

Figure 137. - Lift Variation with Nacelle Exit Chordwise Position at a C_μ of 2.0 on the High Wing Model, $60^\circ/0^\circ$ J/H Flap, 10° Open Deflector, Tail Off

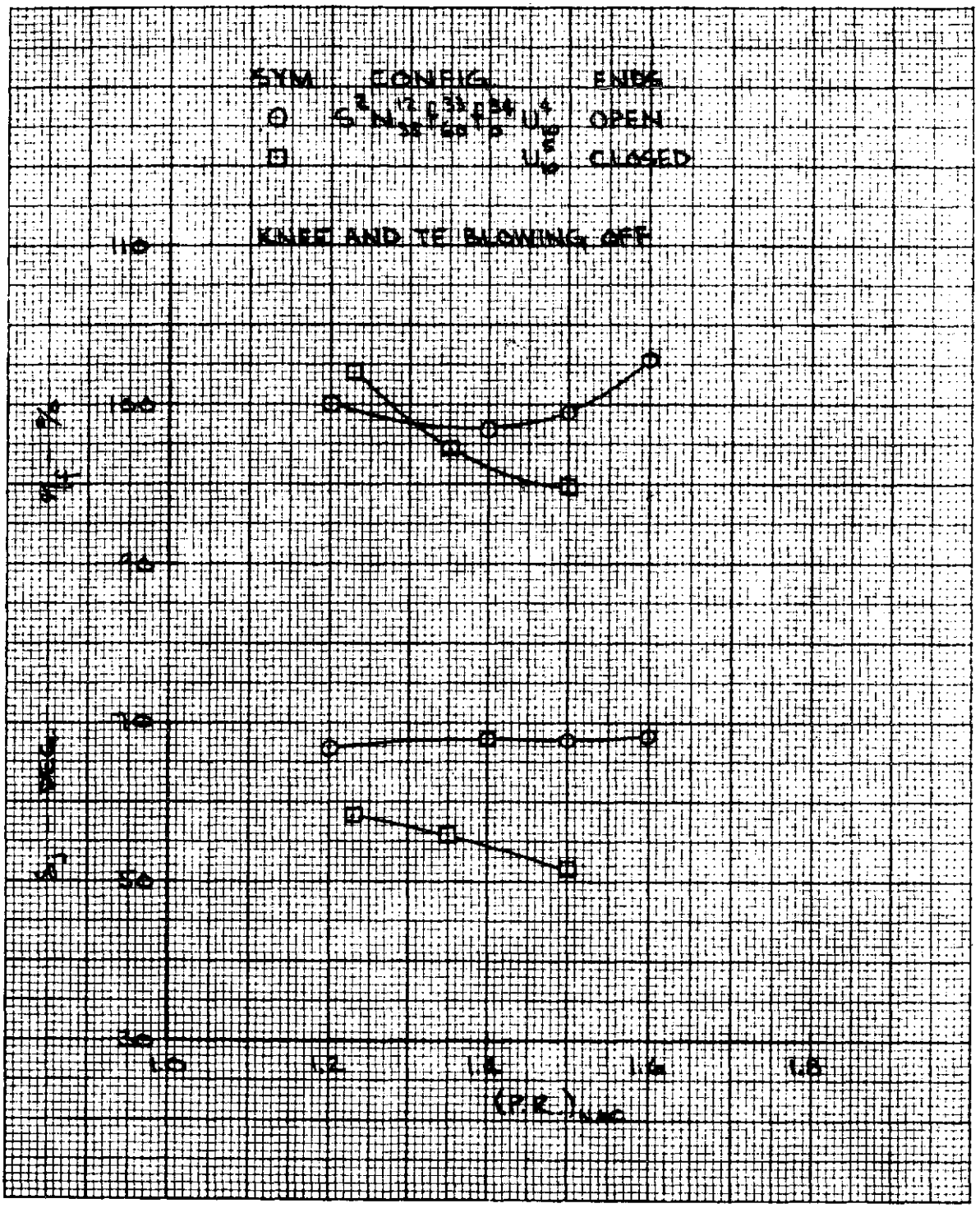

Figure 138. - Static Jet Angle and Turning Efficiency of the High Wing Model with USB only, 10° Open and 10° Closed Deflectors, 60°/0° J/H Flap, Tail Off

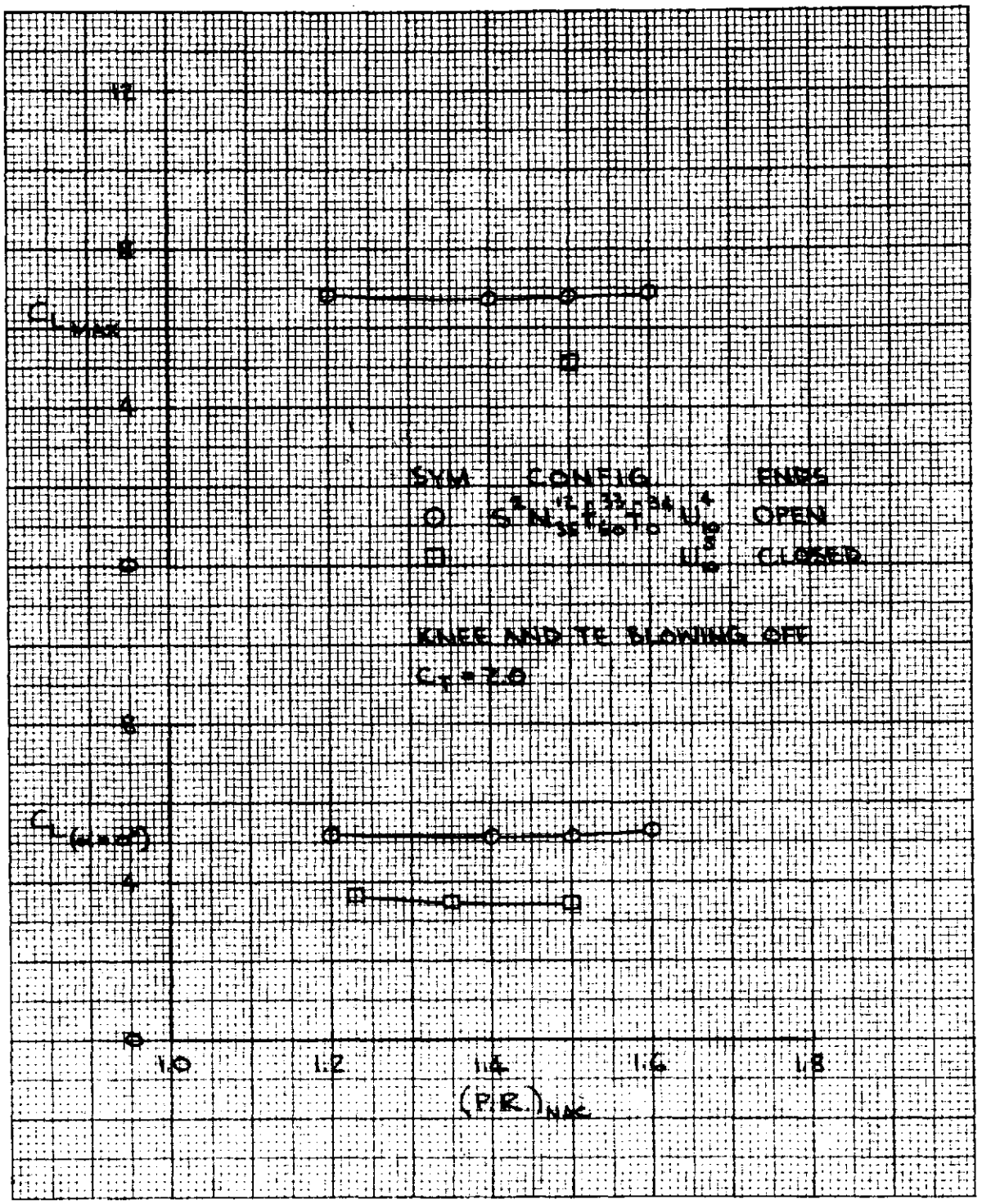

Figure 139. - Lift Variation with Pressure Ratio on the High Wing Model with USB only, 10° Open and 10° Closed Deflectors, 60°/0° J/H Flap, Tail Off

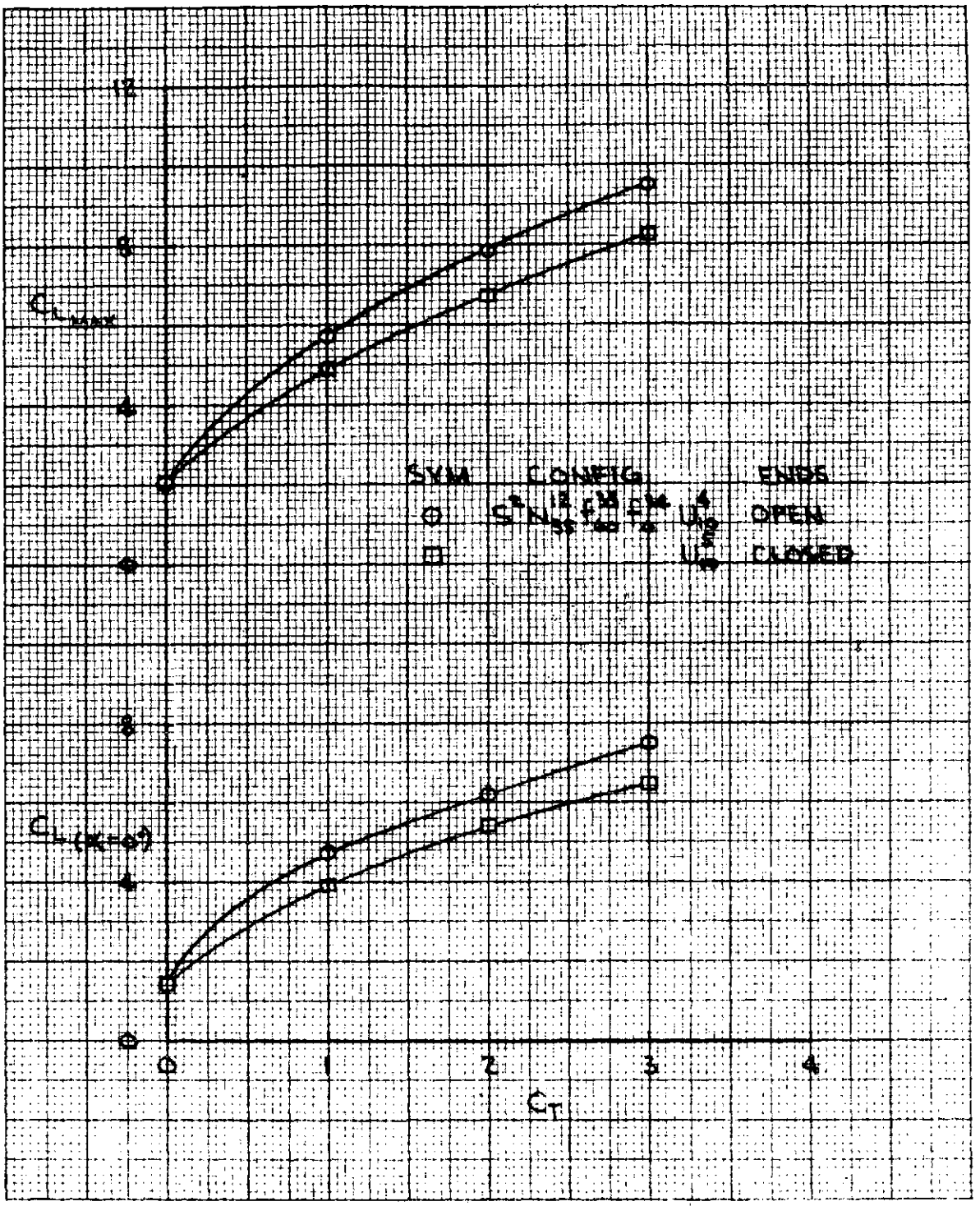

Figure 140. - Lift Variation with C_T on the High Wing Model, 60°/0° J/H Flap, 10° Open and 10° Closed Deflectors, Tail Off

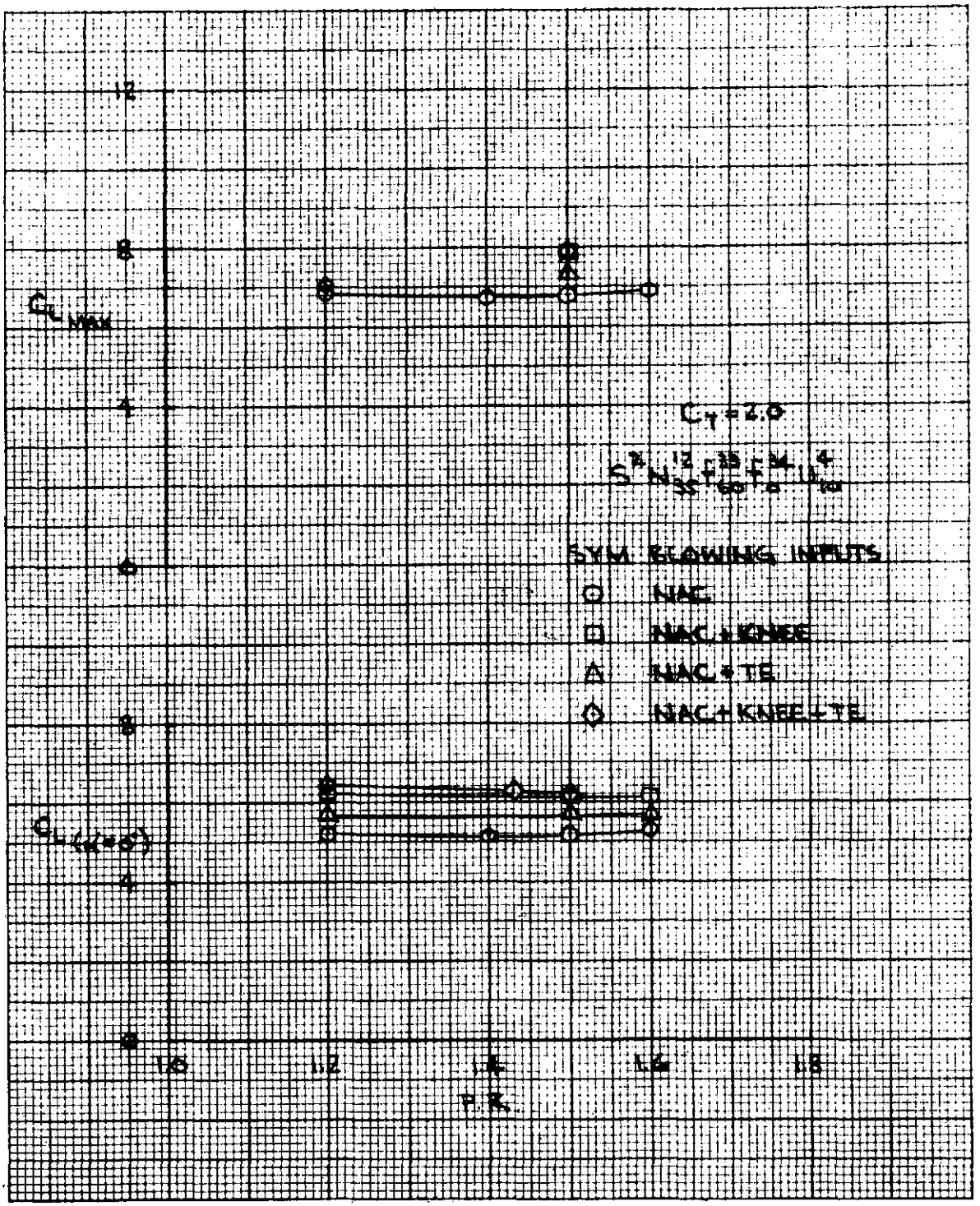

Figure 141. - Lift Variation with Pressure Ratio and Various Blowing Inputs on the High Wing Model, $60^\circ/0^\circ$ J/H Flap, 10° Open Deflector, Tail Off

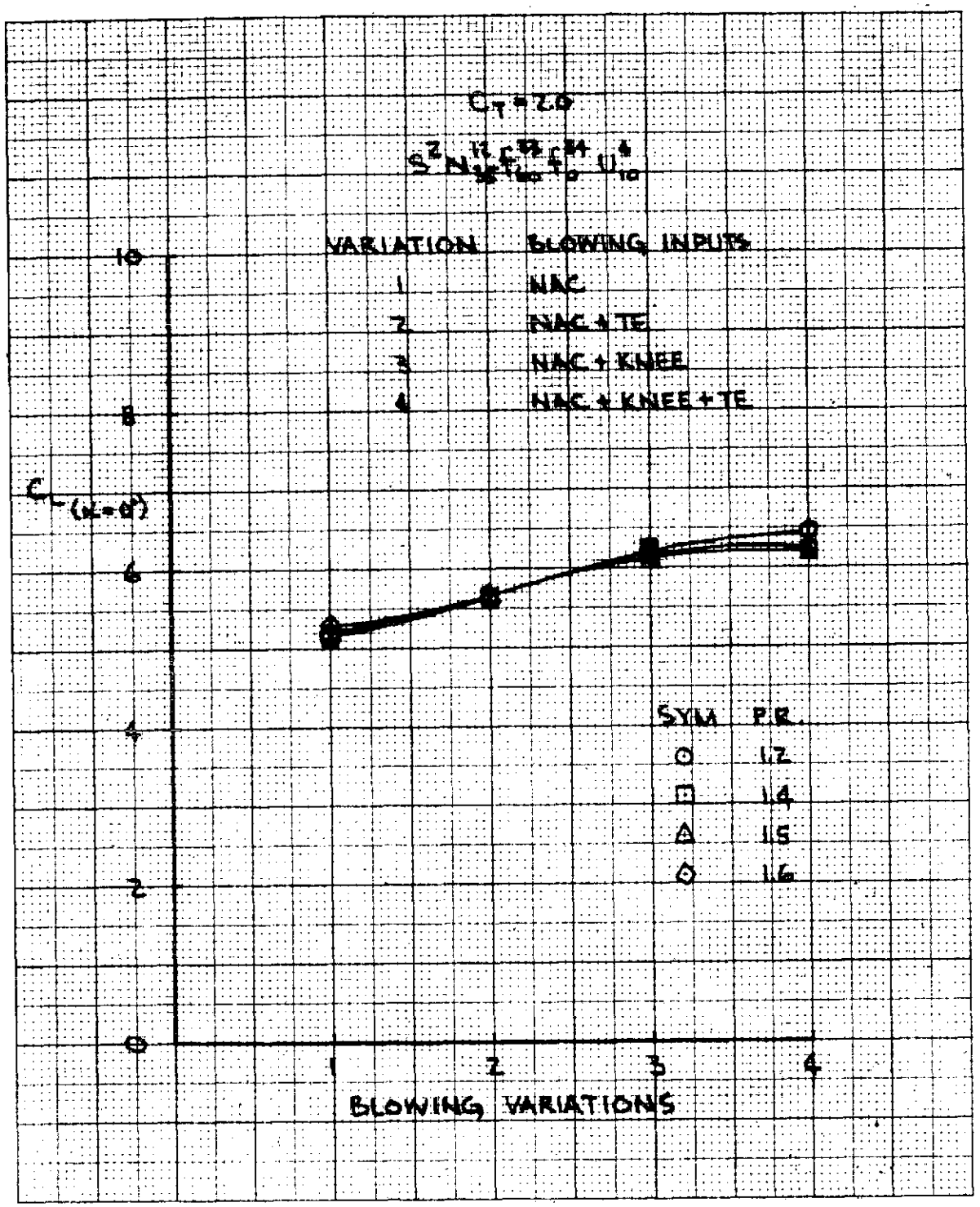

Figure 142. - Lift Variation with Various Blowing Inputs on the High Wing Model, $60^\circ/0^\circ$ J/H Flap, 10° Open Deflector, Tail Off

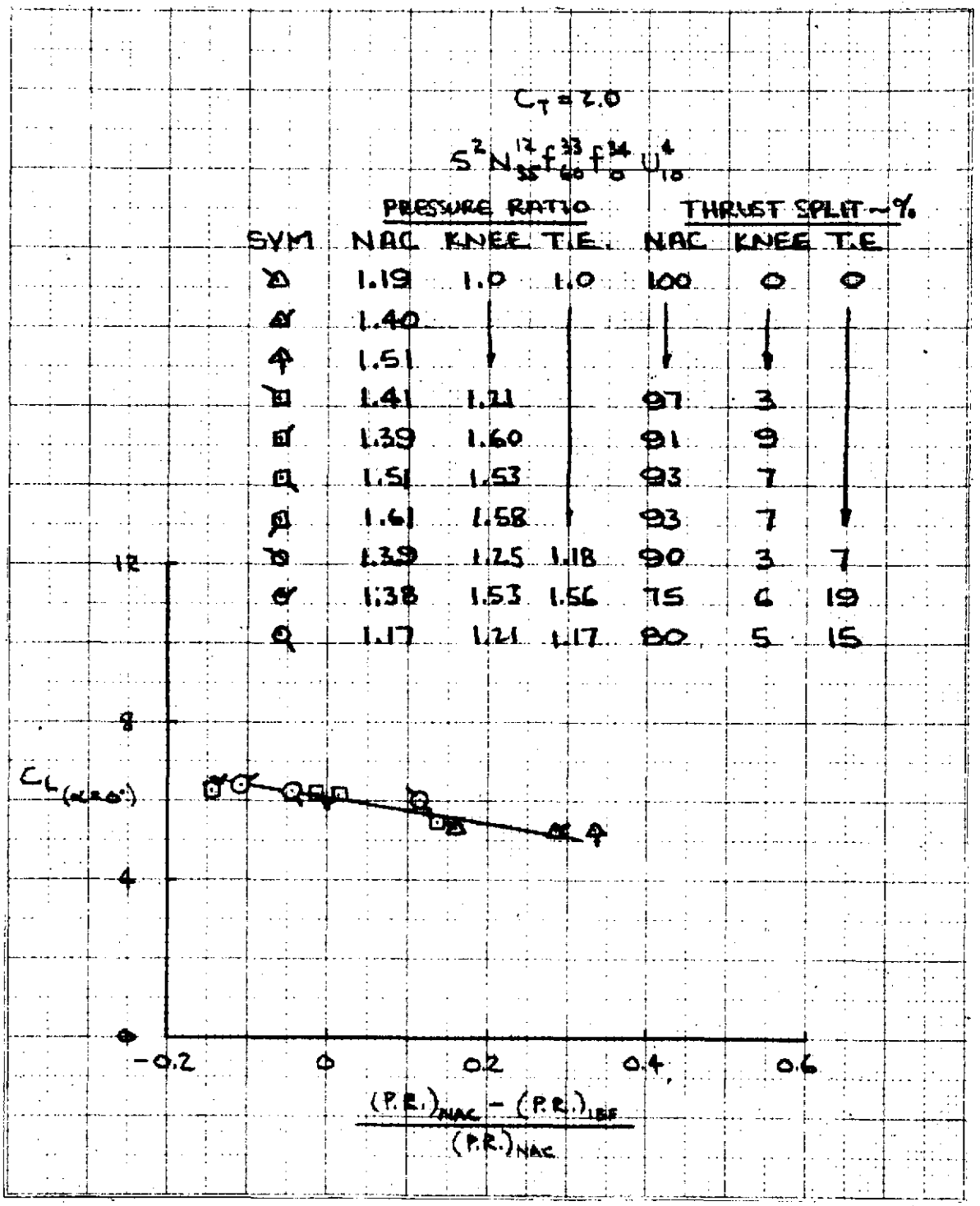

Figure 143. - Lift Variation with Pressure Ratio Differential on the High Wing Model at a C_T of 2.0, $60^\circ/0^\circ$ J/H Flap, 10° Open Deflector, Tail Off